

RETREATING BLADE STALL CONTROL ON A NACA 0015 AEROFOIL BY MEANS OF A TRAILING EDGE FLAP

Fotios K. Tsiachris (BEng, MSc)

Thesis submitted to the Faculty of Engineering, University of Glasgow, for the degree of Doctor of Philosophy. All aspects of the work contained herein are original in content except where indicated.

This thesis is based on research conducted between May 2000 and June 2005 at the Department of Aerospace Engineering, University of Glasgow.

©Fotios K. Tsiachris, June 2005



University
of Glasgow

Tsiachris, Fotios K. (2005) *Retreating blade stall control on a NACA 0015 aerofoil by means of a trailing edge flap*. PhD thesis.

<http://theses.gla.ac.uk/5109/>

Copyright and moral rights for this thesis are retained by the author

A copy can be downloaded for personal non-commercial research or study, without prior permission or charge

This thesis cannot be reproduced or quoted extensively from without first obtaining permission in writing from the Author

The content must not be changed in any way or sold commercially in any format or medium without the formal permission of the Author

When referring to this work, full bibliographic details including the author, title, awarding institution and date of the thesis must be given

Contents

Contents	i
List of Figures	vi
List of Tables	xv
Nomenclature	xviii
List of Acronyms	xxvii
Abstract	xxxi
Acknowledgements	1
1 Introduction	3
1.1 Dynamic stall	5
1.2 Dynamic stall and Aerodynamic damping	12
1.3 Flow control	16
1.3.1 Drag reduction	22

1.3.2	Boundary layer- separation & transition	23
1.3.3	Lift enhancement	28
1.3.4	Vibration reduction	31
1.4	Flapped rotor	33
1.5	Proposed flow control solution	38
1.6	Aim and objectives of the present study	42
1.7	Thesis overview	44
2	Flow solver and experimental validation	45
2.1	General DVM description	46
2.2	Mathematical model	48
2.3	Flow field Discretisation	55
2.4	Pressure and vorticity around the aerofoil	61
2.4.1	Pressure distribution around the aerofoil	61
2.4.2	Vorticity distribution around the aerofoil	63
2.4.3	Airloads around the aerofoil	65
2.5	Simulation of the Dynamic Stall phenomenon	65
2.6	Code validation	67
2.6.1	Dynamic stall vortex convection speed	72
2.7	Concluding remarks	76
3	Flow topology	77
3.1	Assumptions & simplifications	78

3.2	Dynamic stall flow field over clean aerofoil	81
3.3	Influence of the flap on Dynamic stall flowfield	85
3.4	Unsteady pressure	89
3.5	Vorticity	99
3.6	Flap aerodynamic mechanism	108
3.7	Concluding remarks	119
4	Parametric study	120
4.1	Parametric methodology	121
4.2	Geometric Parameters	122
4.2.1	Aerofoil and flap size	122
4.2.2	Flap notches	126
4.3	Actuation parameters	128
4.3.1	Flap deflection amplitude	128
4.3.2	Flap phasing	133
4.3.3	Reduced frequency	136
	Normal force	139
	Pitching moment	142
4.4	Flap dynamic properties and mechanical requirements	144
4.4.1	Flap mass moment of inertia	144
4.4.2	Flap hinge moment	145
4.4.3	Flap actuation power	147
4.5	Concluding remarks	151

5	Control strategy	152
5.1	Formulation of the optimisation problem	153
5.2	Optimisation methodology	157
5.3	Optimisation procedure	163
5.3.1	Optimisation case I	166
5.3.2	Optimisation case II	174
5.3.3	Optimisation case III	182
5.3.4	Optimisation case IV	189
5.4	Grid resolution for the period of actuation.	198
5.5	Concluding remarks	217
6	Conclusions and future work	221
6.1	Conclusions	221
6.2	Future work	224
	Appendices	227
A		227
A.1	Unsteady Bernoulli equation	227
A.2	Circulatory & non-circulatory terms	228
A.3	Vorticity stream function and vorticity transport equation . .	229
A.4	Theorems	231
A.4.1	Gauss' and Green's theorems	231

A.4.2	Stoke's Theorem	233
A.4.3	Biot-Savart law	234
B		236
B.1	Flap aerodynamic hinge moment	236
B.2	Flap moment of inertia	238
B.2.1	Flap centroid determination	240
B.2.2	Calculation of flap moment of inertia	242
B.2.3	Flap dynamic mass balancing	248
Bibliography		251

List of Figures

1.1	Flow topology and unsteady airloads during DS of an oscillating 2-D aerofoil, adapted from [1].	7
1.2	Light- and deep dynamic stall, adapted from [2].	11
1.3	Pitching moment hysteresis loop with positive (counterclockwise) and negative (clockwise) aerodynamic damping.	14
1.4	Concept of helicopter active control strategies. Adapted from [3].	36
2.1	Reference coordinate system and flow regions. Adapted from Lin [4].	50
2.2	Illustration of vorticity layer, adapted from Lin [4].	56
2.3	Creation and wake zone, adapted from Lin [4].	57
2.4	Aerofoil surface panel discretisation, adapted from Lin [4].	58
2.5	Numerical and experimental comparison for sectional normal force and pitching moment.	69
2.6	Determination of streamwise DSV convection speed.	74

3.1 Overview of DSV (dynamic stall vortex) initiation angle as function of the reduced frequency for NACA 0015. $\theta(t) = 15^\circ \pm 7^\circ \sin(\omega t)$, $M = 0.119$, $Re = 1.49 \times 10^6$ 82

3.2 Sequence of the instantaneous vortex particles (LHS) and velocity vectors (RHS) at the trailing edge region of clean NACA 0015: $\theta(t) = 15^\circ \pm 7^\circ \sin(\omega t)$, $k = 0.180$, $M = 0.119$, $Re = 1.49 \times 10^6$. (cont.) 83

3.2 Sequence of the instantaneous vortex particles (LHS) and velocity vectors (RHS) at the trailing edge region of clean NACA 0015: $\theta(t) = 15^\circ \pm 7^\circ \sin(\omega t)$, $k = 0.180$, $M = 0.119$, $Re = 1.49 \times 10^6$ 84

3.3 Time sequence of the instantaneous vortex particles (LHS) and velocity vectors (RHS) at the trailing edge region of flapped NACA 0015: $\theta(t) = 15^\circ \pm 7^\circ \sin(\omega t)$, $k = 0.180$, $M = 0.119$, $Re = 1.49 \times 10^6$. (cont.) 87

3.3 Time sequence of the instantaneous vortex particles (LHS) and velocity vectors (RHS) at the trailing edge region of flapped NACA 0015: $\theta(t) = 15^\circ \pm 7^\circ \sin(\omega t)$, $k = 0.180$, $M = 0.119$, $Re = 1.49 \times 10^6$ 88

3.4 Averaged surface pressure (suction surface) for clean and flapped case: $\theta(t) = 15^\circ \pm 7^\circ \sin(\omega t)$, $k = 0.154$, $M = 0.119$, $Re = 1.49 \times 10^6$ 90

3.5	Instantaneous surface pressure for clean and flapped case: $\theta(t) = 15^\circ \pm 7^\circ \sin(\omega t)$, $k = 0.154$, $M = 0.119$, $Re = 1.49 \times 10^6$. . .	93
3.6	Typical instantaneous surface pressure variation over the suction surface. $\theta(t) = 15^\circ \pm 7^\circ \sin(\omega t)$, $k = 0.154$, $Re = 1.48 \times 10^6$, $M_\infty = 0.1209$	94
3.7	Variation of surface pressure associated with the characteristic peaks. $\theta(t) = 15^\circ \pm 7^\circ \sin(\omega t)$, $k = 0.128$, $Re = 1.48 \times 10^6$, $M_\infty = 0.1209$	95
3.8	Variation of surface pressure associated with the characteristic peaks. $\theta(t) = 15^\circ \pm 7^\circ \sin(\omega t)$, $k = 0.154$, $Re = 1.48 \times 10^6$, $M_\infty = 0.1209$	97
3.9	Variation of surface pressure associated with the characteristic peaks. $\theta(t) = 15^\circ \pm 7^\circ \sin(\omega t)$, $k = 0.180$, $Re = 1.48 \times 10^6$, $M_\infty = 0.1209$	98
3.10	Averaged surface vorticity flux (suction surface) for clean and flapped case: $\theta(t) = 15^\circ \pm 7^\circ \sin(\omega t)$, $k = 0.154$, $M = 0.119$, $Re = 1.49 \times 10^6$	100
3.11	Typical surface vorticity flux variation over the suction surface. $15^\circ \pm 7^\circ \sin(\omega t)$, $k = 0.154$, $Re = 1.48 \times 10^6$, $M_\infty = 0.1209$	101

3.12	Variation of surface vorticity flux associated with the characteristic peaks. $\theta(t) = 15^\circ \pm 7^\circ \sin(\omega t)$, $k = 0.154$, $Re = 1.48 \times 10^6$, $M_\infty = 0.1209$	102
3.13	Instantaneous evolution of surface chordwise vorticity flux for clean NACA 0015. $\theta(t) = 15^\circ \pm 7^\circ \sin(\omega t)$, $k = 0.154$, $Re = 1.48 \times 10^6$, $M_\infty = 0.1209$ (cont)	104
3.13	Instantaneous evolution of surface chordwise vorticity flux for clean NACA 0015. $\theta(t) = 15^\circ \pm 7^\circ \sin(\omega t)$, $k = 0.154$, $Re = 1.48 \times 10^6$, $M_\infty = 0.1209$	105
3.14	Instantaneous evolution of surface chordwise vorticity flux for flapped NACA 0015. $\theta(t) = 15^\circ \pm 7^\circ \sin(\omega t)$, $\delta_{f_{max}} = 20^\circ$, $k = 0.154$, $Re = 1.48 \times 10^6$, $M_\infty = 0.1209$	106
3.14	Instantaneous evolution of surface chordwise vorticity flux for flapped NACA 0015. $\theta(t) = 15^\circ \pm 7^\circ \sin(\omega t)$, $\delta_{f_{max}} = 20^\circ$, $k = 0.154$, $Re = 1.48 \times 10^6$, $M_\infty = 0.1209$	107
3.15	Time sequence of the instantaneous vortex particles at the trailing edge region of clean (LHS) and flapped (RHS) NACA 0015: $\theta(t) = 15^\circ \pm 7^\circ \sin(\omega t)$, $\delta_{f_{max}} = 20^\circ$, $k = 0.128$, $M = 0.119$, $Re = 1.49 \times 10^6$.(cont)	114

3.15	Time sequence of the instantaneous vortex particles at the trailing edge region of clean (LHS) and flapped (RHS) NACA 0015: $\theta(t) = 15^\circ \pm 7^\circ \sin(\omega t)$, $\delta_{f_{max}} = 20^\circ$, $k = 0.128$, $M = 0.119$, $Re = 1.49 \times 10^6$	115
3.16	Time sequence of the instantaneous pressure distribution (LHS) and vorticity gradient (RHS) for clean and flapped NACA 0015: $\theta(t) = 15^\circ \pm 7^\circ \sin(\omega t)$, $\delta_{f_{max}} = 20^\circ$, $k = 0.128$, $M = 0.119$, $Re = 1.49 \times 10^6$.(cont)	116
3.16	Time sequence of the instantaneous pressure distribution (LHS) and vorticity gradient (RHS) for clean and flapped NACA 0015: $\theta(t) = 15^\circ \pm 7^\circ \sin(\omega t)$, $\delta_{f_{max}} = 20^\circ$, $k = 0.128$, $M = 0.119$, $Re = 1.49 \times 10^6$	117
3.17	DSV and TEV trajectory modification for clean- and flapped case: $\theta(t) = 15^\circ \pm 7^\circ \sin(\omega t)$, $\delta_{f_{max}} = 20^\circ$, $M = 0.119$, $Re = 1.48 \times 10^6$	118
4.1	NACA 0015 rotor blade profile equipped with a 15%c plain trailing edge flap.	123
4.2	Pitching moment coefficient for flap sizes varying from 9%c-13%c, $\theta(t) = 15^\circ \pm 7^\circ \sin(\omega t)$, $\delta_f = 25^\circ$, $k = 0.154$, $Re = 1.49 \times 10^6$, $M = 0.119$	125

4.3	Various flap notches on a NACA 0015 equipped with a 0.15c trailing edge flap (a), together with the corresponding pressure distribution (b), (suction surface).	127
4.4	Effect of flap deflection amplitude: $\theta(t) = 15^\circ \pm 7^\circ \sin(\omega t)$, $Re = 1.48 \times 10^6$, $M_\infty = 0.1209$ (cont).	130
4.4	Effect of flap deflection amplitude: $\theta(t) = 15^\circ \pm 7^\circ \sin(\omega t)$, $Re = 1.48 \times 10^6$, $M_\infty = 0.1209$	131
4.5	Initial and final aerofoil incidence as function of the reduced frequency. $\theta(t) = 15^\circ \pm 7^\circ \sin(\omega t)$, $Re = 1.48 \times 10^6$, $M_\infty = 0.1209$	136
4.6	Effect of aerofoil reduced frequency. $\theta(t) = 15^\circ \pm 7^\circ \sin(\omega t)$, $\delta_{f_{max}} = 20^\circ$, $Re = 1.48 \times 10^6$, $M_\infty = 0.1209$	138
4.7	Normal force for clean and flapped NACA 0015 for various reduced frequencies. $\theta(t) = 15^\circ \pm 7^\circ \sin(\omega t)$, $\delta_{f_{max}} = 20^\circ$, $Re = 1.49 \times 10^6$, $M_\infty = 0.119$	141
4.8	Pitching moment for clean and flapped NACA 0015 for various reduced frequencies. $\theta(t) = 15^\circ \pm 7^\circ \sin(\omega t)$, $\delta_{f_{max}} = 20^\circ$, $Re = 1.49 \times 10^6$, $M_\infty = 0.119$	143
4.9	Average flap aerodynamic and inertial moment about the flap hinge required for the flap actuation.	146
4.10	Power required for the flap actuation.	149
5.1	Aerofoil incidence and flap deflection profiles.	159

5.2	Variation of objective function J_1 at the initial grid.	161
5.3	Design space grid resolution.	164
5.4	Grid topology resolution with respect to the design space variable T_{δ_f}	165
5.5	Variation of objective function J_1 over the design space.	169
5.6	Variation of normalised variables for optimisation case I.	170
5.7	Airloads variation subject to table 5.5.	172
5.8	Initiation and duration of flap actuation as function of the reduced frequency for optimisation case I.	173
5.9	Variation of objective function J_2 over the design space.	177
5.10	Variation of normalised variables for optimisation case II.	178
5.11	Airloads variation subject to table 5.7.	180
5.12	Initiation and duration of flap actuation as function of the reduced frequency for optimisation case II.	181
5.13	Variation of objective function J_3 over the design space.	184
5.14	Variation of normalised variables for optimisation case III.	185
5.15	Airloads variation subject to table 5.9.	187
5.16	Initiation and duration of flap actuation as function of the reduced frequency for optimisation case III.	188
5.17	Variation of objective function J_4 over the design space.	191
5.18	Variation of normalised variables for optimisation case IV.	192
5.19	Airloads variation subject to table 5.11.	194

5.20	Initiation and duration of flap actuation as function of the reduced frequency for optimisation case IV.	195
5.21	Airloads variation from extracted t_{start}, T_{δ_f} and k values from fig. 5.8(a,b), fig. 5.12(a,b), fig. 5.16(a,b) and fig. 5.8(a,b). . . .	197
5.22	Variation of objective function J_1 over the design space described by grid-1.	201
5.23	Variation of objective function J_1 over the design space described by grid-2.	202
5.24	Airloads variation subject to the grid resolution displayed in table 5.13.	204
5.25	Variation of objective function J_2 over the design space described by grid-1.	205
5.26	Variation of objective function J_2 over the design space described by grid-2.	206
5.27	Airloads variation subject to the grid resolution displayed in table 5.14.	208
5.28	Variation of objective function J_3 over the design space described by grid-1.	209
5.29	Variation of objective function J_3 over the design space described by grid-2.	210
5.30	Airloads variation subject to the grid resolution displayed in table 5.15.	212

5.31	Variation of objective function J_4 over the design space described by grid-1.	213
5.32	Variation of objective function J_4 over the design space described by grid-2.	214
5.33	Airloads variation subject to the grid resolution displayed in table 5.16.	216
A.1	Illustration of the Biot-Savart law applied to a vortex filament, adapted from Anderson [5].	235
B.1	Illustration of panel pressure and aerodynamic flap hinge moment.	237
B.2	Flap crosssectional area with location of cg and hinge	243

List of Tables

1.1	Summary of flow control methods.	17
1.2	Summary of flow control methods for Drag reduction.	22
1.3	Overview of flow control solutions for flow transition.	24
1.4	Overview of flow control solutions for flow separation.	24
1.5	Overview of flow control solutions for lift enhancement.	29
1.6	Overview of flow control solutions for vibration reduction. . .	31
1.7	Overview of flow control solutions for flapped rotor.	34
1.8	List of various flow control schemes.	41
2.1	Boundary conditions of the current discrete vortex method (DVM) at any point of the flow field.	53
2.2	Limitations of the current discrete vortex method (DVM) . . .	66
2.3	Dynamic stall vortex convection speed, $Re = 1.49M$	75
3.1	Assumptions for blade pitch profile.	80
4.1	List of geometric and actuation parameters.	121

4.2	Summary of aerofoil incidences of the flap's initiation and termination of the actuation event. $\theta(t) = 15^\circ \pm 7^\circ \sin(\omega t)$, $Re = 1.48 \times 10^6$, $M_\infty = 0.1209$	135
5.1	Optimisation strategy.	154
5.2	Overview of optimisation goals.	158
5.3	Lower and upper bounds of the initial design space.	160
5.4	Lower and upper bounds of the extracted design space.	162
5.5	Summary of weighting coefficients, optimisation parameters, design space variables and objective function values for optimisation case I.	171
5.6	Summary of extracted k , t_{start} , and T_{δ_f} values from fig. 5.8(a,b) (optimisation case I).	174
5.7	Summary of weighting coefficients, optimisation parameters and objective function values for optimisation case II.	179
5.8	Summary of extracted k , t_{start} , and T_{δ_f} values from fig. 5.12(a,b) (optimisation case II).	181
5.9	Summary of weighting coefficients, optimisation parameters and objective function values for optimisation case III.	186
5.10	Summary of extracted k , t_{start} , and T_{δ_f} values from fig. 5.16(a,b) (optimisation case III).	188
5.11	Summary of weighting coefficients, optimisation parameters and objective function values for optimisation case IV.	193

5.12	Summary of extracted k , t_{start} , and T_{δ_f} values from fig. 5.20(a,b) (optimisation case IV).	195
5.13	Summary of weighting coefficients, optimisation parameters, design space variables and objective function values for T_{δ_f} grid resolution (optimisation case I).	203
5.14	Summary of weighting coefficients, optimisation parameters, design space variables and objective function values for T_{δ_f} grid resolution (optimisation case II).	207
5.15	Summary of weighting coefficients, optimisation parameters, design space variables and objective function values for T_{δ_f} grid resolution (optimisation case III).	211
5.16	Summary of weighting coefficients, optimisation parameters, design space variables and objective function values for T_{δ_f} grid resolution (optimisation case IV).	215
B.1	Location of flap's mass & geometrical centroid.	242
B.2	Flap non-dimensional cross sectional area.	243
B.3	Flap non-dimensional polar moment of inertia.	248

Nomenclature

symbol: definition:

A_1	longitudinal rotor cyclic pitch component
B_i	area within the aerofoil
B_1	lateral rotor cyclic pitch component
c	aerofoil chord (m)
c_i	i^{th} cost coefficient
c_f	flap chord (m)
c_g	centre of gravity
C_m	pitching moment coefficient
C_{m-}	pitching moment coefficient undershoot
C_{m+}	pitching moment coefficient overshoot

symbol:	definition:
C_n	normal force coefficient
$C_{h_{pressure}}$	hinge moment coefficient due to pressure forces
$C_{h_{inertial}}$	hinge moment coefficient due to flap inertia
$C_{h_{flap\ hinge}}$	total flap hinge moment coefficient
C_P	pressure coefficient
$C_{P_{\delta_f}}$	flap required power coefficient
C_w	work coefficient
$\frac{C_t}{\sigma}$	blade thrust loading coefficient
F_b	area within the control zone
F_w	area outside the control zone
g	acceleration due to gravity ($\frac{m}{s^2}$)
$I_{z_0z_0}$	polar moment of inertia about the axis z_0 ($kg.m^2$)
J	Objective function
k	aerofoil reduced frequency, $\frac{\omega c}{2U_\infty}$
k_f	flap reduced frequency, $\frac{\omega c_f}{2U_\infty}$

symbol:	definition:
\vec{k}	unit vector, in chapter 2)
k	order of the i^{th} bivariate spline, (in chapter 5)
l	aerofoil panel length, (in chapter 2)
l	order of the j^{th} bivariate spline, (in chapter 5)
\vec{l}	unit vector, (in chapter 2)
m_i	flap elementary mass (kg)
M_∞	free stream Mach number
n	unit vector normal to the aerofoil's surface
P	total pressure
P_{δ_f}	required power to deflect the flap (W)
q_∞	free stream dynamic pressure, $\frac{1}{2}\rho U_\infty^2$
R	flap cross-sectional area, (in appendix B) (m^2)
R	blade radius (m)
Re	Reynolds Number

symbol:	definition:
\mathbf{r}	position vector wrt a fixed coordinate system to flap mass element m_i
r	distance between the point in question and the reference coordinate system
r_i	radial distance from the inertia axis
r_p	distance between aerofoil's $\frac{1}{4}c$ pivot point and the point in question
\mathbf{s}	unit vector tangential the aerofoil's surface
S	vorticity flux, (in chapter 2)
S_i	aerofoil contour
S_u	flow field boundary upstream
S_∞	flow field boundary downstream
S_T, S_B	wind tunnel boundaries
$S(x, y)$	bivariate spline, (in chapter 5)
s	aerofoil panel surface
t	time
t_{start}	non-dimensional start actuation time of the flap
T_{δ_f}	non-dimensional duration of the entire flap actuation

symbol: definition:

V volume (m^3)

U_∞ free stream velocity (ms^{-1})

U_p velocity at a given point onto or
away from the aerofoil's surface (ms^{-1})

W work (J)

X design variable vector

Z position in complex notation

Greek characters:

α :

α lift curve slope

symbol:	definition:
α^+	non-dimensional pitch rate, $\frac{\dot{\alpha}c}{2U_\infty}$
α_2	two-dimensional negative aerodynamic damping
$\alpha(i, j)$	coefficient vector of each spline curve
$\gamma :$	
γ	vortex blob circulation strength
Γ	total circulation strength, (in chapter 2) ($\frac{m^2}{s}$)
Γ	flap contour, (in appendix B)
$\delta :$	
δ_f	flap deflection ($^\circ$)
$\dot{\delta}_f$	flap deflection rate ($\frac{^\circ}{s}$)
$\theta :$	
θ	blade pitch angle ($^\circ$)
θ_0	blade collective pitch ($^\circ$)
θ_{1c}	lateral cyclic pitch ($^\circ$)
θ_{1s}	longitudinal cyclic pitch ($^\circ$)
$\hat{\theta}_{start}$	aerofoil AOA at which the flap actuation initiates ($^\circ$)
$\hat{\theta}_{end}$	aerofoil AOA at which the flap actuation terminates ($^\circ$)

symbol: definition:

μ :

μ rotor advance ratio ($\mu = \frac{U_\infty}{\Omega R}$)

ν :

ν kinematic viscosity ($m^2 s^{-1}$)

ρ :

ρ fluid density ($\frac{kg}{m^3}$)

ϕ :

ϕ velocity potential

Ψ :

Ψ stream function, (in chapter 2, appendix A)

Ψ blade azimuth (\circ), ($\Psi = \Omega R$)

ω :

ω vorticity, (in chapter 2, appendix A)

ω vortex particle strength, (in chapter 2)

symbol:	definition:
ω	circular frequency of oscillation (s^{-1}) (in chapter 5)
Ω_i	angular velocity of a fixed point onto the aerofoil's surface, (in chapter 2)
Ω	blade angular velocity ($\frac{rad}{s}$), (in chapter 5)

Symbols:

\uparrow	upstroke of aerofoil and/or flap
\downarrow	downstroke of aerofoil and/or flap
∞	free stream conditions
∇	gradient operator
Δ	Laplace operator, ($=\nabla^2$)
Λ	sweep angle (\circ)
Σ	summation
$[\]$	non-dimensional

symbol: definition:

Subscripts:

0.75R	location at 0.75 blade radius
<i>c</i>	aerofoil reference point
0	incompressible state, (in chapter 1)
0, U	upstream conditions, (in chapter 2)
0	collective angle indication, (in chapters 2-5)
<i>tw</i>	blade twist
<i>(i, j)</i>	indexes
<i>min</i>	minimum value
T, B	wind tunnel walls
<i>start</i>	initiation of flap actuation
<i>end</i>	termination of flap actuation

List of Acronyms

abbreviation: definition:

A:

ACF Actively Controlled Flap
AOA angle of attack

B:

BL Boundary Layer
BVI Blade Vortex Interaction

D:

DERA Defence Evaluation Research Agency
DOA Duration Of Actuation
DS Dynamic Stall

abbreviation: definition:

DDS	Deep Dynamic Stall
DDLE	Dynamically Deforming Leading Edge
DSV	Dynamic Stall Vortex
DSVSP	Dynamic Stall Vortex Suction Peak
DVM	Discrete Vortex Method

H:

HHC	Higher Harmonic Control
HLFC	Hybrid Laminar Flow Control
HSI	High Speed Impulsive

I:

IBC	Individual Blade Control
-----	--------------------------

L:

LS	Light Stall
LE	Leading Edge
LESP	Leading Edge Suction Peak
LFC	Laminar Flow Control
LHS	Left Hand-side

abbreviation: definition:

N:

NACA	National Advisory Committee for Aeronautics
NASA	National Aeronautics and Space Administration
NLFC	Natural Laminar Flow Control
NS	Navier Stokes

O:

OLD	Outer Layer Devices
ODVG	On Demand Vortex Generator

P:

PCHIP	Piecewise Cubic Hermite Interpolating Polynomial
PG	Prandtl-Glauert
PVG	Pulsed Vortex Generator

R:

RHS	Right Hand-side
-----	-----------------

abbreviation: definition:

S:

SCV Smooth Camber Variation

SMA Shape Memory Alloy

SSF Sealed slat/flap

T:

TE Trailing Edge

TEV Trailing Edge Vortex

TEVSP Trailing Edge Vortex Suction Peak

TFC Trailing-Edge Flap Control

TS Tolmien-Schlichting

TSB Tangential Spanwise Blowing

TVB Tangential Vortex Blowing

V:

VG Vortex Generator

VL Vorticity Layer

VLB Variable Length Blade

Abstract

Trailing edge flaps may provide a mechanism for alleviating retreating blade stall. In the present investigation numerical simulations were conducted involving a NACA 0015 aerofoil section fitted with a plain trailing edge (TE) flap. All simulations were conducted using DIVEX, a tool being developed at the University of Glasgow, Department of Aerospace Engineering. In summary, the code uses a surface shedding discrete vortex method (DVM) for the simulation of 2-D incompressible flows around pitching aerofoils. The aerofoil is oscillating in pitch about its quarter chord axis and the flap undergoes negative pitch inputs, i.e. upward. An interesting feature appears to be that the cause of the severe nose down pitching moment introduced during dynamic stall is due to the vortical pair of the DSV and TEV where it is shown that the former feeds the later in the case of the clean aerofoil for the range of reduced frequencies varying between $k = 0.128$ and $k = 0.180$. This fact suggests that manipulation of the vorticity in the vicinity of the trailing edge may be a mechanism for modification of the dynamic stall vortex (DSV) trajectory. This was found to relieve the aerofoil from severe pitching moment

undershoot occurring during dynamic stall under appropriately phased flap actuations. Results obtained so far encourage the employment of a flap with fairly small size, 15% of the aerofoil chord. A parametric study is described which identifies the proper aerodynamic and actuation parameters for the current problem. In addition a simple open loop control scheme is developed based purely on rotor and flap related quantities.

Acknowledgements

At first place, I would like to thank God for kept me going throughout my research. I would like also to express my deepest gratitude to my family, in and out of Greece, particularly my parents Mr. and Mrs. Konstantinos and Maria Tsiachris for their continuous encouragement, love and support.

I would also like to thank the Head of the Aerospace Eng. Department, Dr. Douglas Thomson, for his help and support when required. I am further extremely grateful to my advisor Dr. ken Badcock for his assistance, advice and encouragement. Without them, the completion of this research project would be simply "mission impossible". Likewise to Dr. Marco Vezza for his instant advice when reuired. Furthermore I would also like to thank Prof. Frank Coton for his help when requested. I would further like to acknowledge the whole aero-support group, particularly Mr. Kenneth Stevenson, Mrs. Yassamine Mather, Mrs. Linda Floyd, Mr. Walter Robinson for helping me instantly and effectively.

I wish also to thank the University of Glasgow, the Board of Examiners, the Hardship Fund Comittee, the University Health Service, the Accomo-

dation Office, the Department of Aerospace Engineering and DERA for the support and funding of this research project, contract number MSS/4U 3449.

Chapter 1

Introduction

A major feature in helicopter aerodynamics is the occurrence of dynamic stall on the retreating side of the rotor disk. In forward flight the rotor encounters a difference in dynamic pressure between its advancing and retreating side as a result of the combination of blade rotation and rotor translational velocity. Since a helicopter rotor operates in a highly unsteady aerodynamic environment, the most severe type of stall that the rotor blades experience is *dynamic stall* (DS) [112], [113], [88], [78], [1] a description of which will be presented in this chapter.

Contrary to fixed wing aircraft, stall does not limit the low speed operation of the helicopter. However dynamic stall introduces a loading limit on most of the helicopter flight envelope. A rotor experiencing dynamic stall requires extra shaft power and excessive control loads. These in combination with the changes in blade aerodynamic behaviour, can adversely affect the

helicopter flying handling qualities [78]. On the other hand dynamic stall induced loads, can severely damage the rotor structure (i.e. blade pitch links) and are a source of excessive vibrations.

It is evident that the phenomenon of dynamic stall introduces unwelcome effects for the passenger comfort and can adversely affect the structural and aerodynamic performance of the rotorcraft. From the passengers' point of view, cabin vibrations are a source of discomfort. More seriously, the vibration problem is strongly associated with vibratory loading and fatigue of both rotating and fixed components of the rotor assembly. Therefore inspection procedures are often required together with the expensive manufacture of different rotor parts to meet the flight worthiness requirements, resulting in high design and operational and maintenance costs of a rotorcraft [130], [78], [34], [1].

Flow control could be adopted to provide relief from dynamic stall severity. The current work attempts to address this requirement by investigating the feasibility of alleviating the effects introduced during DS (dynamic stall) using an actively controlled TE (trailing edge) flap. Since different engineering disciplines are involved for successful alleviation of retreating blade stall, an overview of relevant topics is next presented. This includes a brief description of the flow topology of DS, a classification of flow control approaches together with a review on flapped rotor and the current proposed flow control solution.

The current chapter gives a literature survey on dynamic stall with emphasis on the negative aerodynamic damping of the sectional pitching moment hysteresis loop, followed by a literature review on various flow control methods. These methods include flow management for drag reduction, boundary layer separation and transition, lift enhancement, helicopter rotor vibration reduction followed by a review on flapped rotors. The proposed flow control solution is presented together with the aims and objectives of the current investigation. Finally a short overview of the current thesis is presented.

1.1 Dynamic stall

Dynamic stall (DS) implies an aerodynamic phenomenon which consists of a series of events that result in the *dynamic delay* of stall on aerofoils or wings undergoing unsteady motion to angles significantly larger than the static stall angle [1], [112], [78], [121]. This delay is accompanied by benefits such as extra lift and penalties such as large negative pitching moments. As the aerofoil AOA (angle of attack) increases, there is a delay in the occurrence of stall due to the unsteady flow, with high lift and low pitching moment values maintained to an AOA (angle of attack) larger than the static stall angle. When the aerofoil or wing reaches its dynamic stall angle, there is a loss of leading edge suction accompanied by a vortex shedding, usually from

the vicinity of the leading edge. In particular the bound vorticity lost from the vicinity of the aerofoil's leading edge takes the form of free vortex elements which propagate with the local flow velocity and tend to roll up into a dense accumulation of vorticity which is of the same order of magnitude as the aerofoil's bound vorticity before stall [84]. Young proposed that vortex shedding may be caused by acoustic disturbances propagating forward in the lower surface boundary layer, that wake closure is invalid and that the shed vortex leaves a trail of vorticity which further forms a turbulent free shear layer [90]. Due to the DSV (dynamic stall vortex) convection downstream over the aerofoil's upper surface, pressure disturbances are induced, which consequently form a high suction area moving from the leading toward the trailing edge [112], [113]. As a result, these pressure disturbances produce highly transient forces and moments, which characterise the dynamic stall event. After the passage of the vortex, the flow reaches its fully separated state. In addition, the DS phenomenon produces transient variations in forces and moments that are fundamentally different from their steady-state counterparts [1], [88]. Although the effects of DS have been extensively studied, the physical mechanisms involved are not well understood and form a focus for ongoing research.

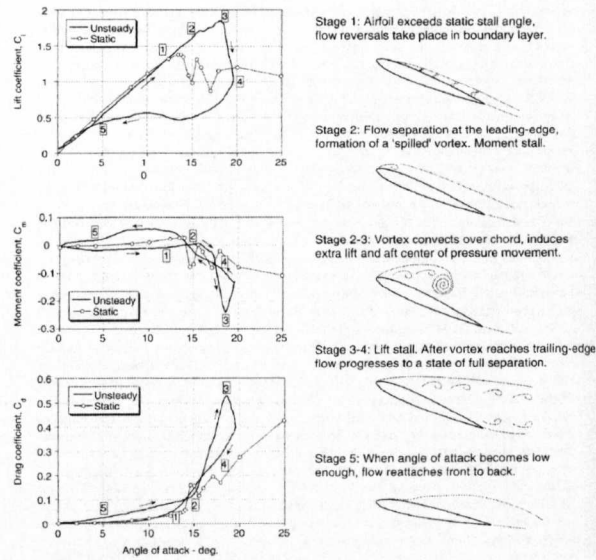


Figure 1.1: Flow topology and unsteady airloads during DS of an oscillating 2-D aerofoil, adapted from [1].

Figure 1.1 summarises the main stages of the entire dynamic stall event: In **Stage 1**, the aerofoil exceeds the static stall angle and flow reversal initiates in the boundary layer [1]. As discussed in [122], [121] and [112], this phase represents the delay in the onset of separation as a result of the reduction in adverse pressure gradients which result from the shed wake, unsteady BL response and induced camber.

Stage 2 involves separated flow and the formation of the DSV (dynamic stall vortex). In the majority of cases, the initial formation of the DSV is associated with supercritical flow conditions near the LE (leading edge) of the aerofoil indicating a close interaction of compressible flow characteristics with the DS (dynamic stall) phenomenon [45]. As a consequence of this

vortex propagation over the aerofoil chord we have benefits and losses which were discussed in the previous paragraph.

In **Stage 3** where the DSV has passed the aerofoil's TE (trailing edge), the flow has already reached its fully separated state. This phase is accompanied by events such as maximum pitching moment and sudden loss of lift [1].

In **Stage 4** when the angle of attack becomes low enough, the flow starts to reattach again to the aerofoil surface. In this phase the vortex shedding reduces and previously shed vortices are eventually convected downstream [90], [1].

A more detailed examination of DS requires different categorisations of the phenomenon. One classification of dynamic stall is the flow reversal initiation in the boundary layer [88], [101], [1]. *Leading edge stall* is preceded by laminar separation that almost immediately reattaches. More specifically, the size of the region between separation and reattachment is comparable to the thickness of the boundary layer and becomes shorter as the stall angle is approached [101]. *Thin aerofoil stall* is also preceded by laminar separation in the LE (leading edge) area, with laminar separation at a point downstream which moves backward (i.e. toward the LE) with increasing AOA. Consequently the streamline which bifurcates at the separation point and joins back at the reattachment point encloses a region known as a *separation bubble* [1]. The term *trailing edge stall* refers to aerofoils where BL (boundary layer) separation moves gradually from TE to LE with increasing AOA. It

is emphasised that in nearly all examples of aerofoil stall, TE separation is almost always involved to a certain extent [119]. In fact even in cases where the flow separates at the LE, the propagation of the BL disturbances due to separation are sufficient to encourage separation at the TE [119].

A dominant characteristic in leading edge and trailing edge dynamic stall is the effect of the accelerated flow generated by the pitch rate. In fact the pitch rate induced flow acceleration delays the adversity of the pressure gradient on the leeward side, thereby introducing a delay in stall and resulting in an overshoot of the static stall [9].

Commenting on the bubble formation in leading edge dynamic stall onset, strongly evident at angles greater than the static stall angle, separation involves a condition where the vorticity is no longer confined to the otherwise thin boundary layer [78], [88], [101]. In other words when the flow separates, the vorticity is no longer diffused through the BL (boundary layer), but instead is shed abruptly by convection into the wake as the flow detaches [52]. The necessary condition for either steady or unsteady separation is the existence of a zero vorticity line (i.e. $\frac{\partial u}{\partial y} = 0$ in a 2-D BL) which appears to start and end on the surface and forms a local recirculating region (i.e. separation bubble). Unconfined outward motion of the bubble will result in bubble-bursting, BL separation and onset of stall [101].

Other mechanisms of DS onset are the arrival of a turbulent boundary layer flow reversal point at the vicinity of the LE which moves forward from the

TE and shock wave-BL interaction behind the aerofoil crest [90]. In the latter case the onset mechanism is different depending upon the formation of the shock waves and their strength [55]. Another mechanism could be propagation in the upstream direction of acoustic waves near the aerofoil's lower surface which perturb the separation and stagnation points [90]. Finally the triggering mechanism of the vortex shedding process may involve more than one of the mechanisms described above.

The unsteady separation process and the corresponding sequence of the DS events discussed earlier are strongly affected by the vorticity which is generated at the wall [85]. For both steady and unsteady flows, the rate of vorticity depends on the instantaneous stream wise pressure gradient, on the vorticity transported by transpiration through the surface and the tangential acceleration of the surface [85]. In the case of constant velocity motion of the aerofoil, as in the present work, and in absence of transpiration, the surface vorticity flux (two-dimensional) is given by:

$$\nu \frac{\partial \omega}{\partial y} = \frac{1}{\rho} \frac{\partial p}{\partial s} \quad . \quad (1.1)$$

Taking into consideration the degree of severity of the DS event which can be judged from the amount of separation and the magnitude of the pitching moment coefficient, there are two types which are illustrated in fig. 1.2 [45]. The term *light dynamic stall* refers to situations where the vertical extend of the viscous layer in the boundary layer is of the order of the aerofoil thickness

whereas in the case of *deep dynamic stall* the viscous layer is of the order of the aerofoil thickness as shown in fig. 1.2(a,b) respectively [2]. Parameters such as reduced frequency, maximum incidence, aerofoil geometry and Mach number also seem to play a significant role within the light dynamic stall regime [100], [88], [2].

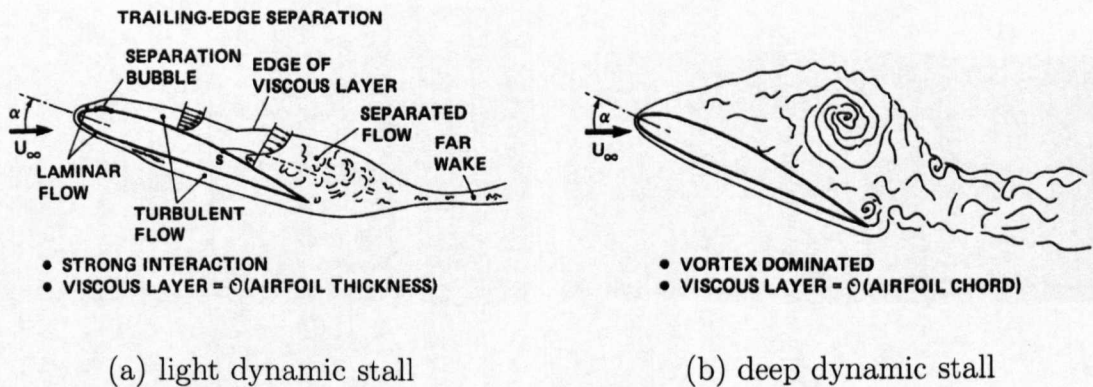


Figure 1.2: Light- and deep dynamic stall, adapted from [2].

In the case of *deep dynamic stall* where parameters such as reduced frequency (k), maximum mean incidence $\theta_{0,max}$ and amplitude $\hat{\theta}_1$ are sufficiently higher than their light stall counterparts, the vortex shedding phenomenon is well defined, the unsteady fluctuations in the airloads are very large and the qualitative results of the DS phenomenon remain independent of aerofoil shape, Reynolds number, and the type of motion [102]. In the case of *light dynamic stall* where less severe conditions prevail, the strength, origin, transient vortex development and the qualitative behaviour of the aerodynamic forces and moments depend on the parameters mentioned in the light DS

case [100], [102] and [1].

Each individual event of the DS phenomenon takes a certain time to develop, and once the events are initiated, they appear to be independent of the aerofoil motion [88]. This independence explains why the airloads result in the attendant aerodynamic forces exhibiting a certain amount of *hysteresis* with respect to the instantaneous AOA, i.e. more than one value of the airloads corresponds to the same AOA. In particular this hysteresis in aerofoil (blade-) AOA appears to be a major difficulty in the modelling of the DS phenomenon. This AOA hysteresis may be presented graphically vs the pitching moment coefficient. The resulting C_m vs AOA is described by two loops of opposite sense. The RHS loop is an indication of the negative aerodynamic damping which is the major source of stall flutter and it is discussed in the next section.

1.2 Dynamic stall and Aerodynamic damping

Aerodynamic damping expresses the net aerodynamic work per cycle of oscillation [88]. For an aerofoil oscillating in pitch, the condition with which the present work is concerned, the instantaneous work done on the fluid by the motion of the aerofoil equals to, i.e.:

$$W = - \oint M(\hat{\theta}_1) d\hat{\theta}_1 \quad (1.2)$$

where $M(\hat{\theta}_1)$ is the sectional pitching moment about an axis of rotation at the same chord location¹, as a function of the angle of attack (AOA) and it is positive for nose-down airloads (i.e. positive for a counterclockwise loop in a C_m vs AOA plot) [1], [113], [112], [88]. The RHS term of eqn. 1.2 is usually positive but it becomes negative during some phases of DS, effectively indicating that the fluid is doing work on the aerofoil. When work is done on the aerofoil by the fluid (i.e. positive damping) this means that the aerofoil is damped. In the opposite case where work is done on the fluid by the aerofoil (i.e. negative damping), this implies aerodynamic excitation which termed as stall flutter [1], [113], [112], [88]. A typical LS (light stall) pitching moment hysteresis loop is shown in fig. 1.3.

¹within the present work, the pitch axis is located at quarter chord measured from the LE.

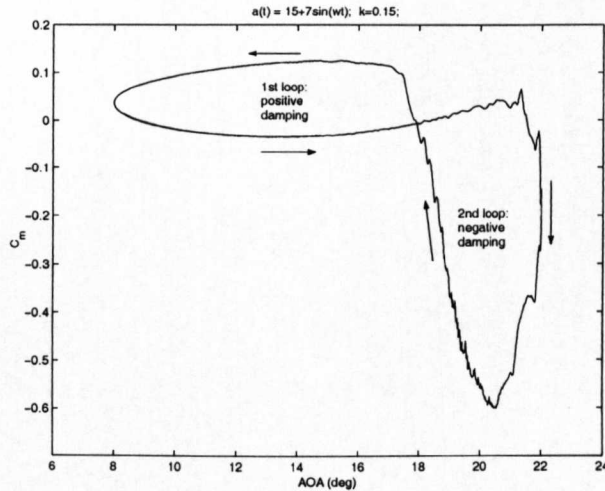


Figure 1.3: Pitching moment hysteresis loop with positive (counterclockwise) and negative (clockwise) aerodynamic damping.

It has already been shown that the onset of light stall introduces a second clockwise loop (i.e. negative damping) into the C_m vs AOA plot which will continue growing with increasing mean AOA. Under more severe conditions, like in the deep stall case, the peak nose-down pitching moment occurs quite early in the cycle of oscillation and when the AOA is still increasing [1]. This fact seems to introduce another loop in the counterclockwise (i.e. positive) sense into the C_m vs AOA plot. According to this mechanism more positive aerodynamic damping is restored. In addition, increasing the reduced frequency serves to delay the stall onset and can also suppress the amount of flow separation, thereby reducing the negative damping [1].

1.2. DYNAMIC STALL AND AERODYNAMIC DAMPING 15

An overview of dynamic stall over a model rotor azimuth suggests that retreating blade stall is a series of separate pressure distribution and boundary layer events leading to a complete blade stall [86]. Experimental evidence of McCroskey and Fisher showed that when the blade passes $\Psi \approx 200^\circ$, a separation-like phenomenon occurs and is characterised by large scale random flow oscillations in the BL and also the surface streamlines on the aerofoil's suction surface suddenly turn radially outward with respect to the ideal sweep angle [86]. At an azimuthal blade position of $\Psi \approx 210^\circ$, the local circulation and lift coefficient were still increasing, while at $\Psi \approx 215^\circ$ the LESP (leading edge suction peak) starts to collapse [86]. The circulation continues to increase until it reaches a maximum value at $\Psi \approx 225^\circ$ and at $\Psi \approx 235^\circ$ the maximum C_n is achieved [86], [79].

Various researchers have been investigating, both experimentally and numerically, the aerodynamics involved in retreating blade stall. Good aerofoil design delays stall but the benefits are limited since all requirements for each blade section at both sides (advancing & retreating) of the rotor, cannot apparently, be met. For example the thickness reduction increases the drag-rise Mach number on the advancing blade but this conflicts with early stall on the retreating blade [80]. For the reasons discussed above flow control appears to broaden the possibilities of alleviating the excessive loads introduced by dynamic stall. An overview of various flow control solutions is next presented.

1.3 Flow control

Modern aerospace technology is developed with a combined approach involving various engineering disciplines including aerodynamics, structural mechanics, materials and control theory. Regarding flow control, the target is accurate flow measurement and prediction, leading to control of unsteady nonlinear aerodynamics. An overview of various flow control concepts is listed in table 1.1 .

Purpose of Flow control method	Flow control method
Transition postponement	-shaping -suction/transpiration -heating/cooling -wave cancellation
separation postponement	-moving wall -vortex generators -wave cancellation -synthetic jets
vibration reduction	-blowing -jet flap
Drag reduction	-wall oscillation
Lift enhancement	-blowing/suction -flow excitation

Table 1.1: Summary of flow control methods.

The first attempts at BL (boundary layer) control, made by Prandtl, go as far back as the beginning of the 20th century. Flow control can be beneficial, for example, in the ability to change lift without changing the AOA (angle of attack) or the ability to manoeuvre without control surface deflection. The latter, widely available to military fixed wing type of aircraft, further leads

to the additional benefit that the aircraft in discussion retains its minimum radar cross section.

In the field of rotorcraft, benefits of employing flow control are among others, vibration reduction, expansion of the helicopter's flight envelope, the reduction in BVI (blade-vortex interaction) and the HSI (high-speed impulsive) noise levels. In particular, HSI is caused by compressibility effects. For example, in high-speed forward flight a phenomenon known as *delocalization* may occur, wherein the supersonic pocket on the blade extends out to the far field beyond the rotor [134]; the noise is then very impulsive in nature and focused ahead in the plane of the rotor.

Several flow control methods have been implemented, depending on the purpose that they serve. In the current project, the TE flap actuator will serve for modifying the trajectory of the DSV. More specifically, the flap will be employed for sectional pitching moment modification, i.e. its deflection will manipulate the flow in the aerofoil's TE vicinity resulting in modification of the DSV trajectory. This manipulation of the trailing edge vorticity is found to reduce the aerofoil from the large pitching moment undershoot [22].

Having defined the purpose for which a flow control method will be applied, the question which arises is how this it can be implemented. A first classifi-

cation can be based on whether the method is applied at the body's surface or away from it. Surface flow control includes methods such as surface -roughness, -porosity, -curvature, temperature, moving wall, and compliant coatings [83]. Flow control devices which are located away from the surface include outer layer devices (OLD), additives which are introduced in the middle of a shear layer or manipulate free stream turbulence.

Another categorisation of flow control methods, can be made with respect to energy expenditure and the control loop involved. Flow control may be distinguished into passive and reactive. For passive flow control no external source of energy is required. Active control may be split into predetermined and reactive. Predetermined flow control involves energy input into the BL for any flow state. Therefore it can be represented as an open loop system [83]. In the case of reactive control, the control input is continually adjusted, something which is achieved by a feedforward or feedback loop.

Flow control for postponing transition includes methods which alter the BL (Boundary Layer) velocity profile in such a way that the linear growth of unstable waves is minimised or suppressed [83]. The simplest means for controlling BL transition is the method of *shaping*. This method implies the use of carefully examined streamlined bodies for suitable molding of the pressure distribution around the body itself. Another method for controlling transition is *suction*. This method delays transition by extracting fluid from the

near wall region of the BL (Boundary Layer), therefore altering its stability. Under the condition that enough fluid is sucked away, laminar flow can be maintained to extremely high Reynolds numbers [83].

A different flow control concept is the *wall heating/cooling* method. In this regard addition or loss of heat from a surface introduces variation (with distance from the wall) in the viscosity of the fluid. For example on the suction surface of an aerofoil, there will be an increase in the velocity gradient near the wall after loss of heat, and therefore the BL velocity profile becomes fuller and thus more stable. Another method for transition control uses the wave cancellation which is feasible under the condition that the disturbances in the BL are still small, their growth can be described by a linear equation and the principle of superposition is still valid [83].

Further flow control techniques for postponing and/or preventing separation are commonly referred to as *velocity profile modifiers*. Among others, solutions for delaying separation shaping are included which also serve for transition control. Another way of averting separation is the method of *transpiration* where withdrawal of fluid near the wall takes place through a porous surface. Effectively transpiration is a suction method as described in the previous paragraph and in addition the methods given above could also serve for separation control. The *moving wall* method contributes significantly to-

ward separation postponement. Examples of this method include rotating cylinders at, such as the leading edge of an aerofoil, and control deflection surfaces like flaps, ailerons and BL vortex generators suitable for controlling the flow around highly swept wings [51]. Smart structures combined with flow control technology can play a vital role in the needed improvements in control surface- effectiveness, size and weight. These technologies may allow continuous re-contouring of the wing or rotor blade surface, therefore improving aerodynamic efficiency.

A single flow management approach can serve multiple purposes. For example a trailing edge flap in rotorcraft applications might serve for vibration reduction, increase the helicopter's forward speed and alleviation of blade-vortex interaction levels. However, and as it will become evident throughout the remainder of this chapter, the classification presented reflects upon the priorities for the design. The trailing edge flap employed for the aim of the current investigation serves primarily for manipulation of the trailing edge vorticity resulting in modification of the sectional pitching moment which further yields to reduction of the two-dimensional aerodynamic damping, lowering the vibration levels introduced during dynamic stall.

In the next sections flow control approaches for specified purposes are presented. These include drag reduction, boundary layer separation and transition, lift enhancement and vibration reduction.

1.3.1 Drag reduction

One way to reduce drag is the maintenance of laminar flow over the most area of the wing. A couple of flow management approaches for drag reduction are given in table 1.2 .

Application	Reference
surface porosity	Mineck & Hartwich [89]
spanwise wall oscillation	Choi <i>et.al.</i> [96]

Table 1.2: Summary of flow control methods for Drag reduction.

This concept is known as LFC (laminar flow control) and can be implemented in various ways. The simplest is the NLF (natural laminar flow control) which in essence maintains a favourable pressure gradient over the most of the wing's surface therefore delaying BL (boundary layer) transition. The NLF concept appears to work satisfactorily for fixed wing aircraft having a low sweep angle (i.e. $\Lambda < 15^\circ$) which is usually found in smaller aircraft. For higher sweep angles the NLF concept might be combined with BL suction yielding to a hybrid flow management solution, often defined as hybrid laminar flow control (HLFC) [39]. Both NLF and HLFC aim to suppress the growth of the unstable disturbances which lead to BL transition.

Choi *et.al.* experimentally demonstrated that skin-friction drag can be reduced by utilising spanwise-wall oscillations resulting in a mechanism which combines the spanwise vorticity generated by the periodic Stokes Layer which further reduces the mean velocity gradient of the boundary layer within the viscous sublayer [96].

Mineck and Hartwich investigated the aerodynamic characteristics of a NACA 0012 with full-chord porosity [89]. Moreover their investigation was based on the fact that at supercritical flow conditions, the compression region on the porous surface is spread over a longer portion of the chord and also that porous aerofoils exhibit an adaptive characteristic in that the thickness and the leading edge radius of an equivalent solid aerofoil decreases with increasing Mach number, therefore altering the behaviour of a porous NACA 0012 profile toward a high-speed aerofoil [89]. In the next section flow control methods for boundary layer separation and transition are given.

1.3.2 Boundary layer- separation & transition

This flow control category usually promotes mixing between higher momentum fluid with the otherwise separated shear layer and the lower momentum fluid near the body's surface. In particular, mixing brings the higher momentum fluid closer to the aerofoil's surface therefore making the boundary layer

less liable to separation. Some methods for BL transition and separation control are listed in tables 1.3, 1.4 respectively.

Application	Reference
wave cancellation, blowing-suction	Joslin <i>et.al.</i> [7]
LFC	Kumar & Hefner [39]

Table 1.3: Overview of flow control solutions for flow transition.

Application	Reference
surface heating	Liepmann & Nosenchuck [98]
wave cancellation	Thomas [29]
blowing-suction	Seifert <i>et.al.</i> [12],[10],[13]
PVG	McManus, [16]
DDLE	Chandrashekhara <i>et.al.</i> [53]
ODVG	Pack & Joslin[14]
synthetic jets	Ravindran [92]
surface shaping	Fleming & Burner [44]
SSF/SCV	Trenker <i>et.al.</i> [54]

Table 1.4: Overview of flow control solutions for flow separation.

Joslin *et.al.* report suppression of instability growth within a flat plate boundary layer utilising a wave cancellation technique [7]. This technique

assumes that a wavelike disturbance might be linearly cancelled due to the introduction of another wave having a similar amplitude as the original one but out of phase. In particular their results demonstrate that two-dimensional (2-D) Tollmien-Schlichting (TS) waves can be superposed upon 2-D waves in such a way resulting in a reduction of the amplitude in the original waves. Liepmann and Nosenchuk used hot strips for generation and controlling travelling waves in an attempt to prevent separation [99].

For separation postponement, vortex generators (VG) are effective. Their working principle is based on introducing longitudinal vorticity into the flow field therefore postponing separation [39]. On fixed wing aircraft VG are located on the wing's surface and remain deployed at all times, (i.e. passive VG) whereas active fluidic vortex generators are sometimes used during some parts of the flight envelope. The later could be used not only for separation control during take off and landing but also during cruise by introducing side slip velocities on the wing's wetted surface [39].

Another realisation of vortex generators (VG) is the on-demand vortex generator (ODVG) developed at NASA Langley, which is applicable for separation control during aircraft take-off and landing and also for drag reduction during cruise conditions [14]. In addition ODVGs can be optimised at off-design conditions and require no further external plumbing, simplifying implemen-

tation. They consist of a cavity with a flat plate which forms the actuation surface and is asymmetrically aligned at the top side in such a way that wide and narrow gaps are formed. The asymmetry in gaps may produce various jets such as a vertical jet (i.e. free jet), a vortex flow, a wall jet and an angled vertical jet, providing a wide range of control possibilities. Pack and Joslin provide a detail description of ODVGs in [14].

McManus *et.al.* experimentally demonstrated the effectiveness of delay in boundary layer (BL) separation by means of pulsed vortex generators (PVG) whose working principle is based on the idea of further enhancement of the mixing process involved in the BL in an otherwise strongly separated flow field, postponing therefore the separation process [16]. As a result, this additional vorticity into the flow field can forestall BL separation. On the other hand their power consumption requirement is fairly low compared to steady flow jets [16].

Another means of active flow control are synthetic jets (i.e. zero-net-mass flux actuators). These piezoelectric devices have a net mass flow of zero and may provide multiple aerodynamic benefits such as lift enhancement, drag reduction, and on-demand control moments, and might eliminate conventional flap and/or slat hardware [14].

Another flow control concept that is employed for postponement of BL transition is achieved by wave cancellation (or wave superposition), which relies on the introduction of an instability wave into the flow field of equal amplitude but opposite phase to the already existing Tollmien-Schlichting (TS) waves which form the main drivers of the transition process. Thomas experimentally presented a flow control scheme based on cancelling of the TS waves [29]. Although successful, this study was performed at low Reynolds number and the effectiveness of the wave superposition remains questionable, certainly at Reynolds numbers typical of aircraft flight.

Seifert performed wind tunnel tests at Reynolds numbers up to 31 million at low Mach numbers, typical of transport aircraft at take-off and landing conditions [12],[10]. Two NACA 0015 profiles were employed, one having a 0.2% chord wide slot at 10% chord and the other was equipped with a 30%*c* trailing edge (TE) flap deflected at 20° and a 0.17% chord wide slot at the flap shoulder, i.e. at 70%*c* aerofoil chord. It was found that oscillatory blowing of the first model (i.e. slot at 10%) postpones aerofoil stall while the second model (i.e. oscillatory blowing at the flap shoulder) improves the flap effectiveness. Seifert and Pack report postponement of separation over the flap, lift enhancement and drag reduction on a similar model mentioned previously [13].

Chandrasekhara *et. al.* demonstrated effective flow control separation on a NACA 0012 profile equipped with a dynamically deforming leading edge (DDLE) [53]. The carbon-fibre skin profile undergoes sinusoidal motion, with the capability of deforming at 20 Hz in unsteady flow, covering a Mach number range up to 0.45 . This particular concept appeared to be successful in altering the flow field under compressible dynamic stall conditions, and despite of its complexity, even fully separated flow was made to reattach [53].

Trenker *et.al.* proposed an adaptive sectional profile capable of dynamically deforming according to local flow conditions [54]. Moreover they proposed two concept models with sealed slat/flap (SSF) and with smooth camber variation (SCV), making their adaptive aerofoil concepts highly suitable candidates for helicopter rotor blade applications [54]. As next flow control approaches for lift enhancement are presented.

1.3.3 Lift enhancement

Devices for lift enhancement are used in combination with mechanical devices (i.e. trailing edge flaps and/or leading edge slats) and normally use periodic blowing and/or suction which is applied to the separated flow in order to achieve reattachment, and increases in the lift at high angles of attack. High lift systems are of complex mechanics and usually combine leading edge slats

and multiple trailing edge flaps as is common in most transonic passenger aircraft. A summary of various approaches for lift enhancement is shown in table 1.5 .

Application	Reference
surface shaping	Barrett [139]
blowing-suction	Seifert <i>et.al.</i> [10] Tinapp & Nitche [40]
LE flap + blowing	Vorobieff & Rockwell [95]
flow excitation	Guy <i>et.al.</i> [15]

Table 1.5: Overview of flow control solutions for lift enhancement.

Ravindran claims a lift increase from utilising synthetic jet actuators on a TAU0015 aerofoil² for flow conditions of $M = 0.15$, $Re = 1.2M$ [92]. Investigations of Seifert have clearly demonstrated that periodic excitation of the separated shear layer could result in partial flow reattachment, therefore increasing lift [10]. Tinapp and Nitche demonstrated experimentally high lift enhancement via excitation of the separating boundary layer on the trailing edge flap on a NACA 4415 profile [40]. Their application was found to work best specially at post-conditions, i.e. while the flow over the trailing edge

²modified NACA 0015, having a 0.4% chord notch at the leading edge and a 3% chord thick trailing edge.

flap is not yet separated [40].

Guy *et.al.* conducted a parametric investigation on the effects of periodic flow excitation with zero net mass flux at the leading edge of a delta wing [15]. They found that a maximum increase of about 38% in the normal force was obtained and a 10° delay of the stall angle was achieved [15]. Donovan claimed lift increases by 29% using synthetic jet actuators in the post-stall regime, [71], [15]. Vorobieff and Rockwell combined a leading edge flap device and trailing edge blowing on a half-delta pitching wing for retarding the onset of vortex breakdown subjected to periodic, large-amplitude manoeuvres at high angle of attack [95].

Fleming and Burner proposed an F-18-E/F planform smart wing fitted with SMA (shape memory alloy) to replace the elevon³ in combination with an embedded torque tube for wing twist generation [44]. The benefit of such a rather complicated flow control method is the absence of deployable control surfaces which induce discontinuities along the aerodynamic surfaces, leading to earlier flow separation, reduced lift and increased drag [44]. Barrett proposed a new type of active aerodynamic surface pitched by an adaptive torque-plate serving as an adaptive missile fin [139]. Some flow control applications for reduction of vibration levels are next presented.

³aileron and elevator integrated into a single control surface

1.3.4 Vibration reduction

As known from fundamental aerodynamics, the vortex flow field produced at the leading edges of delta wings contributes significantly to lift enhancement (i.e. dynamic lift) but at some cases, the path of the emanating vortices might excite vibration to other parts of the aircraft as in the case of twin-tail fighter aircraft. Various flow control concepts have been developed for vibration reduction purposes, with an overview is given in table 1.6 .

Application	Reference
jet flap	Lorber <i>et.al.</i> [8]
TE flap	Straub & Charles [3] Milgram [72] Myrtle & Friedmann [132]
smart structure	Nitzsche & Breitbach [125] (1994)
blowing-suction	Sheta & Harrand [38]

Table 1.6: Overview of flow control solutions for vibration reduction.

Sheta and Harrand employed TVB (tangential vortex blowing) and TSB (tangential spanwise blowing) methods to inject high momentum fluid into the vortex flow of generic fighter aircraft, strengthening the wing vortices and also delaying the onset of breakdown therefore and alleviating twin-tail buffet [38]. Their TVB method appeared to reduce by about 43% the buffet

excitation parameter and by about 40% the amplitude of bending deflection.

Milgram presents a comprehensive analytic model for helicopter rotors equipped with a TE (trailing edge) flap, where up to five per rev flap pitch inputs appear to significantly reduce the vibration levels of the rotor system [72].

Fulton and Ormiston presented a low-tip-speed 7.5-ft diameter hingless rotor equipped with a single elevon (i.e. plain trailing edge control surface) control surface on each of the two blades where their tests successfully demonstrated the effectiveness of elevons in reducing, or even cancelling, individual 3-, 4- and $\frac{5}{rev}$ harmonic blade vibratory flap bending moments at representative forward flight advance ratios [133].

Straub and Charles presented a 12 ft diameter articulated rotor equipped with an actively controlled flap where two per rev flap actuations were shown to reduce rotor main power up to 5% and also flap motions up to five per rev could reduce the vibratory hub loads up to 80% [3]. They actually proposed a TFC rotor model with the blades having chord and radius corresponding to quarter scale of the AH-64 equipped with a plain TE flap of a 25% chord [3]. As a result of their experimental work, performance was improved at the high thrust and speed [3]. More specifically at a value of $C_T = .009$ and $\mu = .25$, a 5° flap input reduces power by 5% and 2-, 3-, $\frac{5}{rev}$ inputs reduced vibratory hub loads by 45%, 82%, 61% respectively [3].

Nitzsche and Breitbach approach the problem of rotary wing vibration reduction in forward flight utilising individual blade control [125]. Moreover,

they employ smart structures as a means to construct geometric modal filters which are able to perform independent modal control of the critical modes in the rotating frame [125]. Lorber *et.al.* studied the feasibility of an oscillating jet flap using an SC1094-R8 aerofoil section for vibration reduction purposes [8]. Although they report advantages compared to the conventional trailing edge flap, its efficiency for once per rev cyclic control which is the case regarding the current research remains questionable [8].

1.4 Flapped rotor

Helicopter rotors employed with TE flaps date back to Pescara's helicopter, which was the first with a flapped rotor for once per rev control [65]. D'Ascanio's rotor concept was designed for controlling the vertical translation of a helicopter equipped with a double coaxial rotor [66]. Sikorsky developed a rotor model with "*aileron mounted on the blade*" claiming to improve torque compensation as well as the helicopter's lateral and longitudinal stability [70]. Kaman proposed a rotor-flap system which modulated the flap motion at once per revolution [69]. Stalker put forward the solution of a helicopter rotor equipped with a TE flap in an attempt to further improve the speed range [68]. Young suggested a similar approach claiming to improve, apart from control and vibrations, the blade aerodynamics by alleviation of retreat-

ing blade-tip stall [67]. In particular, Young's rotor model was employed with a plurality of juxtaposed TE flap segments together with a LE slat [67]. A list of helicopter rotors equipped with trailing edge flap(s) is given in table 1.7 .

Flow control method	Application	Reference
TE flap	rotor torque compensation	Pescara [65]
TE flap	rotor torque compensation	Sikorsky [70]
TE flap	speed increment	Young [67]
TE flap	HHC-IBC	Straub & Charles [3]
TE flap	vibration reduction	Straub & Charles [3]
TE flap	HHC-IBC	Ben-Zeev & Chopra [136]
TE flap	vibration reduction	Milgram [72]
TE flap	BVI-HSI	Baeder & Sim [134]
TE flap	vibration reduction	Myrtle & Friedmann [132]
TE flap	emergency device	Celi [104]
TE flap	vibration reduction	Fulton & Ormiston [133]
blowing-suction	vibration reduction	Sheta & Harrand [38]
servo-flap	vibration control	Giurgiutiu <i>et.al.</i> [42]
VLB	tip Mach-number	Popescu & Giurgiutiu [46]
TE tab	blade tracking	Giurgiutiu & Rogers [43]

Table 1.7: Overview of flow control solutions for flapped rotor.

Giurgiutiu and Popescu proposed a variable length blade (VLB) concept in an attempt to reduce the tip Mach number effects increasing therefore the rotorcraft's forward speed [46]. A direct benefit of this rotor concept yields to further reduction of the blade's flapping motion which translates to decrease the unsteady aerodynamic loading. In addition, Giurgiutiu and Popescu further report a minor reduction in cyclic pitch, thus moving somewhat away from blade stall boundary [46]. However the VLB concept never became popular due to the controllability of the rotor blade in axial direction [46]. Active control for rotorcraft applications may be distinguished into multi-cyclic control, HHC (higher harmonic control) and IBC (individual blade control). A more advanced form of IBC forms the so called TFC (trailing-edge flap control). A conceptual approach of active rotor control is shown in fig. 1.4 .

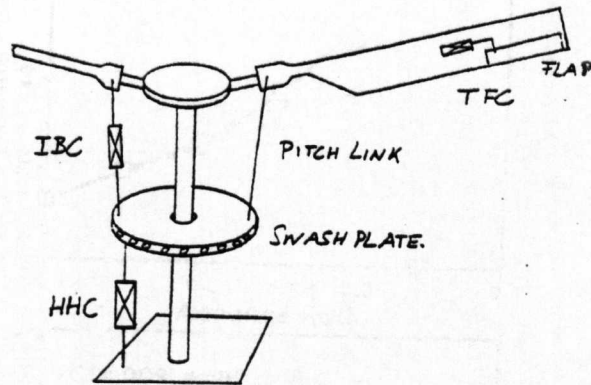


Figure 1.4: Concept of helicopter active control strategies. Adapted from [3].

The term *multicyclic control* refers to all systems which apply periodic inputs to a rotor control device in order to counteract the periodic loads that the blade encounters in forward flight. *Higher harmonic control* (HHC) refers to a multicyclic control system where the control inputs are introduced to the non-rotating side of a swashplate in an otherwise conventional rotor system [131]. Research carried out so far for application of HHC as an effective means of blade vibration reduction has shown most encouraging results[42]. However the reason that limits the application of HHC is twofold. First HHC acts as low-pass frequency filter since the swash plate is considered to be a low frequency device, and second, HHC is applied to all blades at the same time therefore limiting its application to a single (or more, but not all) rotor blade.

The term *individual blade control* (IBC) refers to systems where control is applied directly to the blades while the approach *trailing-edge flap control* (TFC) refers to rotor systems where a TE (trailing edge) flap is mounted near the blade tip [72], [3], [132]. TFC which also forms the main subject of this work, becomes attractive for numerous reasons. First it allows local modification of the blade aerodynamics and also flap deflections are independent of the conventional trim controls at the blade root. In addition, experimental work of Myrtle and Friedmann on their ACF (actively controlled trailing edge flap) concept, using three different flap configurations, servo- plain- and dual servo flap indicated that each of these configurations was very effective at reducing the four per rev vibratory loads [132].

Furthermore Celi addressed the feasibility of using TE flaps in helicopter blades in an attempt to use them as emergency control surfaces [104]. It was claimed that the TE flap device appears to be capable of correcting the otherwise catastrophic consequences of a pitch link failure. More specifically in Celi's model, the flap has a chordwise extension of 20%c of the blade chord and acts by generating a rigid-body pitching motion of the blade with the defect pitch link which further matches with the angles that otherwise would have been generated by the swashplate [104].

Another aspect that should be mentioned and can be indirectly related to flow control is the manufacturing process of helicopter's rotor blades which includes manufacturing tolerances. These might include the blade's mass and

centre of gravity location and aerodynamic contours which might slightly vary from blade to blade. These inherent differences between blades might lead to increase of vibrations levels which increase multiply with increasing forward flight. A solution to this problem leads to mounting of *tracking tabs*⁴ [43]. After presenting various flow management approaches, the flow control solution used in the current investigation is given.

1.5 Proposed flow control solution

Successful alleviation of aerofoil- (and/or rotor-) dynamic stall by means of a TE flap device has been reported by a large number of researchers including among many others the present author [61], [64], [63], [75], [37], [105]. Nevertheless the approach and in particular the control of the flap actuation process, varies significantly according to the application.

Reuster successfully demonstrates alleviation of dynamic stall by leading edge deformation, on various types of aerofoils widely used in helicopter rotor blades such as OLS, VR15, SC1095 and NACA0012, all controlled by means of LESP (leading edge suction peak) [75]. Kretz eliminates rotorcraft stall conditions employing direct action of aerofoil pitch control by pressure feed-

⁴Conventional tracking tabs are thin aluminium plates which are mounted on the blade's trailing edge.

back detection [58].

Adopting a similar flow control concept and despite the fact that it is meant for fixed wing type of aircraft, Darden, [111] demonstrates the remedy of the rolling moment induced on a delta wing configuration due to vortex asymmetry by employment of a movable nose tip to induce and control lateral asymmetry of the forebody vortices, therefore reducing the adverse effects on aircraft rolling moment by using a surface pressure feedback signal.

Prechtl *et. al.* proposed a frequency-based controlled actuation of servo trailing edge flap, essentially cancelling out the hub vertical shear loads otherwise encountered otherwise during rotor operation [63]. In particularly aerodynamic disturbances that the rotor blades encounter during forward flight are due to interactions between the blades and the rotor wake that occur in a periodic fashion, which implies that these perturbations take place at frequencies quite close to the those of rotor speed harmonics. Making use of this fact and under the presence of aerodynamic disturbances associated mainly with turbulence within the rotor inflow due to the asymmetry of the testing environment similar though to harmonics of rotor speed, Prechtl *et. al.* presented a successful means of reducing up to three per rev vibration levels on a two-bladed, $\frac{1}{6}$ th scaled, CH-47D model active rotor blade.

Helin *et. al.* demonstrated alleviation of aerofoil dynamic stall on a NACA 0015 profile undergoing large amplitude pitching motion by pausing the motion for a short period of time, a method which appeared to be capable in

controlling the intensity, cohesiveness and shedding of the shear layer vorticity during DS [107].

In an attempt to enhance rotorcraft control, Potthast and Kerr presented a control system for helicopter applications using integrated rotor blade flap moment to isolate the influence of the undesirable rotor response characteristics introduced during DS [105].

Yu *et. al.* demonstrated a series of flow control methods, such as aerofoil fitted with slats and slots, deformable aerofoils, and aerofoils equipped with suction surface devices, with most encouraging results [94].

Lorber *et. al.* successfully used periodic flow modulation solutions and rather exotic flow control techniques such as plasma actuators for retreating blade stall control purposes [37]. For the latter method, plasma was produced over electrodes located at the aerofoil surface used for boundary layer- or separated shear layer excitation with most promising results.

Shih *et. al.*, demonstrated experimentally vorticity control on a NACA 0012 profile via perturbations on the unsteady shear layer imposed by a LE slat deflection device [109]. Their approach is based on the mutual interaction between the DSV (dynamic stall vortex) and the vortex imposed by the LE slat. A list of the various control approaches is given below, in table 1.8 .

Their applicability and the hardware implementation of these techniques into a full-scale helicopter rotor operating system remains questionable. For example controlling rotor dynamic stall by means of LESP (leading edge

Application	Reference
introduction of rotor flapping moment	Potthast & Kerr [105]
interruption of aerofoil pitching motion	Helin <i>et.al.</i> [107]
frequency-based servo TE flap	Prechtel <i>et.al.</i> [62]
movable wing-nose tip	Darden [111]
LE slat & slots deformable aerofoil suction	Yu <i>et.al.</i> [94]
LE slat	Shih <i>et.al.</i> [108]
plasma actuators	Lorber <i>et.al.</i> [37]
leading edge suction peak	Reuster <i>et.al.</i> [75]

Table 1.8: List of various flow control schemes.

suction peak) implies that pressure tabs should be mounted onto the blade, which in return, apart from disturbing the blade surface, their assemblage and also operation in such a severe aerodynamic environment as at the front portion of a helicopter blade would give high manufacturing and maintenance costs and associated blade corrosion [75],[63].

The same is thought for the flow control solution concept presented by Lorber *et. al.* since their DS (dynamic stall) control approach demands placement of a series of pressure-, strain- and vibration sensors onto the blade [37]. Wave cancellation techniques form also a viable means of rotor control, how-

ever the robustness becomes quite doubtful in terms of their control authority within the whole range of rotor flight operating frequencies.

Despite the successful presentation of flow control approaches such as employed by Helin *et. al.* and Yu *et. al.*, are thought to be doubtful due to lack of the exact knowledge of the flow physics involved during DS (dynamic stall), therefore making the hardware implementation of such a control application highly questionable [107] [94].

The proposed flow control solution employed in the present investigation implements a flow control scheme based on rotorcraft's advance ratio, (μ). Rotor flow control based solely on the rotorcraft's forward velocity, a quantity which can be measured very accurately, is thought to form a reliable means of dynamic stall control.

1.6 Aim and objectives of the present study

The main aim of the current research is to reduce the adverse effects of the dynamic stall phenomenon through modification of the negative pitching moment magnitude. Relieving the aerofoil from the pitching moment undershoot introduced during DS will further improve on the negative aerodynamic damping which is mainly responsible for undesired phenomena such as stall flutter.

In order to successfully meet the above aim, a series of objectives have been set which are given below:

- experimental validation of aerodynamic tools
- presentation of a new dynamic stall onset mechanism
- identification of the flap aerodynamic mechanism and influence on airloads
- examination of the unsteady pressure and vorticity fields around the aerofoil
- examination of the influence of flap-related parameters
- assessment of the control approach

As already demonstrated by numerous researchers, a plain TE flap is found to be capable of relieving the undershoot excess in negative pitching moment magnitude [6], [72], [122], [1], [104]. The unsteady pressure and vorticity production associated with the dynamic stall event and the flap deflection suggests an aerodynamic mechanism based on the mutual interaction between coherent vortex flow structures (i.e. DSV and TEV), providing therefore a useful flow management concept. In addition a parametric study is conducted which aims to give insight into the physical and aerodynamic characteristics. The parameters include flap size, flap notches, deflection amplitude, phasing and flap actuation power. The main aim here is the modification of the DSV

(dynamic stall vortex) trajectory after actuation. The modified airloads are examined and a control scheme is proposed based on rotor related quantities such as advance ratio (μ) and azimuthal blade position (Ψ).

1.7 Thesis overview

The thesis is divided into six chapters. After the introduction, the second chapter aims to give an overview of the numerical tools used in the present study, followed by their experimental validation. The third chapter deals with the flow topology, where the unsteady pressure and vorticity production around the aerofoil are examined. An investigation of the problem parameters is presented in the fourth chapter. In the fifth chapter a control scheme is presented based on quantities such as the start and duration of the actuation event. The sixth chapter summarises concluding remarks on the research conducted so far followed by a set of suggestions for future work. Finally two appendices are provided. The first appendix includes some derivations on vortical aerodynamics and fundamental laws while the second provides extra information on the dynamic and geometric properties of the flap.

Chapter 2

Flow solver and experimental validation

This chapter commences with a description of the discrete vortex method (DVM) used in the current work. A compound description of the mathematical model is given followed by a reference on the flow field discretisation. In addition validation of the flow solver is made against the experimental data obtained by Galbraith *et.al.* [118] with emphasis on the airloads of primary concern, such as sectional pitching moment and normal force followed by an estimation on the convection speed of the dynamic stall vortex.

2.1 General DVM description

The simulations involved throughout the present research are conducted with DIVEX [115], [56], [4] a CFD tool developed at the University of Glasgow, Dept. of Aerospace Engineering. The present discrete vortex method (DVM) is based on representing the continuous vorticity distribution by a series of discrete vortices, which are described in a Lagrangian frame, embedded into a potential flow [4]. In summary, the current flow solver uses a surface shedding discrete vortex method (DVM) for the simulation of two dimensional viscous unsteady flows around pitching aerofoils [117], [115], [56], [4]. In contrast to most flow solvers which are based on sampling of the velocity field, the current DVM method, is based on the discretisation of the vorticity field into vortex particles which are free to move in the flow field [76]. Each of these particles aim to represent a vortex of finite core size, containing a certain amount of circulation, and are convected throughout the flow field that they collectively induce [56], [4], [76].

Compared to grid based methods, the main advantage of a vortex based approach lies in its simplicity which further implies that the flow field can be approximated in the absence of a mesh which in return requires intensive computational effort and time [4], [76]. In addition there is no need of pre-determining the flow separation and reattachment point as this is achieved by the diffusion and convection across zone boundary between the creation

and wake zone (see next section) which further enables the gradual shedding of vorticity into the wake according to viscosity and vortex particle velocities [4].

On the other hand a disadvantage of a flow solver accommodating vorticity stream function compared to a grid based approach is the inability of the former to resolve issues such as compressibility since the Biot-Savart law which provides a sufficient tool for determining vortex associated induced velocities (eqn. 2.16) from an initially given system of vortices, is valid only for incompressible flow [34], [121]. Hence the Prandtl-Glauert (PG) compressibility correction might be employed for determination of approximated compressible local sectional aerodynamic loading [32], [34], [121]. The PG is given by eqn. 2.1 below [5]:

$$C_{p,n,m} = \frac{C_{p0,n0,m0}}{(1 - M_\infty)^{0.5}} \quad (2.1)$$

where p, n, m , denote the coefficients for pressure, normal force and pitching moment respectively and the index 0 denotes their incompressible state. Furthermore, although viscous effects are taken into account far from the aerofoil surface, there is no BL (boundary layer) model as such. Instead a vorticity creation zone (see section flow field discretisation) exists in the vicinity of the aerofoil where the exact model of vorticity creation is presented in the next section. Nevertheless the quantitative aspects of the flow field are captured in great detail as it is demonstrated throughout the remaining chapter, (see section validation). Furthermore capturing leading edge stall becomes an

impossible task, however this limitation does not seem to affect the current work since the aerofoil (i.e. NACA 0015) used for the simulations involved within this work is of trailing edge (TE) stall type [88], [1]. After a global description of the DVM, the mathematical model is presented. This includes formulation of the equations describing the DVM's mathematical model and the corresponding boundary conditions.

2.2 Mathematical model

The flow is governed by the incompressible continuity and the viscous incompressible Navier-Stokes (NS) equations [56],[4], given by:

$$\nabla \cdot U = 0 \quad (2.2)$$

$$\frac{DU}{Dt} = -\frac{1}{\rho}\nabla P + \nu\nabla^2 U \quad (2.3)$$

where $U = U(x, t)$ is the fluid velocity, $P = P(x, t)$ is the scalar pressure, ν is the kinematic viscosity, $\frac{D}{Dt}$ expresses the convective derivative¹ given by $\frac{D}{Dt} = \frac{\partial}{\partial t} + \sum_{j=1}^N U^j \frac{\partial}{\partial x_j}$, the gradient operator ∇ expressed by $\nabla = (\frac{\partial}{\partial x_1}, \frac{\partial}{\partial x_2}, \dots, \frac{\partial}{\partial x_N})$ and the Laplace operator ∇^2 expressed by $\Delta = \nabla^2 = \sum_{j=1}^N \frac{\partial^2}{\partial x_j^2}$, with ν and ρ being the fluid kinematic viscosity and density respectively².

¹This is the derivative along particle trajectories.

²Both fluid density ρ and fluid kinematic viscosity ν are constant under the assumption of incompressibility.

After employing the definitions of vorticity being the curl of velocity , $\omega = \nabla \times U$, vector potential Ψ with $U = \nabla \times \Psi$, $\nabla \cdot \Psi = 0$, and the Reynolds number $Re = \frac{U_\infty c}{\nu}$, equations 2.2 & 2.3 may be expressed in the form of vorticity stream function and vorticity transport equation respectively [56],[4] as:

$$\nabla^2 \Psi = -\omega \quad (2.4)$$

$$\frac{\partial \omega}{\partial t} + (\vec{u} \cdot \nabla) \omega = \frac{1}{Re} \nabla^2 \omega \quad . \quad (2.5)$$

The derivation of eqns. 2.4, 2.5 is given in appendix A for convenience. As shown in the RHS of the above vorticity transport equation (2.5), the contribution of viscous diffusion term decreases with increasing Reynolds number while at the same time convection, i.e. $(\vec{u} \cdot \nabla) \omega$, dominates the time change rate of vorticity [4].

The solutions of the vorticity transport equation are unique after implementation of the appropriate boundary conditions. The kinematic boundary conditions for the current situation are the no-slip and the no-penetration on the aerofoil's surface [4]. The no-slip boundary condition requires that the fluid particles on the aerofoil's surface have the same velocity as that of the aerofoil's surface point in question. The no-penetration condition requires no fluid exchange between the defined flow boundaries which are shown in fig. 2.1(b) for convenience. S_T , S_B , denote the wind tunnel boundaries in an attempt to incorporate the effects of wind tunnel walls. As shown in fig. 2.1(b), far upstream S_T and S_B are connected with S_U and far down-

stream with $S'_\infty \equiv S''_\infty$ respectively. Under the assumption of solenoidal³ and irrotational velocity ⁴ (i.e. $\nabla \cdot \vec{u}_0 = 0$ and $\nabla \times \vec{u}_0 = 0$ respectively) the corresponding stream function satisfies the Laplace equation, i.e. $\nabla^2 \Psi = 0$.

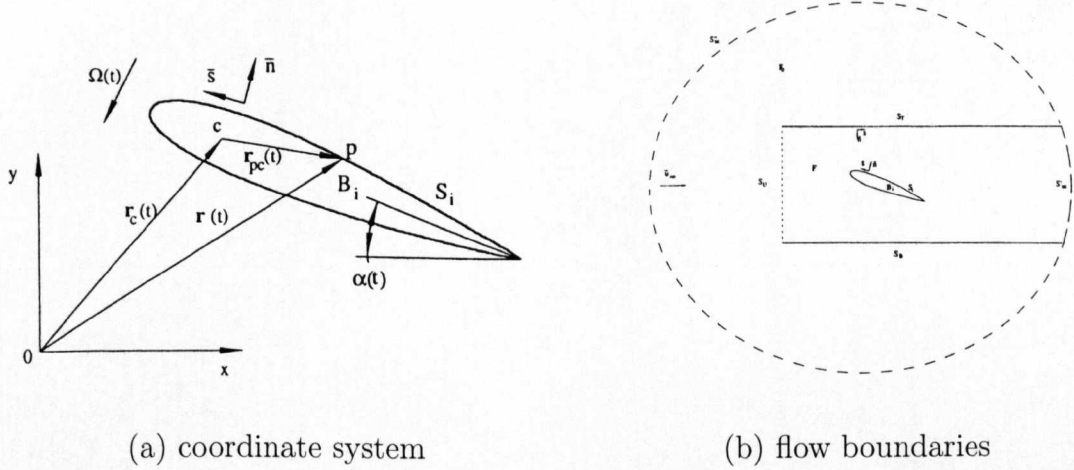


Figure 2.1: Reference coordinate system and flow regions. Adapted from Lin [4].

The essence of the current DVM is how velocity can be expressed in terms of vorticity. Moreover how the velocity field is obtained at any point of the flow field including the aerofoil's surface.

Starting with a point *on* the aerofoil's surface, the velocity at this point is given by [4]

$$\vec{u}_i = \vec{u}_{c_i} + \Omega_i \vec{k} \times (\vec{r} - \vec{r}_{c_i}) \quad (2.6)$$

³When the a fluid particle moves in any kind of closed loop. In other words a vector field whose divergence is everywhere zero.

⁴The motion of the fluid particles through space is a pure translation, i.e. they have no angular velocity.

with \vec{u}_i being the velocity of the fluid particle at the aerofoil's surface, $\vec{u}_{\vec{c}_i}$ being the velocity a fixed point onto the aerofoil's surface, $\vec{\Omega}_i$ and $r_{\vec{c}_i}$ denoting the aerofoil surface point's angular velocity and distance from a reference coordinate system respectively.

Furthermore taking into account the angular velocity of a fluid element, it is easily shown that the vorticity equals twice its angular velocity [5],

$$\omega_i = 2\Omega_i \quad . \quad (2.7)$$

A combination of Stokes's Theorem⁵, the relation between circulation and vorticity and eqn. 2.7, and the circulation of velocity along the aerofoil's surface becomes [5],

$$\Gamma_{S_i} = \oint_{S_i} \vec{u}_i \cdot \vec{s}_i dS_i = \iint_{B_i} (\nabla \times \vec{u}_i) \cdot \vec{k} dB_i = 2\Omega_i B_i \quad (2.8)$$

with all symbols as previously defined, B_i being the area inside the aerofoil and \vec{k} the unit vector, i.e. $\vec{k} = \vec{n} \times \vec{k}$ [4].

Due to the solenoidal property of velocity within B_i (i.e. $\nabla \cdot \vec{u}_i = 0$), a solution of the stream function ψ_i becomes a solution to the following equation:

$$\nabla^2 \psi_i = -2\Omega_i \quad . \quad (2.9)$$

whose boundary conditions are given in table 2.1. Implementation of the boundary conditions listed in table 2.1 and utilisation of Green's second

⁵see appendix A

identity⁶, we obtain for ψ_i [4]:

$$\oint_{S_i} (\phi \nabla \psi_i - \psi_i \nabla \phi) \cdot \vec{n} dS_i = \iint_{B_i} (\phi \nabla^2 \psi_i - \underbrace{\psi_i \nabla^2 \phi}_{=0}) dB_i = - \iint_{B_i} 2\Omega_i \phi dB_i \quad (2.10)$$

with $\phi = \frac{1}{2\pi} \ln |\vec{r} - \vec{r}_p|$, and $\vec{r}_p \notin B_i$. $\nabla^2 \phi = 0$ when $\vec{r} \neq \vec{r}_{ci}$.

In a similar fashion solutions for the stream function are obtained for the exterior flow fields denoted by F and F_0 respectively as shown in fig. 2.1(b).

The stream functions becomes then [4],

$$\nabla^2 \psi = -\omega \quad (2.11)$$

and

$$\nabla^2 \psi_0 = 0 \quad (2.12)$$

Utilising Green's second identity as in eqn. 2.10, we obtain for eqns. 2.11, 2.12 respectively:

$$\oint_{S+S_i} (\phi \nabla \psi - \psi \nabla \phi) \cdot \vec{n} dS_i = \iint_F (\phi \nabla^2 \psi - \psi \nabla^2 \phi) dF \quad (2.13)$$

and

$$\oint_{S_0} (\phi \nabla \psi_0 - \psi_0 \nabla \phi) \cdot \vec{n} dS_i = \iint_{B_i} (\phi \nabla^2 \psi_0 - \psi_0 \nabla^2 \phi) dF_0 = 0 \quad (2.14)$$

with the required boundary conditions given in table 2.1.

After implementation of the boundary conditions listed in table 2.1 solutions for the stream function of eqns.2.9, 2.11 and 2.12 can be obtained. The

⁶see appendix A

boundary conditions for the wind tunnel walls are also presented for convenience.

region F_0	aerofoil's surface	region F'
at S_U, S'_∞ :	at S_i :	at S_T, S_B :
$-\vec{k} \times \nabla \psi = \vec{u}_\infty$	$\vec{n} \cdot \nabla \psi = -\vec{s} \cdot (\vec{u}_{c_i} + \Omega_i \vec{k} \times (\vec{r} - \vec{r}_{c_i}))$ or $\vec{s} \cdot \nabla \psi = \vec{n} \cdot (\vec{u}_{c_i} + \Omega_i \vec{k} \times (\vec{r} - \vec{r}_{c_i}))$	$\vec{n} \cdot \nabla \psi = 0$ or $\vec{s} \cdot \nabla \psi = 0$
at S''_∞		
$\vec{k} \cdot \nabla \psi_0 = \vec{u}_\infty$		

Table 2.1: Boundary conditions of the current discrete vortex method (DVM) at any point of the flow field.

Finally the stream function at point p in the absence of wind tunnel walls becomes,

$$\psi_p = \psi_\infty - \iint_F \phi \omega dF - \iint_{B_i} 2\Omega_i \phi dB_i \quad . \quad (2.15)$$

The velocity field corresponding to eqn. 2.15 is calculated using the Biot-Savart law⁷, which expresses the velocity in terms of the vorticity field and it is given by

$$\vec{u}_p = \vec{u}_\infty + \iint_F \frac{\omega(\vec{r} - \vec{r}_p) \times \vec{k}}{2\pi|\vec{r} - \vec{r}_p|^2} dF + \iint_{B_i} \frac{2\Omega(\vec{r} - \vec{r}_p) \times \vec{k}}{2\pi|\vec{r} - \vec{r}_p|^2} dB_i \quad (2.16)$$

⁷see appendix A

with \vec{u}_p being the velocity of a fluid particle at a given point p , \vec{u}_∞ the free stream velocity, F , B , the flow control area boundaries as displayed in fig. 2.1(b), r_p the distance between the aerofoil's quarter chord and the point in consideration as illustrated in fig. 2.1(a), ω the vorticity, k the unit vector and Ω the fluid's rotational velocity. Equation 2.16 expresses the fluid velocity at a given point in the absence of the wind tunnel boundaries which is composed of the free stream velocity and the vorticity due to the aerofoil motion [56],[4]. Lin provides an extensive overview of the DVM's mathematical model, the derivation and implementation of the boundary conditions [4].

The acceleration of a fluid particle onto the aerofoil's surface as derived by Lin, is given by

$$\frac{D\vec{u}_i}{Dt} = \underbrace{\frac{D\vec{u}_{c_i}}{Dt}}_{\text{linear}} + \underbrace{\frac{D\Omega_i}{Dt} \vec{k} \times (\vec{r} - \vec{r}_{c_i})}_{\text{angular}} - \underbrace{\Omega_i^2 (\vec{r} - \vec{r}_{c_i})}_{\text{centripetal}} \quad (2.17)$$

with the terms of the RHS in eqn. 2.17 representing linear, angular and centripetal acceleration of the reference point respectively and arising from the kinematics of the aerofoil [4]. As it will be demonstrated, eqn. 2.17 is essential for the calculation of pressure. In the next section, the discretisation of the flow field is presented.

2.3 Flow field Discretisation

As it has already been outlined, by definition the vorticity (i.e. $\omega = \nabla \times U$) is related to the spatial gradient of the velocity field at any time [4]. In addition, focusing on the temporal changes of the velocity field, insight can be gained about the vorticity distribution particularly close to the aerofoil's surface.

As it is known from conventional boundary layer theory, significant changes in velocity can occur within a thin layer (i.e. boundary layer) close to the aerofoil's surface whereas outside it, the velocity profile is similar to that for irrotational flow [5]. Although the well known concept of BL (boundary layer) does not apply to the DVM, however a similar layer is identified, it is called the *vorticity layer* (VL) for convenience and it is illustrated in fig. 2.2(a,b) [4]. Under attached flow conditions (see fig. 2.2(a)) there is not much difference between BL and VL, however under separated flow conditions the VL can vary significantly in thickness in contrast to the conventional BL as displayed in fig. 2.2(b).

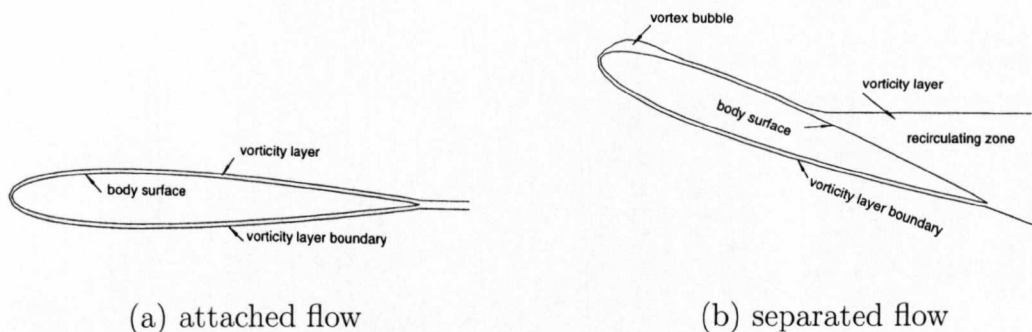


Figure 2.2: Illustration of vorticity layer, adapted from Lin [4].

The introduction of the VL (vorticity layer) gives rise to issues such as its formulation and the determination of the separation point. Regarding the formulation of vorticity in strict mathematical sense, it can be expressed as the individual circulation strength of each vortex particle, and, associated with the Dirac distribution function can be written [4]:

$$\omega(x, y, t) = \sum_i^N \Gamma(x_i, y_i, t) f_i(x, y, t) \quad (2.18)$$

with $f_i(x, y, t) = \delta(|x - x_i| + |y - y_i|)$ representing the Dirac distribution function. This formulation allows modelling of point vortices in discrete points [4]. For the representation of each point vortex the main difficulty is the singular behaviour of the vortex core. In general there is no single vortex core function that can individually represent vorticity distribution with accuracy. However the present DVM incorporates Lamb and Rankine type core functions which generally do not exhibit singular behaviour [4].

Moreover the entire flow field is divided into two zones. i.e. the *creation zone* and the *wake zone*. In the *creation zone* the vortex discretisation is

carried out along a line parallel to the aerofoil contour having a predefined thickness measured from the aerofoil's surface which is further discretized under the assumption of a piecewise linear distribution of the vortex sheet strength within the creation zone [4] and it is illustrated in fig. 2.3:

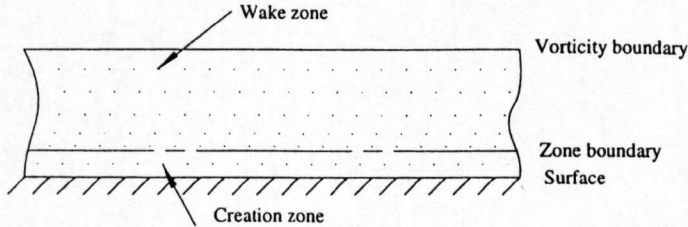
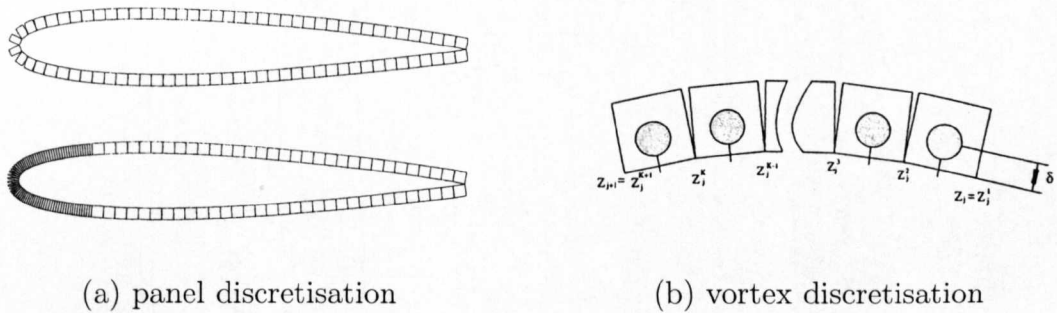


Figure 2.3: Creation and wake zone, adapted from Lin [4].

However in the wake zone the number and location of the former discrete points varies according to flow evolution [4]. The former surface discretisation serves also for vorticity discretisation within the creation zone [4]. Connecting two subsequent points Z_j and Z_{j+1} ⁸ on the aerofoil's surface (fig. 2.4a) which define a segment and a single panel of the surface which in turn are further divided into smaller parts, i.e. subsegments and sub panels [4]. The sub panels are directly connected with the discretisation of vorticity in the creation zone [4]. The former surface subdivision is of great importance when it comes down to representation of areas which show high curvature such as the aerofoil's leading edge as it is illustrated on the lower part of fig. 2.4(a).

⁸in complex notation $Z_j = x_j + iy_j$ and $Z_{j+1} = x_{j+1} + iy_{j+1}$ respectively



(a) panel discretisation

(b) vortex discretisation

Figure 2.4: Aerofoil surface panel discretisation, adapted from Lin [4].

Taking into account the above surface discretisation, equivalently a similar vortex sheet circulation γ is placed at a certain distance above the aerofoil's surface [4]. The variation of this vortex sheet parallel to the aerofoil's surface reflects the vorticity distribution (fig. 2.4b) which is assumed to be linear for each panel and also continuous across panel boundaries [4]. Then the circulation for each segment of each panel and finally for all panels consisting the aerofoil's surface is calculated [4]. This is a straight forward approach when it concerns the creation zone. In the wake zone and when taking into account viscosity effects, the individual vortex particles are given an additional displacement corresponding to a random walk, a process that reflects both convection and diffusion [4].

Furthermore according to the Lagrangian description of the vortices, vorticity is discretized within the *wake zone*. In particular and subject to an addition of random walks for viscous diffusion, vortices in both zones convect with the velocity of the particles to reflect the convection and diffusion of vortic-

ity [56], [4]. The vorticity within the creation zone is re-discretized mutually with the new vorticity generated at the boundary (i.e. aerofoil surface) while the vorticity in the wake zone retains its identity. In addition the shedding of vorticity across the interface between the creation- and the wake zone is represented by newly created vortices within the wake zone [4]. Finally, flow at the far field remains undisturbed, whereas the velocity of flow particles is equal to that of the aerofoil's surface, a demand arising from the no-slip condition. Within the current DVM, vortex amalgamation is employed in order to reduce the total number of vortices in the velocity summation which further reduces the required computational time [4].

The determination of the separation point becomes somewhat evident from fig. 2.2(b) where the flow is in a fully separated state over the aft portion of the aerofoil. The thickness of the VL is significantly greater than in attached flow conditions (fig. 2.2a) and it is determined purely from gradual shedding of vorticity into the wake according to viscosity and vortex particle velocities [4].

In greater detail and as displayed in fig. 2.2(b) where the flow is in a fully separated state over the aft portion of the aerofoil, a flow particle must exhibit a significant change in normal direction contrast to the dominant tangential component under attached flow conditions as it is shown in fig. 2.2(a). As already mentioned the development of vorticity takes place through a

continuous process of creation followed by diffusion and convection causing further increment of the VL [4]. The separated state of the flow as shown in fig. 2.2(b) justifies the dominance of the local velocity gradient in the normal direction. At the same time this increment of the local flow velocity occurs in different places of the aerofoil but it does not grow significantly to cause full separation. The latter manifests itself as a vortex bubble at the aerofoil's leading edge, as shown in fig. 2.2(b) where apparently the tangential velocity component of the local flow is still the most dominant [4]. This fact is certainly amplified at the leading edge area where the surface panel discretisation is finer than the rest of the aerofoil. In addition from general boundary layer theory, the growth of velocity gradients in the normal direction is mainly due to viscous effects, transition and turbulence. The last two are missing from the current DVM modelling, therefore capturing leading edge stall becomes a formidable task. A very detailed analysis of the flow field discretisation is presented in [4]. In the following section a discussion is presented on how pressure and vorticity are distributed along the aerofoil's surface.

2.4 Pressure and vorticity around the aerofoil

The current section deals with the pressure and vorticity distribution on the aerofoil. As shown in section 2.2, the Navier-Stokes and continuity equations contain time derivatives of only three out of the four unknown functions, i.e. there is no time derivative of the pressure. However pressure is related to the vorticity gradient, and, finally a mathematical expression is obtained which represents the pressure distribution onto the aerofoil's surface. In addition it is shown how vorticity is generated, distributed and convected throughout the entire flow field. Finally it is presented how the airloads are obtained.

2.4.1 Pressure distribution around the aerofoil

As it became apparent, there is no pressure term in the vorticity transport expression given by eqn. 2.5. However employing the NS momentum equation and combination with the acceleration relation given by eqns. 2.5 and 2.3, an expression for the pressure can be obtained. Recalling eqns. 2.5 and 2.3 we have respectively,

$$\frac{1}{\rho} \nabla P = -\frac{DU}{Dt} + \nu \nabla^2 U$$

and

$$\frac{D\vec{u}_i}{Dt} = \underbrace{\frac{D\vec{u}_{c_i}}{Dt}}_{\text{linear}} + \underbrace{\frac{D\Omega_i}{Dt} \vec{k} \times (\vec{r} - \vec{r}_{c_i})}_{\text{angular}} - \underbrace{\Omega_i^2 (\vec{r} - \vec{r}_{c_i})}_{\text{centripetal}} .$$

Solving eqn. 2.3 for the pressure term, substitution of the acceleration relation into the NS equation and multiplying with \vec{s} in the tangential direction in order to obtain the pressure variation *along* the aerofoil's surface we obtain:

$$\vec{s} \frac{1}{\rho} \nabla P = -\vec{s} \frac{DU}{Dt} + \vec{s} \nu \nabla^2 U \quad . \quad (2.19)$$

The last term $\nabla^2 \vec{u} = -\nabla \times \vec{\omega}$ with $\vec{\omega} = \vec{k} \omega$ therefore $\nabla^2 \vec{u} = -\nabla \omega \times \vec{k}$.

Then the term $\vec{s} \nabla^2 \vec{u} = \vec{s} \cdot (\vec{k} \times \nabla \vec{\omega}) = (\vec{s} \times \vec{k}) \cdot \nabla \omega = \vec{n} \cdot \nabla \vec{\omega} = \frac{\partial \omega}{\partial \eta}$.

Consequently eqn. 2.19 becomes,

$$\frac{1}{\rho} \frac{\partial P}{\partial s} = -\vec{s} \cdot \frac{DU_c}{Dt} - \underbrace{\vec{n} \cdot (\vec{r} - \vec{r}_c) \frac{D\Omega}{Dt} + \vec{s} \cdot (\vec{r} - \vec{r}_c) \Omega^2}_{\text{non-circulatory}} + \underbrace{\nu \frac{\partial \omega}{\partial \eta}}_{\text{circulatory}} \quad . \quad (2.20)$$

The first three terms of eqns. 2.20 represent the surface tangential components of the acceleration of the point in consideration, its rotational and centripetal acceleration respectively. In other words they associate with the *non-circulatory* or *apparent mass* terms (see appendix 2). The last term reflects the *circulatory* component (eqn. 2.20), it is the most dominant regarding the current situation and represents the negative vorticity creation rate at the surface [56], [4]. For this reason the non-circulatory terms can be neglected and finally eqn. 2.20 reduces to:

$$\frac{1}{\rho} \left(\frac{\partial P}{\partial s} \right)_{y=0} = \nu \left(\frac{\partial \omega}{\partial \eta} \right)_{y=0} \quad . \quad (2.21)$$

The above equation expresses the pressure gradient as a function of the rate of vorticity at the surface [56], [4]. Furthermore the pressure difference between the two nodes of a panel on the aerofoil's surface is given by:

$$P_{j+1} - P_j = \frac{1}{2} \left[\left(\frac{\partial P}{\partial s} \right)_{j+1} + \left(\frac{\partial P}{\partial s} \right)_j \right] l_j \quad (2.22)$$

while the pressure between two successive nodes becomes:

$$P = P_j + \left(\frac{\partial P}{\partial s} \right)_j s + \left[\left(\frac{\partial P}{\partial s} \right)_{j+1} - \left(\frac{\partial P}{\partial s} \right)_j \right] \frac{s^2}{2l_j} \quad (2.23)$$

where s and l correspond to the panel's surface and length respectively while the terms in the square brackets (eqn. 2.23) serve for accommodating flow higher order effects. A final remark on pressure distribution around the aerofoil is that the present DVM provides a relative pressure distribution rather than absolute pressure, for which the value of a reference pressure should be known [4]. The vorticity distribution around the aerofoil is next presented.

2.4.2 Vorticity distribution around the aerofoil

Vorticity is generated due to an interaction between the flow and the aerofoil's surface while the distribution of nascent vorticity results from the no-slip, no-penetration boundary conditions [4]. There is a continuous shedding of vorticity from the creation zone to the wake zone. However there is an augmentation of the total created vorticity (γ_j^{total}) for a very short period of time with the vorticity that remains from the previous shedding process

(γ_j^{old}) due to absorption from the wake, therefore the newly created vorticity (γ_j^{new}) is expressed after subtraction of the existing vorticity from the total vorticity [4], i.e.:

$$\gamma_j^{new} = \gamma_j^{total} - \gamma_j^{old} \quad (2.24)$$

with γ_j^{new} denoting the circulation strength of the new vortex particle j , γ_j^{total} and γ_j^{old} denoting the augmented and existing vorticity in the creation zone respectively. Furthermore the integrated vorticity in the normal direction through the entire vorticity layer remains finite and constant, indicating that vorticity originates at the aerofoil's surface [4].

In addition Reynolds and Carr [41] demonstrated that for either steady or unsteady flows the rate of surface vorticity creation shows dependence on the tangential acceleration of the surface, the vorticity transported by transpiration through the surface and the instantaneous pressure gradient. Regarding the current investigation the flux of vorticity is represented simply by eqn. 2.21 which expresses the normal gradient of vorticity, (i.e. $\frac{\partial \omega}{\partial \eta}$) as function of the surface pressure gradient. In addition, vorticity convection can be also quantified by the measurement of the vorticity flux at a specified location which is defined by eqn. 2.25, [110]:

$$S(x) = \int_0^{\infty} u(x, y) \omega(x, y) dy \quad (2.25)$$

with $S(x)$ denoting the surface chord wise non-dimensional vorticity flux, $u(x, y)$, $\omega(x, y)$ and y denoting the fluid velocity, the vorticity and the dis-

tance perpendicular from the aerofoil's surface respectively. After employing the expression which relates pressure and vorticity distribution, the airloads are obtained.

2.4.3 Airloads around the aerofoil

The airloads of primary concern in the current investigation are the sectional normal force and pitching moment. They are obtained after performing an integration of the pressure and shear stress (see eqn. 2.20) along the aerofoil contour [4]. Once the normal force is calculated the thrust and the flap aerodynamic moment about its flap hinge can be easily obtained. The aerodynamic drag calculated by DIVEX is effectively pressure drag.

2.5 Simulation of the Dynamic Stall phenomenon

The simulations presented within the current investigation are essentially two dimensional. Due to the two dimensionality of the present work detailed features of three-dimensional helicopter rotor dynamic stall such as tip- and whole Ω -shape vortical flow structure cannot be taken into account.

In addition, phenomena such as dynamic effects on the pitching moment which are associated with dynamic pressure distribution across the rotor disc are not included. In particular, the current work focuses on the retreating

side of the rotor disc⁹ where the dynamic pressure maintains low levels [49]. For the sake of completeness, another aspect that should be mentioned is the radial flow effect. The flow over the rotor is greatly affected by its azimuthal rotation, i.e. a centrifugal force that tends to produce a flow outboard toward the rotor tip [49]. In particular the flow direction shows dependency on centrifugal force, wake contraction, undeveloped tip vortex and spanwise pressure gradient [49]. On the other hand neglecting radial flow effects due to the two-dimensionality of the current problem appears to be a reasonable assumption [49]. These limitations are listed in table 2.2 .

Limitations:	Reason of exclusion:
<ul style="list-style-type: none"> - tip flow effects - radial flow effect - Ω-shape vortex - dynamic pressure changes across retreating side of rotor disc 	<ul style="list-style-type: none"> - two dimensionality - two dimensionality - two dimensionality - remain low at retreating side

Table 2.2: Limitations of the current discrete vortex method (DVM)

The simulations conducted within the present research concern an oscillatory aerofoil motion. The motion starts smoothly from -1° aerofoil AOA ensuring therefore that the 0° is included and ramps up to the mean angle.

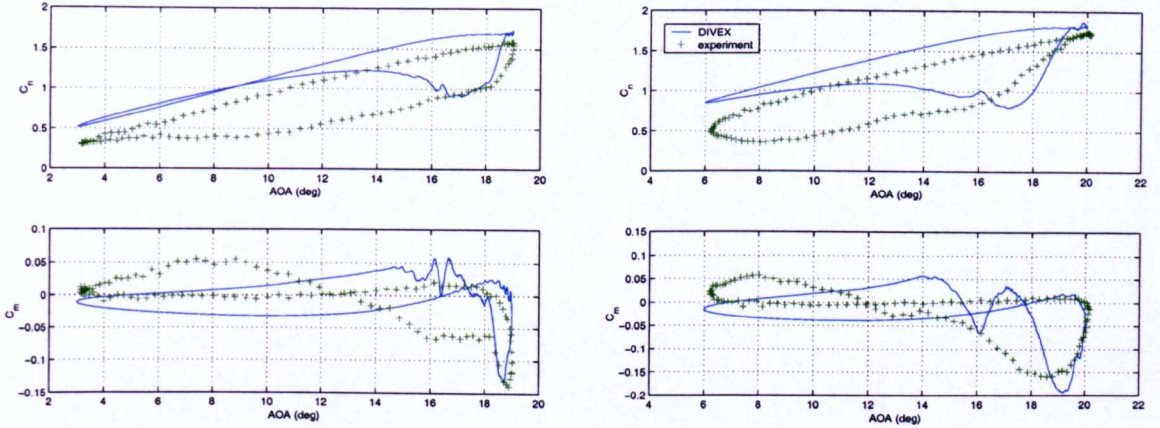
⁹This is the rotor azimuth where the blade encounters dynamic stall

The smooth initiation of the simulation is achieved by fitting a sixth degree polynomial connecting the starting position of the aerofoil and the main part of the ramp motion. With this approach it is believed that the flow history is somewhat better deployed and maintained throughout the entire simulation. The flap deflection is introduced after the flow has settled, i.e. hereafter the subsequent cycles show almost identical aerodynamic characteristics, in other words when the airloads time history repeats in a periodic fashion. In the following section a validation is given on simulations regarding aerofoil oscillatory profiles.

2.6 Code validation

The capabilities of the present DVM flow solver for simulating unsteady flows around a pitching aerofoil have been repeatedly demonstrated; more details about the discrete vortex method can be found in [56], [4], [76]. Validation of the current DVM regarding the present work is demonstrated throughout this section. For the validation of the present DVM, a series of simulations covering a range of mean angles at various reduced frequencies are conducted for the NACA 0015 profile pivoted at quarter chord and oscillating in pitch. The predictions are compared against the experimental data obtained by Galbraith *et. al.* [118]. The validation is presented in terms of pitching

moment(C_m) and normal force(C_n) and are presented in *averaged* hysteresis loops for convenience. The core case for validation is shown in fig. 2.5(a) where aerofoil mean angle and reduced frequency are fairly low. Contrasting with the core case, three more cases are compared with variations of aerofoil mean angles, oscillatory angles and reduced frequencies, fig.2.5(b,c,d).

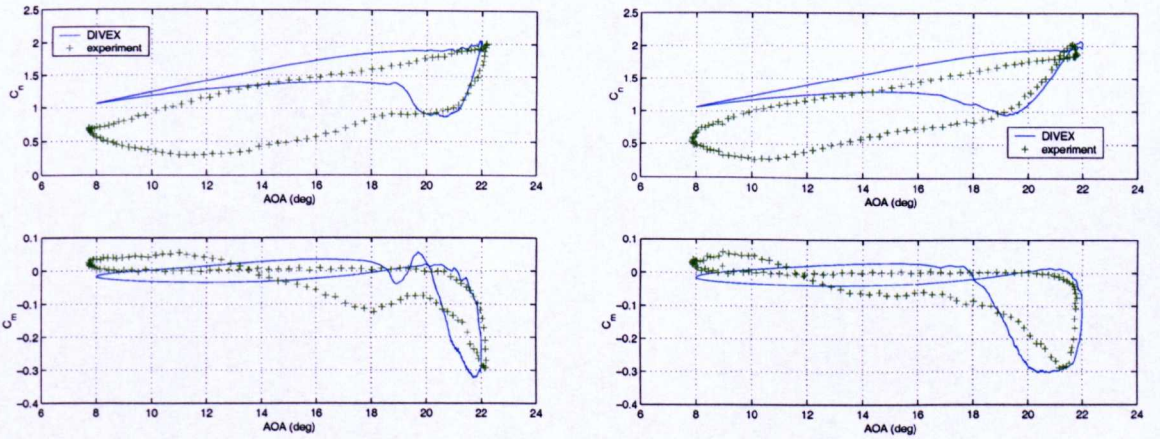


(a) $\theta(t) = 11^\circ \pm 8^\circ \sin(\omega t)$

(b) $\theta(t) = 13^\circ \pm 7^\circ \sin(\omega t)$

$k = 0.102, M = 0.079, Re = 1.01 \times 10^6$

$k = 0.154, M = 0.119, Re = 1.49 \times 10^6$



(c) $\theta(t) = 15^\circ \pm 7^\circ \sin(\omega t)$

(d) $\theta(t) = 15^\circ \pm 7^\circ \sin(\omega t)$

$k = 0.128, M = 0.119, Re = 1.48 \times 10^6$

$k = 0.154, M = 0.121, Re = 1.49 \times 10^6$

Figure 2.5: Numerical and experimental comparison for sectional normal force and pitching moment.

As it becomes evident from fig. 2.5(a), the attached flow phase is somewhat over predicted for C_n , however the predicted trend including the dynamic

stall event is shown to be similar to the experiment. In addition, the normal force drops more abruptly than in the experiment and part of the flow reattachment process agrees well with experiment. The C_m for the attached flow part during the upward motion is somewhat underpredicted and the moment breakdown occurs at approximately half a degree later than in the experiment. The C_m undershoot shows good agreement and part of the post stall phase agrees reasonably with experiment.

By increasing the aerofoil mean angle by two degrees, lowering the oscillation angle by one degree at a reduced frequency of $k = 0.154$, the normal force is found to be over predicted during the attached flow phase and the DS event, the post stall phase shows under prediction and the reattachment part of the loop is found to be over predicted compared to experiment as shown in figs. 2.5(b). The C_m is slightly under predicted for the attached flow phase while the moment breakdown shows excellent agreement with experiment as illustrated in fig. 2.5(b). The C_m magnitude is found to be somewhat under-predicted whereas the moment breakdown shows excellent agreement with experiment.

Further increment of the aerofoil mean angle by two degrees, the oscillation angle lower by one degree compared to the core case and at a reduced frequency of $k = 0.128$, the C_n over prediction is shown to decrease as the cycle approaches the DS (dynamic stall) regime as shown in figs. 2.5(c). After the DS event, post stall and the early part of the reattachment process show

excellent agreement with the experiment. The rest of the reattachment part is shown to be in disagreement with experiment. The attached flow part of the C_m is a bit under predicted, while moment breakdown and undershoot show excellent agreement with experiment as displayed in fig. 2.5(c). The post stall and reattachment part of the cycle show little agreement with experiment.

As in case shown under fig. 2.5(c) at a reduced frequency of $k = 0.154$, the normal force (i.e. C_n) is shown to be slightly over predicted regarding the attached flow and DS event while the post stall part of the cycle shows excellent agreement with experiment, figs. 2.5(d). The reattachment part shows over prediction compared against experiment. The C_m part of the cycle agrees well with experiment, the breakdown and magnitude show excellent agreement with experiment as shown in figs. 2.5(d). The post stall part of the cycle is not captured quite accurately and the reattachment agrees reasonably with experiment.

The pitching moment breakdown and undershoot is very well captured as shown in figs. 2.5(a-d). The attached flow and reattachment parts of the cycle are somewhat under predicted. The normal force is found to be over predicted in all cases. This over prediction is even present also in the attached flow part of the cycle. Lin reports that this fact is associated with the part of vorticity that crosses the boundary between the creation zone and

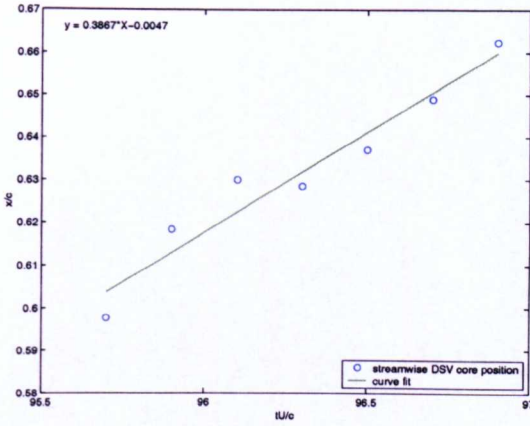
the vorticity zone [4]. In particular, the significance of the contributions to the shedding of vorticity from either diffusion or convection varies strongly according to the flow field state [4]. In the attached flow regime, the main cause of shedding is diffusion, while in the separated flow regime the contribution of vorticity convection increases significantly [4]. This implies that only part of the vorticity crosses the boundary between creation and wake zone yielding to error reduction otherwise encountered by full vortex shedding compared to other models [4]. Although this shedding is more realistic compared to other models, it still causes errors which amplify with time and consequently these errors manifest themselves in the airloads [4].

2.6.1 Dynamic stall vortex convection speed

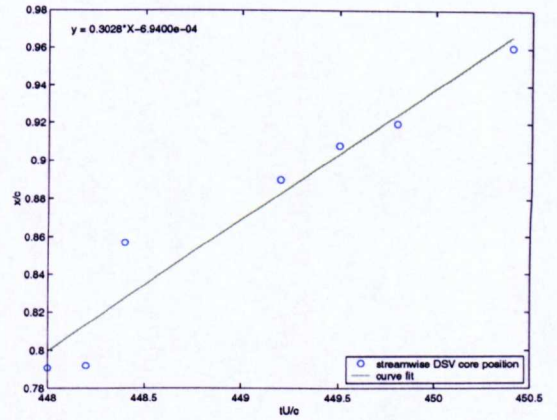
As already shown by various researchers [87], [101], [124], [11], [85] an aspect that certainly deserves attention, is the DSV (dynamic stall vortex) convection speed. Throughout the present investigation it is derived from well validated cases against experiment

In particular and when examining the pressure time-history of the simulations involved in the current work, it becomes evident that the DSV manifests itself at the pressure field by leaving a region of suction. The highest value of this suction peak (over the aft portion of the aerofoil) can be considered as the streamwise (or chordwise) location of the DSV. Although the DSV manifests

itself in the pressure field, it should be reminded that DIVEX is limited to calculate surface pressure only, (see eqn. 2.20). Therefore it becomes apparent that when the DSV leaves the aerofoil's suction surface, there is no more trace to be found back in the pressure field. For this reason it is thought that it is more convenient to determine the convection of the dynamic stall vortex by simply pointing the centre of the DSV vortical structure, i.e. its position with respect to the aerofoil's suction surface. All the measurements are taken after its complete formation at the aft portion (i.e. $\frac{x}{c} > 0.6$) of the aerofoil's suction surface. The above technique was employed for a range of reduced frequencies ($0.051 < k < 0.154$), at various mean angles ($9^\circ < \tilde{\theta}_0 < 15^\circ$) and shown fig. 2.6.



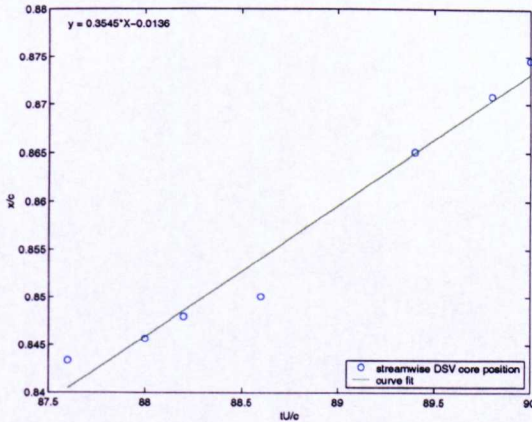
(a) $\theta(t) = 13^\circ \pm 7^\circ \sin(\omega t)$



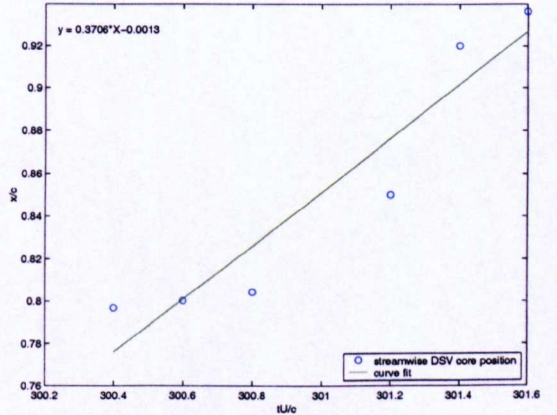
(b) $\theta(t) = 11^\circ \pm 8^\circ \sin(\omega t)$

$k = 0.154, M = 0.119, Re = 1.49 \times 10^6$

$k = 0.102, M = 0.079, Re = 1.01 \times 10^6$



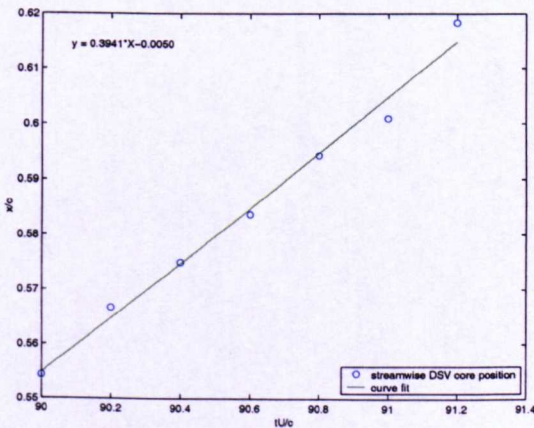
(c) $\theta(t) = 9^\circ \pm 8^\circ \sin(\omega t)$



(d) $\theta(t) = 15^\circ \pm 7^\circ \sin(\omega t)$

$k = 0.051, M = 0.119, Re = 1.47 \times 10^6$

$k = 0.154, M = 0.121, Re = 1.49 \times 10^6$



(e) $\theta(t) = 15^\circ \pm 7^\circ \sin(\omega t)$

$k = 0.128, M = 0.119, Re = 1.48 \times 10^6$

Figure 2.6: Determination of streamwise DSV convection speed.

In more detail the DSV convection speed was found to be roughly constant, i.e. at about $\approx \frac{1}{3}U_\infty$ regarding all presented cases. As it becomes evident from figs. 2.6(a-e), where the non-dimensional time is plotted vs the stream-wise DSV location, a straight line is fitted through the data, therefore quantifying that the DSV convects at a constant speed. This straight line has the form of $y = ax + b$ where the term a represents the convection ratio $\frac{u}{U_\infty}$. The DSV convection speeds presented in figs. 2.6(a-e) show excellent agreement with the results reported by Green *et. al.* [11]. Although the DSV convection speed regarding the present work concerns only oscillatory type of aerofoil motion, it is found that the the DSV convection speed remains constant and show no dependency on aerofoil- amplitude and mean angle [11]. The results discussed here are globally presented into table 2.3 .

mean angle ($\tilde{\theta}_0$)	osc. angle ($\hat{\theta}_1$)	reduced frequency (k)	Mach number (M)	DSV convection speed ($\frac{u}{U_\infty}$)
9°	8°	0.051	0.1190	0.3545
11°	8°	0.102	0.0790	0.3028
15°	7°	0.154	0.1208	0.3706
15°	7°	0.128	0.1192	0.3941
13°	7°	0.154	0.1186	0.3867

Table 2.3: Dynamic stall vortex convection speed, $Re = 1.49M$.

2.7 Concluding remarks

The current chapter provides a description of the mathematical model embedded into the flow solver, the discretisation of the flow field and experimental validation on the airloads and DSV convection speed. Regarding the flow solver and the flow field discretisation, a comprehensive analysis is presented in [4]. The validation on the pitching moment and normal force is reasonably well captured for the aerofoil mean and oscillatory angles and reduced frequencies shown. In addition the validation on the DSV convection speed shows consistency with what is so far reported in the scientific literature.

Chapter 3

Flow topology

An understanding of dynamic stall is required to allow the development of flow control approaches. Within the present work the adopted flow management approach, is based on modifying the aerodynamic state of the flow field in the trailing edge vicinity of the aerofoil in such a way that the desired goal is achieved. This aerodynamic modification originates from a trailing edge flap based on the manipulation of the DSV (dynamic stall vortex) and the TEV (trailing edge vortex).

The current chapter attempts to give insight into the dynamic stall flow topology using the discrete vortex numerical method presented in chapter 2. Emphasis is given to the unsteady pressure and vorticity production involved in both the clean and flapped cases. The peak pressure and vorticity are examined in a similar fashion as reported by Acharya and Metwally who have conducted an investigation for a ramping NACA 0012, [85]. The primary

sources of the surface dimensionless vorticity flux are identified and they are further correlated to vortical interactions that occur during the oscillation cycle. In addition the suggested flap aerodynamic mechanism based on vorticity manipulation in the trailing edge vicinity is presented.

3.1 Assumptions & simplifications

It is assumed that the blade cross-sectional profile undergoes a pure sinusoidal motion. In a real rotor environment the effects of dynamic pressure (i.e. on the airloads particularly with respect to pitching moment and normal force), radial and tip flow effects should be taken into account in order to establish a more realistic rotor blade aerofoil pitch profile. Phenomena such as dynamic effects on pitching moment are associated with dynamic pressure variations across the rotor disc [49]. Prouty reports that the dynamic pressure changes on the retreating side are small, therefore they can be neglected [49].

Another aspect that should be mentioned is the radial (i.e. centrifugal) flow effect. The flow over the rotor is greatly affected by its azimuthal rotation, i.e. a centrifugal force that tends to produce a flow outboard toward the rotor tip [49]. In particular the flow direction shows dependency on centrifugal force, wake contraction, radial flow effects and spanwise pressure gradient [49]. None of these parameters is examined within the present work

due to the two-dimensionality of the flow solver employed. In addition it is further assumed that the aerofoil under consideration is located at $0.75R$ since most of the rotor lift is produced between $0.65R$ and $0.85R$ rotor span [57]. In reality viscous effects have to be taken into account. The way that these effects manifest themselves is twofold. First, the finite aerofoil thickness reduces the leading edge suction and also the effectiveness, otherwise affecting the capability of the flap to generate extra lift and sectional pitching moment [72]. Although the present DVM accommodates viscosity, flow effects otherwise associated with the finite thickness of the boundary layer are not applied within the present research since it does not incorporate any concept as such. In addition, the presence of the flap hinge gap might affect the flap performance in a similar fashion. Furthermore it is assumed that the freestream velocity maintains a constant value. However during the rotorcraft's forward flight, there is a temporal dependency of the blade's velocity distribution as it sweeps over the azimuth, [32]. These assumptions are listed in table 3.1.

Assumptions:
- dynamic effects on airloads are neglected
- exclusion of radial & and tip flow effects
- blade section is located at 75% R
- constant freestream velocity
- influence of the flap hinges is negligible

Table 3.1: Assumptions for blade pitch profile.

Taking into account the above assumptions the crosssectional blade pitch profile is given by:

$$\theta(\Psi)_{0.75R} = \theta_0 - \theta_{tw}x - A_1 \cos(\Psi) - B_1 \sin(\Psi) \quad (3.1)$$

with θ_0 being the blade sectional mean angle (i.e. collective), θ_{tw} the blade sectional twist, A_1 and B_1 being the cyclic pitch component which is applied longitudinally and laterally with respect to the fuselage respectively, [33]. Furthermore in the absence of blade twist and expressing the blade sectional pitch angle only by the collective (i.e. θ_0) and B_1 cyclic terms, eqn. 3.1 reduces to:

$$\theta(\Psi)_{0.75R} = \theta_0 - B_1 \sin(\Psi) \quad (3.2)$$

which is exactly the same expression as $\theta(t) = \tilde{\theta}_0 \pm \hat{\theta}_1 \sin(\omega t)$ with $\tilde{\theta}_0$ denoting the mean angle, $\hat{\theta}_1$ the oscillation angle, ω the natural oscillatory frequency of the aerofoil, and t the time.

Equation 3.2 appears to be reasonable for describing the helicopter's azimuthal blade crosssectional motion and also allows comparison with the experimental data of Galbraith *et.al.* [118] which further describes a series of aerofoils (including a NACA 0015) oscillating in pitch. The dynamic stall flow field over the clean aerofoil is next presented.

3.2 Dynamic stall flow field over clean aerofoil

As already mentioned in the introduction, dynamic stall might be further classified into LS (light dynamic stall) and DDS (deep dynamic stall) [2]. Within the current investigation only the flow mode of light dynamic stall is examined. The reason for this is that since stall flutter may be triggered by the momentum history encountered during LS, it is important to focus the current study at such flow conditions. Nevertheless deep dynamic stall is also of great importance, but it is less common in rotorcraft operation.

A blade pitch motion history given by $\theta(t) = 15^\circ \pm 7^\circ \sin(\omega t)$ is thought to represent a realistic aerofoil pitch profile. The flow field induced by this profile is further examined at a range of reduced frequencies varying between $0.128 \leq k \leq 0.180$. Examination of the flow field implies identification of the DSV's initiation, growth and convection, unsteady surface pressure and

surface vorticity production. The initiation of the DSV in terms of aerofoil angle of attack (AOA) is presented in fig. 3.1.

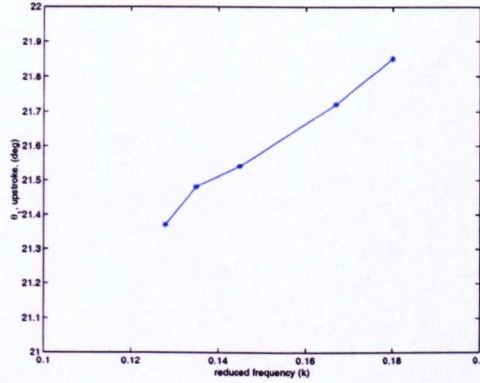


Figure 3.1: Overview of DSV (dynamic stall vortex) initiation angle as function of the reduced frequency for NACA 0015. $\theta(t) = 15^\circ \pm 7^\circ \sin(\omega t)$, $M = 0.119$, $Re = 1.49 \times 10^6$.

The initiation angle of the DSV increases with reduced frequency as it is shown in fig. 3.1. The initiation angle is captured at that aerofoil angle of attack where flow reversal appears for the first in the trailing edge vicinity. Conclusively low reduced frequency values produce the DSV onset earlier in the oscillation cycle. This shows consistency with the results obtained by Robinson *et.al.* [106]. The unsteady separation process, the formation and the ejection of the dynamic stall vortex for the clean NACA 0015 is shown in detail in fig. 3.2(a-h). Both vortex patterns (LHS) and velocity magnitude vectors (RHS) are shown for convenience with the corresponding aerofoil incidence with the arrows indicating either aerofoil upstroke or downstroke.

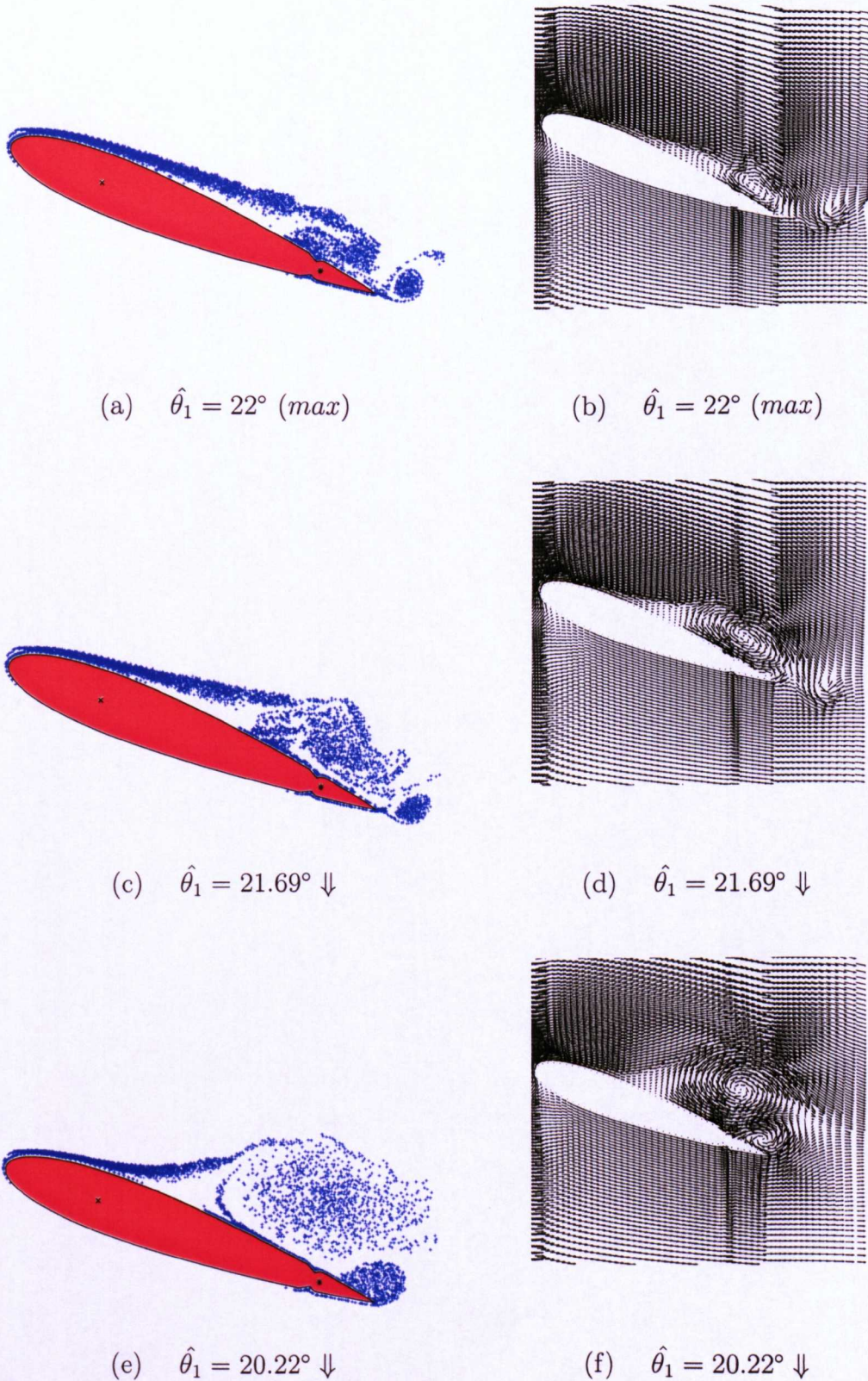


Figure 3.2: Sequence of the instantaneous vortex particles (LHS) and velocity vectors (RHS) at the trailing edge region of **clean** NACA 0015: $\theta(t) = 15^\circ \pm 7^\circ \sin(\omega t)$, $k = 0.180$, $M = 0.119$, $Re = 1.49 \times 10^6$. (cont.)

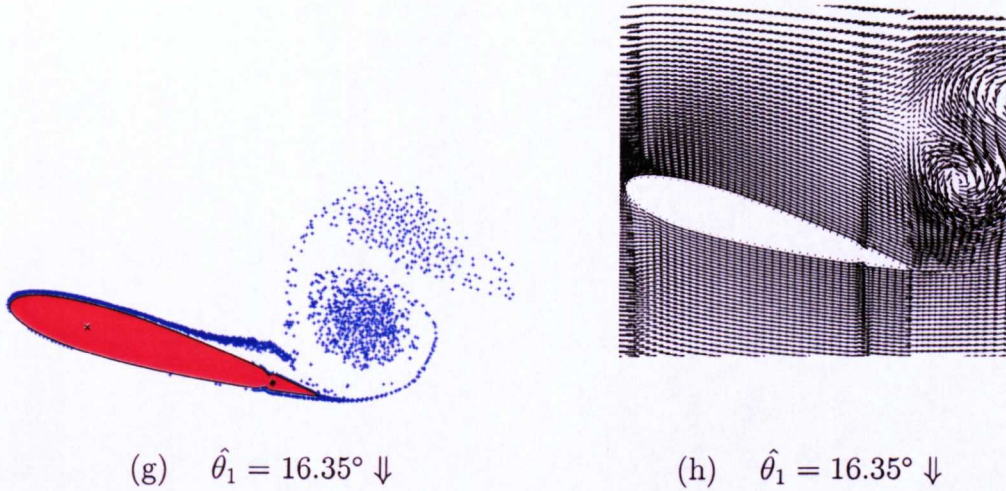


Figure 3.2: Sequence of the instantaneous vortex particles (LHS) and velocity vectors (RHS) at the trailing edge region of **clean** NACA 0015: $\theta(t) = 15^\circ \pm 7^\circ \sin(\omega t)$, $k = 0.180$, $M = 0.119$, $Re = 1.49 \times 10^6$.

As the aerofoil approaches the maximum oscillation angle (i.e. $\hat{\theta}_1 = 22^\circ$), initiation of unsteady separation is triggered in the trailing edge vicinity, fig. 3.2(a,b). The flow reversal tends to continue growing in the upstream direction, and shortly after the aerofoil has exceeded the maximum oscillating angle, a clear vortical pattern is shown occupying about one third over the aerofoil's aft portion, as shown in fig. 3.2(c,d). The DSV (dynamic stall vortex) has completed its formation and it is shown as a clear coherent vortical pattern having rotation of clockwise sense, dominating the local flow field over the aft half of the aerofoil as shown in fig. 3.2(f). At the very same instant a smaller vortical structure of opposite sense appears occupying the flap's suction surface. The aerofoil's downstroke as displayed in fig. 3.2(e,f),

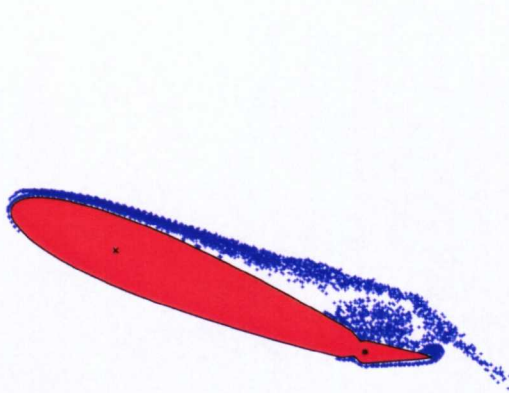
the DSV, convects downstream and the vortical pattern of the TEV identified in the previous frame is more evident. At this stage clockwise vorticity (i.e. DSV) is no longer the only dominant local flow feature. Instead, two vortical structures carrying circulation of opposite sense are present, i.e. the DSV and TEV. The two vortices are coalescing into a much larger vortical structure with the TEV having ejected the DSV from the aerofoil's suction surface. Finally, both DSV and TEV are shed into the wake and the flow starts to reattach, fig. 3.2(g,h). From the flow management point of view, this suggests that careful management of these discrete coherent vortical patterns could be utilised as a means of controlling aerofoil dynamic stall. The influence of the flap on the dynamic stall flow field is next given.

3.3 Influence of the flap on Dynamic stall flowfield

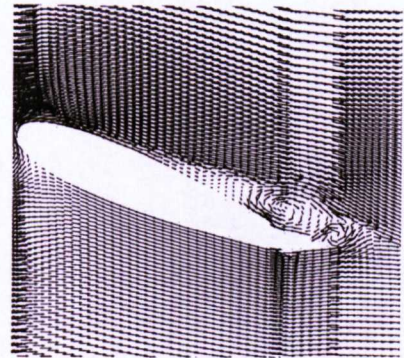
The influence of the flap into the flow field particularly on to the behaviour of the DSV (dynamic stall vortex) and the TEV (trailing edge vortex) for the flapped case is shown in fig. 3.3(a-h) where the vortical patterns and velocity magnitude vectors are shown at the same aerofoil incidence as in the clean case for convenience.

As shown in fig. 3.3(a,b), the flap is already more than halfway¹ through its upstroke and it is shown almost parallel with the oncoming flow. This fact prevents the formation of the TEV and consequently the only dominant vortical pattern is the DSV. The same is shown to be the case a bit later, at both the aerofoil's and flap's downstroke, where the DSV has increased in size as shown in fig. 3.3(c,d). In addition a TEV initiates and both DSV and TEV continue to grow as displayed in fig. 3.3(e,f). Particularly the TEV has increased in size as a result of the flow influx from the flap's pressure surface and its curvilinear motion. Regarding the later, the tip of the flap adds rotational momentum to the flow particles in its vicinity. After the TEV has completed its formation, it is pushed away from the flap's suction surface as it is evident from fig. 3.3(g,h).

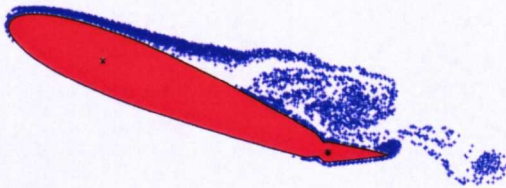
¹ $\delta_{f_{max}} = 20^\circ$



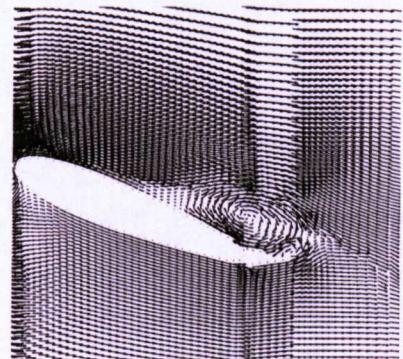
(a) $\hat{\theta}_1 = 22^\circ$ (*max*), $\delta_f = 17.81^\circ$ \uparrow



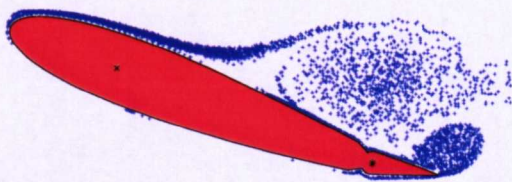
(b) $\hat{\theta}_1 = 22^\circ$ (*max*), $\delta_f = 17.81^\circ$ \uparrow



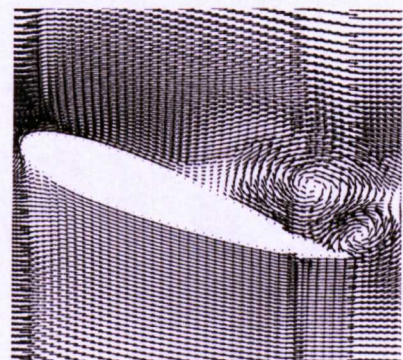
(c) $\hat{\theta}_1 = 21.69^\circ$ \downarrow , $\delta_f = 19.71^\circ$ \downarrow



(d) $\hat{\theta}_1 = 21.69^\circ$ \downarrow , $\delta_f = 19.71^\circ$ \downarrow



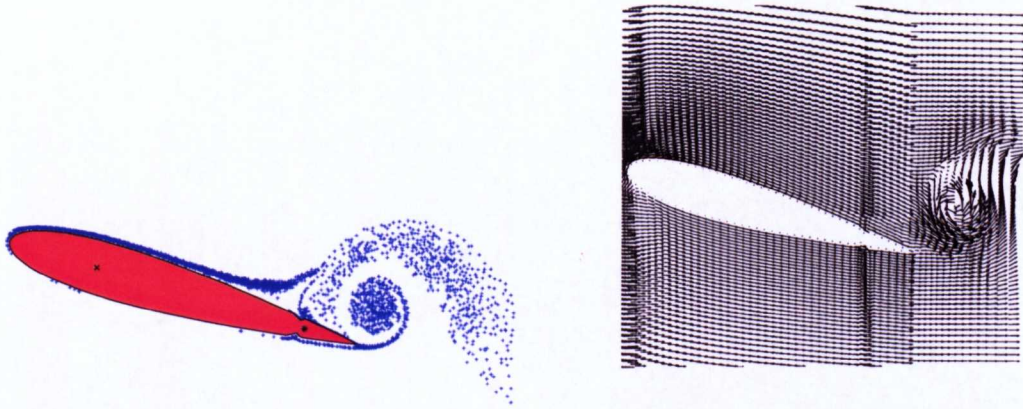
(e) $\hat{\theta}_1 = 20.22^\circ$ \downarrow , $\delta_f = 9.60^\circ$ \downarrow



(f) $\hat{\theta}_1 = 20.22^\circ$ \downarrow , $\delta_f = 9.60^\circ$ \downarrow

Figure 3.3: Time sequence of the instantaneous vortex particles (LHS) and velocity vectors (RHS) at the trailing edge region of **flapped** NACA 0015:

$\theta(t) = 15^\circ \pm 7^\circ \sin(\omega t)$, $k = 0.180$, $M = 0.119$, $Re = 1.49 \times 10^6$. (cont.)



(g) $\hat{\theta}_1 = 16.35^\circ \downarrow, \delta_f = 0^\circ$

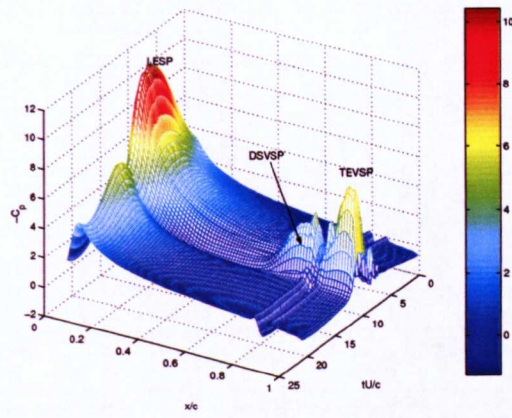
(h) $\hat{\theta}_1 = 16.35^\circ \downarrow, \delta_f = 0^\circ$

Figure 3.3: Time sequence of the instantaneous vortex particles (LHS) and velocity vectors (RHS) at the trailing edge region of **flapped** NACA 0015:

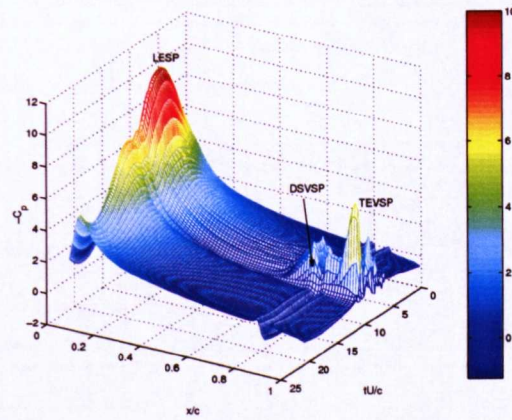
$$\theta(t) = 15^\circ \pm 7^\circ \sin(\omega t), k = 0.180, M = 0.119, Re = 1.49 \times 10^6 .$$

3.4 Unsteady pressure

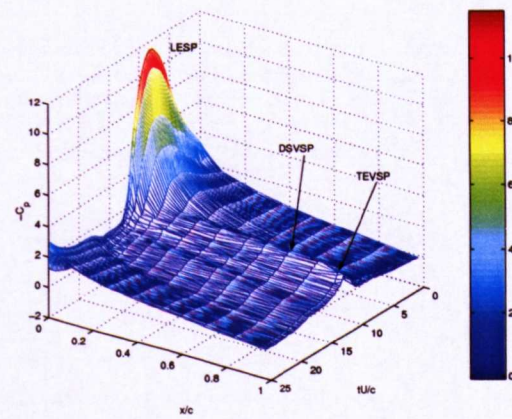
The variation of the unsteady surface pressure over the aerofoil's suction surface is examined in detail. Figures 3.4(a), 3.4(b) for the suction surface of the clean and flapped case respectively, show three distinctive peaks over the averaged cycle: the LESP (leading edge suction peak), the DSVSP (dynamic stall vortex suction peak) and the TEVSP (trailing edge vortex suction peak). The LESP does not seem to affect the flow downstream at the trailing edge region for the case shown as it reaches its maximum value earlier in the cycle. Furthermore there is a distinctive groove at both sides of the DSVSP and TEVSP which is due to the flap notches. The experimental averaged pressure distribution over the aerofoil's suction surface is also presented for convenience.



(a) NACA 0015 clean



(b) NACA 0015 with 15%c flap



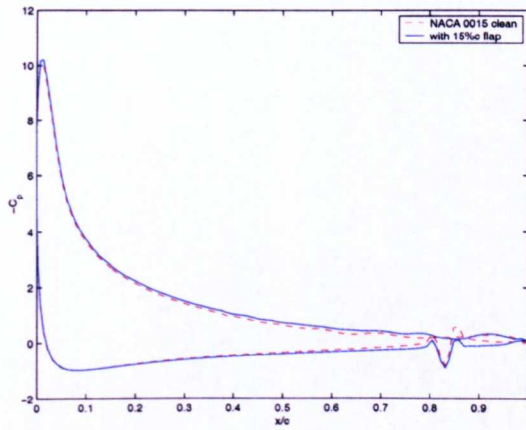
(c) NACA 0015 clean (experiment)

Figure 3.4: Averaged surface pressure (suction surface) for clean and flapped case: $\theta(t) = 15^\circ \pm 7^\circ \sin(\omega t)$, $k = 0.154$, $M = 0.119$, $Re = 1.49 \times 10^6$.

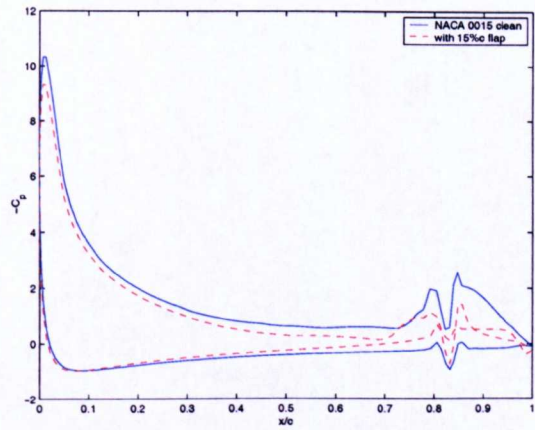
Instantaneous chordwise surface pressure plots are shown for both clean and flapped cases in fig. 3.5(a-f). The corresponding aerofoil AOA (angle of attack) together with the flap's deflected position are shown for convenience with the arrows indicating either aerofoil upstroke or downstroke. The suction peaks are over the aft portion of the aerofoil covering approximately the last 30% of the aerofoil's chord. In the flapped case these suction peaks are shown to be lower in magnitude compared to the clean case. This justifies a successful manipulation of the DSV and the TEV.

A very interesting feature is illustrated in fig. 3.5(e). There is a massive suction peak corresponding to the clean case, covering about the last 15% of the aerofoil's chord, i.e the flap's suction surface. Further observation of figs. 3.2(e,f) illustrates the presence of the TEV covering the whole flap suction surface and, in addition, the DSV being on top of the TEV. As presented by Tsiachris there is a possible mechanism triggering dynamic stall for the given profile (NACA 0015): the combined vortical structure which consists of both DSV and TEV [22]. This triggers dynamic stall and consequently introduces the large undershoot in the pitching moment hysteresis loop for a trailing-edge stall profile [1] such as the NACA 0015. This massive suction peak is a result of the DSV whose circulation is increased due to the interaction with the TEV. In fact the TEV feeds the DSV as already shown in figs.3.2(e,f), therefore increasing the amount of circulation carried by the DSV. For the flap case shown in fig. 3.5(e), the DSV's amount of circulation

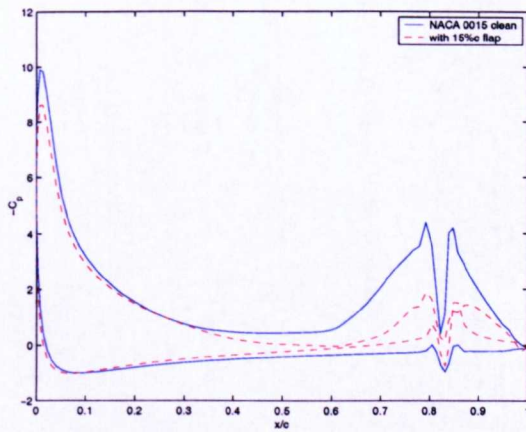
is lower compared to its clean counterpart. This further implies that the DSV does not increase in size due to the presence of the TEV therefore implying that it maintains lower levels of circulation than in the clean case.



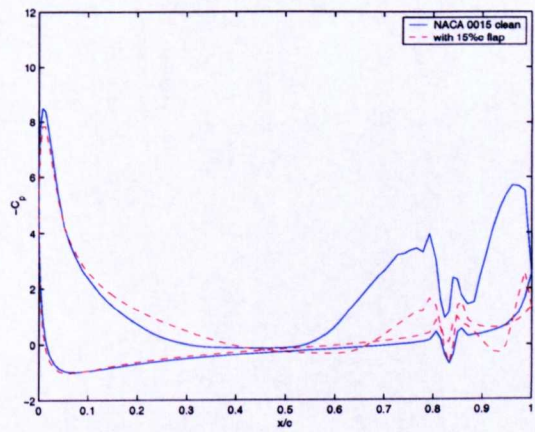
(a) $\theta_1 = 21.32^\circ \uparrow, \delta_f = 8.16^\circ \uparrow$



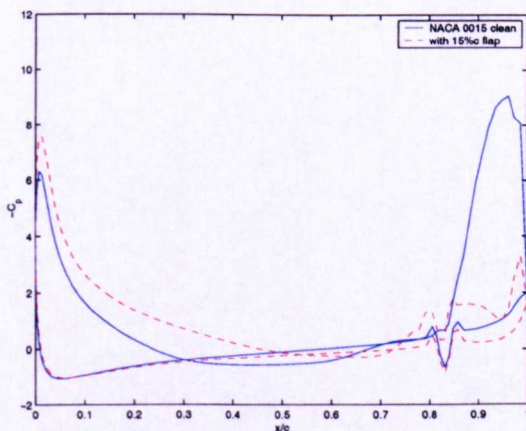
(b) $\theta_1 = 21.98^\circ \uparrow, \delta_f = 18.92^\circ \uparrow$



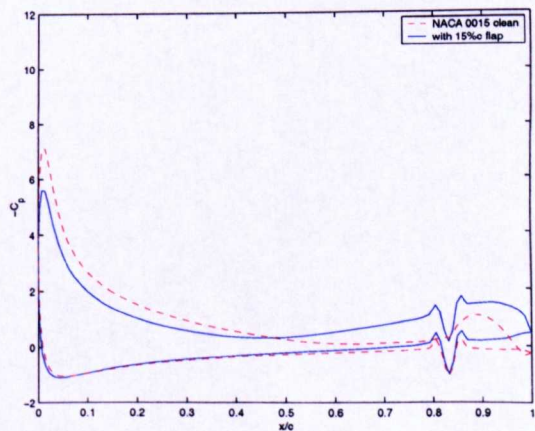
(c) $\theta_1 = 21.89^\circ \downarrow, \delta_f = 19.24^\circ \downarrow$



(d) $\theta_1 = 21.39^\circ \downarrow, \delta_f = 13.42^\circ \downarrow$



(e) $\theta_1 = 20.51^\circ \downarrow, \delta_f = 4.86^\circ \downarrow$



(f) $\theta_1 = 19.29^\circ \downarrow, \delta_f = 0.14^\circ \downarrow$

Figure 3.5: Instantaneous surface pressure for clean and flapped case: $\theta(t) = 15^\circ \pm 7^\circ \sin(\omega t)$, $k = 0.154$, $M = 0.119$, $Re = 1.49 \times 10^6$.

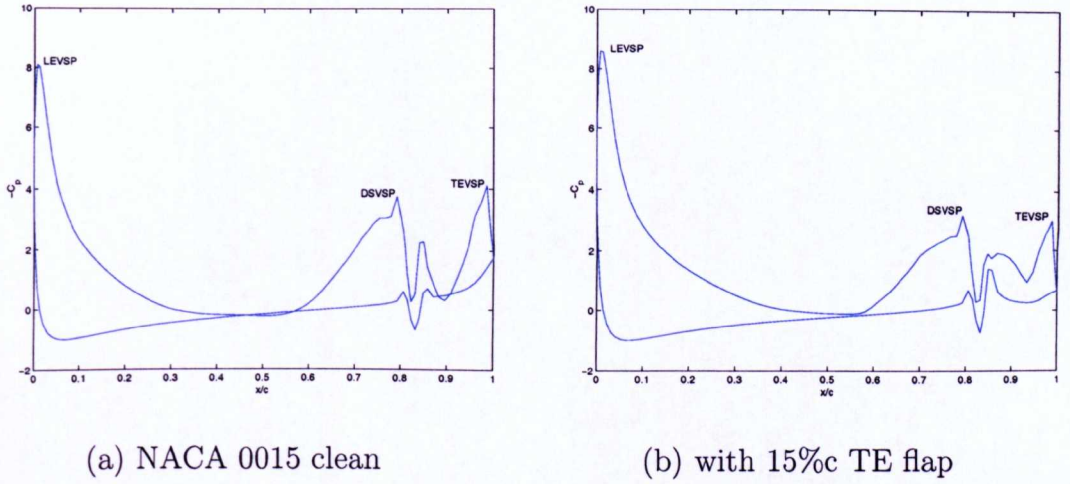
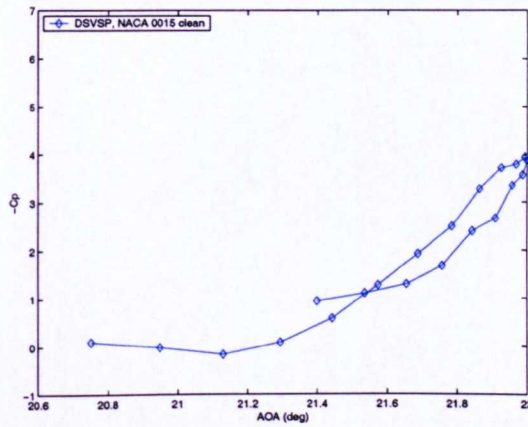


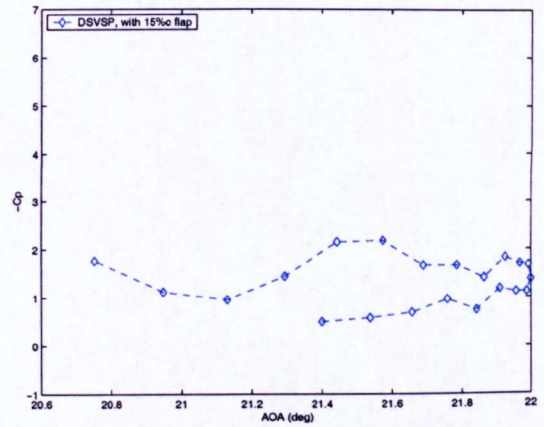
Figure 3.6: Typical instantaneous surface pressure variation over the suction surface. $\theta(t) = 15^\circ \pm 7^\circ \sin(\omega t)$, $k = 0.154$, $Re = 1.48 \times 10^6$, $M_\infty = 0.1209$.

The DSVSP and the TEVSP are captured while the aerofoil exhibits dynamic stall at three different reduced frequencies $k = 0.124$, 0.154 , 0.180 and are shown in figs. 3.7, 3.8 and 3.9 respectively. Since it is difficult to examine in detail the pressure distribution over the whole cycle as shown in figs. 3.4(a,b), individual pressure traces are extracted at different angles of attack. Figure 3.6 serves for labelling the three distinctive peaks, i.e. LEVSP, DSVSP and the TEVSP. The current study is focused only on the DSVSP and TEVSP since we are dealing with a trailing edge stall profile such as the NACA 0015 [112]. In addition the LEVSP occurs earlier in the cycle compared to the dynamic stall event and it is of little significance for the present investigation. Moreover the maximum values of these suction peaks are extracted over the portion of the cycle that the aerofoil encounters dynamic stall and

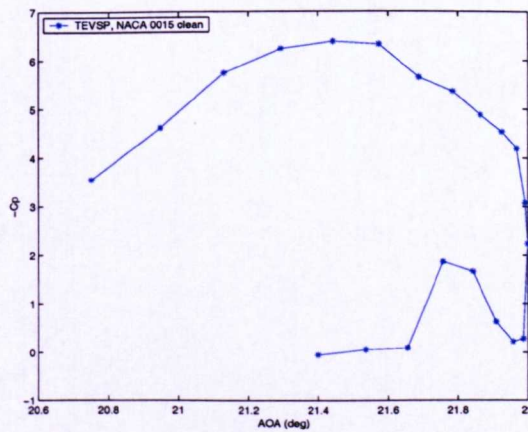
a line is plotted between the different maximum suction peak values in order to establish a trend.



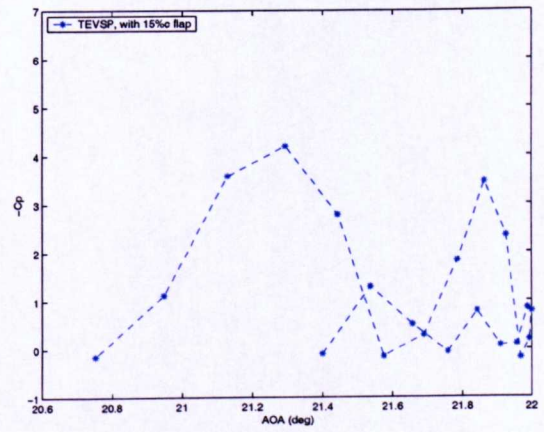
(a) NACA 0015 clean ($k=0.128$)



(b) with 15% TE flap ($k=0.128$)



(c) NACA 0015 clean ($k=0.128$)



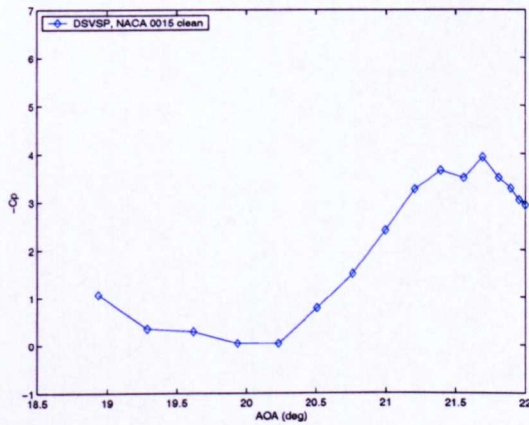
(d) with 15% TE flap ($k=0.128$)

Figure 3.7: Variation of surface pressure associated with the characteristic peaks. $\theta(t) = 15^\circ \pm 7^\circ \sin(\omega t)$, $k = 0.128$, $Re = 1.48 \times 10^6$, $M_\infty = 0.1209$.

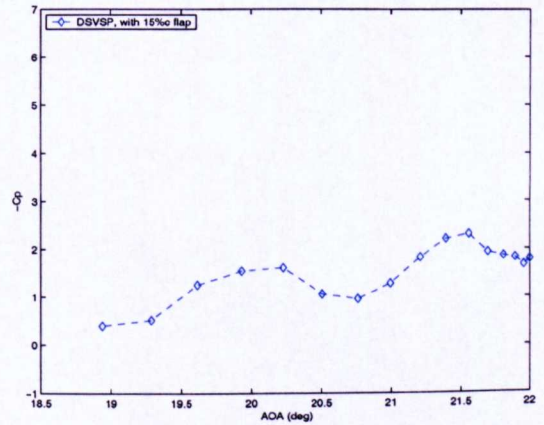
At a reduced frequency of $k = 0.128$, the DSVSP seems to deliver a maximum value at about $C_p \approx -4$, at the maximum oscillating AOA, i.e. $\hat{\theta}_1 = 22^\circ$ for

the clean case, as shown in fig. 3.7(a). After the DSVSP reaches its maximum value it drops rapidly, suggesting that it leaves the aerofoil's suction surface. The TEVSP for the clean case reaches its maximum value at about $\hat{\theta}_1 \approx 21.4^\circ$, almost half a degree less compared to the DSVSP, as displayed in fig. 3.7(c). The TEVSP shows a magnitude of about two and half times more than the DSVSP. This implies that there is a vortical pair formed which consists both of DSV and TEV. This fact forms also evidence that the suction peak imposed by the DSVSP increases due to the additional suction imposed by the TEVSP. Consequently the latter feeds the former by adding extra amount of circulation. This already suggests that this vortex pairing can be manipulated. After the aerofoil reaches the maximum oscillating angle ($\hat{\theta}_1 = 22^\circ$) there is a short increase indicating the formation of a new TEV. However this newly formed vortex is found to be small in size since it introduces a small amount of suction as shown in fig. 3.7(c). The corresponding DSVSP for the flapped case fluctuates around the value of $C_p \approx -2$ which is half the suction magnitude of compared to its clean counterpart as shown in fig. 3.7(b). The same is shown to be true for the TEVSP which is found to be almost one and a half times less than its clean counterpart, as displayed in fig. 3.7(d). Notice that the TEVSP in the flapped case reaches the value of $C_p \approx -5$ twice, indicating therefore that its formation takes place twice until the maximum oscillating angle is reached. In addition its fluctuating behaviour forms solid evidence that no vortex pairing occurs as in the clean

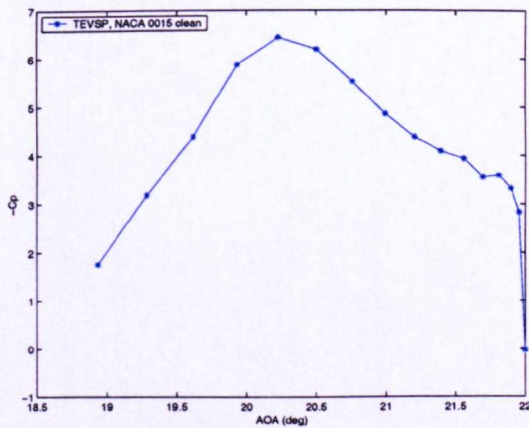
case and also justifies the fact that the flap can alter the flow in the trailing edge vicinity. After the aerofoil reaches its maximum oscillating angle, the TEVSP is shown to form twice during the downstroke of the motion.



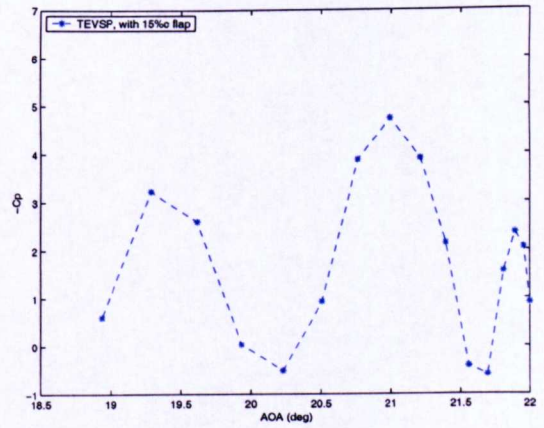
(a) NACA 0015 clean ($k=0.154$)



(b) with 15% TE flap ($k=0.154$)



(c) NACA 0015 clean ($k=0.154$)

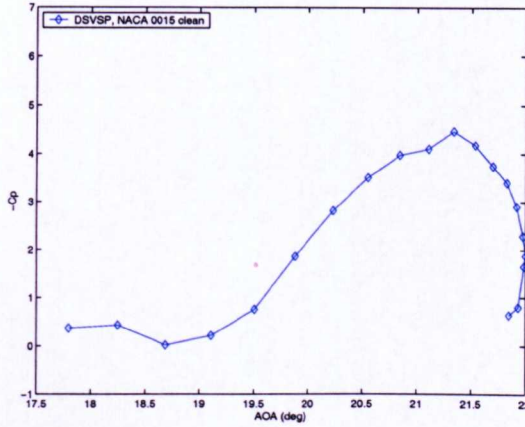


(d) with 15% TE flap ($k=0.154$)

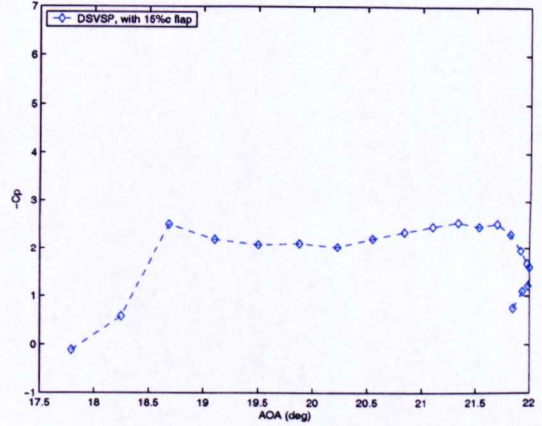
Figure 3.8: Variation of surface pressure associated with the characteristic peaks. $\theta(t) = 15^\circ \pm 7^\circ \sin(\omega t)$, $k = 0.154$, $Re = 1.48 \times 10^6$, $M_\infty = 0.1209$.

A similar situation is observed for this data set (i.e. $k = 0.154$) as for

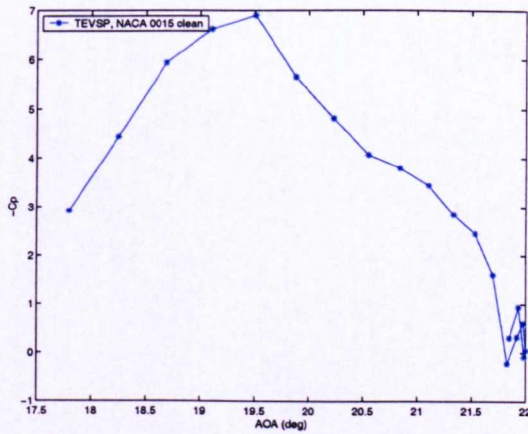
$k = 0.128$ shown in fig. 3.7(a-d).



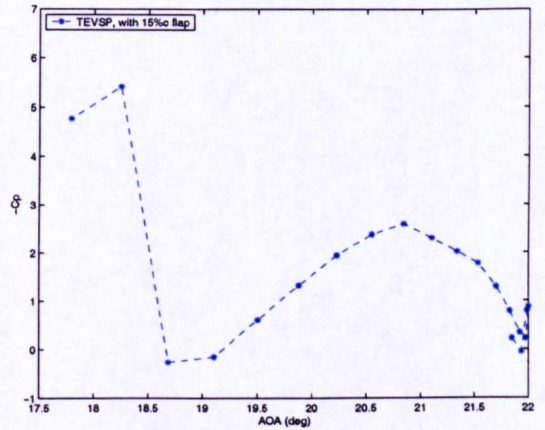
(a) NACA 0015 clean ($k=0.180$)



(b) with 15% TE flap ($k=0.180$)



(c) NACA 0015 clean ($k=0.180$)



(d) with 15% TE flap ($k=0.180$)

Figure 3.9: Variation of surface pressure associated with the characteristic peaks. $\theta(t) = 15^\circ \pm 7^\circ \sin(\omega t)$, $k = 0.180$, $Re = 1.48 \times 10^6$, $M_\infty = 0.1209$.

Regarding the set of data for $k = 0.180$, the DSVSP (see fig. 3.9(a)) is shown to reach the highest value compared to the cases corresponding to $k = 0.128$ and $k = 0.154$. The TEVSP for the flapped case reaches a maximum value

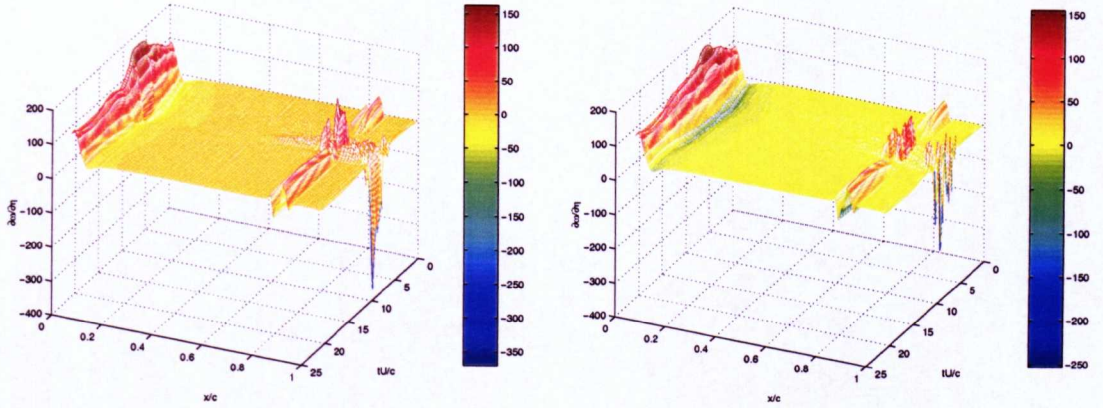
of about $C_p \approx -3$ and maintains almost a constant trend thereafter until about the maximum oscillation aerofoil AOA is reached, fig.3.9(b) .

The TEVSP for the clean case (i.e. $k = 0.180$, fig. 3.9(c)) shows the steepest drop. The TEVSP for the flapped case is found to show the least fluctuating trend,fig. 3.9(d) .

3.5 Vorticity

It has become already apparent that the vorticity flux emanating from the trailing edge can be an essential quantity of controlling aerofoil dynamic stall. Observation of figs. 3.10(a), 3.10(b) demonstrates that most of the vorticity emerges from the leading edge vicinity due to the LESP and at the trailing edge vicinity due to the DSV and TEV. In order to gain insight into the flow behaviour in the trailing edge vicinity, the variation of the vorticity gradient² (i.e. pressure gradient) is examined.

²As shown by eqn. 2.21, the vorticity gradient forms an indication of the pressure gradient along the aerofoil's surface.



(a) NACA 0015 clean

(b) NACA 0015 with 15% flap

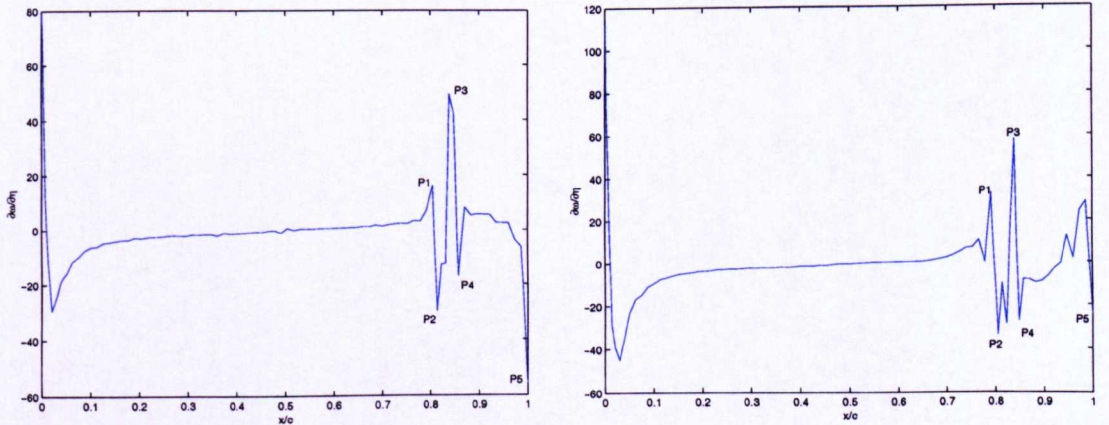
Figure 3.10: Averaged surface vorticity flux (suction surface) for clean and flapped case: $\theta(t) = 15^\circ \pm 7^\circ \sin(\omega t)$, $k = 0.154$, $M = 0.119$, $Re = 1.49 \times 10^6$.

At first as it becomes evident from figs. 3.10(a) & 3.10(b), vorticity is introduced into the flow field mainly from a region at the aerofoil's aft portion, i.e. approximately the last 25% of the chord. Clearly there is a region of peak vorticity at the leading edge area but it does not seem to affect the vorticity flux downstream in the trailing edge vicinity since the vorticity gradient shows very low and fairly constant values between 10% and 70% of the chord on the aerofoil's suction surface.

In principle the detailed features of the surface vorticity flux peaks cannot be observed in detail directly from figs. 3.10(a), 3.10(b); instead they are extracted in the incidence range which includes dynamic stall and are further illustrated in figs. 3.12(a), 3.12(b) for the clean and flapped case respectively. Figures 3.11(a), 3.11(b) which serve as basis for labelling of the suction peaks,

i.e. P1-P5. Peaks P1 and P3 represent the amount of vorticity introduced due to the dynamic stall vortex while peaks P2 and P4 are due to the TEV (trailing edge vortex) and they are opposite in sign since they contain circulation of opposite sense.

Observation of figs. 3.11(a), 3.11(b) reveals that most of the vorticity flux is included in five characteristic peaks located over the last 25% of the chord. In both figs. 3.11(a), 3.11(b), the chordwise variation of the dimensionless surface vorticity flux with the five peaks labelled P1-P5 is illustrated. These peaks are identified during the dynamic stall event shortly after the maximum oscillating aerofoil angle of attack, during the downstroke of the motion for the results shown. The maximum values of the term $\frac{\partial \omega}{\partial \eta}$ at each peak are determined and are shown in figs. 3.12(a), 3.12(b) .

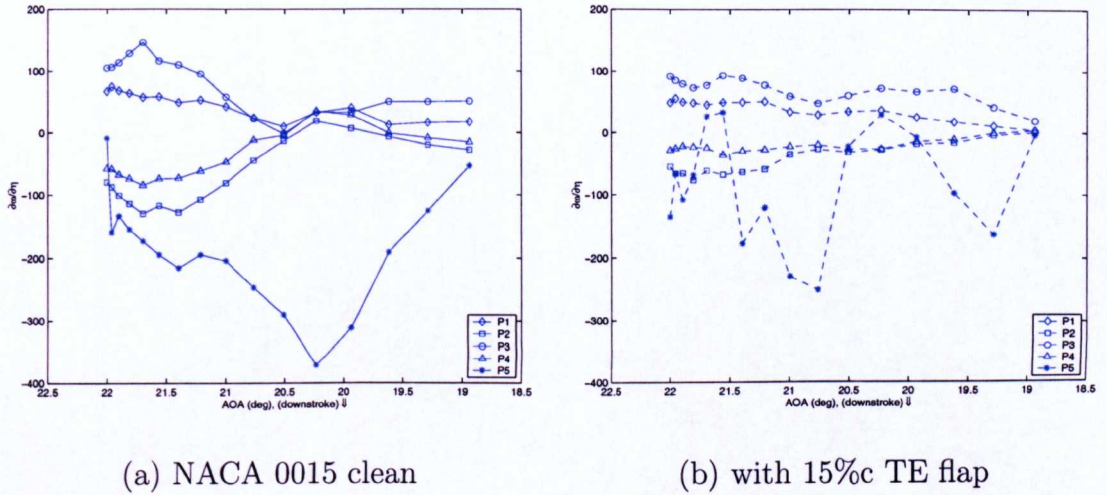


(a) NACA 0015 clean

(b) with 15% TE flap

Figure 3.11: Typical surface vorticity flux variation over the suction surface.

$$15^\circ \pm 7^\circ \sin(\omega t), \quad k = 0.154, \quad Re = 1.48 \times 10^6, \quad M_\infty = 0.1209.$$



(a) NACA 0015 clean

(b) with 15% TE flap

Figure 3.12: Variation of surface vorticity flux associated with the characteristic peaks. $\theta(t) = 15^\circ \pm 7^\circ \sin(\omega t)$, $k = 0.154$, $Re = 1.48 \times 10^6$, $M_\infty = 0.1209$.

Owing to the vorticity balance concept as suggested by Reynolds and Carr, where vorticity is produced it should be equally transported [41]. This occurs by convection due to free stream or diffusion due to viscosity. If this balance is somehow perturbed, this yields to the formation of discrete organised vortical structures such as the DSV and the TEV.

Moreover, the generation of vorticity is balanced by convection for the attached flow region, in other words vorticity has a uniform distribution along the aerofoil's surface. On the other hand, a local imbalance between vorticity production and its convection/diffusion will result in the accumulation of vorticity causing flow breakdown. In more detail, clockwise vorticity emanating from the trailing edge where there is an adverse pressure gradient

distorts this balance and results in the formation of the DSV which is fed with counterclockwise vorticity from the TEV.

The instantaneous development of the vorticity flux along the aerofoil's surface is illustrated in fig. 3.13(a-o) for the clean aerofoil. The corresponding aerofoil angles of incidence are shown for convenience with the arrows indicating upstroke or downstroke of the profile motion. In particular as shown in fig. 3.13(a-c), the local vorticity over the aft part of the aerofoil starts to accumulate in a region covering approximately 75 to 85% of the chord. After the aerofoil reaches the maximum angle of attack (i.e. $\hat{\theta}_1 = 22^\circ$), fig. 3.13(a), the peaks denoted by P3 and P5 (see fig. 3.11) start to increase in magnitude indicating amplification of the local vorticity, 3.13(b-e). As the peak vorticity is shown in fig. 3.13(e), the peak P3 reaches its maximum value, therefore justifying the completion of the DSV formation. In the meantime peak P5 continues to increase in magnitude as illustrated in fig. 3.13(a-m). At the same time peak P3 continues to decrease in magnitude since it is fed with vorticity of opposite sense due to the TEV. This shows that the DSV is fed by the trailing edge vortex. Eventually the peaks that appear on the aerofoil's suction surface start to flatten indicating flow reattachment, fig. 3.13(j-l). The TEV reaches a maximum value at an aerofoil incidence of $\hat{\theta}_1 = 20.23^\circ$ on the downstroke, fig. 3.13(l).

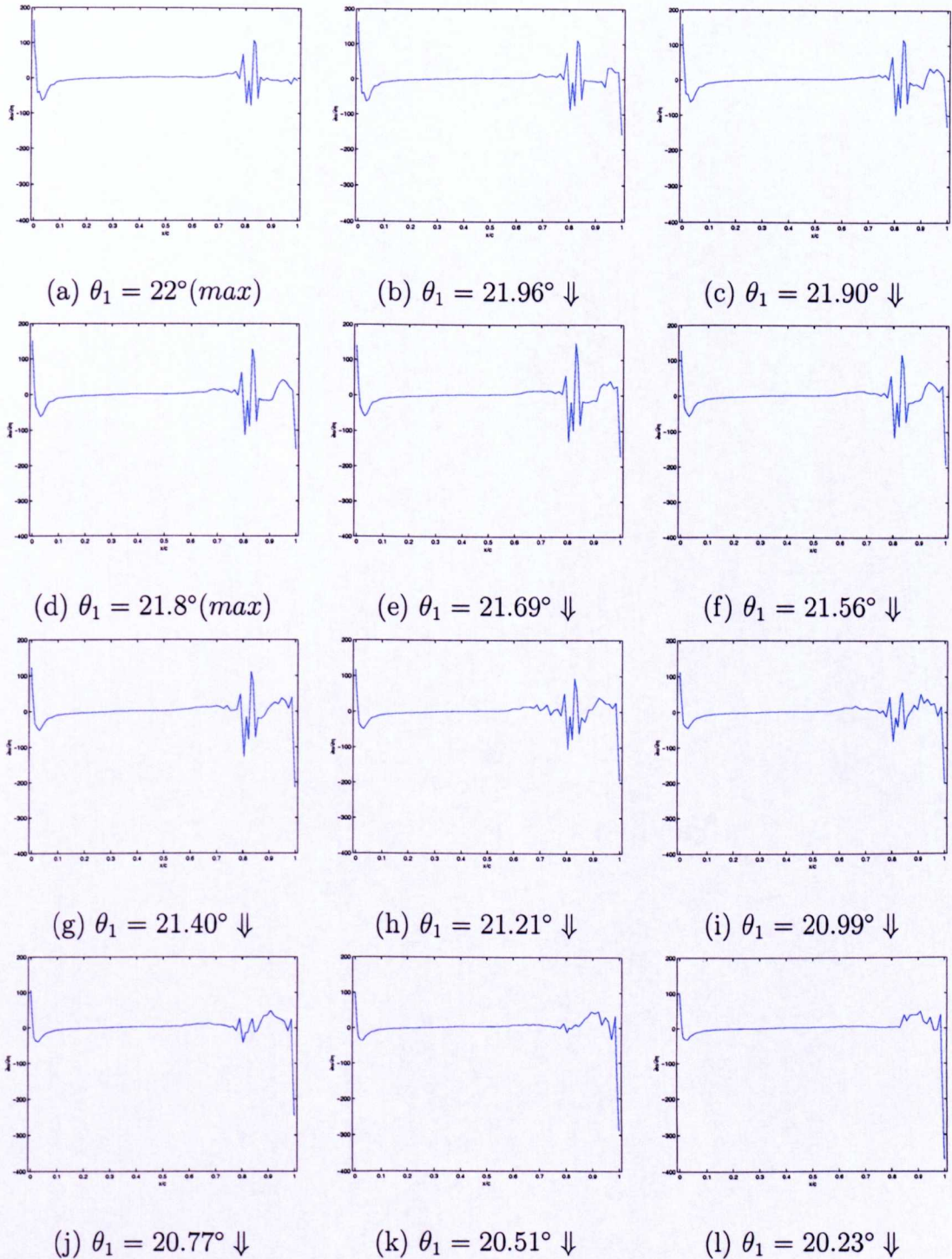


Figure 3.13: Instantaneous evolution of surface chordwise vorticity flux for clean NACA 0015. $\theta(t) = 15^\circ \pm 7^\circ \sin(\omega t)$, $k = 0.154$, $Re = 1.48 \times 10^6$, $M_\infty = 0.1209$ (cont) .

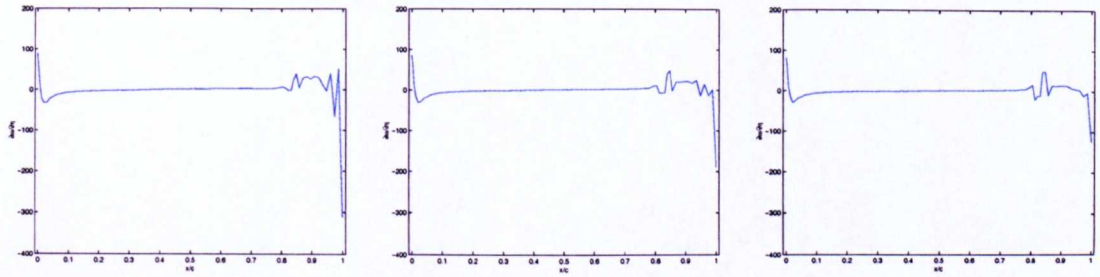
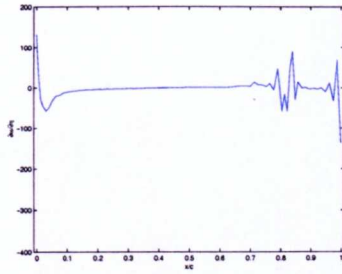
(m) $\theta_1 = 19.94^\circ \Downarrow$ (n) $\theta_1 = 19.62^\circ \Downarrow$ (o) $\theta_1 = 19.29^\circ \Downarrow$

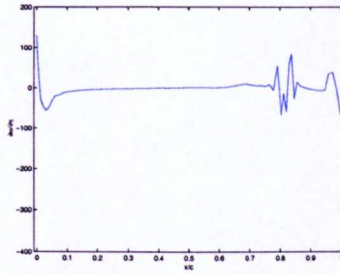
Figure 3.13: Instantaneous evolution of surface chordwise vorticity flux for **clean** NACA 0015. $\theta(t) = 15^\circ \pm 7^\circ \sin(\omega t)$, $k = 0.154$, $Re = 1.48 \times 10^6$, $M_\infty = 0.1209$.

A similar examination for the peak vorticity is repeated for the flapped case. For reasons of clarity the peak vorticity is captured at the same aerofoil incidence as in the clean case. In addition the flap's deflected position is shown for convenience.

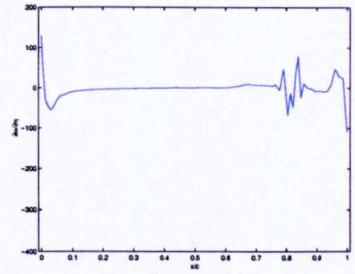
For the flapped case, peaks P1-P5 are found to have lower values compared to the clean case, fig. 3.14(a-o). This is due to successful manipulation of the trailing edge vorticity which results in surface vorticity flux reduction. In more detail the DSV's circulation is not increased due to the TEV. Therefore the aforementioned vortex pairing does not seem to take place. This justifies the lower in magnitude pressure gradient peaks shown in fig. 3.14(a-o) than their clean counterparts.

(a) $\theta_1 = 22^\circ (max)$

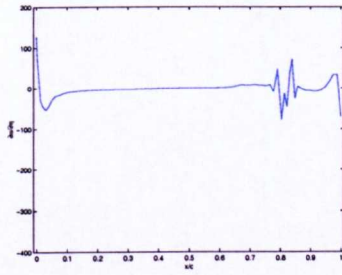
$$\delta_f = 19.99^\circ \uparrow$$

(b) $\theta_1 = 21.96^\circ \downarrow$

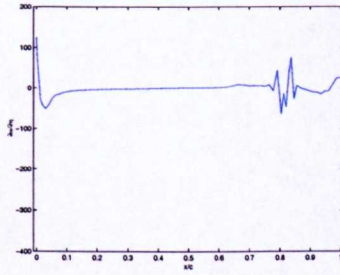
$$\delta_f = 19.84^\circ \downarrow$$

(c) $\theta_1 = 21.90^\circ \downarrow$

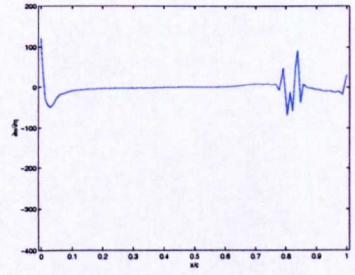
$$\delta_f = 19.24^\circ \downarrow$$

(d) $\theta_1 = 21.8^\circ \downarrow$

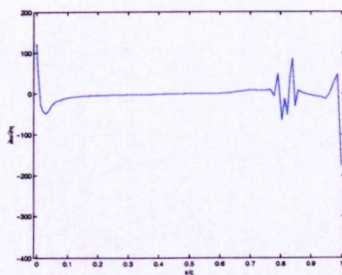
$$\delta_f = 18.21^\circ \downarrow$$

(e) $\theta_1 = 21.69^\circ \downarrow$

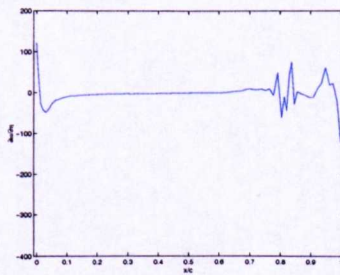
$$\delta_f = 16.81^\circ \downarrow$$

(f) $\theta_1 = 21.56^\circ \downarrow$

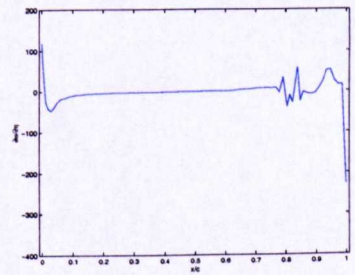
$$\delta_f = 15.10^\circ \downarrow$$

(g) $\theta_1 = 21.40^\circ \downarrow$

$$\delta_f = 13.14^\circ \downarrow$$

(h) $\theta_1 = 21.21^\circ \downarrow$

$$\delta_f = 11.04^\circ \downarrow$$

(i) $\theta_1 = 20.99^\circ \downarrow$

$$\delta_f = 8.90^\circ \downarrow$$

Figure 3.14: Instantaneous evolution of surface chordwise vorticity flux for flapped NACA 0015. $\theta(t) = 15^\circ \pm 7^\circ \sin(\omega t)$, $\delta_{fmax} = 20^\circ$, $k = 0.154$, $Re = 1.48 \times 10^6$, $M_\infty = 0.1209$.

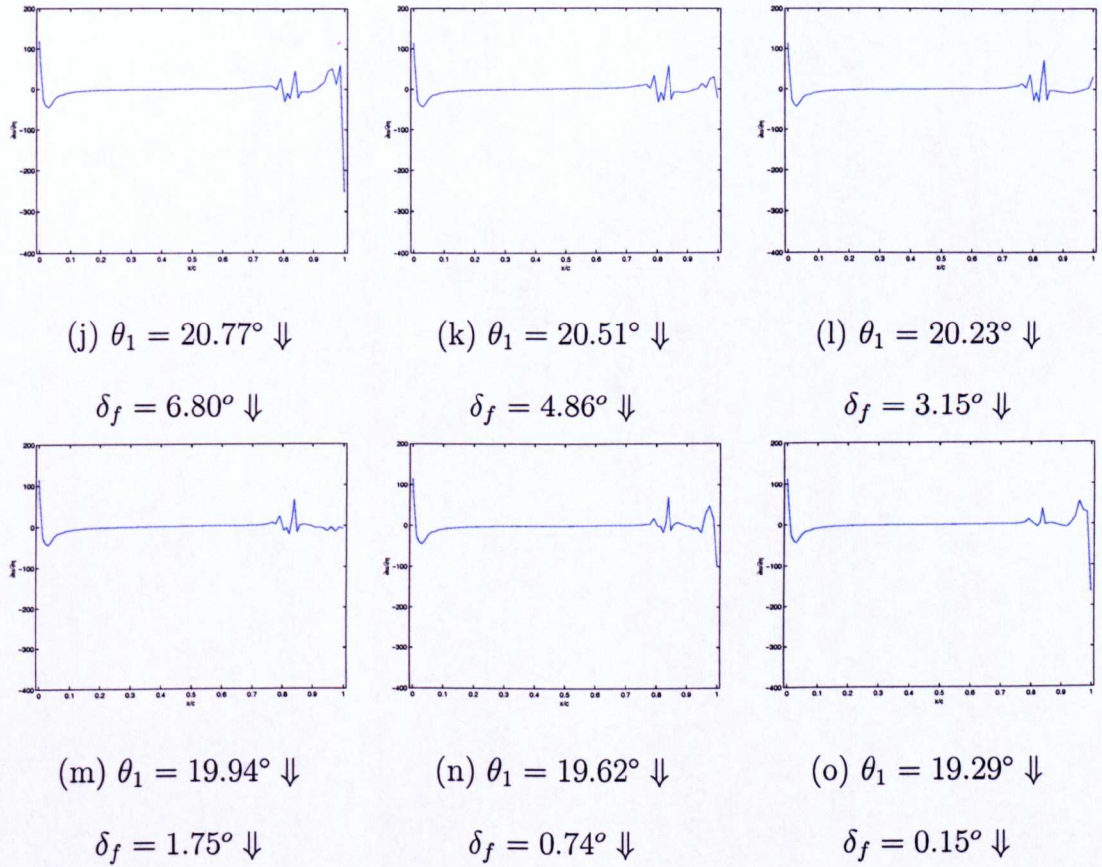


Figure 3.14: Instantaneous evolution of surface chordwise vorticity flux for **flapped** NACA 0015. $\theta(t) = 15^\circ \pm 7^\circ \sin(\omega t)$, $\delta_{f_{max}} = 20^\circ$, $k = 0.154$, $Re = 1.48 \times 10^6$, $M_\infty = 0.1209$.

Regarding the DSV, separation initiates at the TE vicinity, grows in the upstream direction until the complete DSV formation which will convect downstream an instant later. At the same time the simulations revealed a repeatable vortical pattern of opposite circulation compared to the DSV (i.e. TEV) which is shed almost immediately into the wake. It is the latest formed of these trailing edge vortices whose formation is strongly encouraged by the

negative (i.e. upward) flap deflection which will interact with the DSV before it is shed into the wake.

More detailed examination of the peak vorticity regarding the peaks discussed previously is presented in figs. 3.12(a), 3.12(b) where the peak vorticity during the dynamic stall event is shown. The primary sources of vorticity are shown to be due to the presence of peaks P3 and P5 for both clean and flapped case which contain vorticity of counterclockwise- and clockwise sense respectively and shown to introduce the highest amount of vorticity into the flowfield. Further observation of figs. 3.10(a), 3.10(b) suggests that the flap notches manifest themselves by leaving a groove footprint. The flap aerodynamic mechanism is presented as next.

3.6 Flap aerodynamic mechanism

Contrary to fixed wing aircraft, the flap in the current application serves a rather different purpose. In essence, it does not introduce positive camber onto the aerofoil therefore enhancing lift but it alters the vorticity field in the vicinity of the aerofoil's trailing edge, resulting in the DSV trajectory modification, therefore finally reducing the sectional pitching moment undershoot introduced during dynamic stall.

Various approaches have been suggested so far for successful flow manage-

ment of organised coherent vortical structures. A similar approach on vortical interaction is reported in the work of Hassan *et. al.* [6], who developed a numerical scheme for predicting the two dimensional parallel interaction between a NACA 0012 aerofoil equipped with a leading- and trailing edge integral type flaps and a free convecting vortex. Robinson *et. al.* report successful airloads modification based on interaction of the vortex wake using a NACA 0015 aerofoil at Reynolds numbers varying between $50K < Re < 200K$ [106]. Within the current research a similar procedure is adopted.

Examination of the peak pressure and vorticity revealed that manipulation of the trailing edge vorticity with the TE flap suggests a candidate aerodynamic mechanism capable of controlling dynamic stall as it is demonstrated in this chapter. An appropriately phased flap deflection of moderate amplitude (i.e. $\delta_f \leq 20^\circ$) for the examined case (i.e. $\theta(t) = 15^\circ \pm 7^\circ \sin(\omega t)$) seems sufficient in modifying the trailing edge vorticity. As a matter of fact the flap undergoes negative deflection since only by an upward flap pitch input, the suggested aerodynamic flow field alteration can be achieved. The flap deflection makes use of the fact that the flow in the trailing edge vicinity has the tendency to roll up, something that it becomes more evident with increasing aerofoil angle of attack. Thus by an upward flap pitch input of sufficient amplitude the flap comes almost *parallel* with the oncoming flow, therefore disrupting the flow mass influx from the aerofoil's pressure side.

The term parallel already indicates that the amplitude of the flap deflection should be of the order of the maximum aerofoil incidence,

$$\|\delta_{f_{max}}\| = O(\theta_{1_{max}}) \quad (3.3)$$

This further justifies and also rejects at the same time the option of positive flap deflection (i.e. downward). In fact eqn. 3.3 suggests that a flap deflection should have an amplitude similar to the maximum aerofoil AOA. Under this condition, discontinuation of the mass flow influx from the pressure side can occur, yielding therefore to disruption of the DSV's growth. Conclusively the flap deflection amplitude can be determined from the maximum aerofoil incidence, at least for the flow mode of light dynamic stall when $0.128 \leq k \leq 0.180$ as within the present study. Note that eqn. 3.3 should not be applied in a strict sense. A few degrees of difference³ between $\delta_{f_{max}}$ and $\theta_{1_{max}}$ seem to justify the former by taking into account numerical and experimental inaccuracies. This alteration of the flow in the trailing edge vicinity yields to modification of the DSV trajectory, in other words it will not leave the aerofoil from the TE but rather at some place toward the aft part of the system (i.e. aerofoil + flap) which further results in modification (i.e. reduction) of the pitching moment undershoot.

In more detail the flap aerodynamic mechanism is illustrated in fig. 3.15(a-j) for the clean case (LHS column) and flapped case (RHS column) in terms of instantaneous velocity vector plots. The corresponding instantaneous pres-

³2° regarding the examined case

sure (LHS) and vorticity gradient distribution (RHS) around the aerofoil are additionally shown in fig. 3.16(a-j) for convenience.

As shown in figs. 3.15(a,b), the DSV continues to grow in the upstream direction for both the clean and flapped cases respectively. There is no significant difference in terms of the DSV circulation and this can be justified from the figs. 3.16(a,b) where the instantaneous pressure and vorticity gradient (i.e. pressure gradient) distribution are shown respectively.

After the aerofoil has reached the maximum oscillation angle (i.e. $\hat{\theta}_1 = 22^\circ$), at the beginning of the downstroke the DSV shows significantly growth (fig. 3.15c) compared to its flapped counterpart shown in fig. 3.15(d). This is also evident from observation of the pressure and vorticity distribution shown in fig. 3.16(c,d) respectively.

Lower in the downstroke of the motion, there is a clear pair of vortices carrying circulation of opposite sense, as shown in fig. 3.15(e). In particular the DSV shows significant growth and in addition the TEV seems to enhance the former. This fact manifests itself in the pressure distribution around the aerofoil shown in fig. 3.15(e) where a massive suction peak is shown in the trailing edge vicinity. As presented by Tsiachris [22] and as suggested throughout the current thesis, it is the pair of the DSV and TEV that cause the large pitching moment undershoot rather than only the DSV itself. In fact as illustrated in fig. 3.15(e), the TEV appears to participate in circulation enhancement of the DSV. Apparently there is a flow influx from the TEV

which initiates from the flap's pressure surface and results in the growth of the DSV. This influx is justified by the massive peak of the vorticity gradient shown in the aerofoil's trailing edge vicinity in fig. 3.16(f). At the very same instant the corresponding flapped case (fig. 3.15f) shows a DSV with a significantly lower height compared to the clean case and as also displayed in the pressure distribution and in the vorticity gradient distribution in figs. 3.16e,f respectively.

After the dynamic stall event, the flow seems to reattach earlier in the clean case (figs. 3.15g,i) than in the flapped case as shown in figs. 3.15(h,j). In the clean case the TEV seems to eject away the DSV from the aerofoil's suction surface. Moreover in the clean case both DSV and TEV are placed in a higher position from the aerofoil's surface. In the flapped case there is no evidence of this. This becomes also evident from the vortex trajectories illustrated in fig. 3.17(a-c) for three different reduced frequencies. For all clean cases shown in the vortex trajectories, both DSV and TEV are located higher than their flapped counterparts. Conclusively in the flapped case the DSV will remain longer on the aerofoil's surface, however there is no additional circulation added to it due to the absence of interaction with the TEV.

Due to the stall onset mechanism suggested previously, the flap serves to prevent the growth of the DSV due to the TEV. As it is shown in fig. 3.17(a-c), both DSV and TEV are located in a higher position for the clean case than in the flapped case. This is due to the fact that in the flapped case there is

no ejection of the DSV due to the TEV. It should be also mentioned that at lower reduced frequencies (i.e. $k = 0.128$, fig. 3.17a), the TEV for both the clean and flapped case appears to fluctuate parallel to the chord. This is explained by the fact that its formation repeats several times over the cycle.

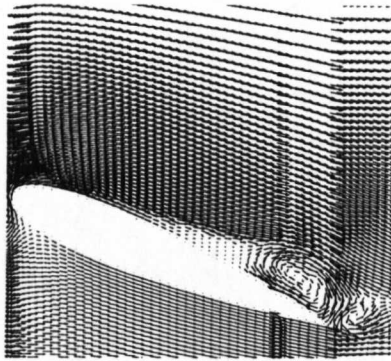
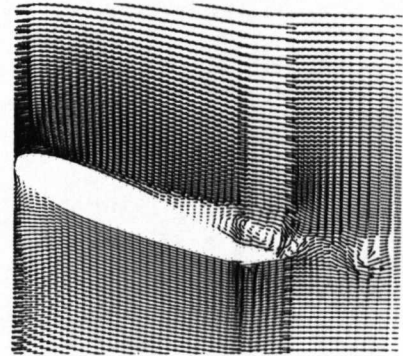
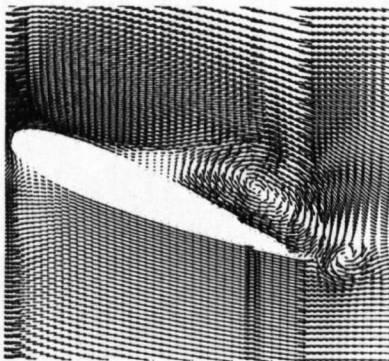
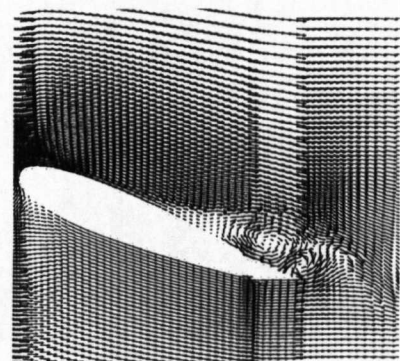
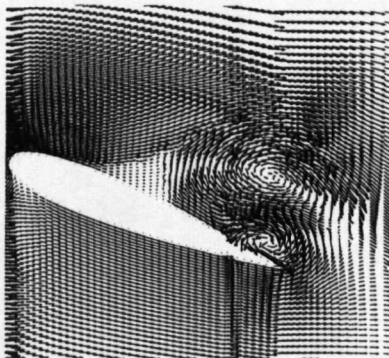
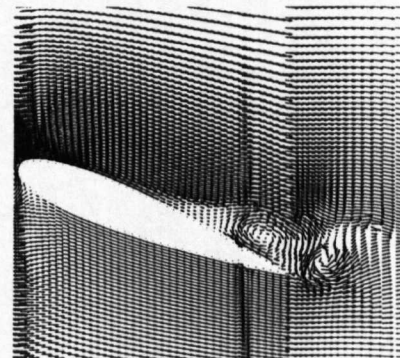
(a) $\theta_1 = 21.84^\circ \uparrow$ (b) $\theta_1 = 21.84^\circ \uparrow, \delta_f = 19.89^\circ \downarrow$ (c) $\theta_1 = 21.97^\circ \downarrow$ (d) $\theta_1 = 21.97^\circ \downarrow, \delta_f = 11.43^\circ \downarrow$ (e) $\theta_1 = 21.44^\circ \downarrow$ (f) $\theta_1 = 21.44^\circ \downarrow, \delta_f = 0.94^\circ \downarrow$

Figure 3.15: Time sequence of the instantaneous vortex particles at the trailing edge region of clean (LHS) and flapped (RHS) NACA 0015: $\theta(t) = 15^\circ \pm 7^\circ \sin(\omega t)$, $\delta_{f_{max}} = 20^\circ$, $k = 0.128$, $M = 0.119$, $Re = 1.49 \times 10^6$.(cont)

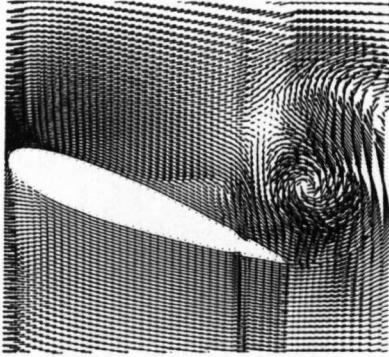
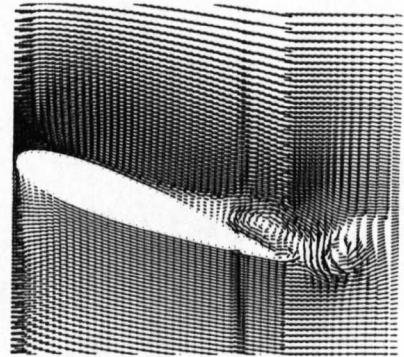
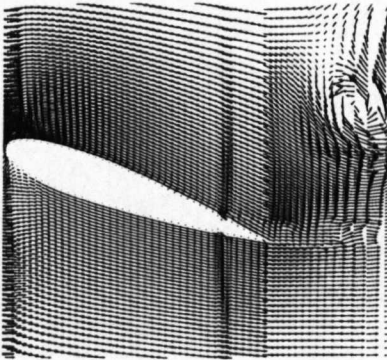
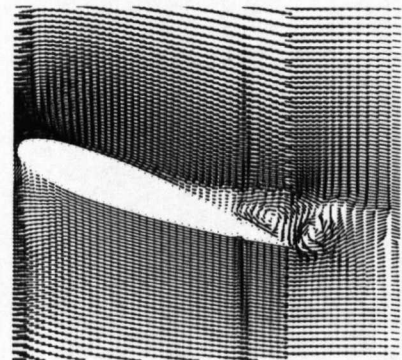
(g) $\theta_1 = 20.54^\circ \downarrow$ (h) $\theta_1 = 20.54^\circ \downarrow, \delta_f = 0^\circ \downarrow$ (i) $\theta_1 = 19.82^\circ \downarrow$ (j) $\theta_1 = 19.82^\circ \downarrow, \delta_f = 0^\circ \downarrow$

Figure 3.15: Time sequence of the instantaneous vortex particles at the trailing edge region of clean (LHS) and flapped (RHS) NACA 0015: $\theta(t) = 15^\circ \pm 7^\circ \sin(\omega t)$, $\delta_{f_{max}} = 20^\circ$, $k = 0.128$, $M = 0.119$, $Re = 1.49 \times 10^6$.

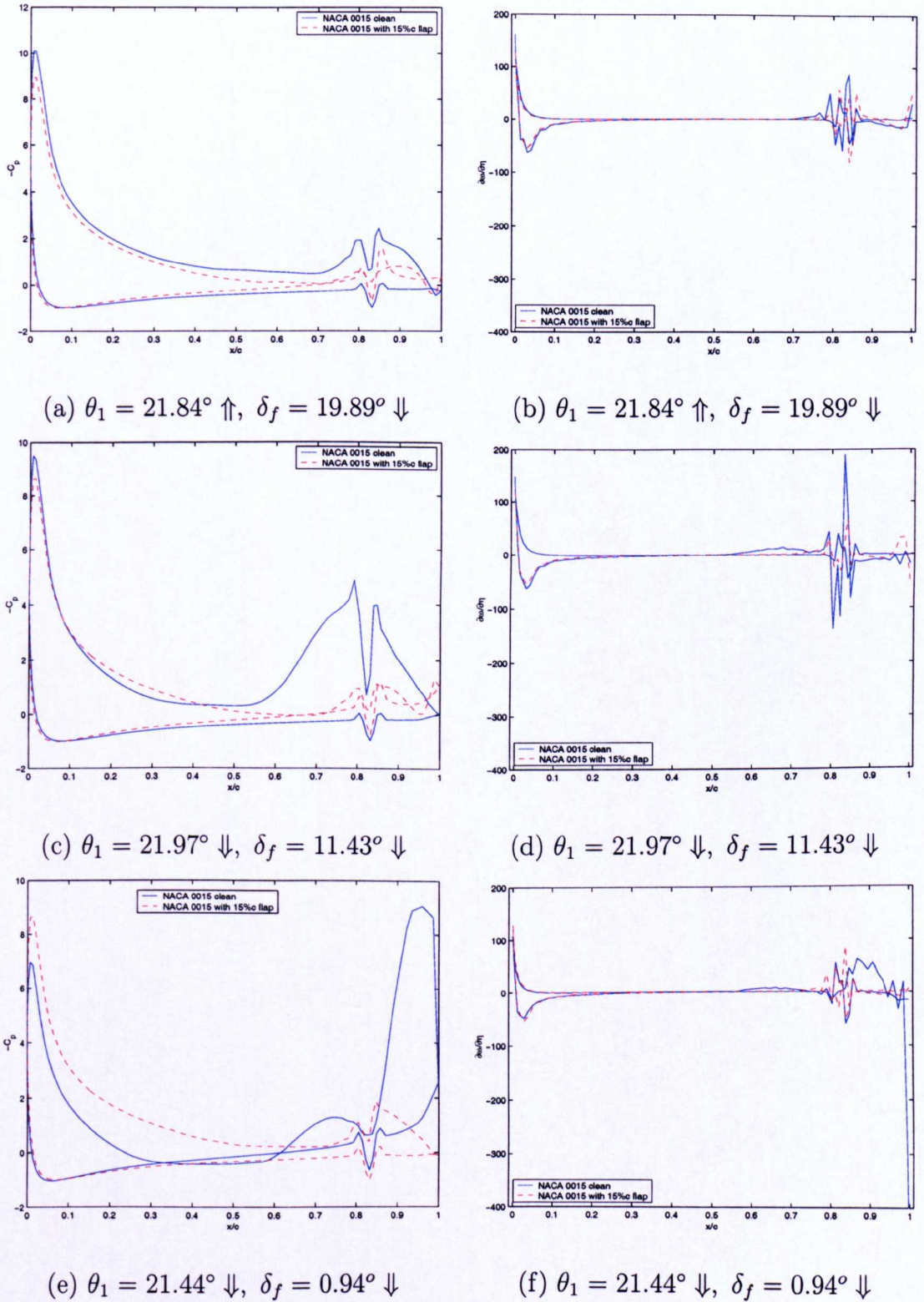
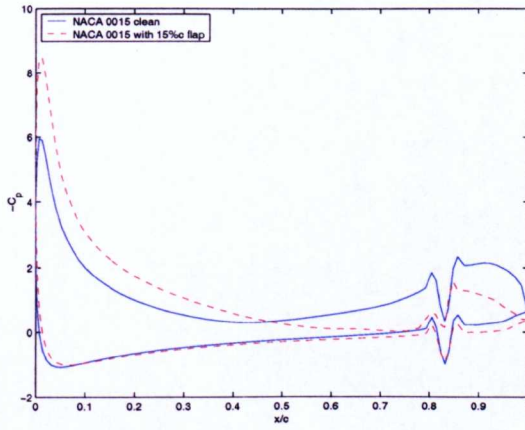
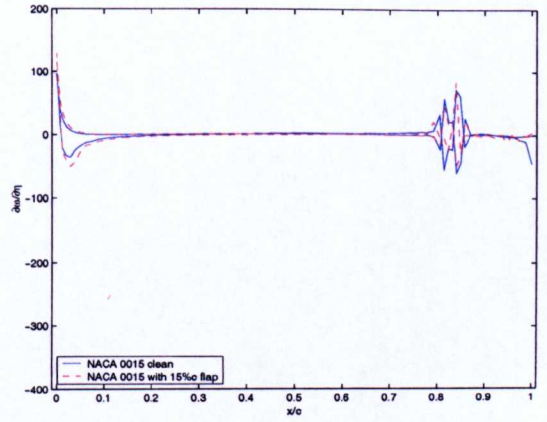


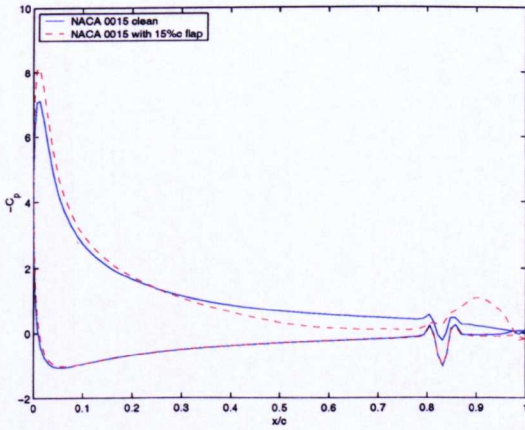
Figure 3.16: Time sequence of the instantaneous pressure distribution (LHS) and vorticity gradient (RHS) for clean and flapped NACA 0015: $\theta(t) = 15^\circ \pm 7^\circ \sin(\omega t)$, $\delta_{f,max} = 20^\circ$, $k = 0.128$, $M = 0.119$, $Re = 1.49 \times 10^6$.(cont)



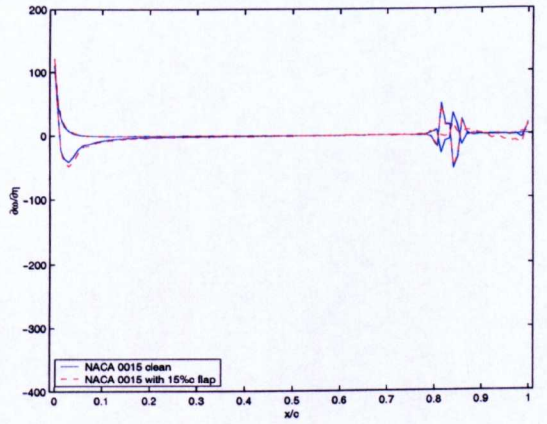
(g) $\theta_1 = 20.54^\circ \downarrow, \delta_f = 0^\circ \downarrow$



(h) $\theta_1 = 20.54^\circ \downarrow, \delta_f = 0^\circ \downarrow$

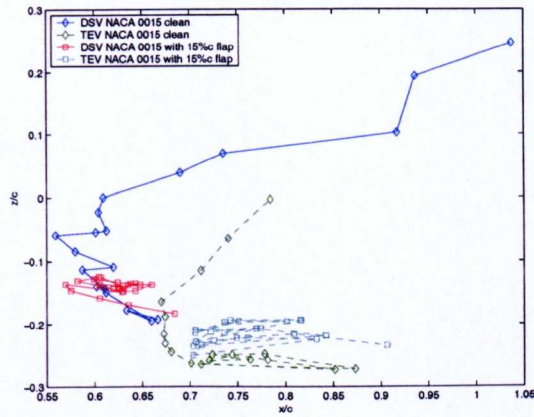


(i) $\theta_1 = 19.82^\circ \downarrow, \delta_f = 0^\circ \downarrow$

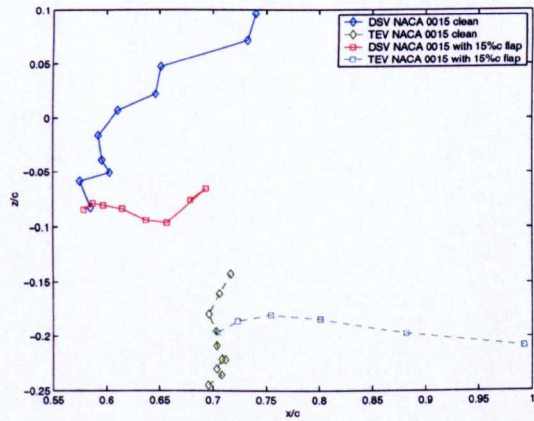


(j) $\theta_1 = 19.82^\circ \downarrow, \delta_f = 0^\circ \downarrow$

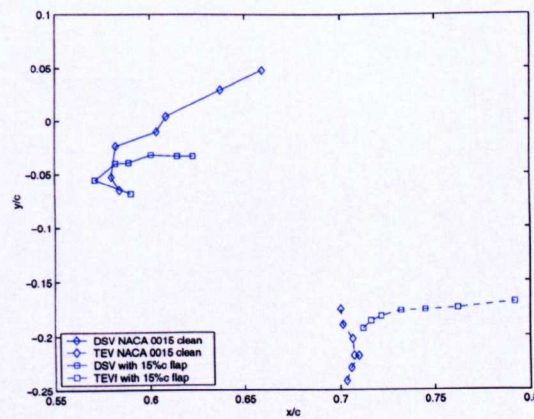
Figure 3.16: Time sequence of the instantaneous pressure distribution (LHS) and vorticity gradient (RHS) for clean and flapped NACA 0015: $\theta(t) = 15^\circ \pm 7^\circ \sin(\omega t)$, $\delta_{f_{max}} = 20^\circ$, $k = 0.128$, $M = 0.119$, $Re = 1.49 \times 10^6$.



(a) $k = 0.128$



(b) $k = 0.154$



(c) $k = 0.180$

Figure 3.17: DSV and TEV trajectory modification for clean- and flapped case: $\theta(t) = 15^\circ \pm 7^\circ \sin(\omega t)$, $\delta_{fmax} = 20^\circ$, $M = 0.119$, $Re = 1.48 \times 10^6$.

3.7 Concluding remarks

The dynamic stall flow topology for both the clean and flapped aerofoils is examined. The results reveal a new mechanism responsible for the stall onset. This is in essence the vortical group of DSV and TEV which introduce a massive suction peak at the aerofoil's suction side over the trailing edge vicinity, therefore responsible for the large C_m undershoot in the pitching moment hysteresis loop. The flap serves to manipulate the trailing edge vorticity, in other words it serves for the control of the TEV's production. The above mechanisms, for stall onset and flap actuation are examined in detail by investigation of the peak pressure and peak vorticity.

Chapter 4

Parametric study

The flap seems capable of reducing the sectional pitching moment undershoot introduced when the retreating blade exhibits dynamic stall. To obtain a detailed understanding of the flap's operating conditions, a number of parameters are investigated. The current chapter deals with the geometric and actuation related parameters.

Geometric parameters include the type of aerofoil, the flap size and the flap notches. An actuation parametric study is also conducted and it includes flap phasing, flap deflection amplitude and effects of the aerofoil and flap reduced frequency on the airloads.

4.1 Parametric methodology

In this section the methodology for this chapter is presented. There is a coupling between the different parameters involved. However the effect of each parameter is investigated individually to examine its influence. The parameters are further listed in table 4.1.

Geometric parameters:	Actuation parameters:
<ul style="list-style-type: none"> - flap size - flap notches 	<ul style="list-style-type: none"> - flap phasing - flap amplitude - flap deflection (fixed: upward) - aerofoil & flap reduced frequency

Table 4.1: List of geometric and actuation parameters.

The flap size is examined by simulating various flap sizes in order to conclude which is the most suitable for the current application. The flap phasing is investigated by simulating a series of flap profiles, each one having a fixed amplitude and duration, in an attempt to achieve the best realisation of the aerodynamic mechanism suggested in chapter 3. The flap deflection amplitude is examined for values varying between $16^\circ \leq \delta_f \leq 25^\circ$. The main criterion for determining the flap deflection amplitude is the amount of pos-

itive aerodynamic damping that the flap imposes into the pitching moment hysteresis loop. The aerofoil reduced frequency varies for the range between $0.1347 \leq k \leq 0.180$ and the flap reduced frequency is chosen accordingly.

4.2 Geometric Parameters

4.2.1 Aerofoil and flap size

Throughout the present research a NACA 0015 aerofoil is used equipped with a 15% trailing edge flap, as displayed in fig. 4.1. The perpendicular axis shown in fig. 4.1 is labelled as $\frac{z}{c}$ in order to keep consistency with the axis convention used in rotorcraft analyses.

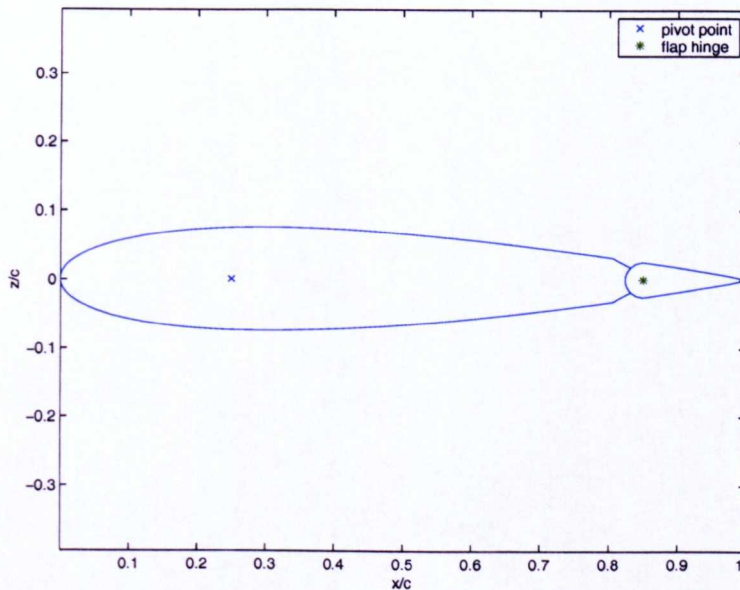


Figure 4.1: NACA 0015 rotor blade profile equipped with a 15% plain trailing edge flap.

The choice of the aerofoil forms an input to the present work since there is an extensive experimental database available [118]. In addition, the NACA 0015 profile is of trailing-edge-stall-type [88] and therefore it can be simulated with the DVM mentioned in chapter 2. For such sections, the onset of stall tends to occur in a less abrupt manner. Furthermore the aerofoil is pitching about its quarter chord and it is equipped with a plain TE flap having a nominal length of 0.15 aerofoil chord lengths. A nominal flap length of 0.15 chord lengths implies that the flap hinge is located at 0.85 chordwise location on the aerofoil. Effectively it should be added ≈ 0.01 chord length to the nominal flap size. On the other hand the flap portion upstream of

the hinge depends on the actuation mechanism and may vary accordingly. This falls beyond the scope of the current investigation. However the nominal flap length (i.e. $c_f = 0.15 c$) is used throughout the present work, see fig. 4.1. All the simulated flap sizes have the same actuation profile, i.e. the same deflection amplitude and (DOA) duration of the entire actuation. The criterion of the flap's size choice (fig. 4.2a-e) is the aerodynamic damping, both positive and negative. A suitable flap size candidate combined with the appropriate deflection profile has a twofold task, i.e.: reduction of the negative aerodynamic damping and at the same time no addition of extra positive aerodynamic damping. The former is the source of stall flutter which tends to occur when the aerofoil oscillates in and out of stall [49]. Moreover the negative aerodynamic damping, in other words the sensitivity to stall induced vibrations (i.e. stall flutter), depends strongly on the coupling between the aerofoil's various degrees of freedom, [28], [27], [93]. In addition, negative aerodynamic damping becomes an essential quantity for reduction since it might excite the torsional vibration mode when it comes to dynamic consideration of the entire rotor blade [49], [88].

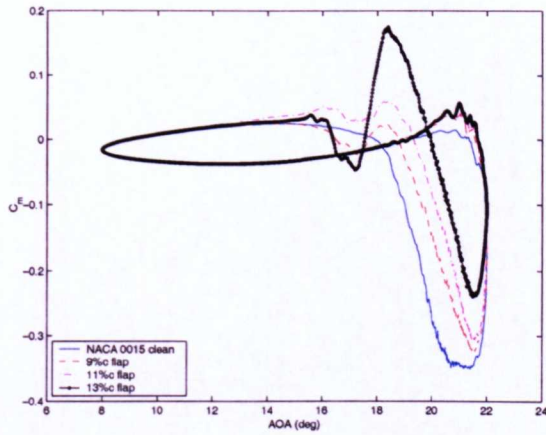
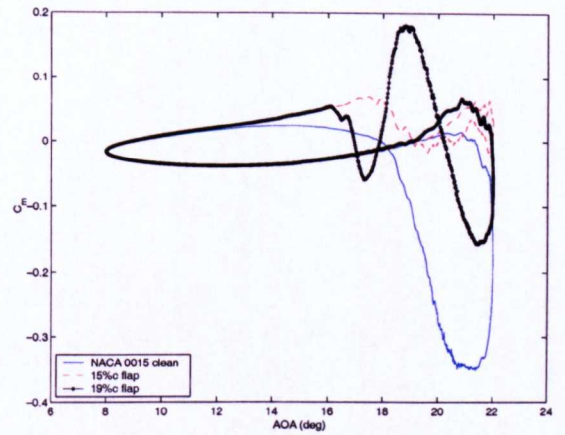
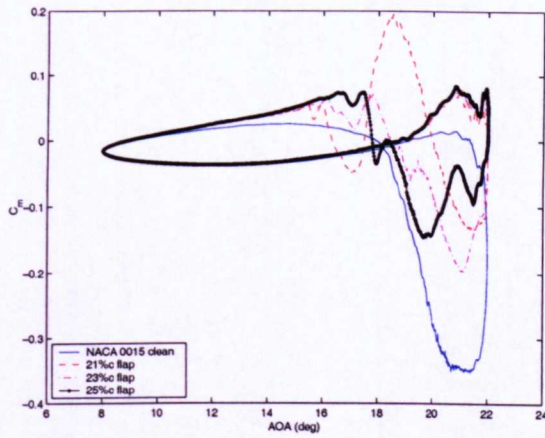
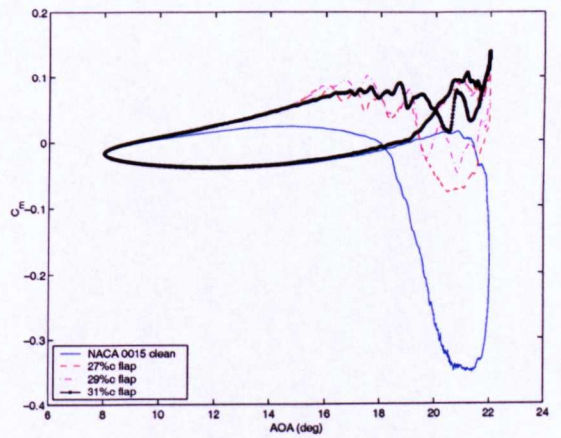
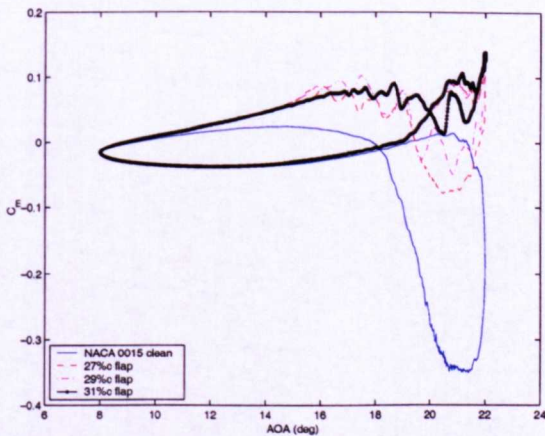
(a) $9\%c \leq c_f \leq 13\%c$ (b) $15\%c \leq c_f \leq 19\%c$ (c) $21\%c \leq c_f \leq 25\%c$ (d) $27\%c \leq c_f \leq 31\%c$ (e) $35\%c \leq c_f \leq 37\%c$

Figure 4.2: Pitching moment coefficient for flap sizes varying from 9%-13%,

$$\theta(t) = 15^\circ \pm 7^\circ \sin(\omega t), \delta_f = 25^\circ, k = 0.154, Re = 1.49 \times 10^6, M = 0.119.$$

Second, the flap deflection should not further introduce an amount of positive aerodynamic damping. This later becomes evident after observing figs. 4.2(d,e). The most convenient flap size in terms of introducing the least aerodynamic damping is found to be the one that has nominal length of 0.15 aerofoil chord lengths. Further observation of figs. 4.2(a-e) reveal that the amount of positive aerodynamic damping increases with increasing flap size. As it can be seen from fig. 4.2(b), $c_f \geq 0.19c$ appear to introduce already a small amount of positive damping, at least for the flow case considered here. This becomes strongly evident for flap sizes varying from $0.23c \geq c_f \geq 0.37c$ as illustrated in fig. 4.2(d,e). In addition flap sizes with $c_f \leq 0.15c$ are found to be entirely ineffective in terms of modifying the sectional pitching moment undershoot.

4.2.2 Flap notches

The effect of the flap notches is examined. Since the notches most certainly perturb the flow field by introducing surface discontinuities, a series of flap notches having different geometry were simulated in order to establish their influence around the flap area as illustrated in fig. 4.3(a,b). The geometry of the notches together with the corresponding pressure distribution are shown respectively in figs. 4.3(a,b). The maximum flap notch has a length of 0.0327 chord lengths and it causes a noticeable footprint into the flow field in the

chordwise direction as shown in the pressure distribution around the notch in fig. 4.3. Nevertheless the overall flow characteristics are found not to be significantly affected by the presence of the flap gap. Due to the two dimensionality of the current problem, the presence of the flap notch does not seem to affect the overall flow characteristics although the presence of the flap notch footprint is evident in the pressure distribution as shown in fig. 4.3(b). However in the case of a full rotor blade the flap notch influence can be significant. Lian *et.al.* report a weak circulation region around the flap-gap area [36].

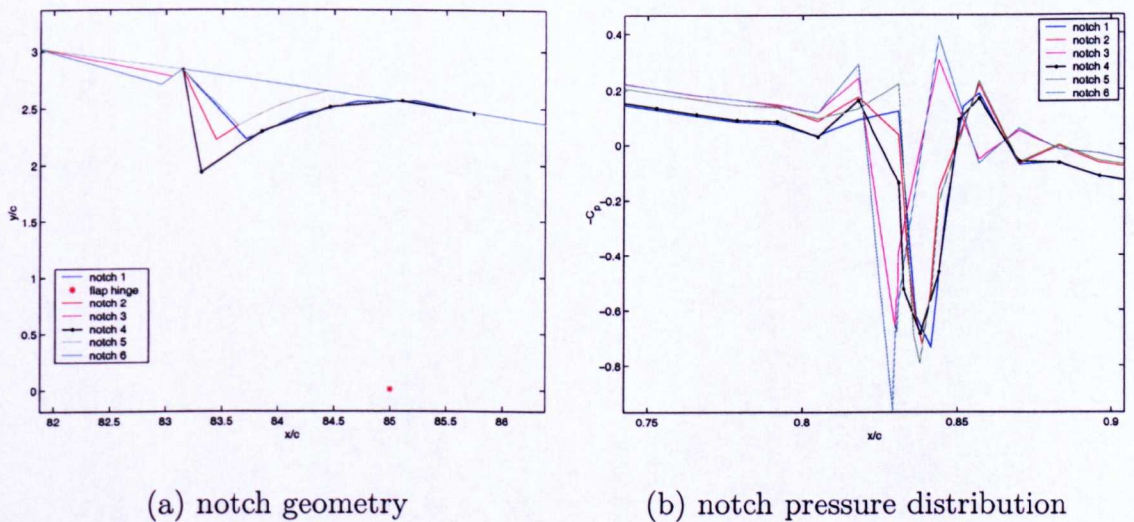


Figure 4.3: Various flap notches on a NACA 0015 equipped with a 0.15c trailing edge flap (a), together with the corresponding pressure distribution (b), (suction surface).

These reasons and also for the aim of simplification, the influence of the flap notch geometry is assumed to be negligible throughout the current re-

search. It is further assumed that the flap is perfectly sealed, i.e. there are no pressure losses around the flap notch area. In the following section an investigation of the actuation related parameters is presented.

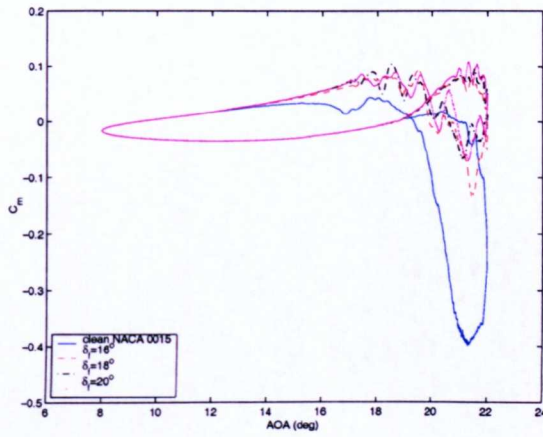
4.3 Actuation parameters

4.3.1 Flap deflection amplitude

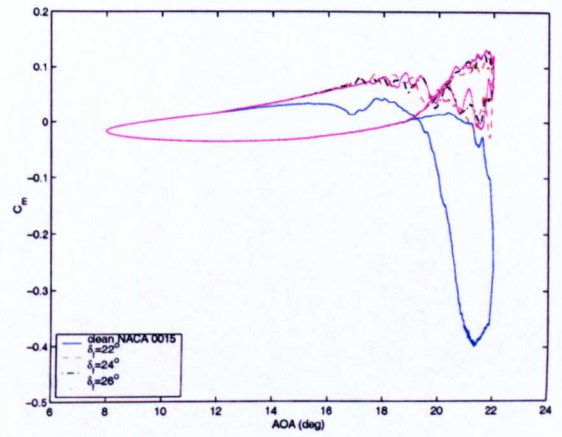
This is one of the most essential parameters involved. It is the flap deflection amplitude which will influence the pitching moment undershoot and at the same time will not introduce any extra positive damping onto the aerofoil. Within the frame of the current investigation the flap undergoes a moderate amplitude deflection, i.e. $\delta_f = 20^\circ$ employing the assumption 3.3 given in chapter 3. Deflection amplitudes less than $\delta_f < 20^\circ$ under properly phased conditions will not be able to achieve the aforementioned vortical manipulation suggested in chapter 3. In addition deflection amplitudes higher than $\delta_f > 20^\circ$ will add extra positive aerodynamic damping into the pitching moment hysteresis loop, as shown in fig. 4.2(a-e) where $\delta_f = 25^\circ$ is applied. Given a predefined amplitude, the pulsed cosine representing the flap deflection is given by

$$\delta_f = \|\hat{\delta}_f\| \cdot \left(1 - \cos\left(\frac{\omega t}{\rho\omega t}\right)\right) \quad (4.1)$$

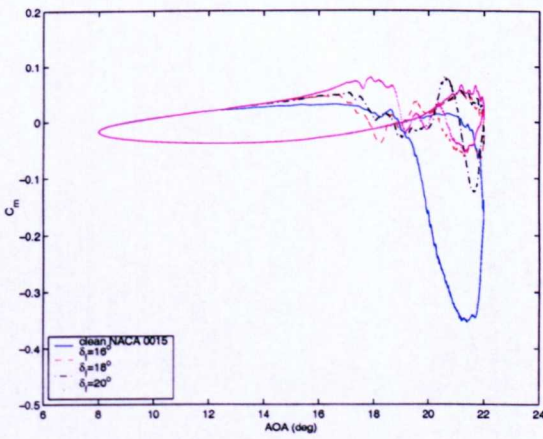
with ω and t denoting the oscillatory frequency and time respectively. An examination of the flap deflection amplitude is illustrated in fig. 4.4(a-h). A series of flap amplitudes is given varying from 16° to 26° with an intermediate increment of 2° for four different reduced frequencies, i.e. $k = 0.1347$, $k = 0.154$, $k = 0.1671$ $k = 0.180$. The flap reduced frequency is chosen accordingly.



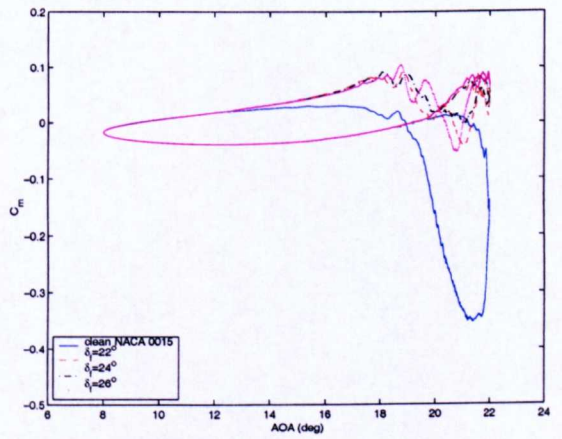
(a) $k = 0.1347, k_f = 0.1698$



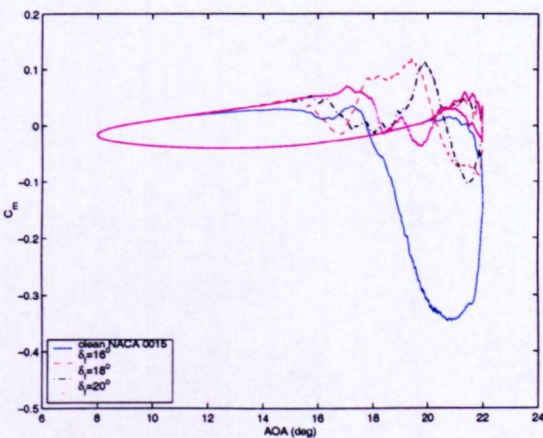
(b) $k = 0.1347, k_f = 0.1698$



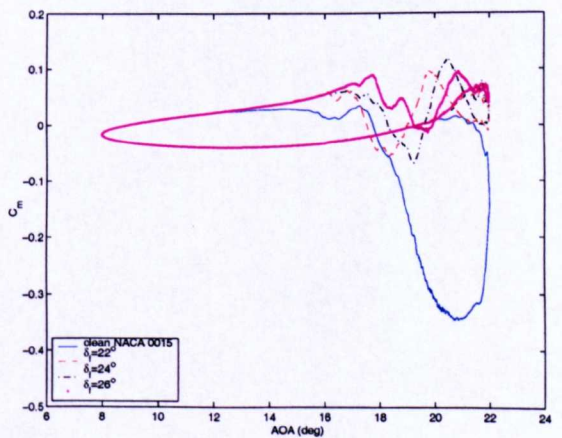
(c) $k = 0.1547, k_f = 0.1706$



(d) $k = 0.1547, k_f = 0.1706$



(e) $k = 0.1671, k_f = 0.1736$



(f) $k = 0.1671, k_f = 0.1736$

Figure 4.4: Effect of flap deflection amplitude: $\theta(t) = 15^\circ \pm 7^\circ \sin(\omega t)$, $Re = 1.48 \times 10^6$, $M_\infty = 0.1209$ (cont).

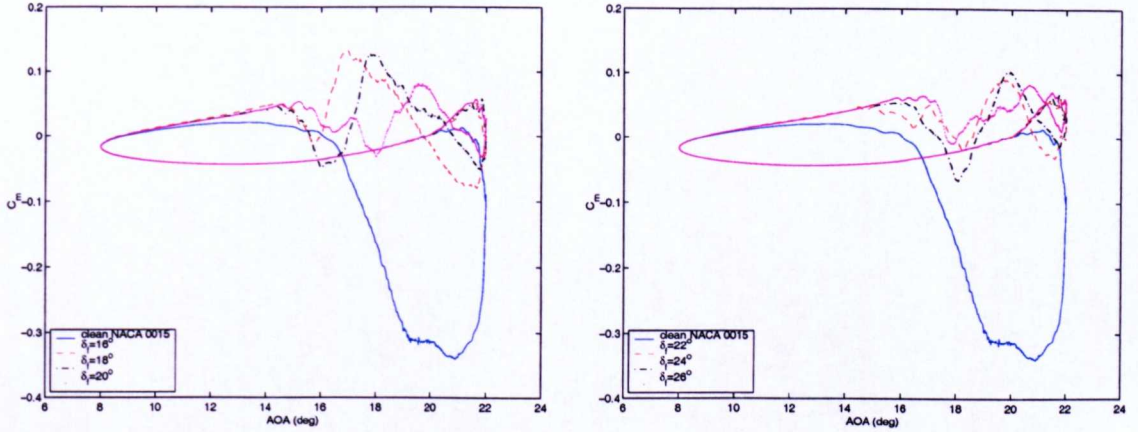
(g) $k = 0.180$, $k_f = 0.1818$ (h) $k = 0.180$, $k_f = 0.1818$

Figure 4.4: Effect of flap deflection amplitude: $\theta(t) = 15^\circ \pm 7^\circ \sin(\omega t)$, $Re = 1.48 \times 10^6$, $M_\infty = 0.1209$.

For $k = 0.1347$ a flap amplitude of $\delta_f = 20^\circ$ is found to significantly modify the C_m undershoot compared to deflections of 16° and 18° as shown in fig. 4.4(a). However the lowest pitching moment negative magnitude appears to be for $\delta_f = 26^\circ$ as it is shown in fig. 4.4(b). For $k = 0.154$, a flap amplitude of 20° is found to significantly reduce the pitching moment undershoot as shown in fig. 4.4(c). For the same reduced frequency, flap deflection amplitudes of 22° , 24° and 26° are shown to modify the pitching moment undershoot in a similar manner as $\delta_f = 20^\circ$ while at the same time they increase the amount of positive aerodynamic damping in the C_m hysteresis loop. For $k = 0.1671$ the minimum aerodynamic damping is achieved for $\delta_f = 20^\circ$ as shown in figs. 4.4(e,f). For $k = 0.180$, the lowest C_m undershoot is achieved with $\delta_f = 26^\circ$ while at the same time the amount of positive

aerodynamic damping maintains low levels as shown in figs. 4.4(g,h).

From the examination presented in figs. 4.4(a-h), a flap deflection of $\delta_f = 20^\circ$ is shown to be sufficient in reducing the C_m undershoot without adding any significant amount of positive aerodynamic damping for reduced frequencies varying between $k = 0.1347$ and $k = 0.154$. In the case of $k = 0.180$ the reduction of C_m with $\delta_f = 26^\circ$ is not significantly large compared to the C_m reduction achieved with $\delta_f = 20^\circ$. At the same time numerical inaccuracies and experimental uncertainty justify the fact that for the range of $0.1347 \leq k \leq 0.180$ a flap deflection amplitude of $\delta_f = 20^\circ$ is meaningful in reducing the negative pitching moment undershoot and maintains a low level of positive damping, therefore it will be used throughout the current research. In addition, employing a flap amplitude of $\delta_f = 20^\circ$ for the flow mode of light stall within the range of reduced frequencies $0.1347 \leq k \leq 0.180$, appears to justify the relation (eqn. 3.3) suggested in chapter 3. Likewise the suggested tolerance of a few degrees between $\delta_{f_{max}}$ and $\hat{\theta}_{1_{max}}$ is also greatly justified with the employed deflection amplitude of 20° in the case examined.

In addition the flap undergoes negative deflection (i.e. upward) since it is used as a different means when compared to a fixed wing aircraft where the flap is deflected in the opposite sense. Within the present investigation, the flap serves to modify the trailing edge vorticity while in the case of fixed wing aircraft the flap serves for introduction of positive camber, enhancing therefore the lift. Although the scope of the current research aims to benefit

from the dynamic lift, the introduction of negative camber reduces abruptly the lift hysteresis loop.

4.3.2 Flap phasing

Probably the key for a successful alleviation of retreating blade stall is the phasing of the flap, i.e. the start of its deflection (t_{start}) and also the duration of the entire actuation event (T_{δ_f}). At first the initiation of the actuation should occur at the retreating side of the rotor disk where actually the blade encounters dynamic stall in forward flight [45]. Apart from identifying the exact azimuthal location of the actuation's initiation, it is further of use to identify also at what aerofoil AOA (or equivalently rotor azimuth) and additionally if it should be the upstroke or downstroke of the aerofoil's motion. Furthermore the flow mode (i.e. in and out-, light-, or deep stall) that the aerofoil operates is directly connected with the phasing of the flap. Throughout the current work only LS (light stall) is discussed since this occurs the most frequently during the rotorcraft's forward flight.

A representative aerofoil pitch profile (i.e. $\theta(t) = 15^\circ \pm 7^\circ \sin(\omega t)$) is employed for a range of reduced frequencies, i.e.: $0.128 \leq k \leq 0.180$. Examination of this profile throughout this k -range is thought to represent well and also cover a range of reduced frequencies typical of rotorcraft retreating blade

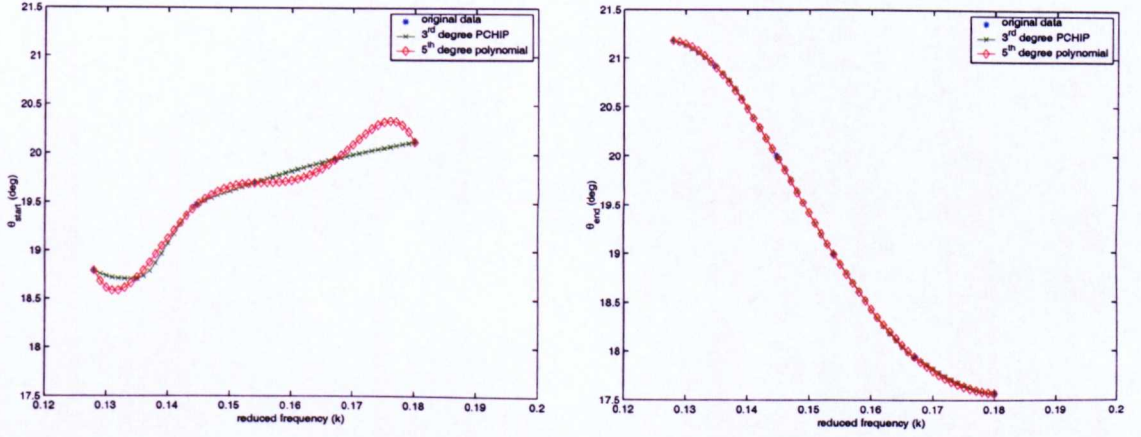
stall. In addition, since the flow physics do not significantly change, the current flap phasing investigation can be employed more generally for the flow mode of light stall.

From the investigation conducted so far, it is found that the flap should be deflected around the the maximum oscillating angle of the aerofoil section. This is justified by the fact that the dynamic stall event starts around the maximum aerofoil pitching angle. Furthermore the actuations concerning the flow mode in discussion (i.e. light dynamic stall), suggest that actuations of one per rev negative (i.e. upward) flap pitch inputs are found to be sufficient in modifying the sectional pitching moment. The aerofoil incidences of the flap actuation are summarised in table 4.2.

reduced frequency: (k)	0.1280	0.1347	0.1447	0.1540	0.1671	0.180
aerofoil AOA at start of δ_f : ($\hat{\theta}_{start}$)	18.79° ↑	18.70° ↑	19.47° ↑	19.70° ↑	19.94° ↑	20.12° ↑
aerofoil AOA at end of δ_f : ($\hat{\theta}_{end}$)	21.17° ↓	20.91° ↓	19.99° ↓	18.99° ↓	17.93° ↓	17.56° ↓

Table 4.2: Summary of aerofoil incidences of the flap's initiation and termination of the actuation event. $\theta(t) = 15^\circ \pm 7^\circ \sin(\omega t)$, $Re = 1.48 \times 10^6$, $M_\infty = 0.1209$.

Based on the results presented in the previous section, the initiation and termination aerofoil incidences are shown in figs. 4.5(a,b) as a function of the reduced frequency. The initiation of the flap actuation aerofoil incidence (i.e. $\hat{\theta}_{1_{start}}$) occurs earlier in the cycle with decreasing reduced frequency, see fig. 4.5(a). This is due to the fact that the dynamic stall vortex initiates later in the cycle with increasing reduced frequency. This is in accordance with the results obtained by Robinson *et.al.* [106]. A curve fit is used to give a continuous representation of $\hat{\theta}_{1_{start}} = f(k)$ for $0.128 \leq k \leq 0.180$ providing an accurate fit, as shown in fig. 4.5(a).



$$(a) \theta_{1_{start}}^{\hat{}} = f(k)$$

$$(b) \theta_{1_{end}}^{\hat{}} = f(k)$$

Figure 4.5: Initial and final aerofoil incidence as function of the reduced frequency. $\theta(t) = 15^\circ \pm 7^\circ \sin(\omega t)$, $Re = 1.48 \times 10^6$, $M_\infty = 0.1209$.

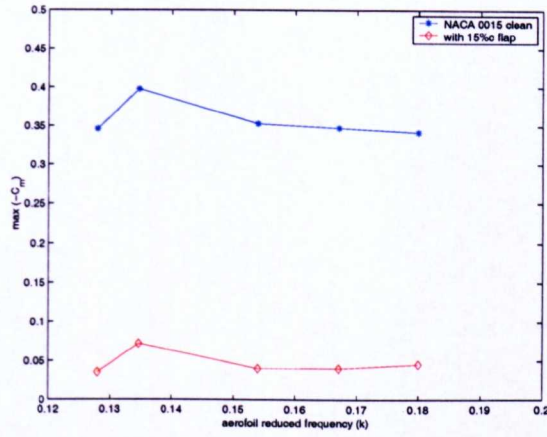
A decreasing trend of the aerofoil actuation's termination incidence (i.e. $\theta_{1_{end}}^{\hat{}}$) as a function of the reduced frequency is shown in fig. 4.5(b). This is expected since the aerofoil pitch rate increases with reduced frequency.

4.3.3 Reduced frequency

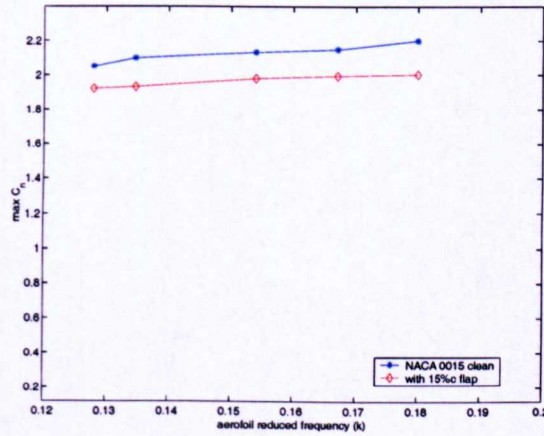
The effect of the aerofoil reduced frequency is examined for a set of values varying between $0.128 \leq k \leq 0.180$. The variation of the flap reduced frequency k_f is applied according to the variation of the aerofoil's frequency. The influence on the airloads, such as sectional normal force and pitching moment, is presented.

It is found that low reduced frequency values produce vortices (DSV, TEV)

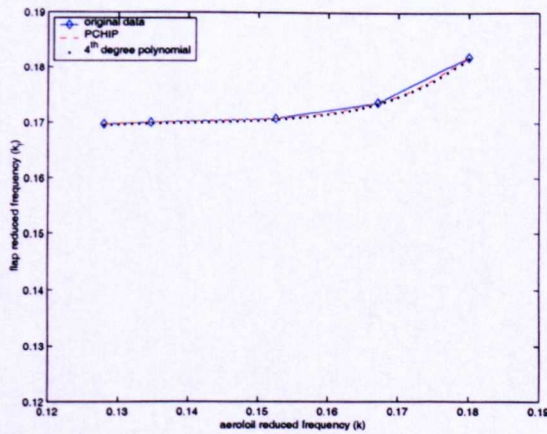
which initiate earlier in the cycle. This is consistent with the findings reported by Robinson *et. al.*, [106] where a larger range of reduced frequencies was examined than in the current investigation. In addition the intensity of the DSV increases with reduced frequency and this implies an increase of the normal force with increasing k as shown in fig. 4.6(b). Nevertheless the C_m undershoot for the k -range mentioned earlier, appears to be fairly constant as shown in fig. 4.6(a). Furthermore the variation of the flap's reduced frequency k_f with the aerofoil's is shown in fig. 4.6(c). As expected, k_f increases with k .



(a) pitching moment



(b) normal force



(c) flap reduced frequency

Figure 4.6: Effect of aerofoil reduced frequency. $\theta(t) = 15^\circ \pm 7^\circ \sin(\omega t)$, $\delta_{f_{max}} = 20^\circ$, $Re = 1.48 \times 10^6$, $M_\infty = 0.1209$.

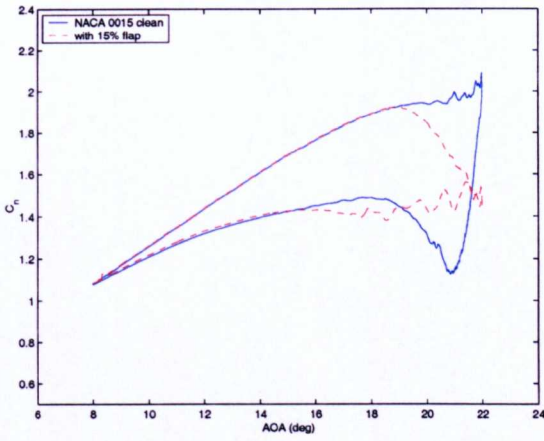
Normal force

The averaged normal force appears to be adversely affected due to the flap actuation, fig. 4.7(a-f). The reason for this is that the flap undergoes negative deflection (i.e. upward) which translates into an introduction of negative camber onto the aerofoil. Furthermore there is no benefit from the dynamic lift and in particular in all presented cases the lift drops rapidly before the aerofoil enters dynamic stall.

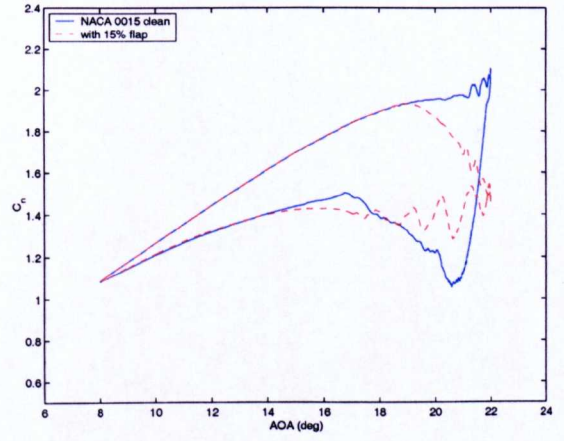
Further observation of fig. 4.7(a-f) reveals that the normal force is maintained to higher aerofoil angles of attack (AOA) with increasing reduced frequency. This is explained by the fact that the flap is deflected at later aerofoil AOA with increasing reduced frequency.

In more detail the aerofoil begins the oscillation from the mean angle (i.e. 15°), and it progresses on the upstroke to a normal force coefficient which varies between 1.95 and 2, i.e. ($1.95 \leq C_{n_{max}} \leq 2$ for $0.128 \leq k \leq 0.180$). At this point the aerofoil experiences dynamic stall which is characterised by a sudden lift increment whose duration is about 1° of its motion. After that the normal force drops suddenly for all displayed reduced frequencies, fig. 4.7(a-f). It is noticeable that with increasing reduced frequency the normal force after the dynamic stall event is shown to drop less rapidly. This can be easily explained by the fact that the flow reattaches earlier with increasing reduced frequency.

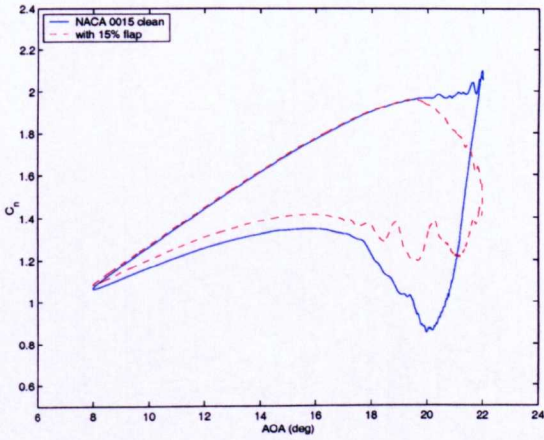
Another important feature is the fact that with increasing reduced frequency the hysteresis of the normal force approaches the clean case as shown in fig. 4.7(a-f) . This is explained by the fact that the airloads distribution over the aerofoil changes significantly between the clean and flapped cases, in other words the pressure distribution significantly varies between clean and flapped case, see fig. 3.5(a-f).



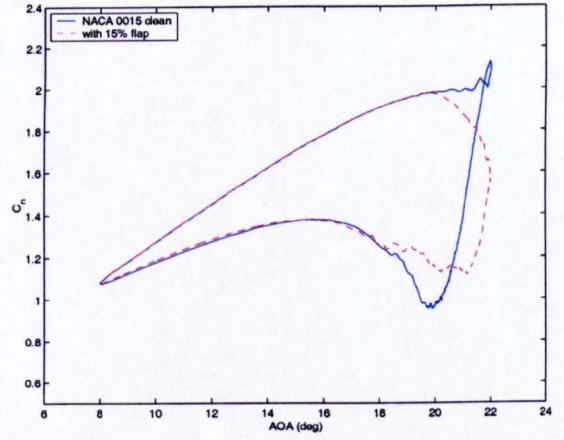
(a) $k=0.128$



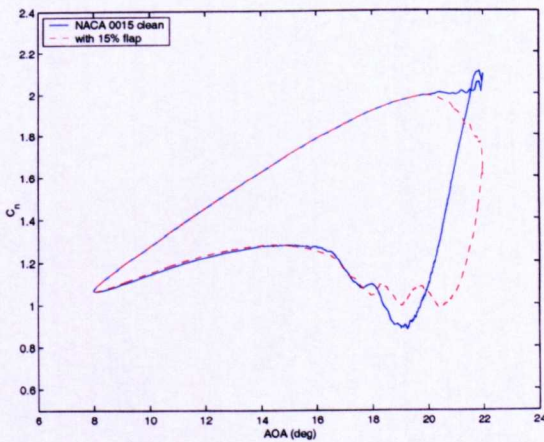
(b) $k=0.135$



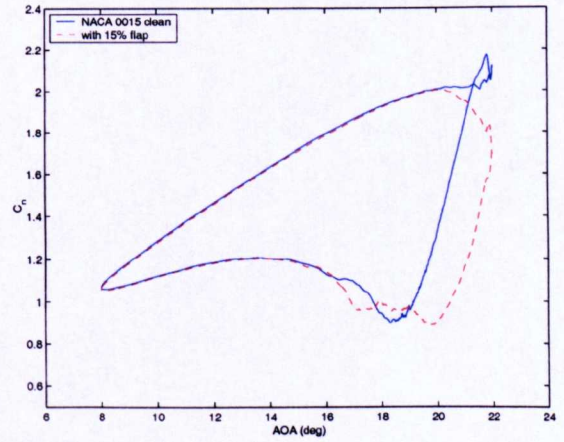
(c) $k=0.145$



(d) $k=0.154$



(e) $k=0.167$

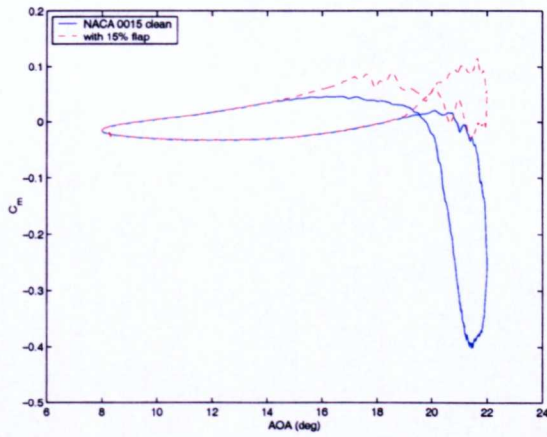


(f) $k=0.180$

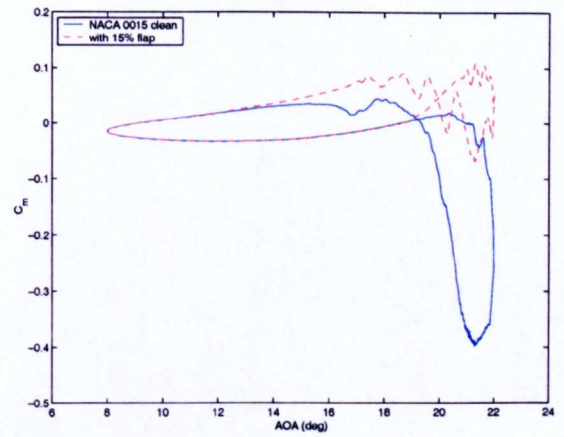
Figure 4.7: Normal force for clean and flapped NACA 0015 for various reduced frequencies. $\theta(t) = 15^\circ \pm 7^\circ \sin(\omega t)$, $\delta_{f_{max}} = 20^\circ$, $Re = 1.49 \times 10^6$, $M_\infty = 0.119$.

Pitching moment

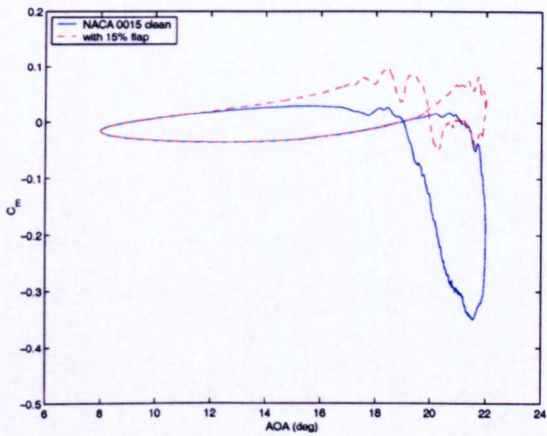
The averaged sectional pitching moment undershoot appears to be successfully modified for the range of reduced frequencies shown in fig 4.8(a-f). In addition to the reduction of the C_m undershoot, the amount of negative aerodynamic damping introduced during the dynamic stall event has been also significantly reduced. Furthermore there is little extra positive damping introduced into the C_m vs AOA loop which is maintained at very low levels as displayed in figs. 4.8(a-f).



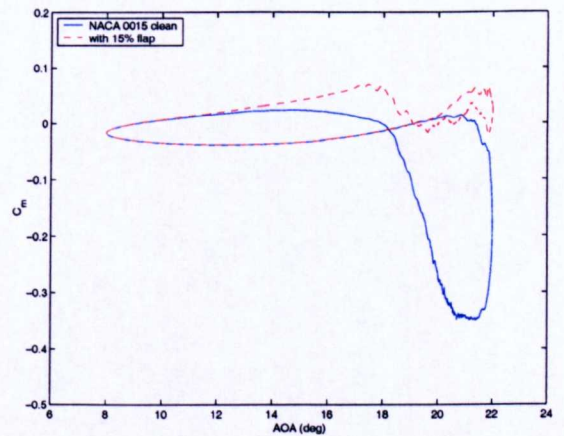
(a) $k=0.128$



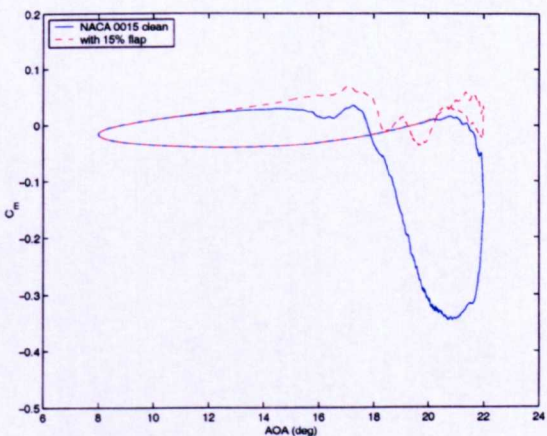
(b) $k=0.135$



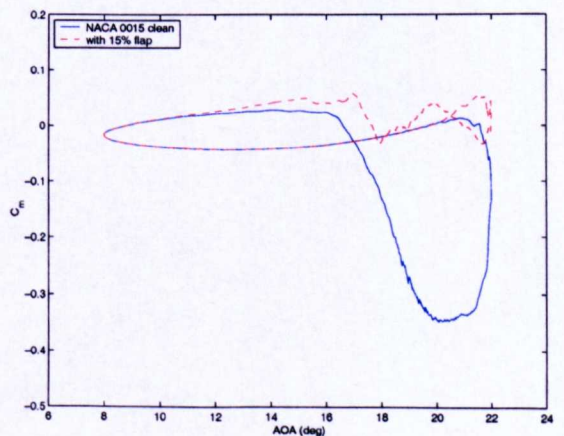
(c) $k=0.145$



(d) $k=0.154$



(e) $k=0.167$



(f) $k=0.180$

Figure 4.8: Pitching moment for clean and flapped NACA 0015 for various reduced frequencies. $\theta(t) = 15^\circ \pm 7^\circ \sin(\omega t)$, $\delta_{f_{max}} = 20^\circ$, $Re = 1.49 \times 10^6$, $M_\infty = 0.119$.

4.4 Flap dynamic properties and mechanical requirements

The dynamic properties and mechanical requirements of the flap are presented in this section. The former include polar mass moment of inertia while the latter involve the hinge moment, flap actuation power.

4.4.1 Flap mass moment of inertia

For obvious reasons the flap mass should remain the minimum required, a fact that already points toward a smaller flap size. This is examined by the looking at the mass moment of inertia related to a specific flap size. In more detail, the flap mass moment of inertia should remain low since it further reduces the actuation power. The flap's mass polar moment of inertia [31] is given by

$$I_{z_0z_0} = \sum r_i^2 m_i = \rho_{flap} \int r_{z_0}^2 dm \quad (4.2)$$

where r_i is the radial distance from the inertia axis to the elementary mass m_i integrated over the whole body and ρ_{flap} being the density of the flap, assumed to be constant over its entire volume. A complete derivation of the unbalanced flap's mass moment of inertia including determination of its mass- and geometrical centroid is given in Appendix B. Furthermore the flap inertial hinge moment for the current flap size, i.e. $c_f = 0.15$ aerofoil chord lengths is found to be significantly lower compared to the aerodynamic hinge

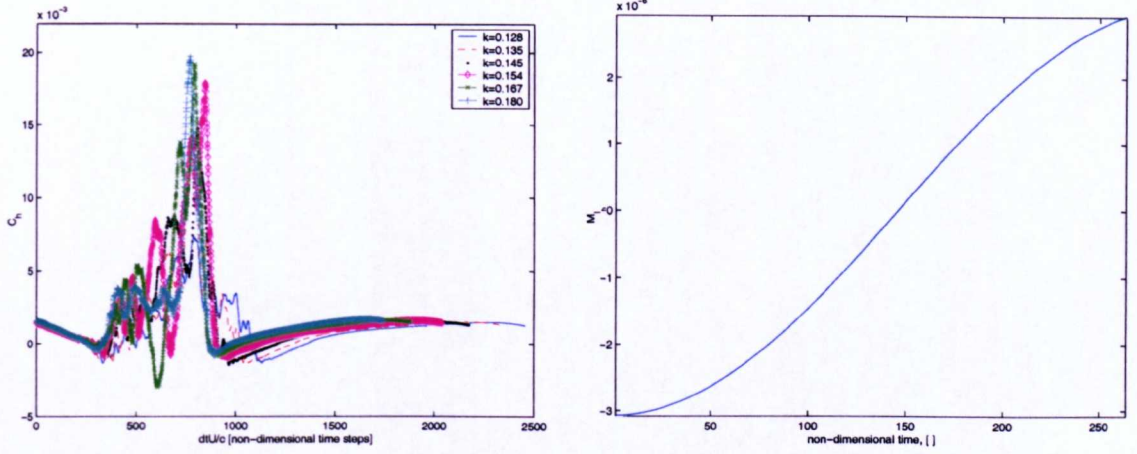
moment as shown in fig. 4.9(a,b).

4.4.2 Flap hinge moment

This parameter involves the moment that should be applied around the flap hinge in order to actuate the flap. The total flap hinge moment required for the actuation consists of two terms, i.e. the aerodynamic and the inertial term and it is given below in coefficient form by

$$C_{h_{flap\ hinge}} = C_{h_{pressure}} + C_{h_{inertial}} \quad . \quad (4.3)$$

The first term of eqn. 4.3 is due to pressure forces resulting from the on-coming flow which acts on the flap, at both its pressure- and suction surface while the second term represents the flap's inertial contribution to the moment about its hinge which is obviously involved during its entire actuation, i.e. both deflection and retraction.



(a) flap aerodynamic moment

(b) flap inertial moment, $c_f = 0.15c$

Figure 4.9: Average flap aerodynamic and inertial moment about the flap hinge required for the flap actuation.

So far only the aerodynamic contribution of the required flap hinge moment has been discussed. Its inertial contribution is also significant but as it becomes apparent from 4.9(b), it is one order of magnitude (i.e. 10^3) lower than the aerodynamic moment for the employed flap size, i.e. $c_f = 0.15c$. Conclusively the dominant term in eqn. 4.3 is the aerodynamic moment. As shown in fig. 4.9(a), the hinge moment increases with reduced frequency ($0.128 \leq k \leq 0.180$) which is explained by the fact that the DSV vortical intensity increases and consequently the suction peak induced by the DSV increases with reduced frequency. Both derivations of the hinge moment and flap mass polar of inertia are given in appendix B.

4.4.3 Flap actuation power

The flap actuation power is directly connected with the instantaneous state of the flow field. Apart from the aerodynamic effects that the flap imposes into the flow field, it should also have the minimum length required which further translates into the least mass inertia and finally delivers the minimum deflection power required.

The power required for the flap actuation can be expressed as the product of the forces acting on it multiplied by its angular deflection rate. In more detail, the forces acting on the flap are of aerodynamic and inertial nature. As it has been shown in the previous paragraph, the inertial forces can be neglected, at least for the employed flap size, 0.15 chord lengths. Regarding the present system of bodies, i.e. the 2-D aerofoil profile fitted with a 0.15c flap, rotating about the flap hinge with an angular deflection rate $\dot{\delta}_f$ acted upon by a moment H_f parallel to the axis of rotation [25] and in the absence of flap inertial forces, finally the required power for the flap actuation becomes,

$$P_{\delta_f} = \frac{dW}{dt} = H_f \frac{d\delta_f}{dt} = H_f \dot{\delta}_f \quad (4.4)$$

with H_f being the aerodynamic moment about the flap hinge and $\dot{\delta}_f$ representing the angular flap's actuation velocity. In coefficient form eqn. 4.4 becomes,

$$C_{P_{\delta_f}} = C_{H_f} \dot{\delta}_f \quad (4.5)$$

As becomes evident from fig. 4.10, the retraction phase of the entire actuation requires more power than its deflection counterpart. This is due to the fact that the actuation starts shortly before the max AOA of aerofoil oscillation and the DSV (dynamic stall vortex) has not been completely formed yet. This further implies that the suction imposed by the DSV which is still under formation onto the aerofoil's suction surface, works favourably toward the flap's (negative, i.e upward) deflection in terms of reducing the actuation power required for deflection. Regarding the retraction of the flap, there is obviously more power required which is due to the fact that DSV and TEV work adversely toward the retraction of the flap. It is reminded that the flap is actuated before the DSV is completely formed, therefore during its retraction the DSV has increased in terms of circulation and consequently more power is required to retract the flap. The required power for the flap deflection is shown in fig. 4.10 .

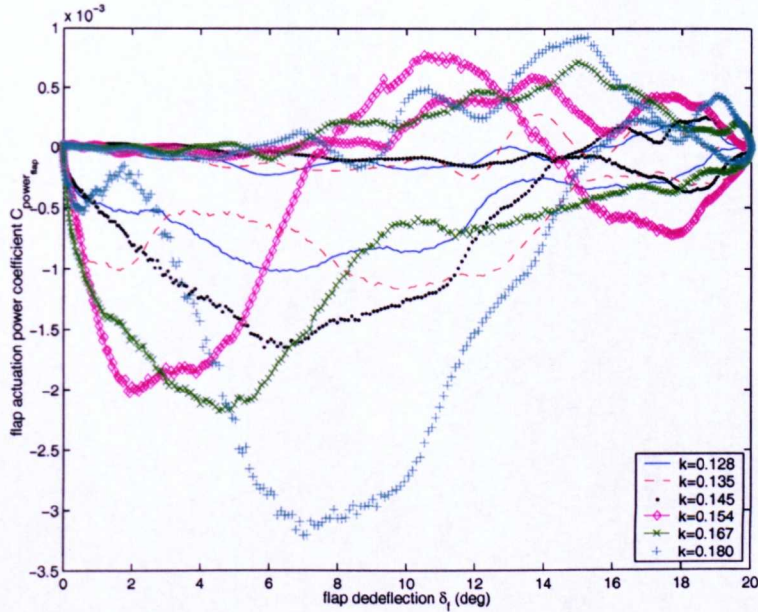


Figure 4.10: Power required for the flap actuation.

First the flap power seems to change sign which is due to the sign definition of the flap aerodynamic hinge moment.

Second, it becomes immediately evident that the amount of flap power actuation required for deflection differs from that required for retraction. This was expected since the flap actuation power is determined purely from the flap hinge moment which further has a pure aerodynamic nature in the absence of inertial effects. In more detail and in combination with the aerodynamic mechanism that the flap is set to actuate, the flow field varies more while the flap is deflected than when it is retracted. More specifically, the flap deflects when the DSV (dynamic stall vortex) has not formed completely yet, and it retracts while the DSV has grown in size. Although an appropriately phased

actuation prevents the formation of the TEV during the DSV's formation, however the short duration implies that the TEV will be formed at a later instant without amplifying the circulation of the DSV. This further implies that the pressure field around the flap area shows considerable variation, being actually more severe in pressure terms, therefore yielding to higher suction values, delivering larger aerodynamic forces which further imply higher flap aerodynamic hinge moment, having as a final effect an increased amount of flap actuation power in the retraction part than in the deflection part of the actuation.

In addition, it should be also mentioned that the instantaneous change of sign over some portions of the flap actuation (or rotor azimuth) would be extremely difficult to be translated into actuator terms, meaning that the actuator itself will not be able in general to transfer back to the flap the proper amount of power required for deflection or retraction. For this reason Milgram [72] suggested that a power conversion factor $f(H_f, \dot{\delta}_f)$ should be applied. In order to employ such a conversion factor, knowledge of the actuator dynamics is required, something that falls beyond the scope of the present study.

4.5 Concluding remarks

For the range of aerofoil reduced frequency mentioned earlier a series of flap sizes was examined. The most suitable flap size for the current work was found to have a nominal flap length of 0.15 aerofoil chord lengths. A flap deflection amplitude of 20° is found to be sufficient in reducing the C_m undershoot. Due to the negative flap deflection, the dynamic lift was not maintained. The flap notches are found not to significantly affect the flow field in the vicinity of the flap gap. Examination of the flap phasing reveals that the flap should be deflected at around the maximum aerofoil AOA for the current range of aerofoil reduced frequency. The pitching moment for the clean and flapped cases vary significantly with aerofoil reduced frequency. In contrast a small increase is found with the normal force. The flap's reduced frequency increases with aerofoil reduced frequency. The hinge moment and flap actuation power are found to increase with reduced frequency.

Chapter 5

Control strategy

The current investigation aims to demonstrate the effectiveness of a plain TE flap in rotorcraft applications to modify the aerofoil (or rotor blade cross-section) pitching moment behaviour by reducing its undershoot and consequently the amount of negative aerodynamic damping introduced during dynamic stall while at the same time benefiting the most from the dynamic lift.

This is now achieved by using the knowledge gained on the flap aerodynamic mechanism presented in chapter 3. The current chapter deals with the formulation of the optimisation problem to exploit this knowledge. Emphasis is given to sensitivity analysis which is performed with respect to optimisation parameter changes, cost coefficients and design space grid resolution.

5.1 Formulation of the optimisation problem

The methodology is based on defining a control mechanism, an objective for control and finally to develop a systematic method which finds controls that best meet the objective. The objective is to define a flap schedule for the given NACA 0015 aerofoil with improved aerodynamic performance when it exhibits dynamic stall, i.e. low pitching moment undershoot, benefiting most of the dynamic lift and reduction of the two-dimensional negative aerodynamic damping in the LS (light stall) flow regime with no or little addition of positive damping at the same time for aerofoil reduced frequencies varying between $0.128 \leq k \leq 0.180$. Modification of the aforementioned airloads with great emphasis on the negative aerodynamic damping has a direct benefit in reduction of the rotor vibration levels, which is a major problem in rotorcraft operation.

Moreover, unconstrained optimisation of the involved parameters is applied in order to assess their variation over the design space purely determined by rotor and flap related quantities. These quantities are the rotor's advance ratio (μ), the initiation of the flap actuation (t_{start}) and the period (i.e. deflection & retraction) of the entire flap actuation event (T_{δ_f}). Although the presence of the helicopter's advance ratio ($\mu = \frac{U_\infty}{\Omega R}$) is not directly evident due

to the two-dimensionality of the current problem, however since the rotor azimuth is given by $\Psi = \Omega R$, then the rotor angular speed Ω can be correlated with the two-dimensional angular frequency ω of the aerofoil's oscillation, i.e. $\theta(t) = \tilde{\theta}_0 \pm \hat{\theta}_1 \sin(\omega t)$. This further translates into a reduced frequency, i.e. $k = \frac{\omega c}{2U_\infty}$ which characterises the two-dimensional aerofoil blade sinusoidal pitch profile. It is shown throughout the current chapter that these quantities (i.e. t_{start} , T_{δ_f}) are indeed useful objectives for control. The intermediate steps of the current optimisation strategy are listed in table 5.1.

- selection of control parameters
- definition of design space variables
- formulation of objective function
- determination of weighting coefficients
- sensitivity analysis

Table 5.1: Optimisation strategy.

The first step is the selection of the aerodynamic coefficients involved in the adopted control strategy. These are chosen to be the aerofoil sectional pitching moment undershoot and overshoot (C_{m-} and C_{m+} respectively), the maximum normal force ($C_{n_{max}}$) and the negative aerodynamic damping (a_2). The latter is defined as the area of the RHS loop in the double pitching moment hysteresis loop similar to Carta's definition. Using Carta's definition

for the coefficient of the negative two dimensional aerodynamic damping, we have [135]

$$a_2 = -\frac{C_w}{\pi\hat{\theta}_1^2} \quad (5.1)$$

with C_w being the work coefficient expressed in terms of the C_m integral,

$$C_w = \oint C_m d\theta_1 \quad (5.2)$$

with θ_1 being the aerofoil oscillatory angle. Carta evaluated the integral of eqn. 5.2 from experimental results as the area within the pitching moment hysteresis loop [135]. In essence the area of the part of the pitching moment hysteresis loop (i.e. RHS loop¹) which indicates the amount of negative aerodynamic damping was calculated and, after application of a successful flap pitch input, this area should be reduced the most possible.

The variables that determine the design space are thought to be the start of the flap's actuation² (t_{start}) and the duration of the entire actuation event³ (T_{δ_f}). Next the setup of the objective function is given, followed by the determination of the weighting coefficients for every aerodynamic coefficient and finally the sensitivity of the control parameters subject to changes is examined. These changes are subject to the the combination of inclusion of the optimisation variables and the grid resolution of the design space.

¹The term RHS applies only to a double pitching moment hysteresis loop which is typical of light dynamic stall, i.e. two loops.

²Due to the two-dimensionality of the current problem it is expressed as the non-dimensional time which translates in the aerofoil AOA.

³as in 2.

The objective is to select the best possible decision for a given set of circumstances without having to enumerate all the possibilities. This is a problem of unconstrained optimisation whose design space is defined by an orthogonal grid ($t_{start} \times T_{\delta_f}$). The range of this grid initially is chosen such that it certainly covers most of the retreating side of the rotor disc, therefore ensuring that the portion of the rotor area where the blade encounters dynamic stall is certainly included. In addition the control parameters defined in the design space are normalised with their corresponding maximum values.

The objective function constitutes the implementation of the problem to be solved. For the aim of simplicity and since we are dealing with an unconstrained type of optimisation problem, a quadratic cost function is thought to be employed. Moreover the cost function is presented as a sum of squares and is given by:

$$J(\mathbf{X}) = c_j \| J(x) \|^2 = c_j \sum_{i=1}^n [J_i(x)]^2 \quad (5.3)$$

having $i = 1, \dots, N$ and $j = 1, 2, 3, 4$

with $[\mathbf{X}]_i$ and c_j denoting the design variables vector and cost coefficients respectively. The reason that a least squares cost function is employed lies mainly in its simplicity and also that minimisation of such a quadratic cost function is indicative of its efficiency and behaviour in the neighbourhood of the solution [26]. The optimisation methodology is next presented.

5.2 Optimisation methodology

A minimum is sought which will deliver the sectional pitching moment with the lowest undershoot. Equivalently this should translate to the smallest area described by the first part (i.e. RHS) of the C_m vs AOA loop. At the same time the maximum attained lift should be maintained. This becomes a difficult task since the flap deflection introduces negative camber onto the aerofoil therefore adversely affecting the lift. Another necessary condition for obtaining the global minimum of the objective function (J) is that the actuation of the flap should not introduce any extra positive damping into the C_m hysteresis loop. Complete elimination of this issue is not possible since the flap actuation introduces a certain amount of positive damping. Nevertheless, this amount is kept as low as possible. In addition the flap undergoes moderate amplitude (i.e. $\delta_f = 20^\circ$) as shown in chapter 4 and the duration of the entire actuation event should be kept minimum. An overview of the optimisation goals is given in table 5.2 .

Optimisation goals:
minimum pitching moment undershoot, $C_{m-} = C_{m-} _{min}$
minimum pitching moment overshoot, $C_{m+} = (C_{m+})_{min}$
minimum negative aero. damping, $a_2 = a_2 _{min}$
maximum attained lift, $C_n = (C_n)_{max}$
minimum duration of actuation, $T_{\delta_f} = (T_{\delta_f})_{min}$
minimum deflection amplitude, $\hat{\delta}_f = (\hat{\delta}_f)_{min} = 20^\circ$

Table 5.2: Overview of optimisation goals.

To avoid confusion since $(C_{m-})_{min}$ and $(a_2)_{min}$ have negative values, their maximum is sought in strict mathematical sense. However the presence of the absolute values is thought to eliminate any confusion as such. A series of simulations have been conducted using the Discrete Vortex Method (DVM) presented in chapter 2 and have a prescribed flap actuation profile (i.e. $\delta_f = 20^\circ$), initiation of the actuation (t_{start}) and duration of the entire flap deflection event (T_{δ_f}). Recalling eqn. 4.1 for the flap deflection amplitude we have,

$$\delta_f = \|\delta_f\| \cdot \left(1 - \cos\left(\frac{\omega t}{e^{\omega t}}\right)\right) \quad .$$

A reference case for the aerofoil pitch history is chosen as $\theta(t) = 15^\circ \pm 7^\circ \sin(\omega t)$ at a reduced frequency of $k = 0.154$. The above equation together with the aerofoil pitch profile ($15^\circ \pm 7^\circ \sin(\omega t)$) are plotted in fig. 5.1 for

convenience.

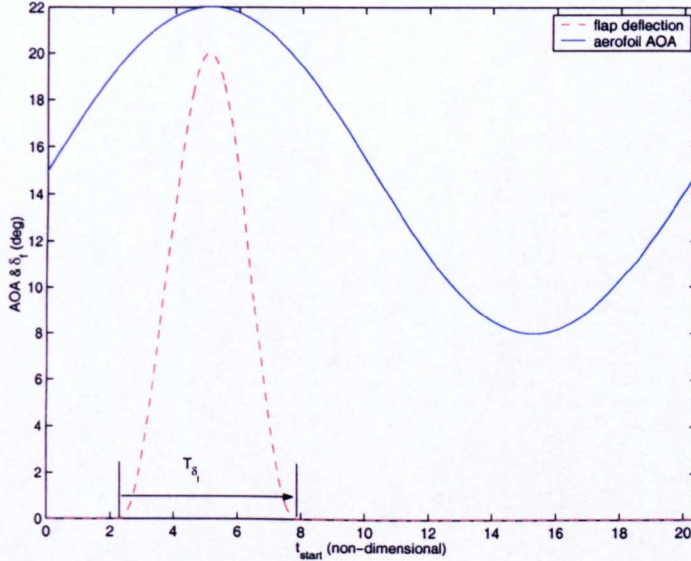


Figure 5.1: Aerofoil incidence and flap deflection profiles.

The position of the flap actuation profile could be on any azimuthal location (i.e. t_{start}) and could have any length (i.e. T_{δ_f}) within the retreating side limits. Notice that the pulse which describes the flap deflection initiates rather abruptly in an attempt to reduce even more the duration of the entire actuation event.

For the optimisation procedure, there are four cases selected (see next section, optimisation methodology). Each case has been individually examined in order to define the global minimum of the quadratic cost function given by eqn. 5.3 which in return will indicate the position of t_{start} and T_{δ_f} in the design space. Every simulation is plotted on a grid determined by the range of all initiations of the flap actuation and the duration of the entire

actuation event, i.e.: $\sum_{i=1}^n (T_{\delta_f})_i$ and $\sum_{i=1}^n (t_{start})_i$ respectively. Finally the quadratic objective function (eqn. 5.3) is presented as function of the design space variables,

$$J(\mathbf{X}) = J(t_{start}, T_{\delta_f}) \quad . \quad (5.4)$$

The reference case is exhausted in terms of simulating various start actuation times (t_{start}) and durations of the entire flap deflection (T_{δ_f}). The initial grid is described within the non-dimensional time upper and lower bounds given in table 5.3.

Lower bound:	Upper bound:
$(t_{start})_{min} = 2$	$(t_{start})_{max} = 5$
$(T_{\delta_f})_{min} = 2$	$(T_{\delta_f})_{max} = 6$

Table 5.3: Lower and upper bounds of the initial design space.

Equation 5.4 is plotted over the grid defined in table 5.3 and shown in fig. 5.2(a,b) where the minimum is also shown for convenience. It should be mentioned that eqn. 5.4 is equivalent to eqn. 5.3 having as design variables C_{m-} , C_n and a_2 .

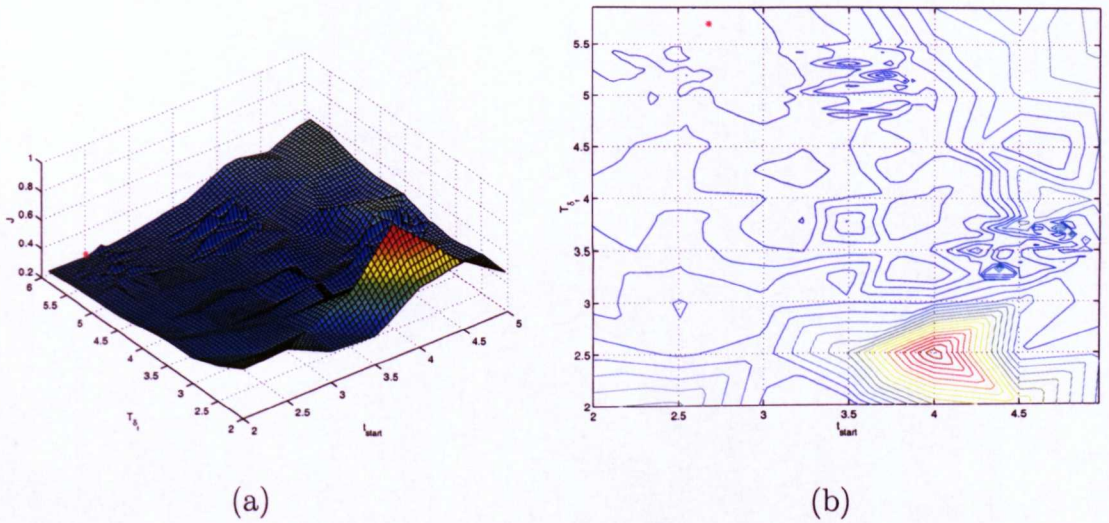


Figure 5.2: Variation of objective function J_1 at the initial grid.

With the appropriate weighting coefficients the relative minimum is determined. The location of the global minimum in combination with the proper cost coefficients is best to be on a flat region of the (initial) grid rather than on peaky region in order to ensure reduction of the sensitivity to the control parameters. Finally a small portion of the grid where the relative minimum lies is extracted and on this new grid with the same cost coefficients the next optimisation cases are presented.

A finer grid is defined around the global minimum shown in fig. 5.2(a,b) and has boundaries shown in table 5.4.

Lower bound:	Upper bound:
$(t_{start})_{min} = 1.95$	$(t_{start})_{max} = 2.95$
$(T_{\delta_f})_{min} = 5$	$(T_{\delta_f})_{max} = 6$

Table 5.4: Lower and upper bounds of the extracted design space.

It is worth mentioning that since the analytic form of a continuous function $J = J(t_{start}, T_{\delta_f})$ is unknown, the final objective function should be smoothed out without losing viable information. This is achieved by spline curve fitting using the Spline MATLAB® toolbox [21] through the grid values of the objective function at every grid point. The original grid consists of threads in x - (i.e. t_{start}) and y - (i.e. T_{δ_f}) dimension. Each thread consists of, say N knots, therefore implying that there are $N-1$ parts to be connected. These parts⁴ are connected by means of a PCHIP (piecewise cubic interpolating Hermite polynomials) rather than connecting all nodes of the same thread with a single polynomial, which would yield to a high degree polynomial, (i.e. ≥ 10) and consequently to very peaky derivatives. Finally the nodes are connected with a bivariate spline⁵ of the form,

$$S(x, y) = \sum_{k=0}^3 \sum_{l=0}^3 a_{kl}^{(i,j)} (x - x_i)^k (y - y_j)^l \quad (5.5)$$

with $S(x, y) \equiv S(t_{start}, T_{\delta_f})$, k and l being the order of the i -th and j -th spline

⁴A part is defined as the connection between two consecutive nodes.

⁵A bivariate spline should be considered as a subsequent piecewise polynomial approximation in two dimensions.

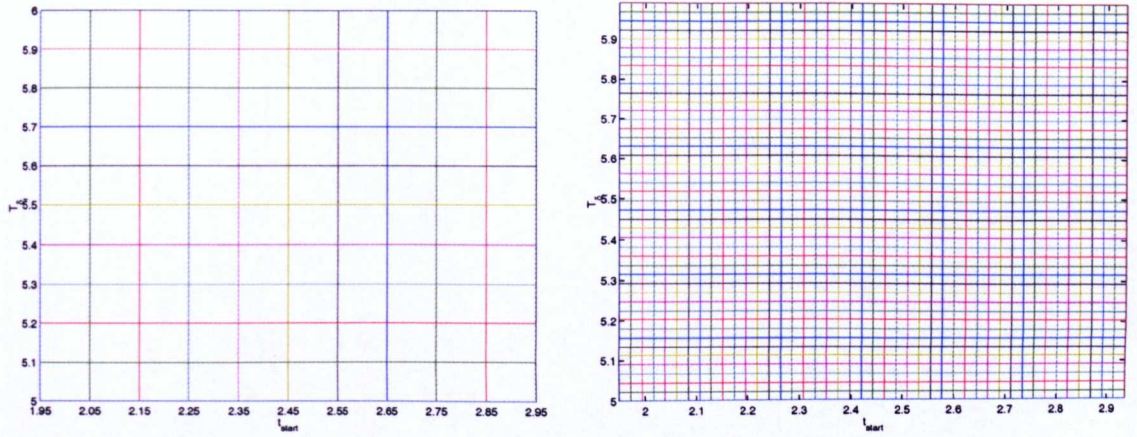
respectively and $a(i, j)$ being a coefficient vector of each spline curve, [35],[21].

The optimisation procedure is next presented.

5.3 Optimisation procedure

The target becomes the identification of the global minimum which will deliver the appropriate t_{start} and T_{δ_f} . The optimum for the current problem would result from a number of factors: the grid resolution that describes the design space, the intermediate grid step between the subsequent T_{δ_f} values used for the simulations, the choice of the appropriate cost coefficients and the combination of the control parameters. All these factors are referred to as sensitivity analysis and have generated four different optimisation cases (i.e. J_{1-4}) to be minimised.

In more detail, the grid resolution that describes the design space is examined by employing the simulations resolution labelled as grid-A and another one four times finer than the original one, labelled as grid-B. Both design space resolution grids are displayed in fig. 5.3(a,b) for convenience. The aforementioned grid resolution was found not to significantly affect the delivered t_{start} and T_{δ_f} , therefore justifying the adopted interpolation scheme, as it is demonstrated throughout the current chapter.

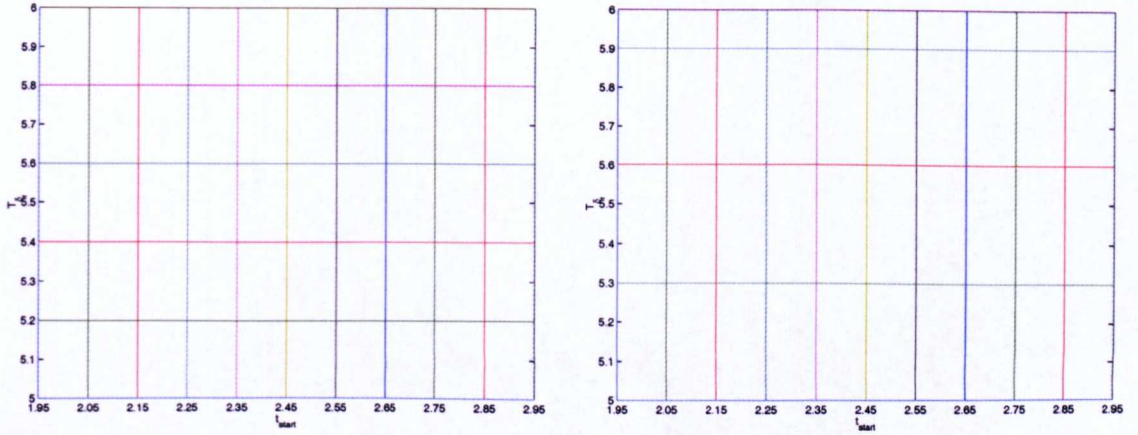


(a) grid-A (simulations grid)

(b) grid-B ($\times 4$ finer)

Figure 5.3: Design space grid resolution.

In addition grid resolution analysis is performed with respect to the intermediate non-dimensional time step that describes the sequence of the T_{δ_f} values deployment. Moreover sensitivity analysis is performed to each objective function J_{1-4} by applying a coarser non-dimensional time-step in the grid which describes the design space defined in the T_{δ_f} direction. The two new coarser grids are labelled as grid-1 and grid-2 respectively and shown in fig. 5.4(a,b) for convenience. This procedure is conducted in order to examine how the controls (i.e. t_{start} and T_{δ_f}) for each objective function (J_{1-4}) are affected.



(a) grid-1

(b) grid-2

Figure 5.4: Grid topology resolution with respect to the design space variable T_{δ_f} .

Examination of the cost coefficients for each objective function is also performed. For their determination a wide combination of values was tested. Owing to the nonlinear nature of the current unconstrained optimisation problem, the location of the global minimum in the design space grid defined by $t_{start} \times T_{\delta_f}$ was found to be insensitive for a large combination of cost coefficients. As it becomes evident from eqns. 5.6-5.9, describing each J , the most weight is given to the pitching moment undershoot and the two-dimensional aerodynamic damping, as shown in tables, 5.5, 5.7, 5.9, 5.11. Obviously we are dealing with some kind of conflicting situation since the C_{m-} undershoot should be kept minimum while C_n should be kept maximum. The contradiction is that the negative flap deflection (i.e. upward) achieves entirely

the first goal (i.e. low C_{m-} undershoot) but does not satisfactorily meet the second goal which is maintenance of the dynamic lift. However the choice of the cost coefficients c_i aims to influence the contribution of each optimisation parameter to the cost function.

After the aforementioned sensitivity analysis is performed, the $J_{min_{1-4}}$ values are obtained together with the corresponding t_{start} and T_{δ_f} . The latter are plotted vs the aerofoil reduced frequency ($0.128 \leq k \leq 0.180$) in order to establish a trend, where new values of t_{start} , T_{δ_f} and k are extracted. This procedure is repeated for all four optimisation cases and the new t_{start} and T_{δ_f} are simulated in the same (new) reduced frequencies and the new obtained airloads are examined.

Finally regarding the minimisation procedure, the global minimum is sought for each of the four optimisation cases $J_{min_{1-4}}$ using only function values. Its location is tracked by means of comparison, i.e. marching through all elements of $J(\mathbf{X})$ using the MATLAB® function "min" [20]. Every optimisation case is examined individually in the next section.

5.3.1 Optimisation case I

The optimisation parameters for case I are the pitching moment undershoot (C_{m-}), the maximum normal force ($C_{n_{max}}$) and the negative aerodynamic

damping (α_2) and are given by,

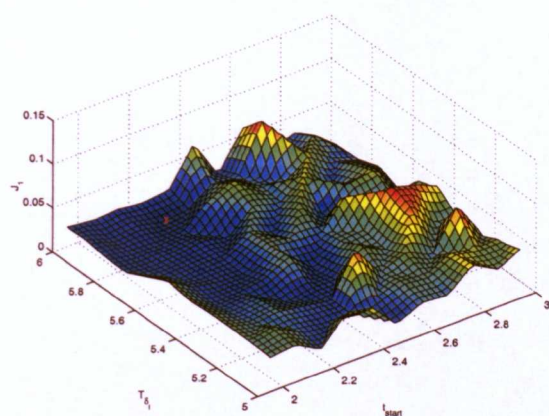
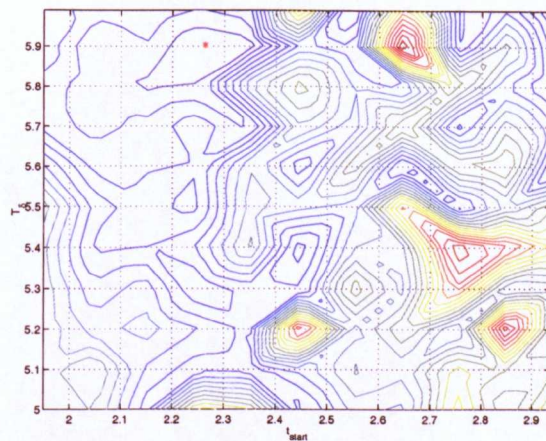
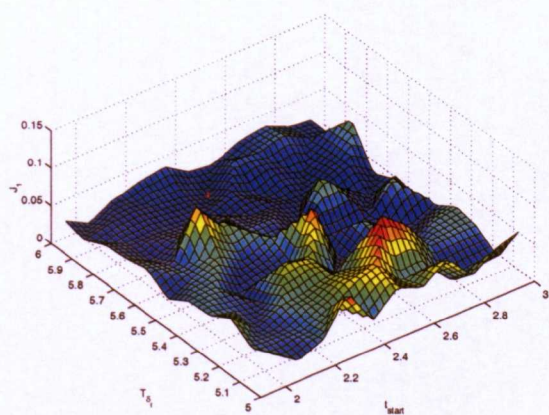
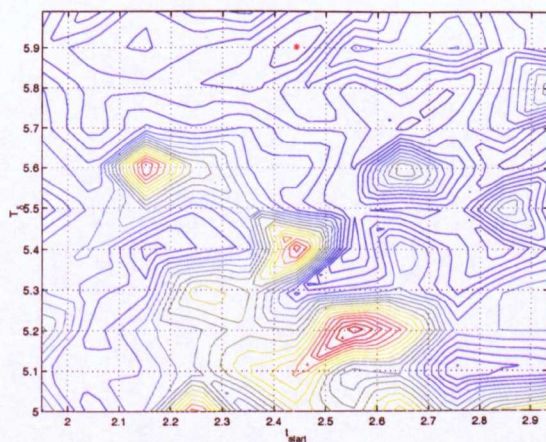
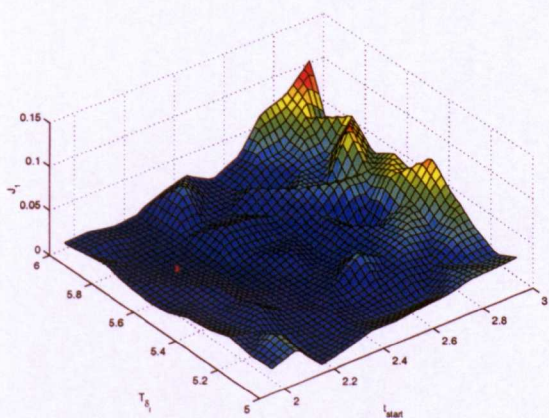
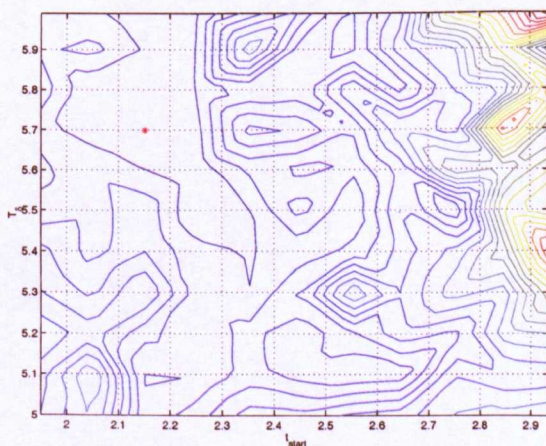
$$J_1(\mathbf{X})_i = \left[c_1(C_{m-})^2 + c_2 \left(\frac{1}{C_{n_{max}}} \right)^2 + c_3(\alpha_2)^2 \right]_i \quad (5.6)$$

In fig. 5.5(a-f) the variation of the objective function J_1 is shown. The minimum values $J_{1_{min}}$ for three different reduced frequencies are also shown in table 5.5. For reasons of accuracy the variation of J_1 is plotted in the design space defined by grid-B shown in fig. 5.3(b). However the finer grid did not seem to affect significantly the J_1 values and the corresponding controls, t_{start} and T_{δ_f} respectively, therefore justifying the grid resolution illustrated in fig. 5.3. Furthermore J_1 for all three k values is shown to be fluctuating which is due to the first (C_{m-}) and the third term (a_2) of eqn. 5.6 where all terms are shown in fig. 5.6(a-c) for convenience. The cost coefficients are listed in table 5.5. They are further examined in two different grid resolutions of the design space. Their values for the two different grids are kept equal to unity initially which delivered the controls t_{start} and T_{δ_f} at the design space boundaries. Variations of the cost coefficients other than unity delivered controls were found to be within the design space away from the boundaries. Their values for the two different grids are kept equal for all three aerofoil reduced frequencies and, as shown in table 5.5, they do not appear to be significantly affected by the design space grid resolution.

The airloads variation for three different reduced frequencies (i.e. $k = 0.128$, $k = 0.154$ and $k = 0.180$) is shown in fig. 5.7(a-f). The main optimisation target which is reduction of the C_{m-} undershoot is shown to be met for all

three reduced frequencies shown, with both sets of cost coefficients shown in table 5.5. However employing the controls as suggested when utilising weighting coefficients equal to unity seems to deliver slightly more C_m undershoot than $c_i \neq 1$ and better maintenance of lift for the case of $k = 0.128$ as shown in fig. 5.7(a,b) respectively. The opposite is found to be for the case of $k = 0.154$ shown in fig. 5.7(c,d). The controls delivered for $k = 0.180$, are found to be smoother (particularly C_{m-}) using $c_i \neq 1$.

An interesting feature appears to be the improved lift maintenance by employing the value of controls which coincide with the RHS boundary of the design space. This fact actually suggests that using control values further than the current design space might yield to even more improved aerodynamic characteristics. This vanishes with increasing reduced frequency (fig. 5.7(f), for the range used throughout the current work. In addition maintaining control values within the design space as defined so far appears to be sufficient in modifying satisfactorily the airloads.

(a) $k=0.128$ (b) $k=0.128$ (c) $k=0.154$ (d) $k=0.154$ (e) $k=0.180$ (f) $k=0.180$ Figure 5.5: Variation of objective function J_1 over the design space.

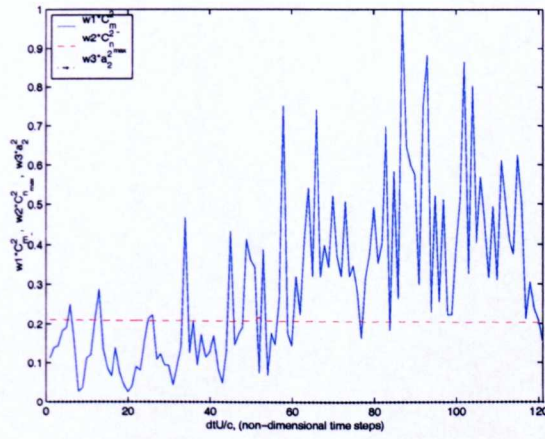
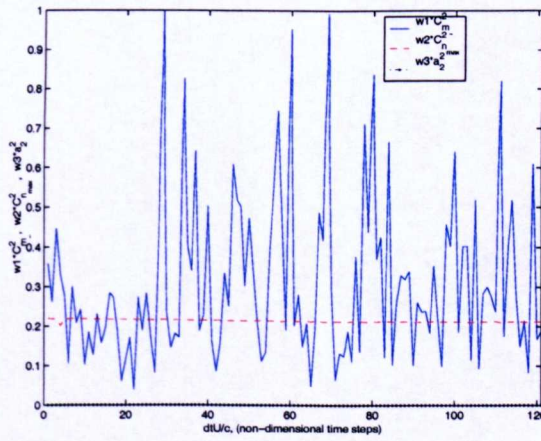
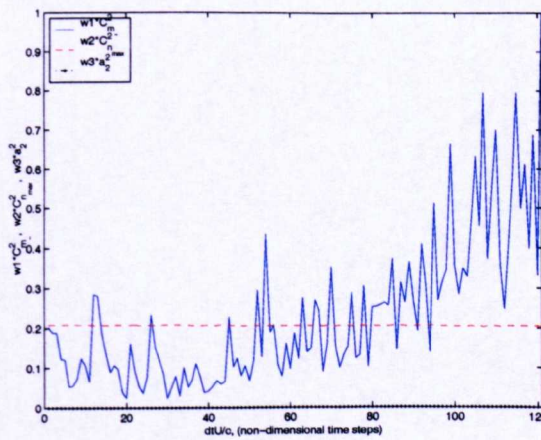
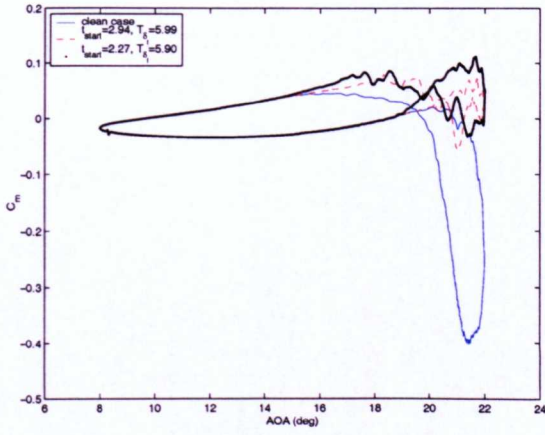
(a) $k = 0.128$ (b) $k = 0.154$ (c) $k = 0.180$

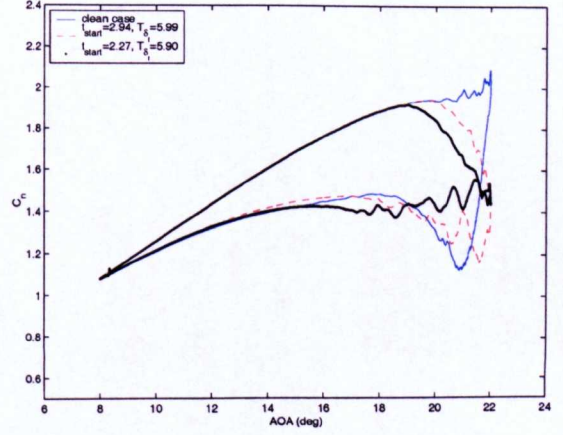
Figure 5.6: Variation of normalised variables for optimisation case I.

case I:					
$k = 0.128$, (grid-A):					
c_1 for C_{m-} :	c_2 for $C_{n_{max}}$:	c_3 for α_2 :	t_{start}	T_{δ_f}	J_{1min}
1	1	1	2.950000	6.000000	1.221894
0.08	0.001	0.03	2.250000	5.900000	0.012030
$k = 0.128$, (grid-B):					
1	1	1	2.936480	5.990000	1.273587
0.08	0.001	0.03	2.263880	5.900000	0.012306
$k = 0.154$, (grid-A):					
c_1 for C_{m-} :	c_2 for $C_{n_{max}}$:	c_3 for α_2 :	t_{start}	T_{δ_f}	J_{1min}
1	1	1	2.950000	5.700000	1.159518
0.08	0.001	0.03	2.450000	5.900000	0.006819
$k = 0.154$, (grid-B):					
1	1	1	2.935600	5.675000	1.187473
0.08	0.001	0.03	2.442800	5.900000	0.007638
$k = 0.180$, (grid-A):					
c_1 for C_{m-} :	c_2 for $C_{n_{max}}$:	c_3 for α_2 :	t_{start}	T_{δ_f}	J_{1min}
1	1	1	2.250000	5.500000	1.098355
0.08	0.001	0.03	2.150000	5.700000	0.004764
$k = 0.180$, (grid-B):					
1	1	1	2.263600	5.495000	1.107228
0.08	0.001	0.03	2.151600	5.697500	0.004826

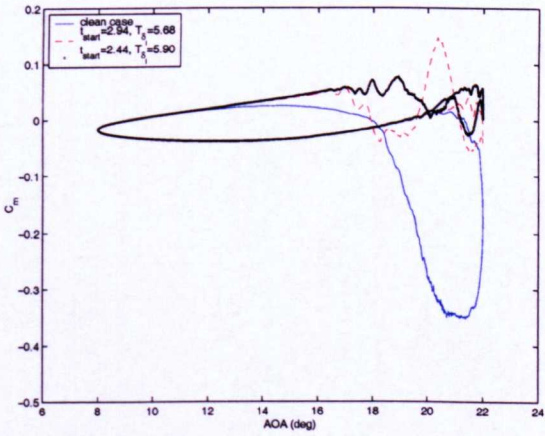
Table 5.5: Summary of weighting coefficients, optimisation parameters, design space variables and objective function values for optimisation case I.



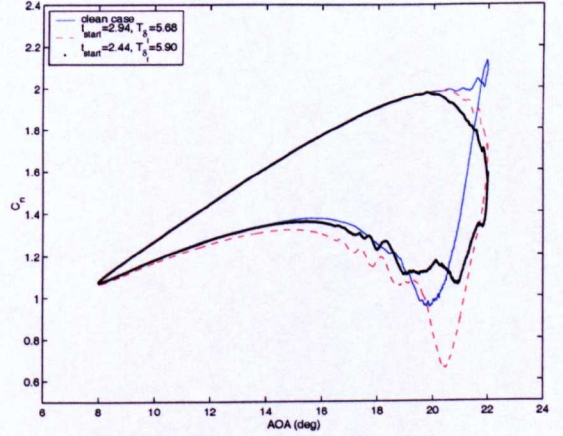
(a) C_m , $k = 0.128$



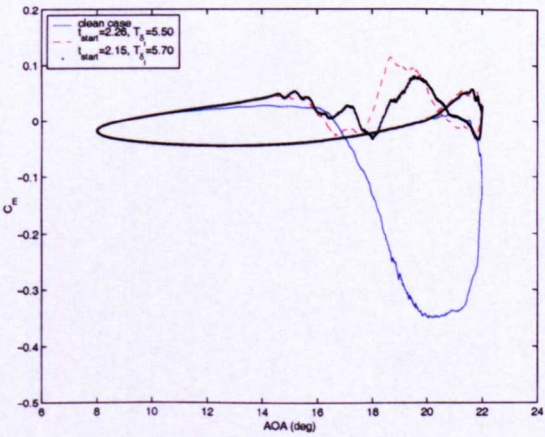
(b) C_n , $k = 0.128$



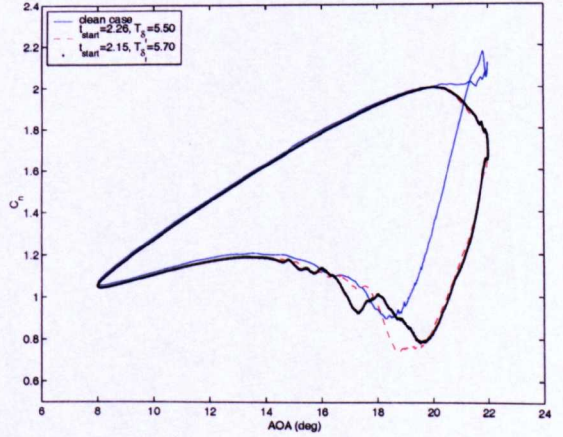
(c) C_m , $k = 0.154$



(d) C_n , $k = 0.154$



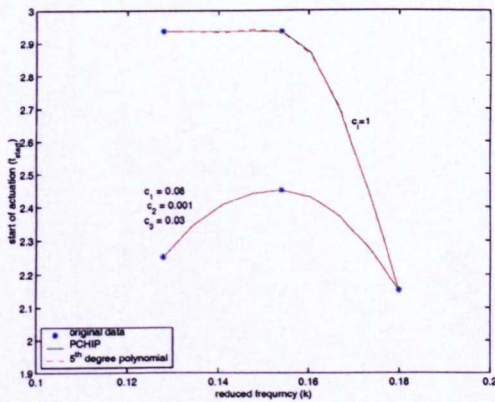
(e) C_m , $k = 0.180$



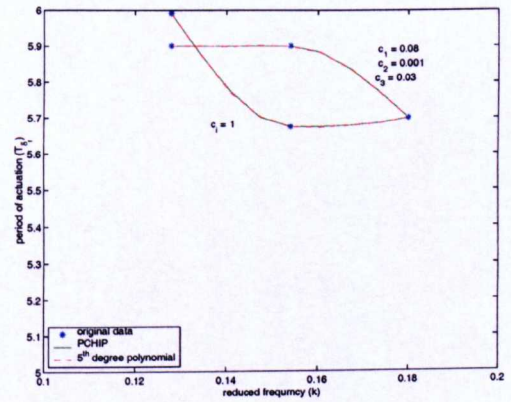
(f) C_n , $k = 0.180$

Figure 5.7: Airloads variation subject to table 5.5.

Finally the t_{start} and T_{δ_f} values shown in table 5.5 are plotted vs the aerofoil's reduced frequency for both sets of cost coefficients (i.e. $c_i = 1$ and $c_i \neq 1$) and shown in fig. 5.8. Since it is decided to maintain the cost coefficients other than unity, three new k , t_{start} and T_{δ_f} values are extracted and simulated. These values are listed in table 5.6. The same procedure is repeated to all optimisation cases for these new reduced frequencies and, finally the modified airloads are presented in fig. 5.21(a-f).



(a) $t_{start} = f(k)$



(b) $T_{\delta_f} = f(k)$

Figure 5.8: Initiation and duration of flap actuation as function of the reduced frequency for optimisation case I.

$k = 0.131$	$k = 0.146$	$k = 0.170$
$t_{start} = 2.29$	$t_{start} = 2.43$	$t_{start} = 2.33$
$T_{\delta_f} = 5.90$	$T_{\delta_f} = 5.90$	$T_{\delta_f} = 5.81$

Table 5.6: Summary of extracted k , t_{start} , and T_{δ_f} values from fig. 5.8(a,b) (optimisation case I).

5.3.2 Optimisation case II

The parameters included in optimisation case II are the sectional pitching moment undershoot and overshoot (C_{m-} and C_{m+} respectively), the maximum normal force ($C_{n_{max}}$) and the negative aerodynamic damping (α_2) and are given by

$$J_2(\mathbf{X})_i = \left[c_1(C_{m-})^2 + c_2(C_{m+})^2 + c_3 \left(\frac{1}{C_{n_{max}}} \right)^2 + c_4(\alpha_2)^2 \right]_i . \quad (5.7)$$

The variation of the objective function J_2 is shown in fig. 5.9(a-f). As under case I, J_2 is plotted in the design space defined by grid-B shown in fig. 5.3(b). Again there was no significant variation of the controls (i.e. t_{start} & T_{δ_f}) and J_2 with the design space grid resolution. The fluctuating behaviour of J_2 is due to the terms C_{m-} and α_2 in eqn. 5.7 where all normalised terms are shown in fig. 5.10 for convenience.

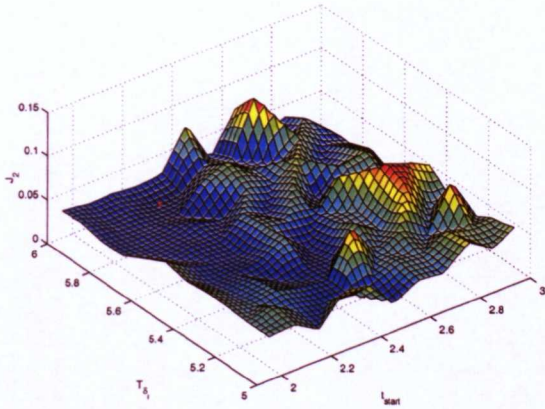
The cost coefficients of J_2 with the corresponding controls are shown in table 5.7. As under case I, they are further examined in both grid resolutions

of the design space. Their values for the two different grids are kept equal to unity initially and contrast to case I, controls t_{start} and T_{δ_f} at $k = 0.128$ delivered values at the design space boundaries. Variations of the cost coefficients other than unity they delivered controls which were found to be within the design space away from the boundaries. Their values for the two different grids are kept equal for $k = 0.128$, $k = 0.154$ reduced frequencies and, as shown in table 5.7, they do not appear to be significantly affected by the grid resolution. However this is not found to be the case at $k = 0.180$ where the grid resolution appeared to have significant influence on the controls when employing cost coefficients other than unity. Nevertheless the values of J_2 for both grids and sets of cost coefficients are not found to vary significantly from each other.

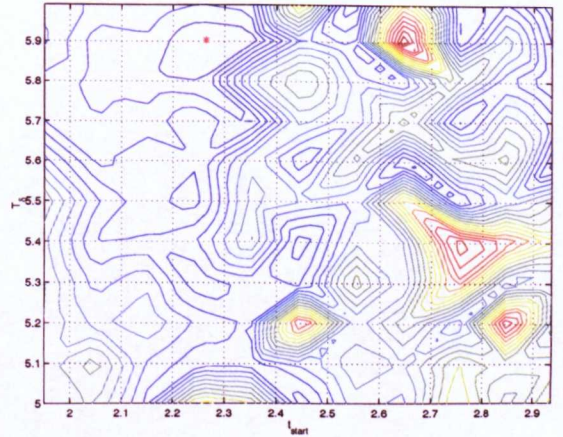
The variation of the airloads for three different reduced frequencies (i.e. $k = 0.128$, $k = 0.154$ and $k = 0.180$) is shown in fig. 5.11(a-f). The main optimisation target which is reduction of the C_{m-} undershoot is shown to be met for all three reduced frequencies shown, with both sets of cost coefficients as illustrated in table 5.7. However employing the controls as suggested when employing weighting coefficients equal to unity seems to deliver slightly more C_m undershoot than $c_i \neq 1$ for and better maintenance of lift for the case of $k = 0.128$ as shown in fig. 5.7(a,b) respectively. The opposite is found to be for the case of $k = 0.154$ shown in fig. 5.7(c,d). The controls delivered for $k = 0.180$, are shown to be less fluctuating (particularly C_{m-}) using $c_i \neq 1$.

Each normalised term of eqn. 5.7 is shown in figs. 5.10 for convenience. In addition a similar trend of the improved aerodynamic characteristics with respect to the maintenance of the normal force is observed as in case I.

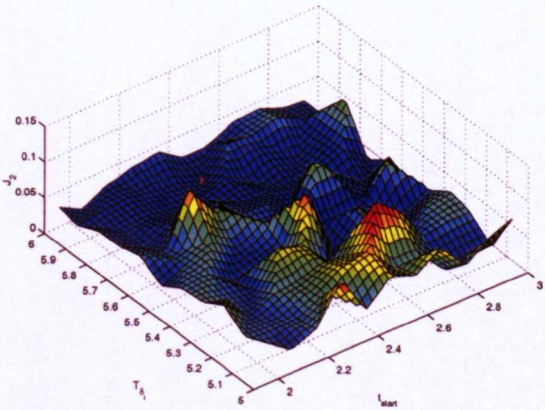
Actually the inclusion of C_{m+} does not seem to significantly affect the obtained controls for $k = 0.128$ and $k = 0.154$. However variation of T_{δ_f} , $k = 0.180$ is observed with inclusion of C_{m+} in the objective function. Although the obtained airloads under case I and II for $k = 0.180$ do not show significant variation, however in the case of a similar optimisation problem with data from more than a single case could question the validity of the employed MATLAB® minimisation function algorithm.



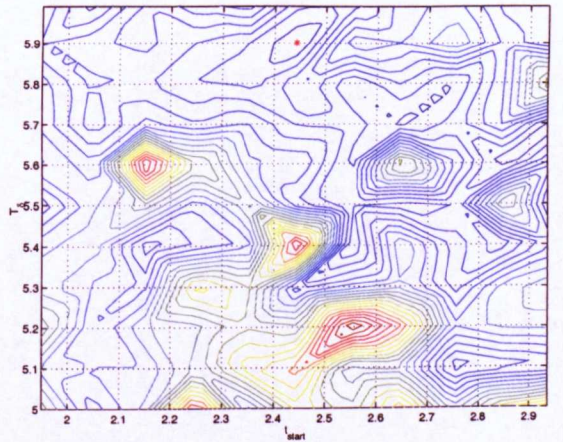
(a) $k=0.128$



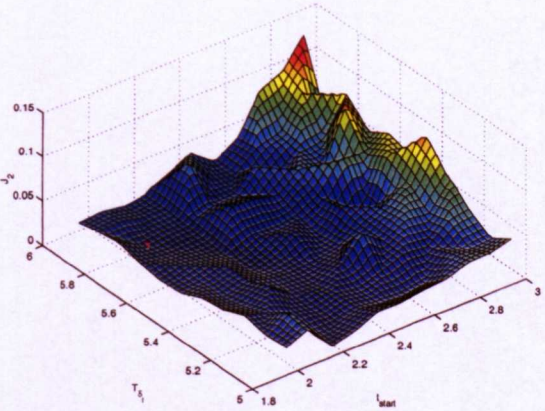
(b) $k=0.128$



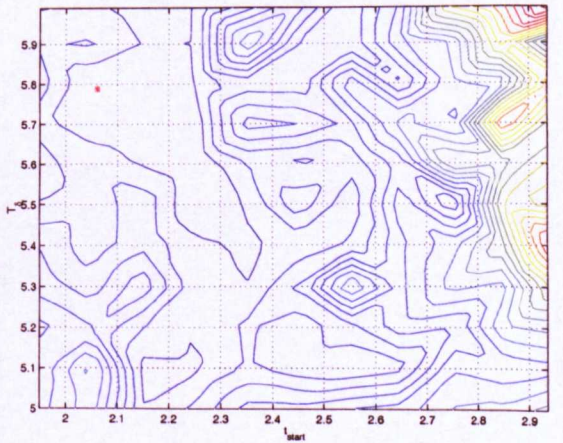
(c) $k=0.154$



(d) $k=0.154$

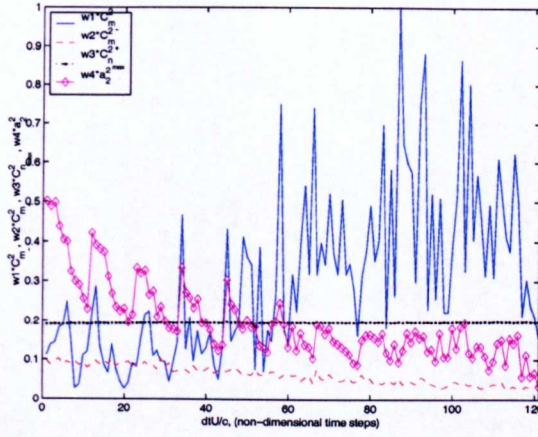


(c) $k=0.180$

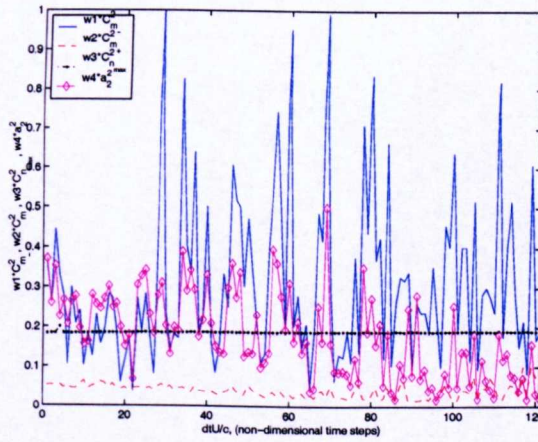


(d) $k=0.180$

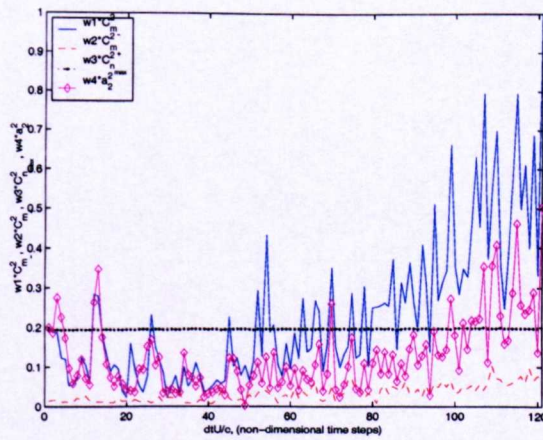
Figure 5.9: Variation of objective function J_2 over the design space.



(a) $k = 0.128$



(b) $k = 0.154$

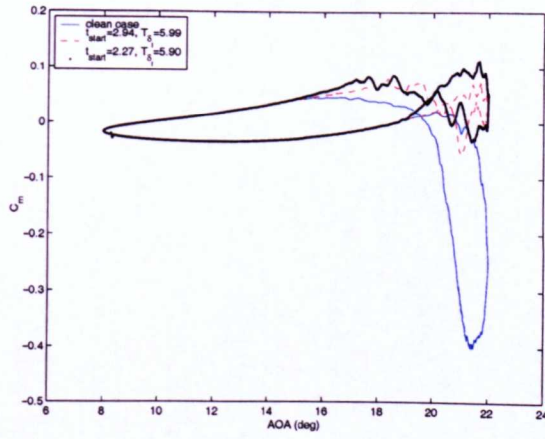


(c) $k = 0.180$

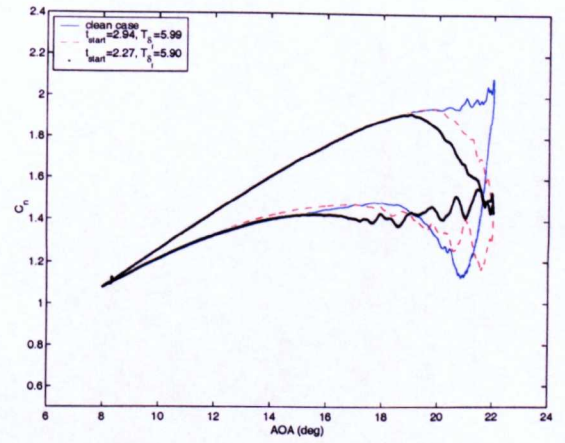
Figure 5.10: Variation of normalised variables for optimisation case II.

case II:						
$k = 0.128$: original grid						
c_1 for C_{m_-} :	c_2 for C_{m_+} :	c_3 for $C_{n_{max}}$:	c_4 for α_2 :	t_{start}	T_{δ_f}	J_{2min}
1	1	1	1	2.950000	6.000000	1.547763
0.09	0.01	0.001	0.03	2.250000	5.900000	0.019333
$k = 0.128$: x4 finer grid						
1	1	1	1	2.935600	5.990000	1.600439
0.09	0.01	0.001	0.03	2.263600	5.900000	0.019490
$k = 0.154$: original grid						
c_1 for C_{m_-} :	c_2 for C_{m_+} :	c_3 for $C_{n_{max}}$:	c_4 for α_2 :	t_{start}	T_{δ_f}	J_{2min}
1	1	1	1	2.850000	5.600000	1.191987
0.09	0.01	0.001	0.03	2.450000	5.900000	0.009876
$k = 0.154$: x4 finer grid						
1	1	1	1	2.846000	5.607500	1.222886
0.09	0.01	0.001	0.03	2.442800	5.900000	0.010708
$k = 0.180$: original grid						
c_1 for C_{m_-} :	c_2 for C_{m_+} :	c_3 for $C_{n_{max}}$:	c_4 for α_2 :	t_{start}	T_{δ_f}	J_{2min}
1	1	1	1	2.250000	5.600000	1.122235
0.09	0.01	0.001	0.03	2.250000	5.500000	0.006352
$k = 0.180$: x4 finer grid						
1	1	1	1	2.241200	5.607500	1.133409
0.09	0.01	0.001	0.03	2.062000	5.787500	0.006449

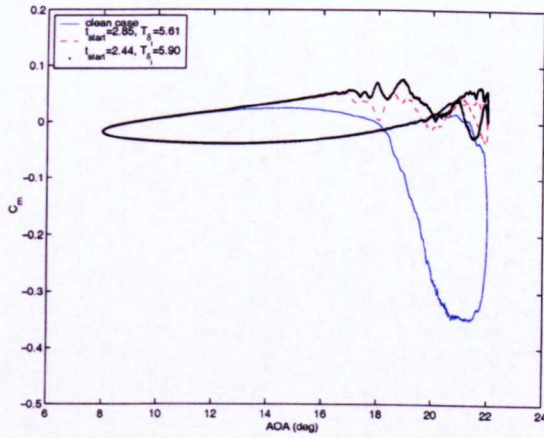
Table 5.7: Summary of weighting coefficients, optimisation parameters and objective function values for optimisation case II.



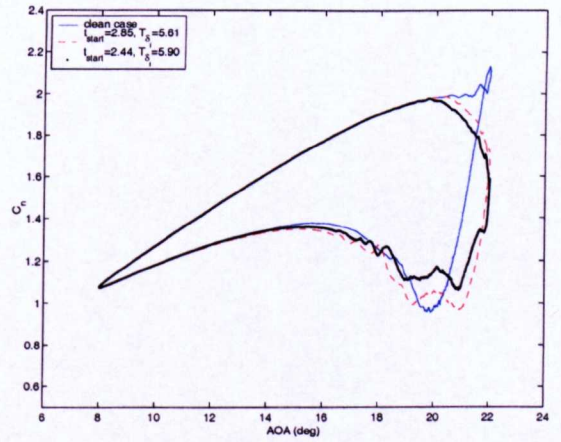
(a) C_m , $k = 0.128$



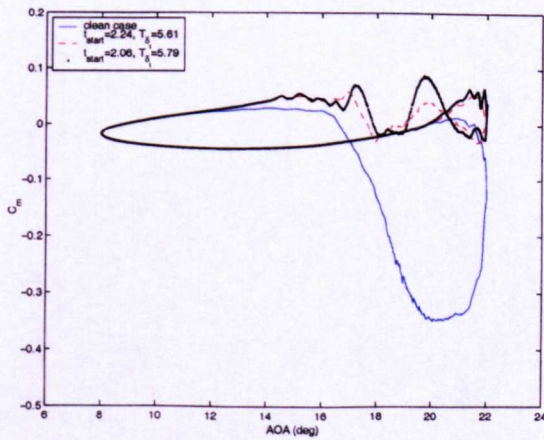
(b) C_n , $k = 0.128$



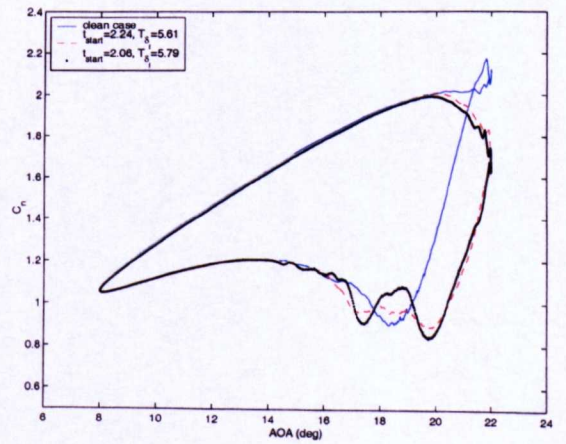
(c) C_m , $k = 0.154$



(d) C_n , $k = 0.154$



(e) C_m , $k = 0.180$



(f) C_n , $k = 0.180$

Figure 5.11: Airloads variation subject to table 5.7.

The t_{start} and T_{δ_f} values shown in table 5.7 are plotted vs aerofoil reduced frequency for both sets of cost coefficients (i.e. $c_i = 1$ and $c_i \neq 1$) and shown in fig. 5.12. Since it is decided to maintain the cost coefficients other than unity, three new k , t_{start} and T_{δ_f} values are extracted, simulated and listed in table 5.8. As under case I, these new reduced frequencies and, finally the modified airloads are presented in fig. 5.21(a-f).

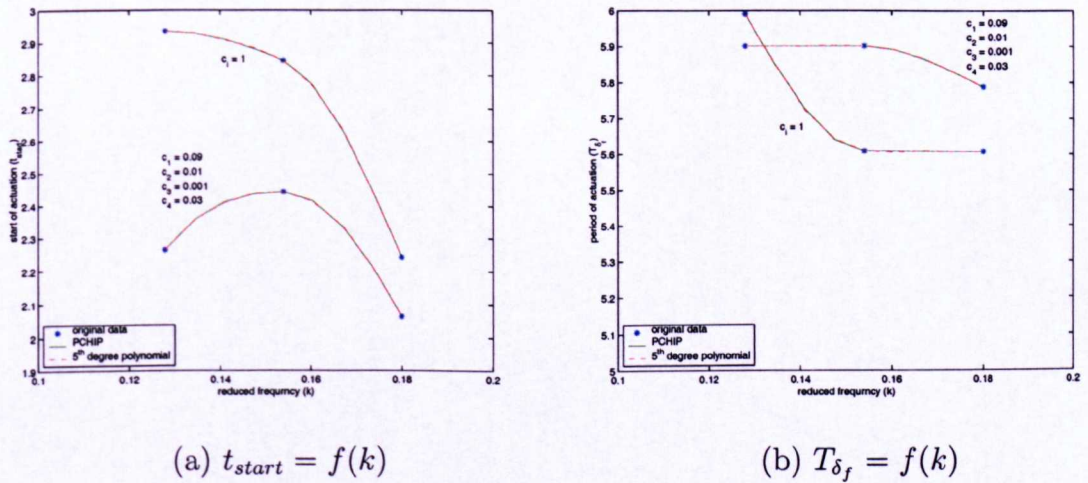


Figure 5.12: Initiation and duration of flap actuation as function of the reduced frequency for optimisation case II.

$k = 0.131$	$k = 0.146$	$k = 0.170$
$t_{start} = 2.38$	$t_{start} = 2.78$	$t_{start} = 2.62$
$T_{\delta_f} = 5.85$	$T_{\delta_f} = 5.65$	$T_{\delta_f} = 5.60$

Table 5.8: Summary of extracted k , t_{start} , and T_{δ_f} values from fig. 5.12(a,b) (optimisation case II).

5.3.3 Optimisation case III

The optimisation parameters for case III are the pitching moment undershoot (C_{m-}), the pitching moment overshoot (C_{m+}) and the negative aerodynamic damping (α_2) and are given by,

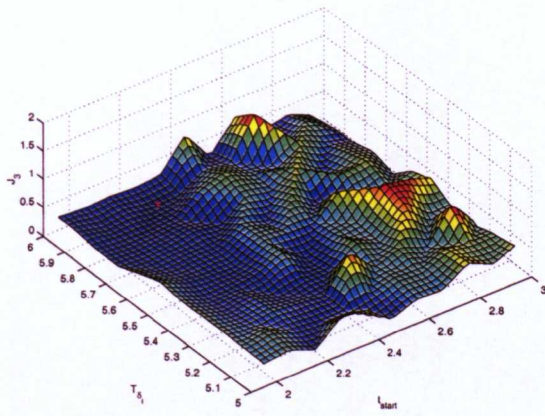
$$J_3(\mathbf{X})_i = \left[c_1(C_{m-})^2 + c_2(C_{m+})^2 + c_3(\alpha_2)^2 \right]_i . \quad (5.8)$$

In fig. 5.13(a-f) the variation of the objective function J_3 is shown in the design space defined by grid-B shown in fig. 5.3(b). However for $k = 0.128$ the finer grid seems to affect significantly the J_3 values and the corresponding controls, t_{start} and T_{δ_f} , respectively, therefore justifying the adopted grid resolution. For $k = 0.154$ and $k = 0.180$ only the values of T_{δ_f} show variation when employing grid-A (i.e. simulations) while there is almost no variation when employing grid-B (i.e. $\times 4$ finer grid) as shown in table 5.9. Furthermore J_3 for all three k values is shown to be fluctuating which is due to the first term (C_{m-}) of eqn. 5.8 where all terms are shown in fig. 5.14(a-c) for convenience.

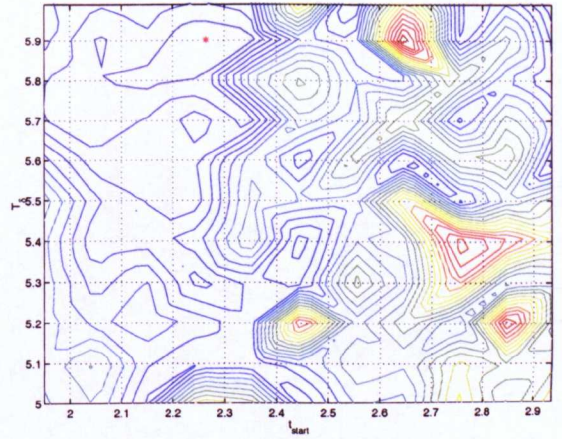
The cost coefficients together with the corresponding controls are listed in table 5.9. As under case I and II, they are further examined in two different grid resolutions of the design space, i.e. grid-A and grid-B. Their values for the two different grids are kept equal to unity initially which delivered the controls t_{start} and T_{δ_f} at the design space boundaries only for $k = 0.128$. Variations of the cost coefficients other than unity the delivered controls were

found to be within the design space away from the boundaries. Their values for the two different grids are kept the same for all three aerofoil reduced frequencies and, as shown in table 5.9, they do not appear to be significantly affected by the grid resolution with exception of T_{δ_r} for $k = 0.154$ and $k = 0.180$ for $c_i = 1$ at grid-A (i.e. simulations).

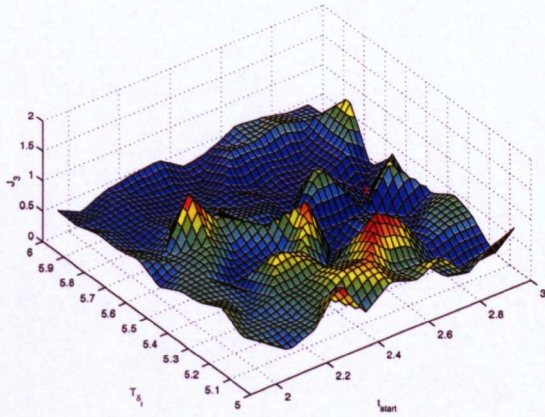
The airloads variation for three different reduced frequencies (i.e. $k = 0.128$, $k = 0.154$ and $k = 0.180$) are shown in fig. 5.15(a-f). The main optimisation target which is reduction of the C_{m-} undershoot is shown to be met for all three reduced frequencies shown, with both sets of cost coefficients shown in table 5.9. Employing the controls as suggested when using weighting coefficients equal to unity seems to deliver slightly more C_m undershoot than $c_i \neq 1$ and better maintenance of lift for the case of $k = 0.128$ as shown in fig. 5.15(a,b) respectively. The opposite with respect to the cost coefficients (i.e. $c_i \neq 1$) is found to be for the case of $k = 0.154$ and $k = 0.180$ shown in fig. 5.15(c,d) and fig. 5.15(e,f) respectively. Regarding the lift maintenance a similar trend is observed as under cases I and II. Exclusion of $C_{n_{max}}$ from J_3 did not seem to affect the obtained airloads shown in fig. 5.15. In addition, the location of the minimum value of J_3 shows strong variation with increasing reduced frequency.



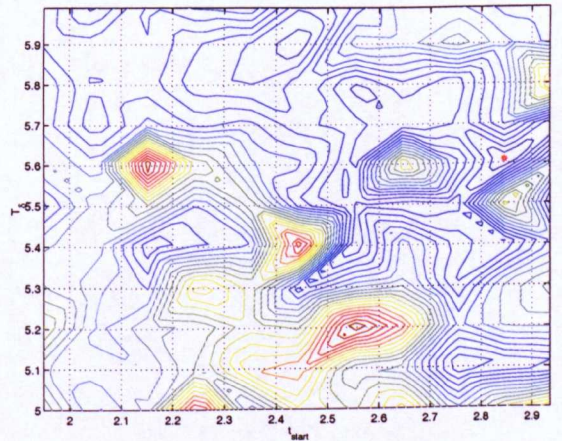
(a) $k=0.128$



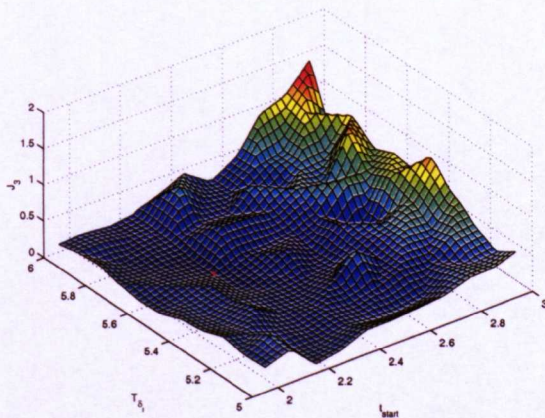
(b) $k=0.128$



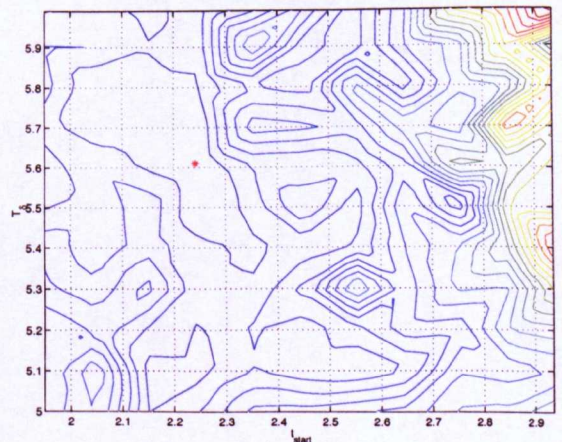
(c) $k=0.154$



(d) $k=0.154$

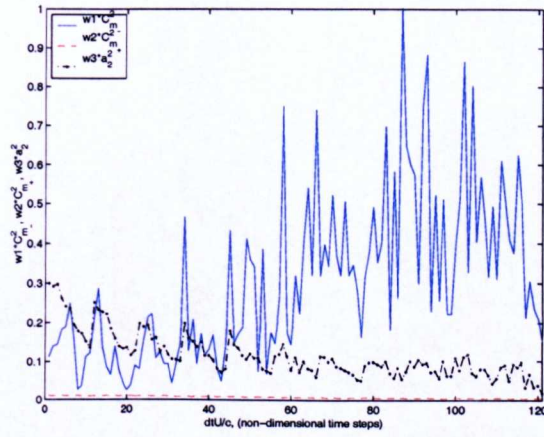


(e) $k=0.180$

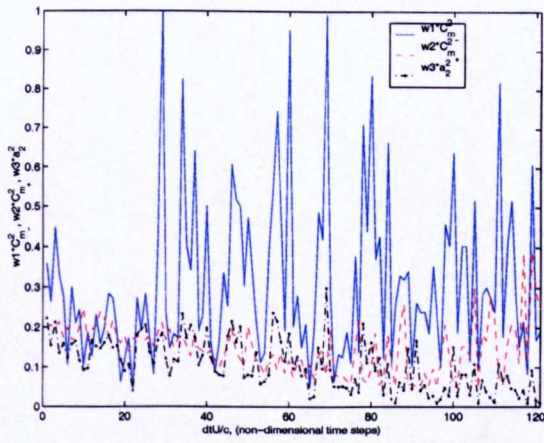


(f) $k=0.180$

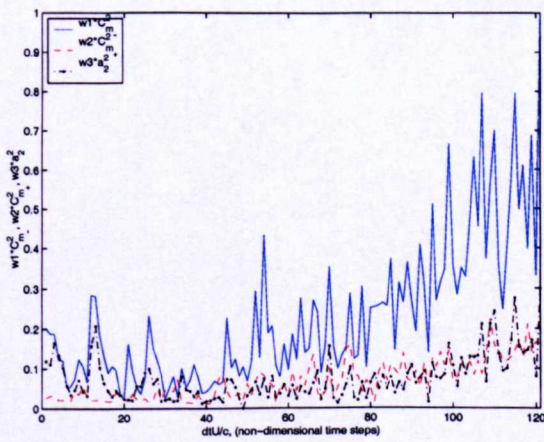
Figure 5.13: Variation of objective function J_3 over the design space.



(a) $k = 0.128$



(b) $k = 0.154$

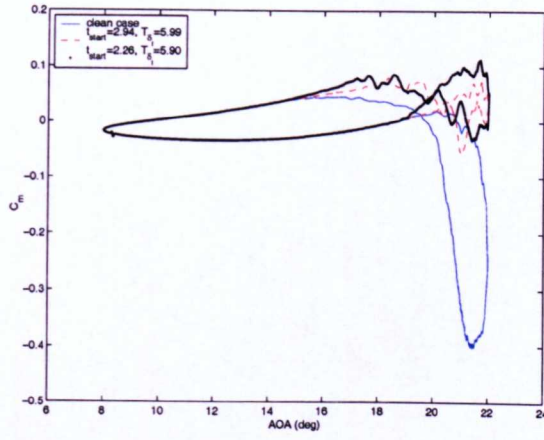


(c) $k = 0.180$

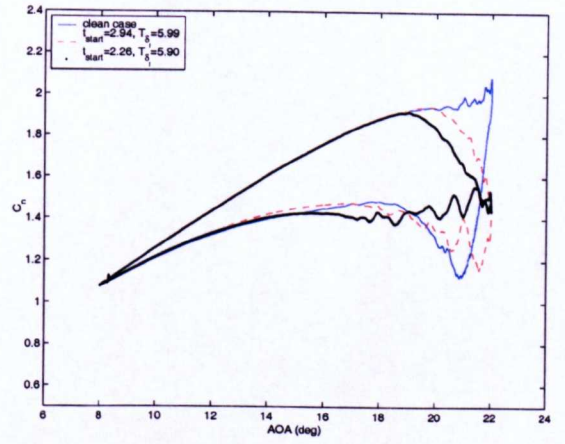
Figure 5.14: Variation of normalised variables for optimisation case III.

case III:					
$k = 0.128$ (grid-A):					
c_1 for C_{m_-} :	c_2 for C_{m_+} :	c_3 for α_2 :	t_{start}	T_{δ_f}	J_{3min}
1	1	1	2.950000	6.000000	0.554337
1	0.01	0.3	2.250000	5.900000	0.126282
$k = 0.128$ (grid-B):					
1	1	1	2.935600	5.990000	0.606868
1	0.01	0.3	2.263600	5.900000	0.129406
$k = 0.154$ (grid-A):					
c_1 for C_{m_-} :	c_2 for C_{m_+} :	c_3 for α_2 :	t_{start}	T_{δ_f}	J_{3min}
1	1	1	2.850000	5.600000	4.790896
1	0.01	0.3	2.850000	5.600000	0.148587
$k = 0.154$ (grid-B):					
1	1	1	2.846000	5.090000	5.162151
1	0.01	0.3	2.846000	5.607500	0.167266
$k = 0.180$ (grid-A):					
c_1 for C_{m_-} :	c_2 for C_{m_+} :	c_3 for α_2 :	t_{start}	T_{δ_f}	J_{3min}
1	1	1	2.250000	5.700000	1.151736
1	0.01	0.3	2.250000	5.600000	0.067406
$k = 0.180$ (grid-B):					
1	1	1	2.241200	5.292500	1.328919
1	0.01	0.3	2.241200	5.607500	0.069361

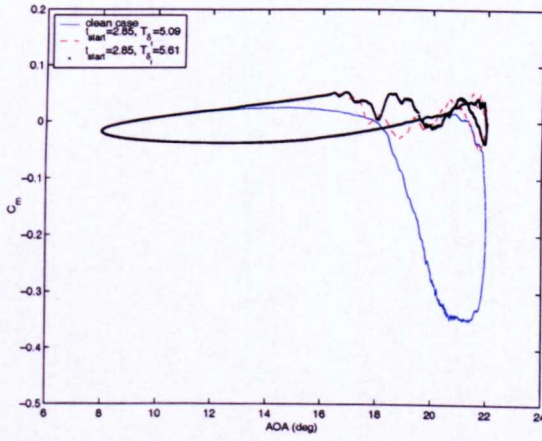
Table 5.9: Summary of weighting coefficients, optimisation parameters and objective function values for optimisation case III.



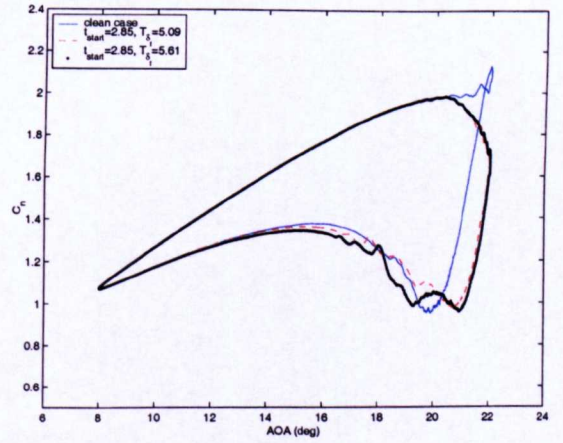
(a) C_m , $k = 0.128$



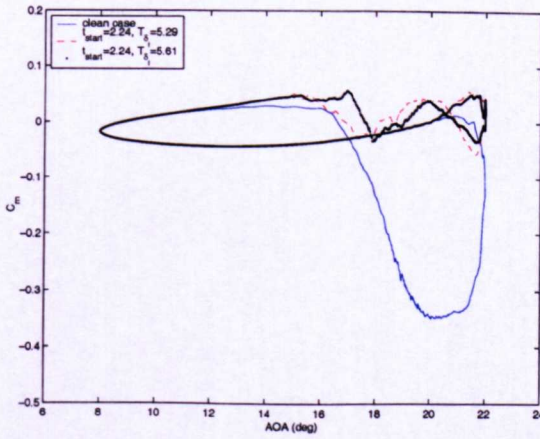
(b) C_n , $k = 0.128$



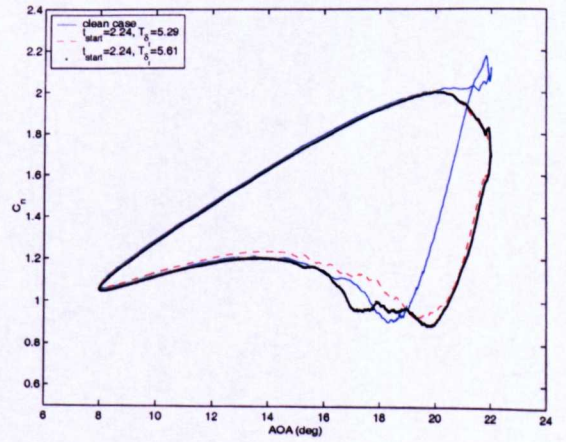
(c) C_m , $k = 0.154$



(d) C_n , $k = 0.154$



(e) C_m , $k = 0.180$



(f) C_n , $k = 0.180$

Figure 5.15: Airloads variation subject to table 5.9.

The t_{start} and T_{δ_f} values shown in table 5.9 are plotted vs aerofoil reduced frequency for both sets of cost coefficients (i.e. $c_i = 1$ and $c_i \neq 1$) and shown in fig. 5.16. Since it is decided to maintain the cost coefficients other than unity, three new k , t_{start} and T_{δ_f} values are extracted, simulated and listed in table 5.10. As under cases I and II, these new reduced frequencies and, finally the modified airloads are presented in fig. 5.21(a-f).

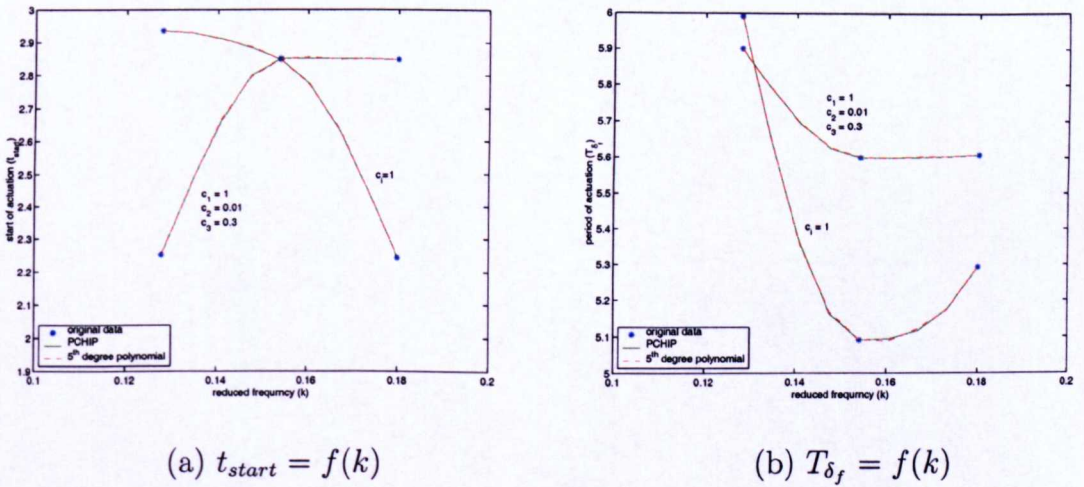


Figure 5.16: Initiation and duration of flap actuation as function of the reduced frequency for optimisation case III.

$k = 0.131$	$k = 0.146$	$k = 0.170$
$t_{start} = 2.35$	$t_{start} = 2.76$	$t_{start} = 2.85$
$T_{\delta_f} = 5.85$	$T_{\delta_f} = 5.64$	$T_{\delta_f} = 5.60$

Table 5.10: Summary of extracted k , t_{start} , and T_{δ_f} values from fig. 5.16(a,b) (optimisation case III).

5.3.4 Optimisation case IV

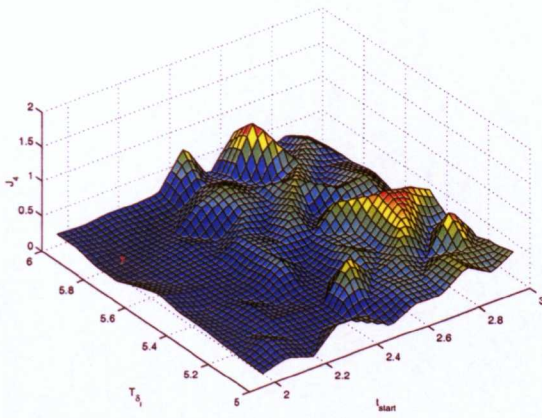
The last optimisation case concerns only the sectional pitching moment undershoot and overshoot, (C_{m-} and C_{m+} respectively), and the objective function is given by,

$$J_4(\mathbf{X})_i = \left[c_1(C_{m-})^2 + c_2(C_{m+})^2 \right]_i \quad . \quad (5.9)$$

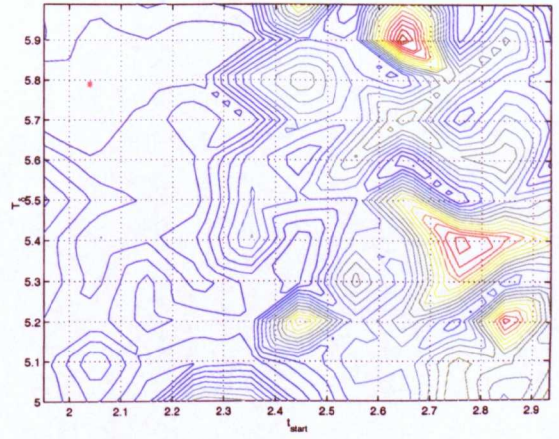
The variation of the objective function J_4 is shown in fig. 5.17(a-f) for $k = 0.128$, $k = 0.154$ and $k = 0.180$. The minimum values $J_{4_{min}}$ for these reduced frequencies are also shown in table 5.11 for two different sets of cost coefficients. The controls t_{start} and T_{δ_f} appear not to be influenced by the grid resolution, however they are slightly affected by employing cost coefficients other than unity as shown in table 5.11.

The airloads variation for three different reduced frequencies (i.e. $k = 0.128$, $k = 0.154$ and $k = 0.180$) are shown in fig. 5.19(a-f). The main optimisation target which is reduction of the C_{m-} undershoot is shown to be met for all three reduced frequencies shown, with both sets of cost coefficients shown in table 5.11. However employing the controls as suggested when employing weighting coefficients equal to unity seems to deliver slightly more C_m undershoot than $c_i \neq 1$ for and better maintenance of lift for the case of $k = 0.128$ as shown in fig. 5.19(a,b) respectively. The same is found to be true for the case of $k = 0.154$ shown in fig. 5.19(c,d). However the controls delivered for $k = 0.180$, are shown to be somewhat fluctuating, (particularly C_{m-}) when

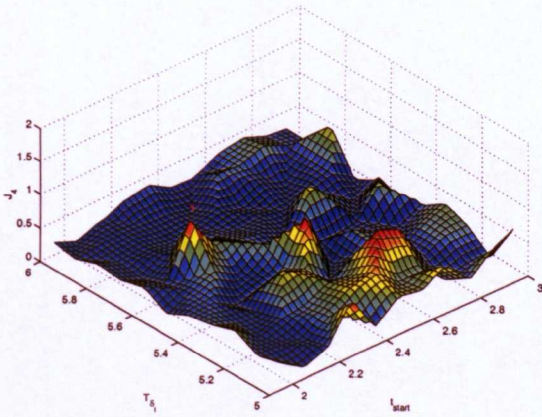
using $c_i \neq 1$. The main reason of the fluctuation in eqn. 5.9 owns to the terms C_{m-} . In addition the fluctuating of J_4 is due to the term C_{m-} as shown in fig. 5.18(a-c) where both terms for all three reduced frequencies are shown for convenience. Regarding the dynamic lift maintenance a similar trend is observed as under cases I, II and III. The location of J_4 global minimum varies significantly compared to J_3 under case III. However it is reasonably close to the global minimum of J_1 and J_2 .



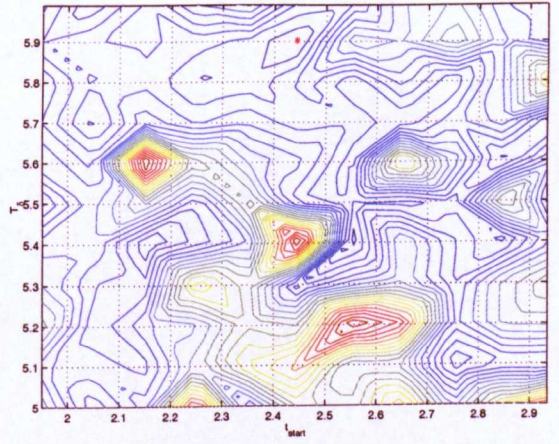
(a) $k=0.128$



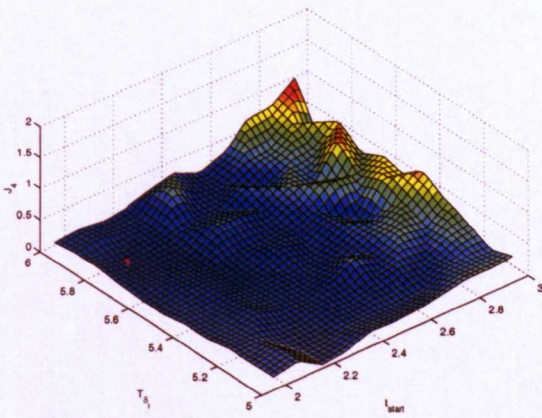
(b) $k=0.128$



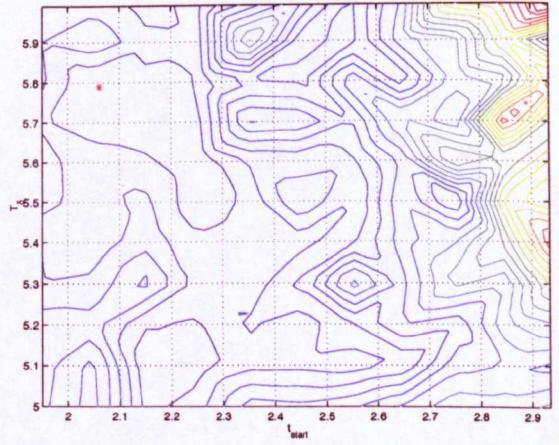
(c) $k=0.154$



(d) $k=0.154$



(e) $k=0.180$



(f) $k=0.180$

Figure 5.17: Variation of objective function J_4 over the design space.

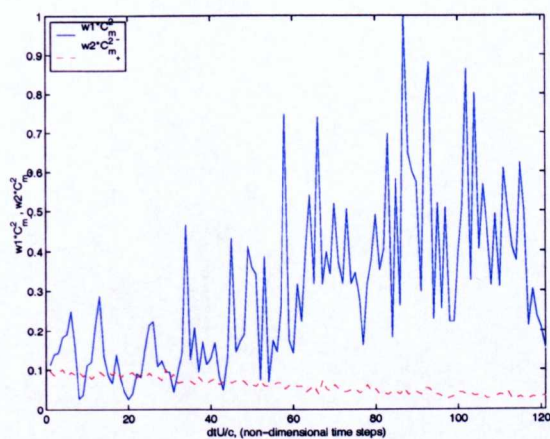
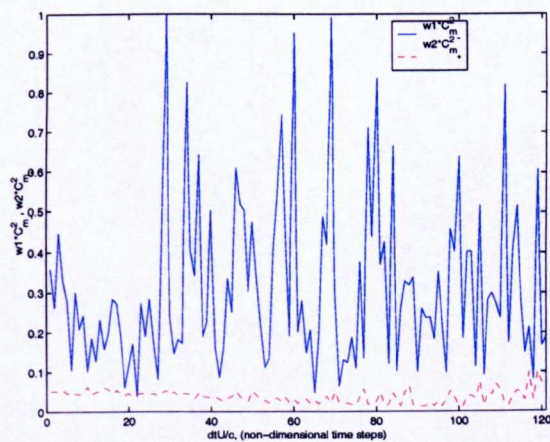
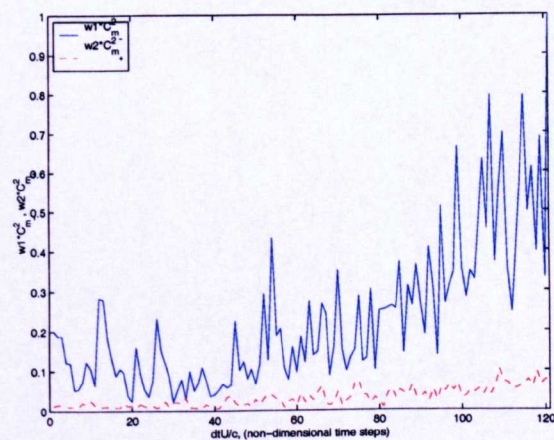
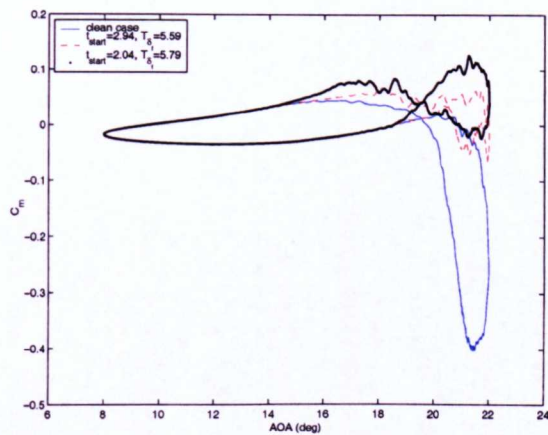
(a) $k = 0.128$ (b) $k = 0.156$ (c) $k = 0.180$

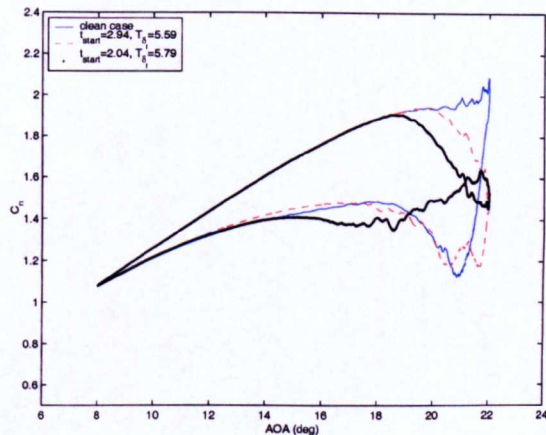
Figure 5.18: Variation of normalised variables for optimisation case IV.

case IV:				
$k = 0.128$ (grid-A):				
c_1 for C_{m_-} :	c_2 for C_{m_+} :	t_{start}	T_{δ_f}	J_{4min}
1	1	2.950000	5.600000	0.455757
1	0.1	2.050000	5.800000	0.111822
$k = 0.128$ (grid-B):				
1	1	2.935600	5.585000	0.500593
1	0.1	2.039600	5.787500	0.112932
$k = 0.154$ (grid-A):				
c_1 for C_{m_-} :	c_2 for C_{m_+} :	t_{start}	T_{δ_f}	J_{4min}
1	1	2.850000	5.600000	0.211877
1	0.1	2.450000	5.900000	0.073328
$k = 0.154$ (grid-B):				
1	1	2.846000	5.607500	0.236038
1	0.1	2.442800	5.900000	0.079112
$k = 0.180$ (grid-A):				
c_1 for C_{m_-} :	c_2 for C_{m_+} :	t_{start}	T_{δ_f}	J_{4min}
1	1	2.250000	5.600000	0.087099
1	0.1	2.050000	5.800000	0.032608
$k = 0.180$ (grid-B):				
1	1	2.241200	5.607500	0.097667
1	0.1	2.062000	5.787500	0.033561

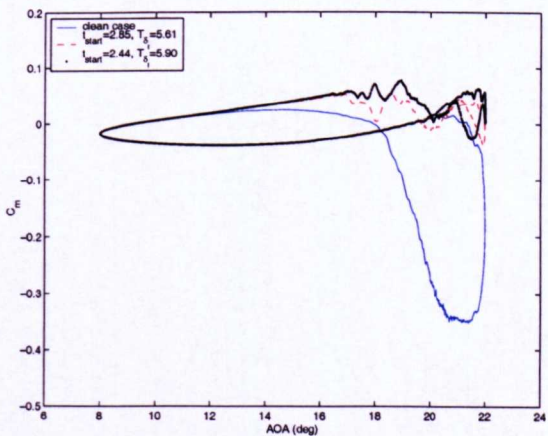
Table 5.11: Summary of weighting coefficients, optimisation parameters and objective function values for optimisation case IV.



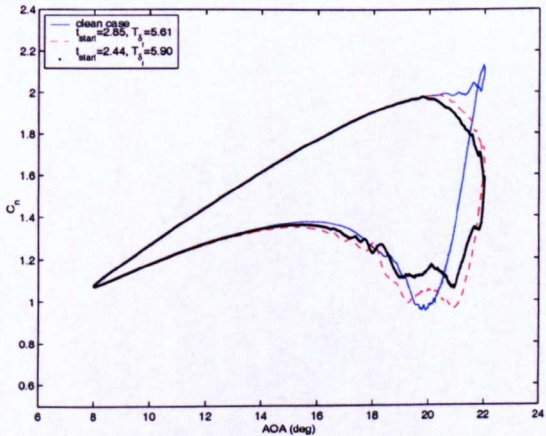
(a) C_m , $k = 0.128$



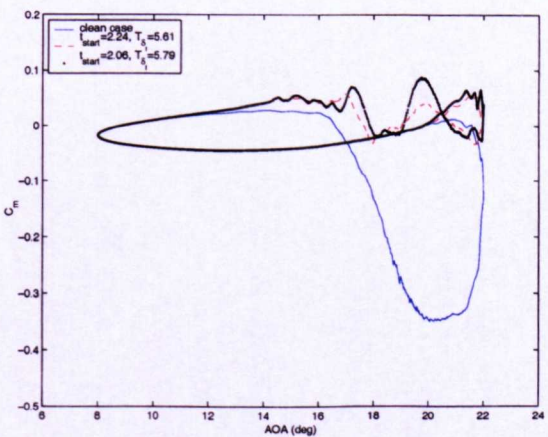
(b) C_n , $k = 0.128$



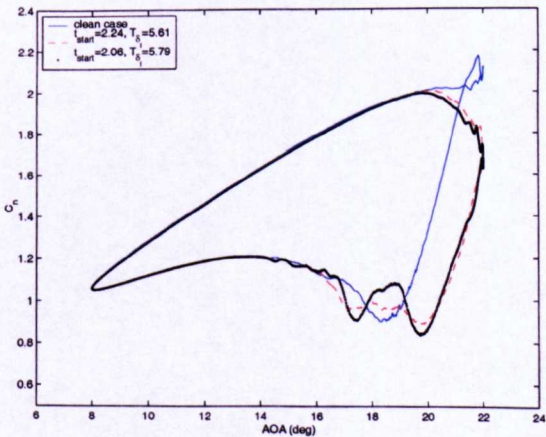
(c) C_m , $k = 0.154$



(d) C_n , $k = 0.154$



(e) C_m , $k = 0.180$



(f) C_n , $k = 0.180$

Figure 5.19: Airloads variation subject to table 5.11.

The controls t_{start} and T_{δ_f} values shown in table 5.11 are plotted vs aerofoil reduced frequency for both sets of cost coefficients (i.e. $c_i = 1$ and $c_i \neq 1$) and shown in fig. 5.20(a,b). For the extraction of the new controls values which are listed in table 5.10 a similar procedure is adopted as in the previous cases.

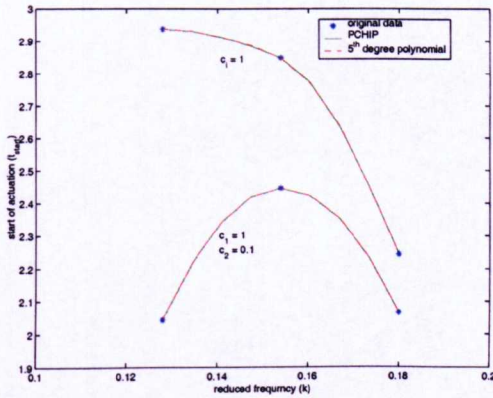
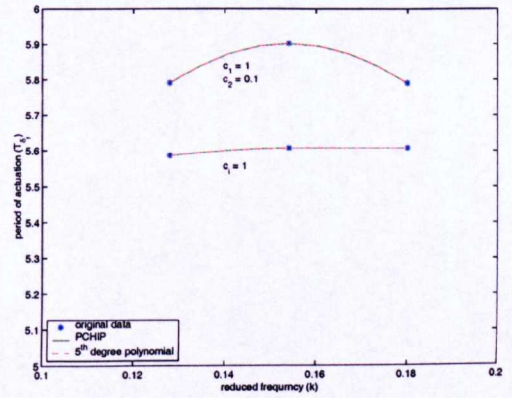
(a) $t_{start} = f(k)$ (b) $T_{\delta_f} = f(k)$

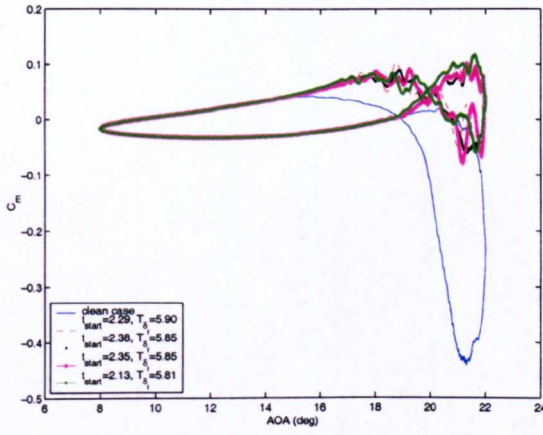
Figure 5.20: Initiation and duration of flap actuation as function of the reduced frequency for optimisation case IV.

$k = 0.131$	$k = 0.146$	$k = 0.170$
$t_{start} = 2.13$	$t_{start} = 2.40$	$t_{start} = 2.29$
$T_{\delta_f} = 5.81$	$T_{\delta_f} = 5.89$	$T_{\delta_f} = 5.86$

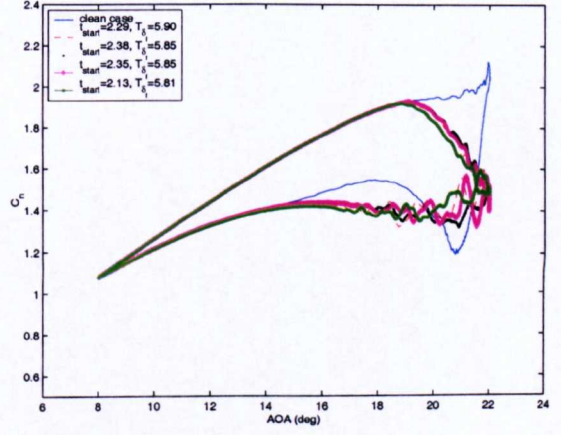
Table 5.12: Summary of extracted k , t_{start} , and T_{δ_f} values from fig. 5.20(a,b) (optimisation case IV).

After all four optimisation cases are examined, all the new extracted k , t_{start} ,

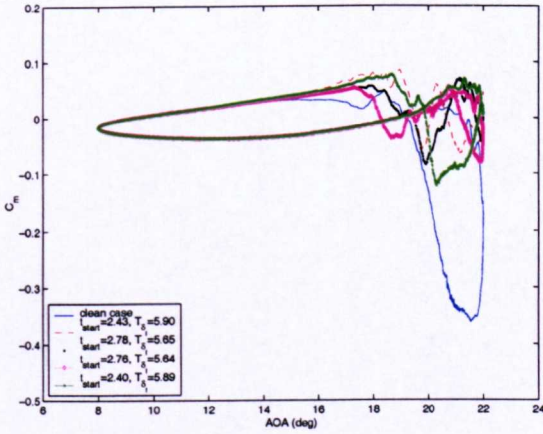
and T_{δ_f} values shown in tables 5.6, 5.8, 5.10, 5.12 are simulated in order to assess the newly obtained controls and the validity of all four objective functions. The new airloads are presented in fig. 5.21(a-f). The pitching moment undershoot is significantly reduced for all three extracted reduced frequencies whereas the dynamic lift is not maintained. However the latter shows improvement with increasing reduced frequency.



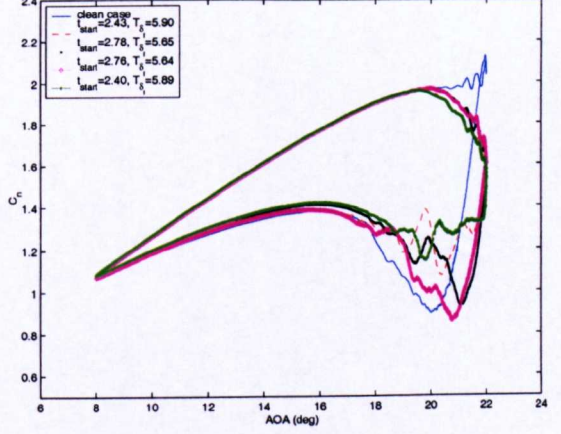
(a) C_m , $k = 0.131$



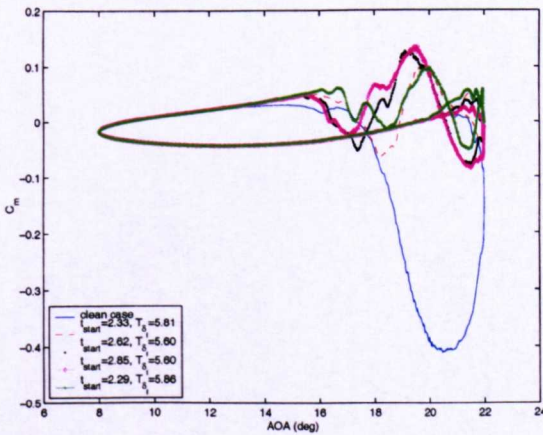
(b) C_n , $k = 0.131$



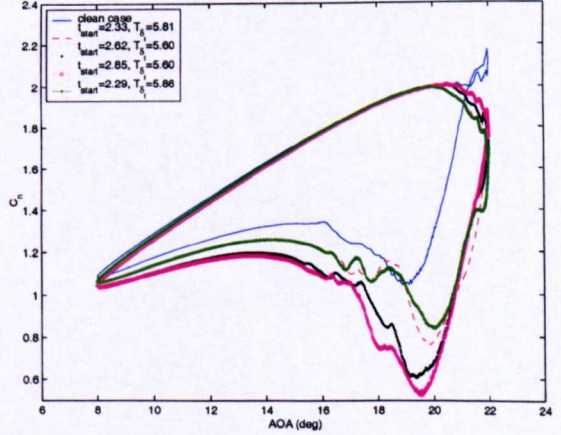
(c) C_m , $k = 0.146$



(d) C_n , $k = 0.146$



(e) C_m , $k = 0.170$



(f) C_n , $k = 0.170$

Figure 5.21: Airloads variation from extracted t_{start}, T_{δ_f} and k values from fig. 5.8(a,b), fig. 5.12(a,b), fig. 5.16(a,b) and fig. 5.8(a,b).

5.4 Grid resolution for the period of actuation.

Grid refinement is also applied with respect to the inclusion of values regarding the period of the entire actuation. Compared to grid-A, two coarser grids, labelled as grid-1 and grid-2 and shown in fig. 5.4(a,b) respectively, are applied in order to examine how the controls and the corresponding airloads are affected. The cost coefficients are maintained the same as in tables 5.5, 5.7, 5.9 and 5.11.

For the *optimisation case I*, the controls appear to be the same for grid-1 and show very little variation for grid-2 when the cost coefficients are equal to unity when $k = 0.128$ (see tables 5.5, 5.13). Adopting the appropriate cost coefficients (i.e. $c_i \neq 1$) affects the t_{start} and T_{δ_f} for grid-1 while for grid-2 the variation seems to be negligible. When $k = 0.154$, grid-1 produces controls with significant variation compared to those in table 5.5, for both sets of cost coefficients with exception of those in grid-2. For the reduced frequency of $k = 0.180$, the employed grid resolution delivered different controls for both grids with exception of t_{start} in grid-2 as shown in tables 5.5, 5.13. The airloads with respect to grid-1 and grid-2 are shown in fig. 5.24(a-f). The pitching moment undershoot is significantly reduced for all three reduced frequencies for both grids. The same is found for the pitching moment overshoot which is maintains fairly low levels as required for a successful flap

actuation. The exception to this is the pitching moment loop for grid-B at $k = 0.180$ which is shown to have some amount of overshoot, as shown in fig. 5.13(e). The dynamic lift is generally not maintained and shows an increment with reduced frequency.

Regarding *optimisation case II*, the grid resolution for $k = 0.128$ only the controls for grid-1 (when $c_i \neq 1$) appear to be affected after comparison of tables 5.7, 5.14. A similar situation is observed for grid-1 when $k = 0.154$ and $k = 0.180$. The airloads for both grid-A and grid-B are shown in fig. 5.27(a-f). A similar trend is observed for the pitching moment and the normal force as under case I.

The grid resolution for *optimisation case III* produced different controls for grid-1 at $k = 0.128$ when $c_i \neq 1$) as shown in tables 5.9, 5.15. When $k = 0.154$ only the T_{δ_f} value for grid-2 seems to be affected whereas for $k = 0.180$ the T_{δ_f} values for both grid-1 and grid-2 appear in table 5.15 show variation from their counter parts displayed in table 5.9. The airloads shown in fig. 5.30(a,b) and are displayed only for $k = 0.128$. For $k = 0.154$ and $k = 0.180$ they are identical to the airloads displayed in fig. 5.15(c,d) and 5.15(e,f) respectively.

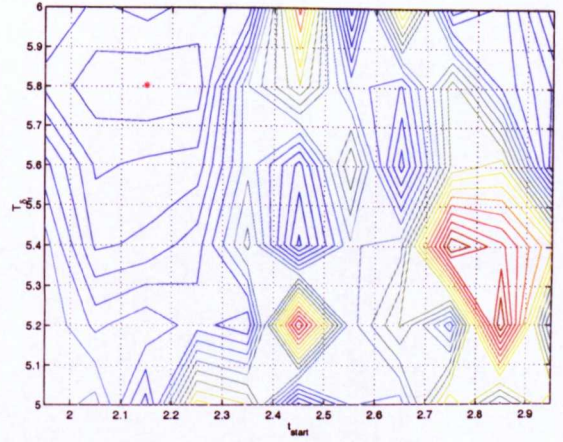
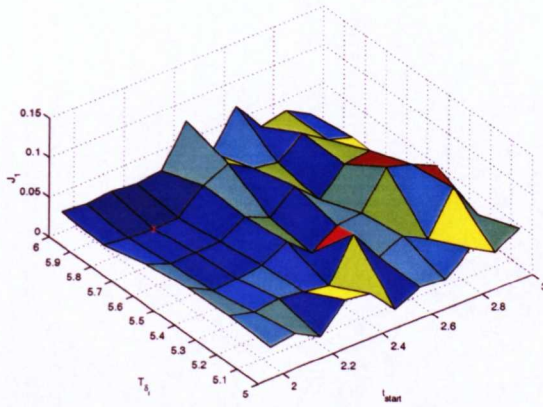
Examination of *optimisation case IV* with respect to the grid resolution revealed that for grid-2 ($c_i \neq 1$) when $k = 0.128$ and $k = 0.180$, the delivered controls illustrated in table 5.16 vary from their counterparts displayed in table 5.11. When $k = 0.154$ and $c_i \neq 1$ only the controls for grid-1 vary

**5.4. GRID RESOLUTION FOR THE PERIOD OF
ACTUATION.**

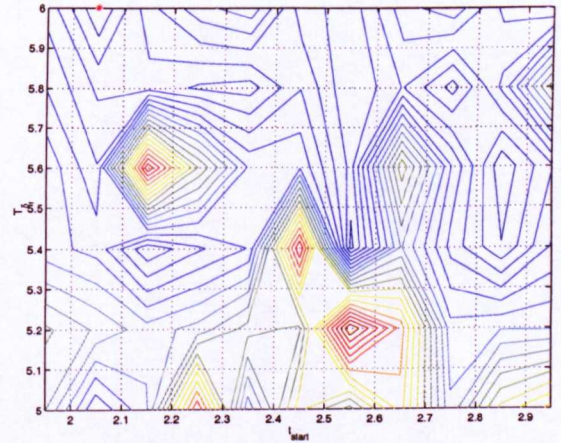
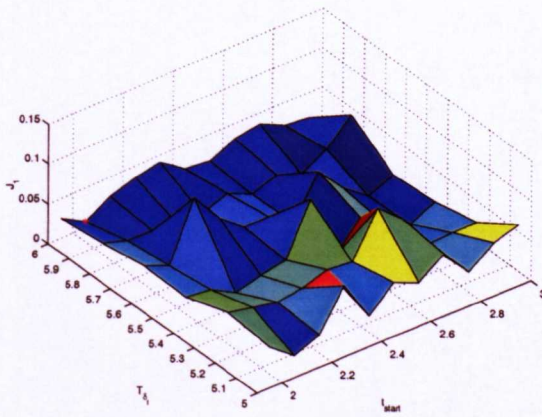
200

from their counterparts in table 5.11. The airloads show a similar trend as in the previous cases.

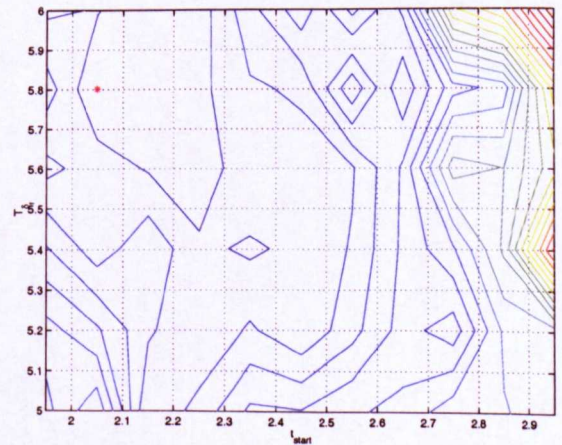
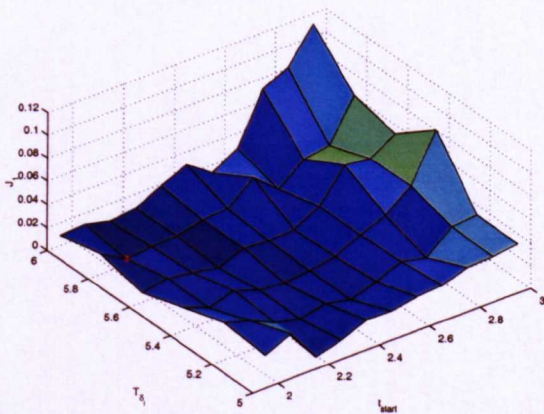
5.4. GRID RESOLUTION FOR THE PERIOD OF ACTUATION.



$$k = 0.128, \quad c_1 = 0.08, \quad c_2 = 0.001, \quad c_3 = 0.03$$

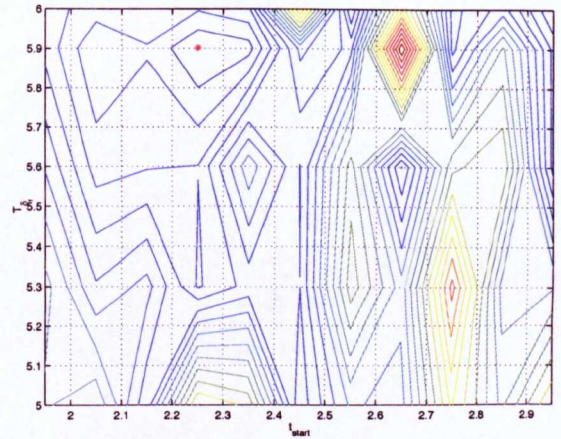
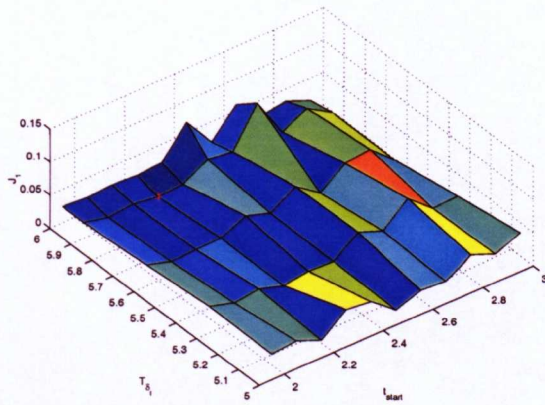


$$k = 0.154, \quad c_1 = 0.08, \quad c_2 = 0.001, \quad c_3 = 0.03$$

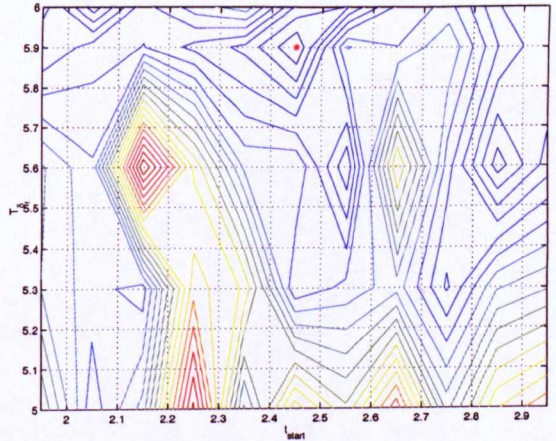
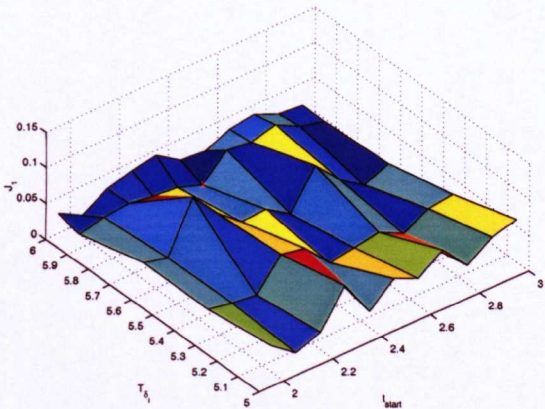


$$k = 0.180, \quad c_1 = 0.08, \quad c_2 = 0.001, \quad c_3 = 0.03$$

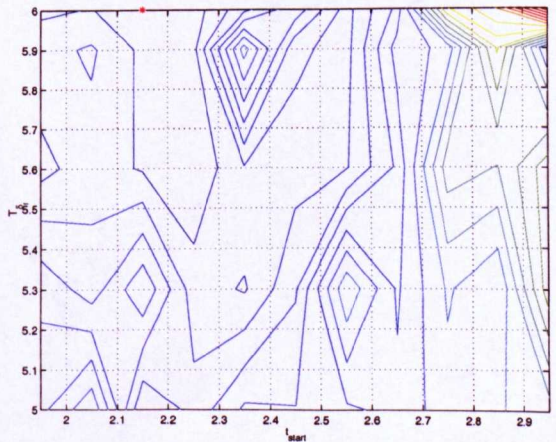
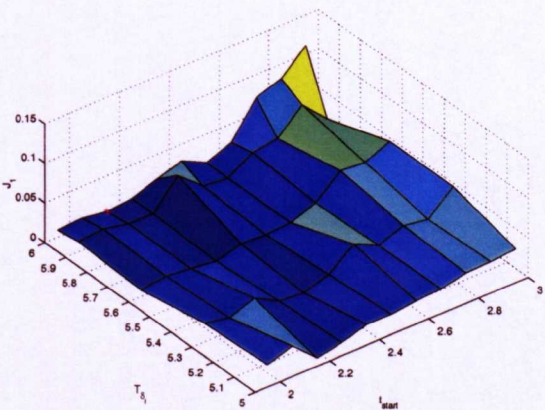
Figure 5.22: Variation of objective function J_1 over the design space described by grid-1.



$$k = 0.128, c_1 = 0.08, c_2 = 0.001, c_3 = 0.03$$



$$k = 0.154, c_1 = 0.08, c_2 = 0.001, c_3 = 0.03$$



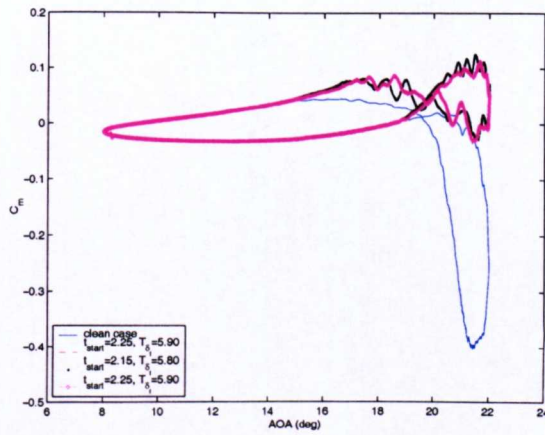
$$k = 0.180, c_1 = 0.08, c_2 = 0.001, c_3 = 0.03$$

Figure 5.23: Variation of objective function J_1 over the design space described by grid-2.

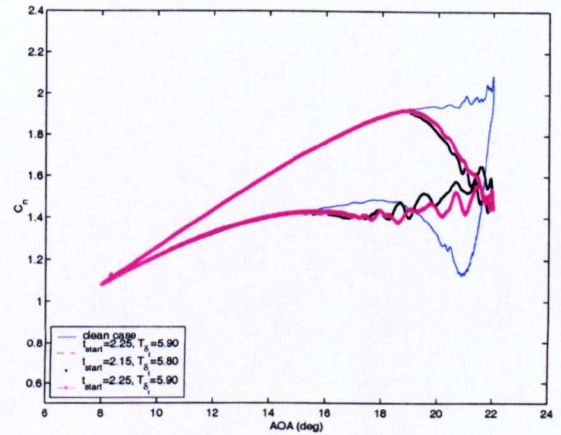
case I:					
$k = 0.128$, (grid-1):					
c_1 for C_{m_-} :	c_2 for $C_{n_{max}}$:	c_3 for α_2 :	t_{start}	T_{δ_f}	$J_{1_{min}}$
1	1	1	2.950000	6.000000	1.242698
0.08	0.001	0.03	2.150000	5.800000	0.015434
$k = 0.128$, (grid-2):					
1	1	1	2.950000	6.000000	1.221894
0.08	0.001	0.03	2.250000	5.900000	0.012030
$k = 0.154$, (grid-1):					
c_1 for C_{m_-} :	c_2 for $C_{n_{max}}$:	c_3 for α_2 :	t_{start}	T_{δ_f}	$J_{1_{min}}$
1	1	1	2.850000	5.600000	1.131620
0.08	0.001	0.03	2.050000	6.000000	0.007938
$k = 0.154$, (grid-2):					
1	1	1	2.850000	5.600000	1.186177
0.08	0.001	0.03	2.450000	5.900000	0.007370
$k = 0.180$, (grid-1):					
c_1 for C_{m_-} :	c_2 for $C_{n_{max}}$:	c_3 for α_2 :	t_{start}	T_{δ_f}	$J_{1_{min}}$
1	1	1	2.350000	5.400000	1.116008
0.08	0.001	0.03	2.050000	5.800000	0.005065
$k = 0.180$, (grid-2):					
1	1	1	2.150000	6.000000	1.116211
0.08	0.001	0.03	2.150000	6.000000	0.005108

Table 5.13: Summary of weighting coefficients, optimisation parameters, design space variables and objective function values for T_{δ_f} , grid resolution (optimisation case I).

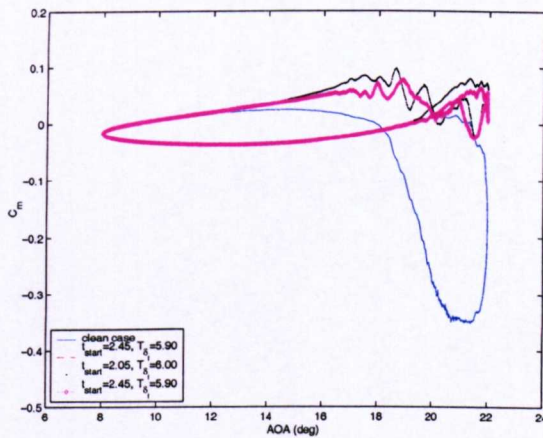
5.4. GRID RESOLUTION FOR THE PERIOD OF ACTUATION.



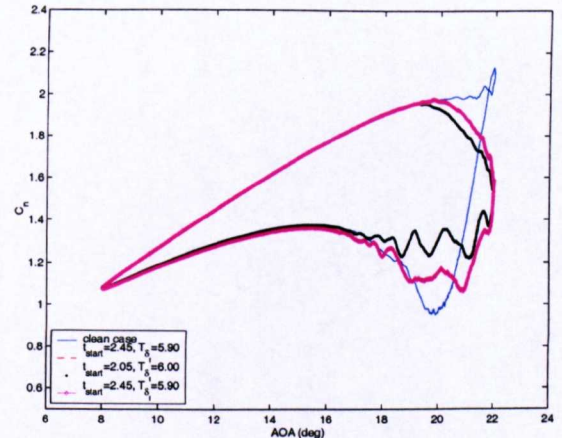
(a) C_m , $k = 0.128$



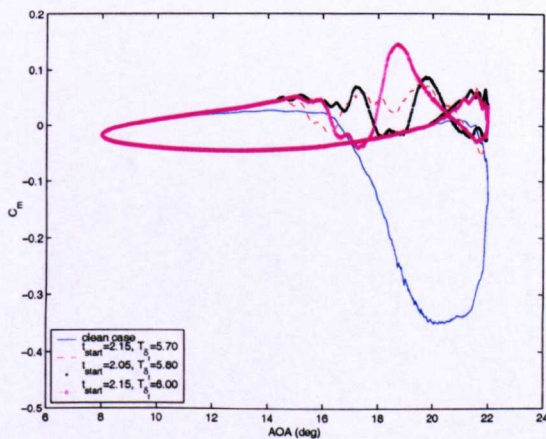
(b) C_n , $k = 0.128$



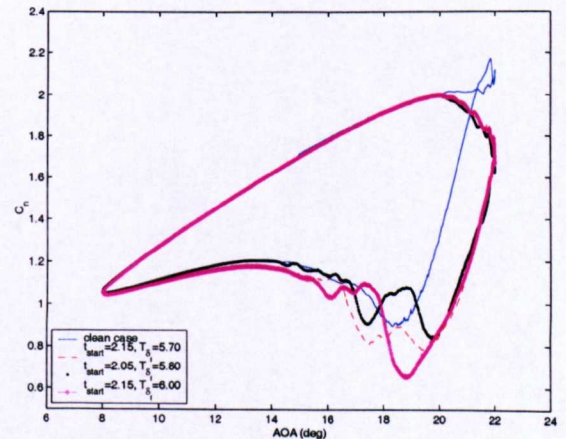
(c) C_m , $k = 0.154$



(d) C_n , $k = 0.154$

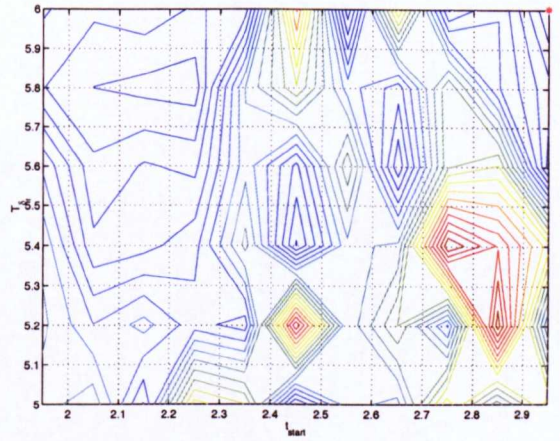
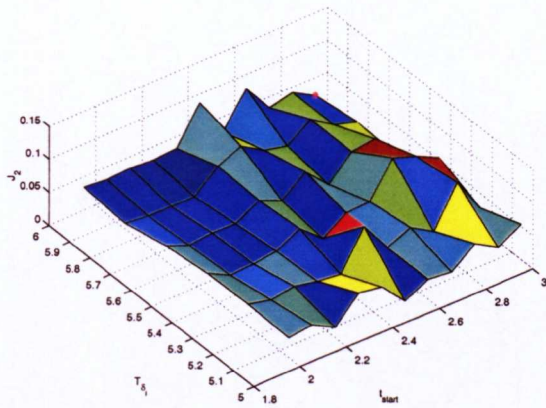


(e) C_m , $k = 0.180$

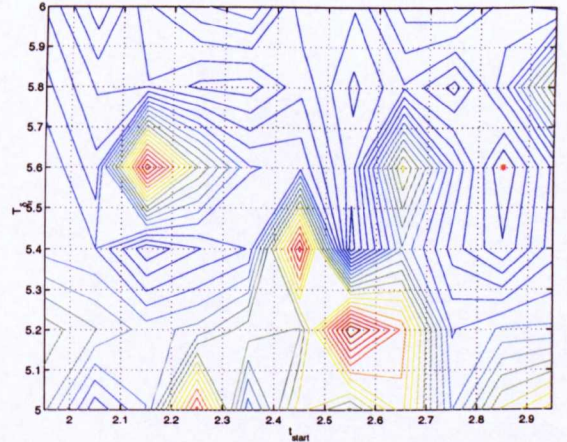
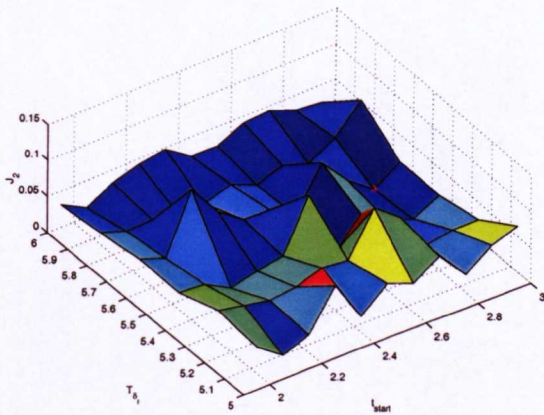


(f) C_n , $k = 0.180$

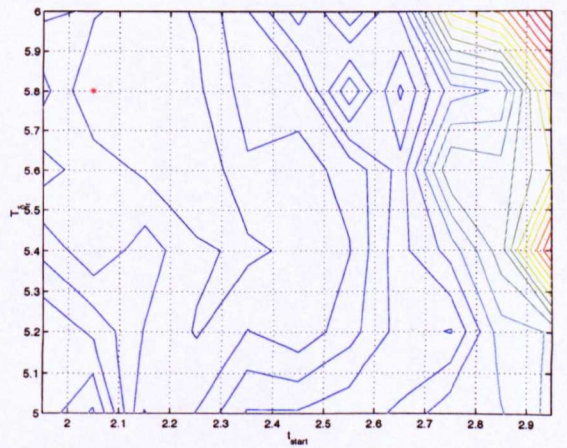
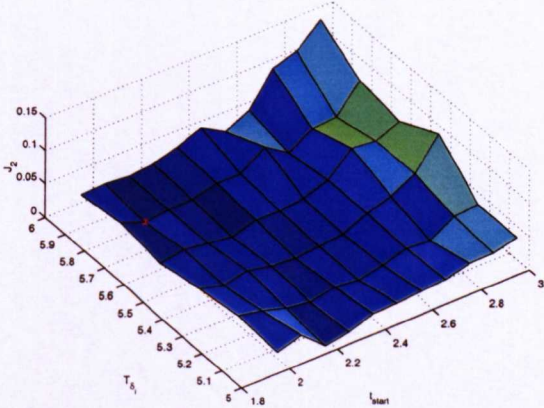
Figure 5.24: Airloads variation subject to the grid resolution displayed in table 5.13.



$$k = 0.128, c_1 = 0.09, c_2 = 0.01, c_3 = 0.001, c_4 = 0.03$$



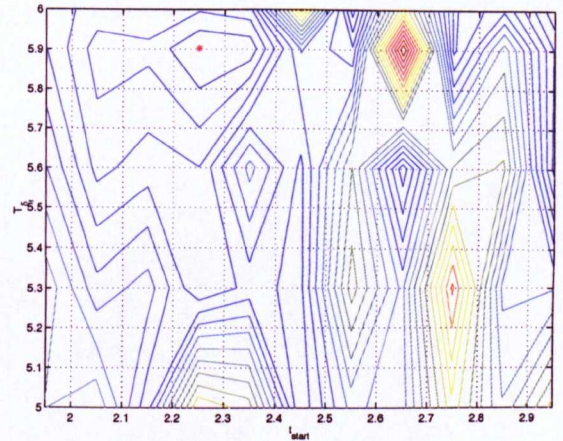
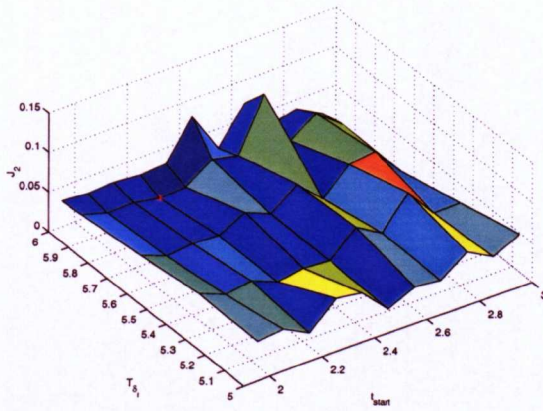
$$k = 0.154, c_1 = 0.09, c_2 = 0.01, c_3 = 0.001, c_4 = 0.03$$



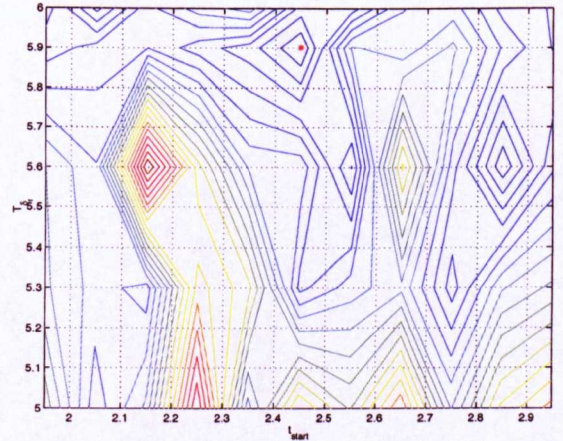
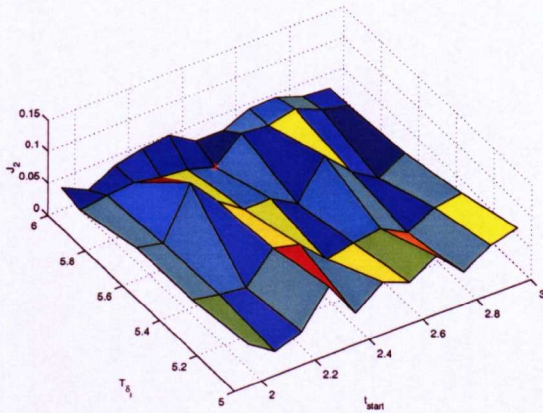
$$k = 0.180, c_1 = 0.09, c_2 = 0.01, c_3 = 0.001, c_4 = 0.03$$

Figure 5.25: Variation of objective function J_2 over the design space described by grid-1.

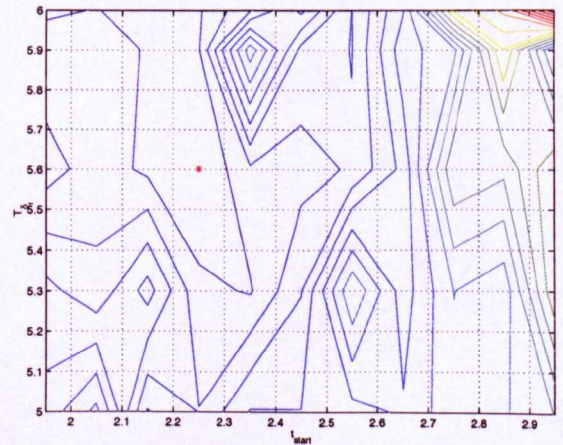
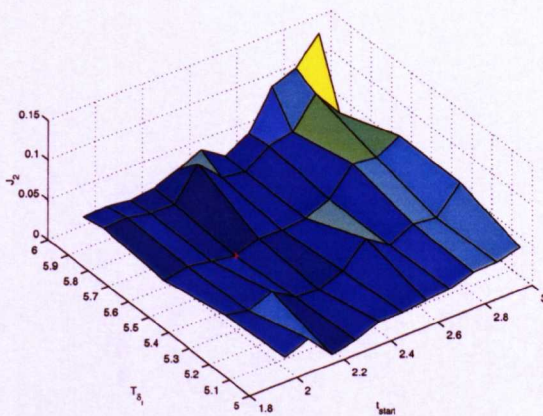
5.4. GRID RESOLUTION FOR THE PERIOD OF ACTUATION.



$$k = 0.128, c_1 = 0.09, c_2 = 0.01, c_3 = 0.001, c_4 = 0.03$$



$$k = 0.154, c_1 = 0.09, c_2 = 0.01, c_3 = 0.001, c_4 = 0.03$$

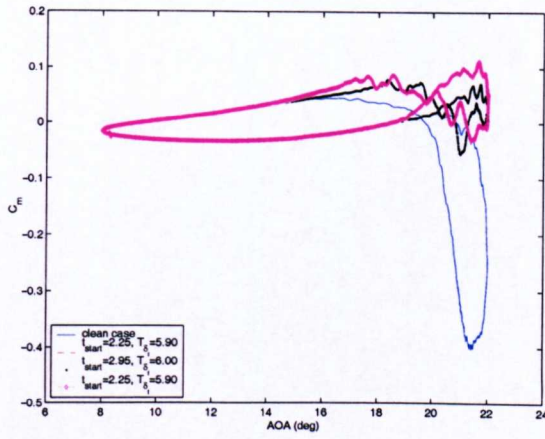


$$k = 0.180, c_1 = 0.09, c_2 = 0.01, c_3 = 0.001, c_4 = 0.03$$

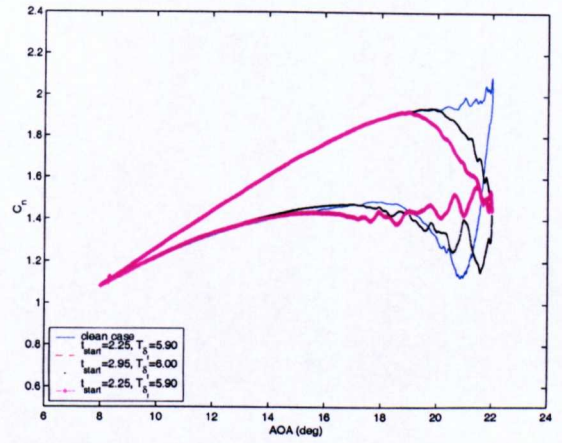
Figure 5.26: Variation of objective function J_2 over the design space described by grid-2.

case II:						
$k = 0.128$: (grid-1)						
c_1 for C_{m-} :	c_2 for C_{m+} :	c_3 for $C_{n_{max}}$:	c_4 for α_2 :	t_{start}	T_{δ_f}	J_{2min}
1	1	1	1	2.950000	6.000000	0.021933
0.09	0.01	0.001	0.03	2.950000	6.000000	1.570074
$k = 0.128$: (grid-2)						
1	1	1	1	2.950000	6.000000	1.547763
0.09	0.01	0.001	0.03	2.250000	5.900000	0.019333
$k = 0.154$: (grid-1)						
c_1 for C_{m-} :	c_2 for C_{m+} :	c_3 for $C_{n_{max}}$:	c_4 for α_2 :	t_{start}	T_{δ_f}	J_{2min}
1	1	1	1	2.850000	5.600000	1.235471
0.09	0.01	0.001	0.03	2.850000	5.600000	0.011452
$k = 0.154$: (grid-2)						
1	1	1	1	2.850000	5.600000	1.202313
0.09	0.01	0.001	0.03	2.450000	5.900000	0.010471
$k = 0.180$: (grid-1)						
c_1 for C_{m-} :	c_2 for C_{m+} :	c_3 for $C_{n_{max}}$:	c_4 for α_2 :	t_{start}	T_{δ_f}	J_{2min}
1	1	1	1	2.250000	5.600000	1.145370
0.09	0.01	0.001	0.03	2.050000	5.800000	0.006870
$k = 0.180$: (grid-2)						
1	1	1	1	2.250000	5.600000	1.125140
0.09	0.01	0.001	0.03	2.250000	5.600000	0.006748

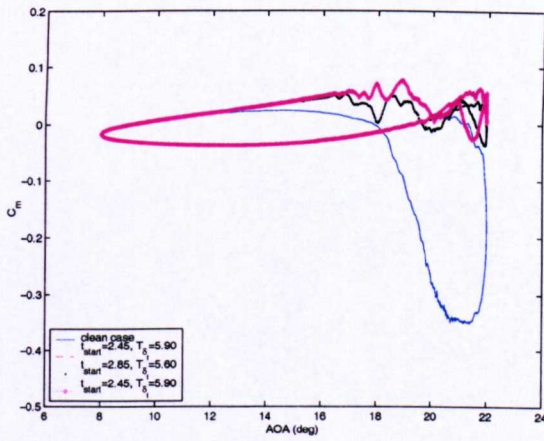
Table 5.14: Summary of weighting coefficients, optimisation parameters, design space variables and objective function values for T_{δ_f} grid resolution (optimisation case II).



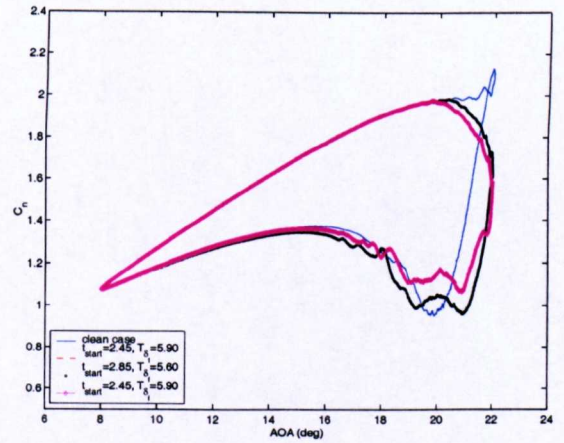
(a) C_m , $k = 0.128$



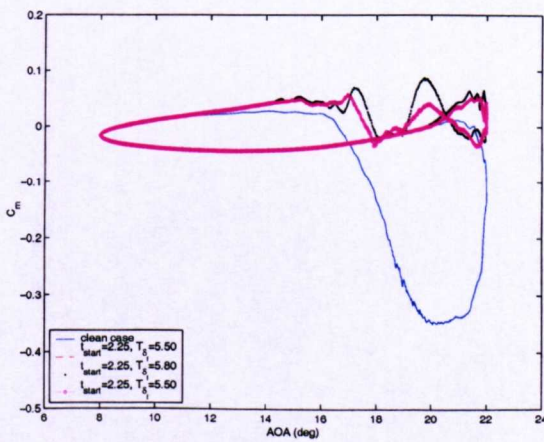
(b) C_n , $k = 0.128$



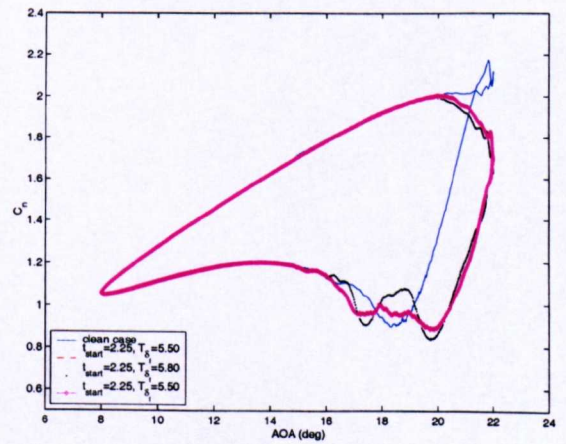
(c) C_m , $k = 0.154$



(d) C_n , $k = 0.154$

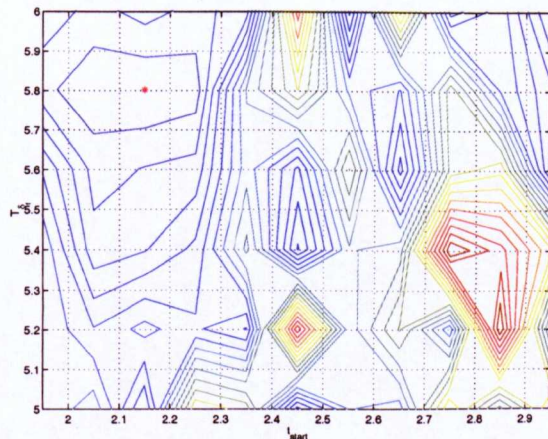
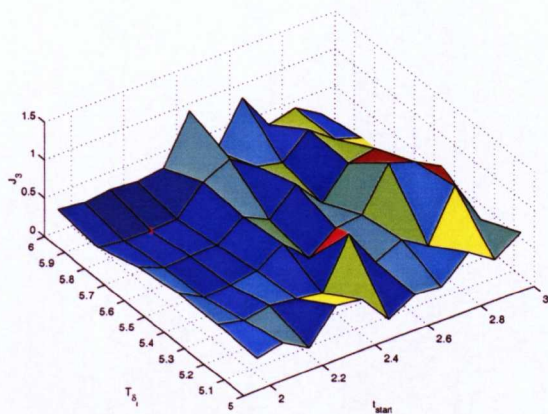


(e) C_m , $k = 0.180$

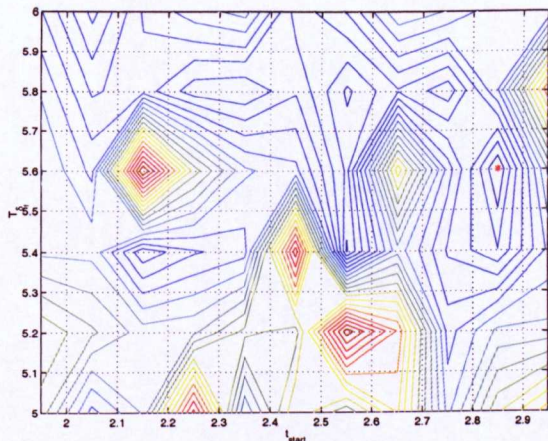
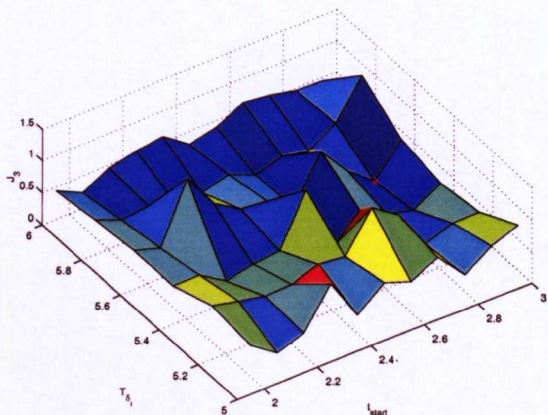


(f) C_n , $k = 0.180$

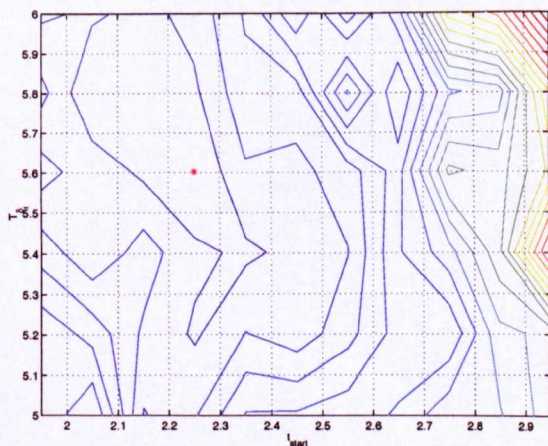
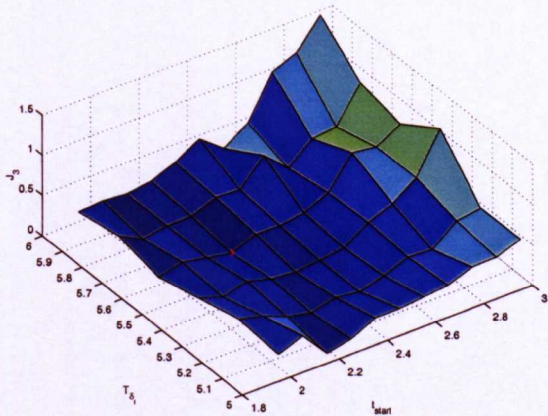
Figure 5.27: Airloads variation subject to the grid resolution displayed in table 5.14.



$$k = 0.128, \quad c_1 = 1, \quad c_2 = 0.01, \quad c_3 = 0.3$$



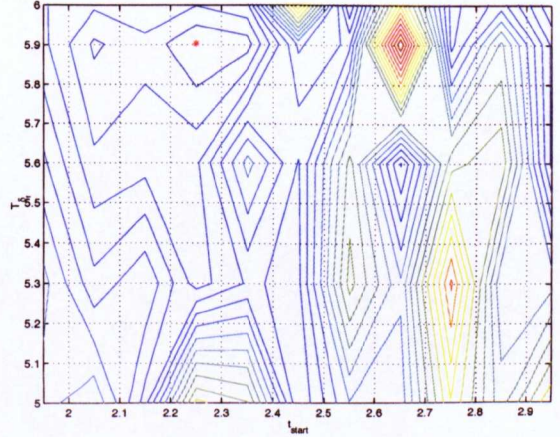
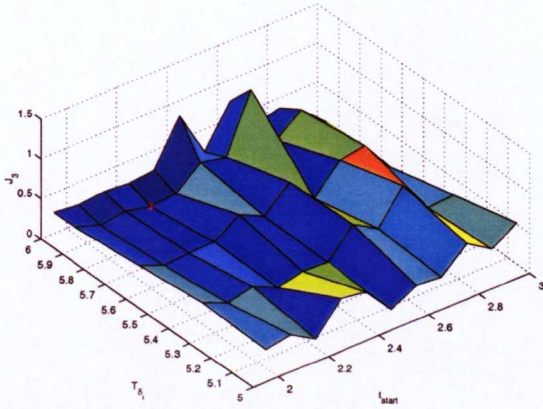
$$k = 0.154, \quad c_1 = 1, \quad c_2 = 0.01, \quad c_3 = 0.3$$



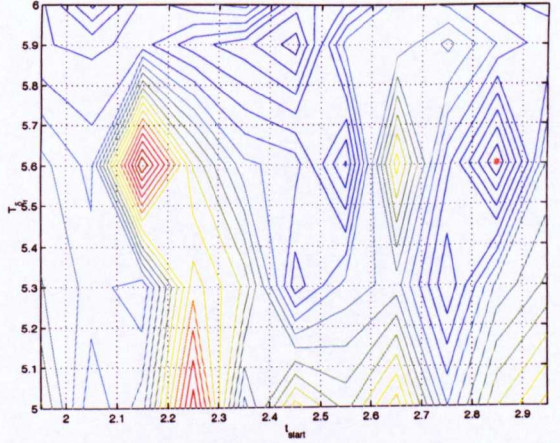
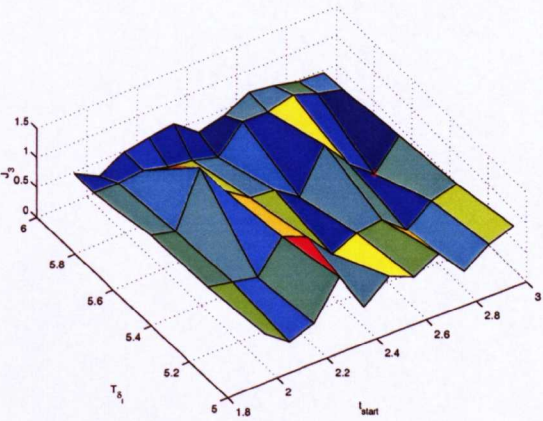
$$k = 0.180, \quad c_1 = 1, \quad c_2 = 0.01, \quad c_3 = 0.3$$

Figure 5.28: Variation of objective function J_3 over the design space described by grid-1.

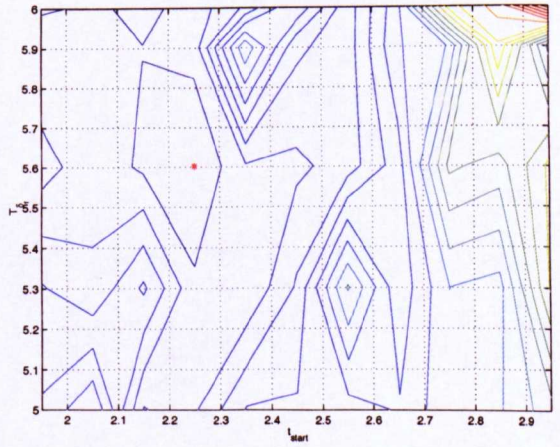
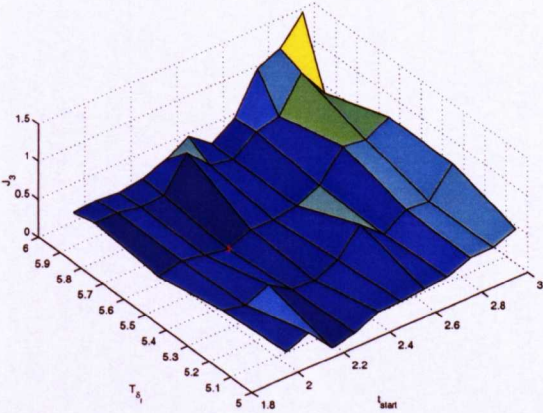
5.4. GRID RESOLUTION FOR THE PERIOD OF ACTUATION.



$$k = 0.128, c_1 = 1, c_2 = 0.01, c_3 = 0.3$$



$$k = 0.154, c_1 = 1, c_2 = 0.01, c_3 = 0.3$$

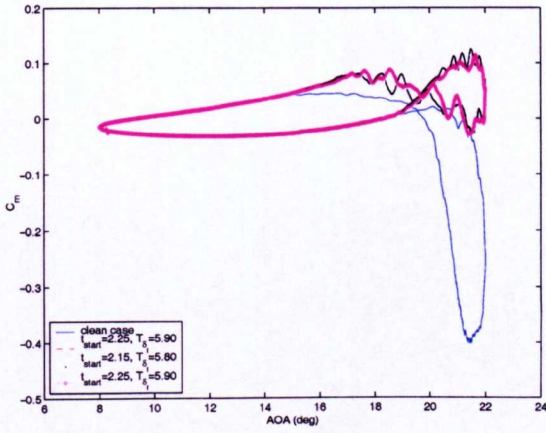


$$k = 0.180, c_1 = 1, c_2 = 0.01, c_3 = 0.3$$

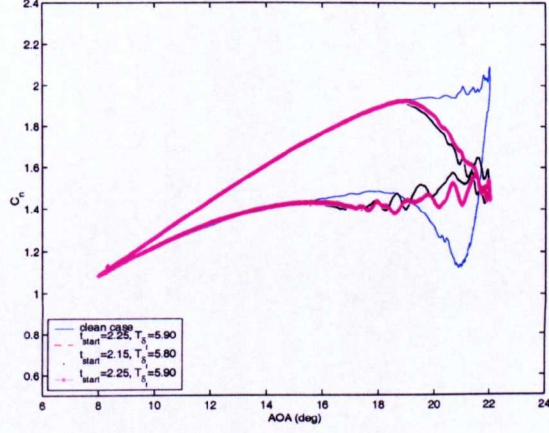
Figure 5.29: Variation of objective function J_3 over the design space described by grid-2.

case III:					
$k = 0.128$ (grid-1):					
c_1 for C_{m_-} :	c_2 for C_{m_+} :	c_3 for α_2 :	t_{start}	T_{δ_f}	J_{3min}
1	1	1	2.950000	6.000000	0.576647
1	0.01	0.3	2.150000	5.800000	0.162240
$k = 0.128$ (grid-2):					
1	1	1	2.950000	6.000000	0.554337
1	0.01	0.3	2.250000	5.900000	0.126282
$k = 0.154$ (grid-1):					
c_1 for C_{m_-} :	c_2 for C_{m_+} :	c_3 for α_2 :	t_{start}	T_{δ_f}	J_{3min}
1	1	1	2.850000	5.600000	4.790896
1	0.01	0.3	2.850000	5.600000	0.148587
$k = 0.154$ (grid-2):					
1	1	1	2.850000	5.600000	4.799265
1	0.01	0.3	2.850000	5.600000	0.151098
$k = 0.180$ (grid-1):					
c_1 for C_{m_-} :	c_2 for C_{m_+} :	c_3 for α_2 :	t_{start}	T_{δ_f}	J_{3min}
1	1	1	2.250000	5.600000	1.098253
1	0.01	0.3	2.250000	5.600000	0.066779
$k = 0.180$ (grid-2):					
1	1	1	2.250000	5.600000	1.160911
1	0.01	0.3	2.250000	5.600000	0.067406

Table 5.15: Summary of weighting coefficients, optimisation parameters, design space variables and objective function values for T_{δ_f} grid resolution (optimisation case III).



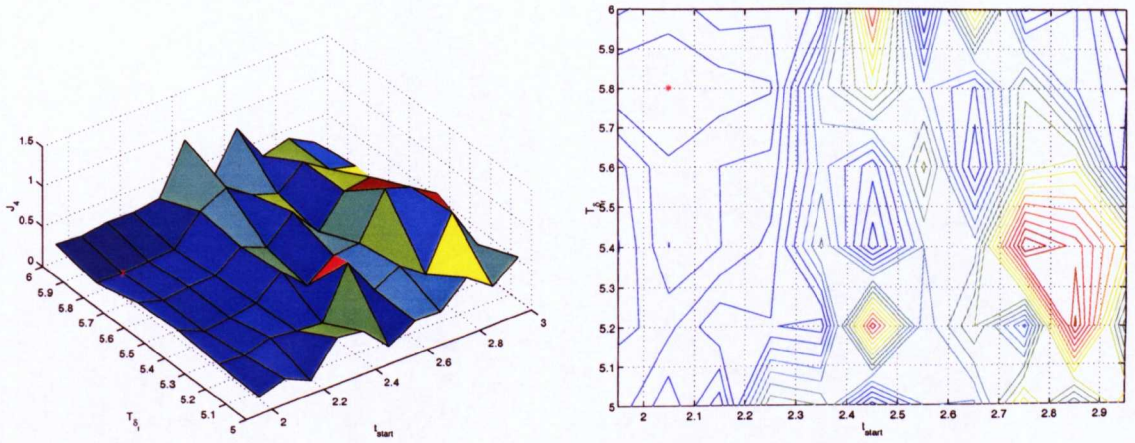
(a) C_m , $k = 0.128$



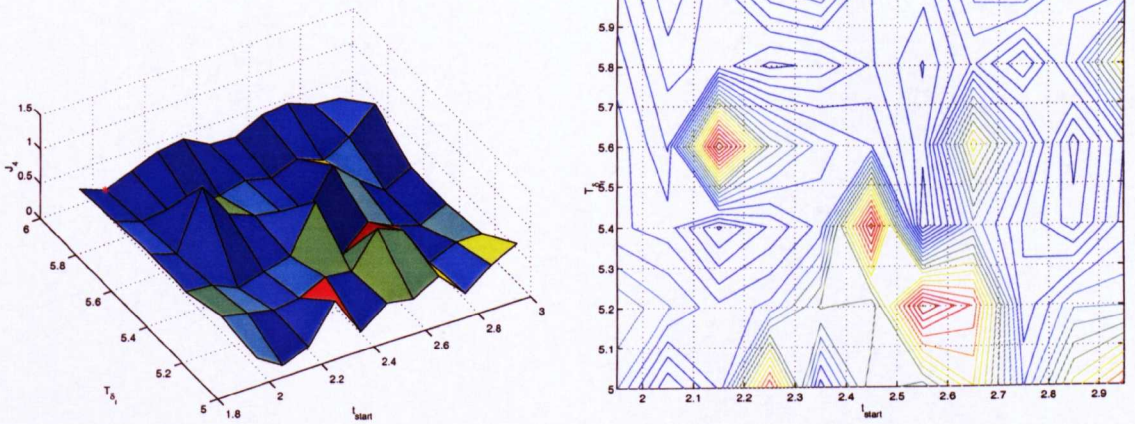
(b) C_n , $k = 0.128$

Figure 5.30: Airloads variation subject to the grid resolution displayed in table 5.15.

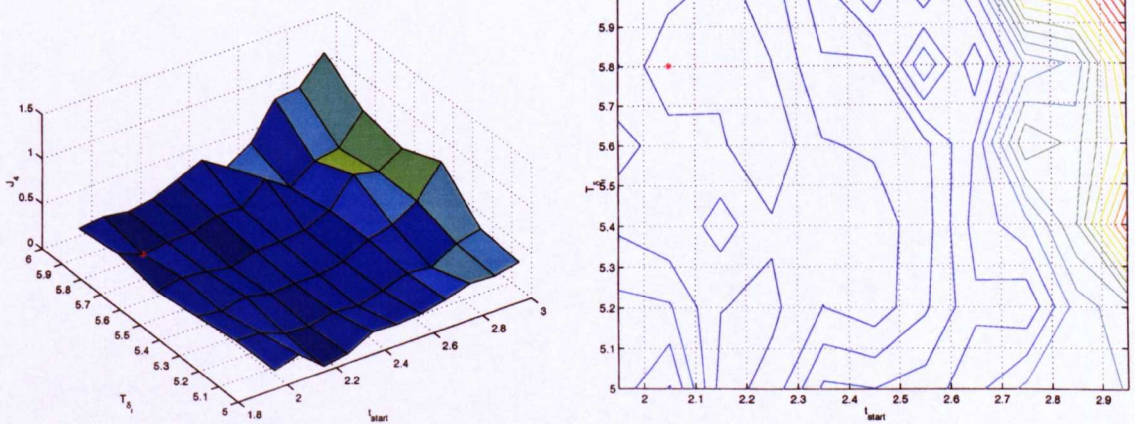
5.4. GRID RESOLUTION FOR THE PERIOD OF ACTUATION.



$$k = 0.128, c_1 = 1, c_2 = 0.01, c_3 = 0.3$$



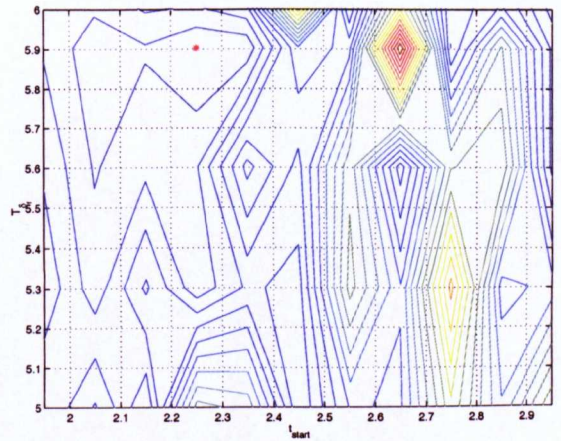
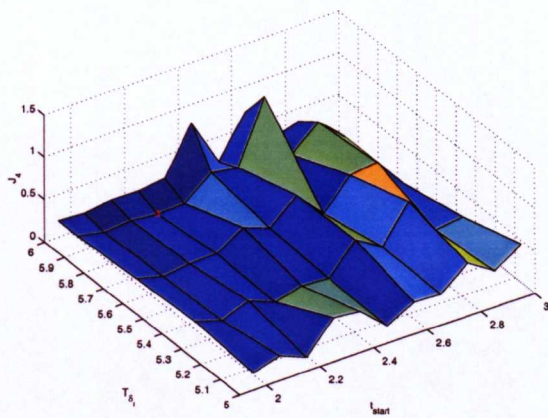
$$k = 0.154, c_1 = 1, c_2 = 0.01, c_3 = 0.3$$



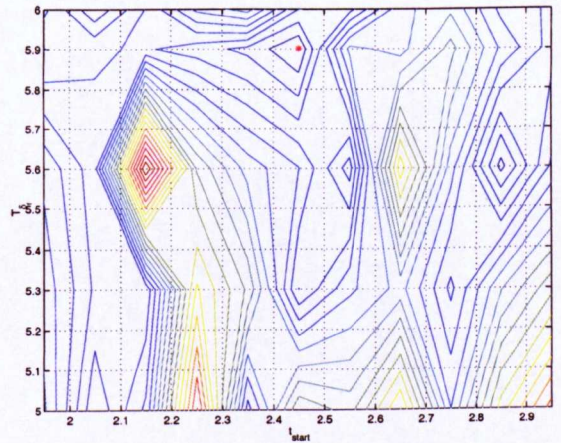
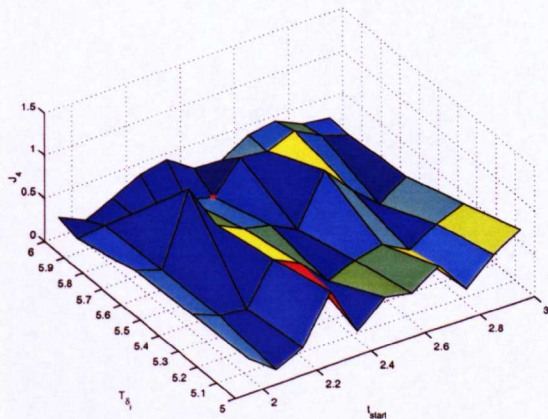
$$k = 0.180, c_1 = 1, c_2 = 0.01, c_3 = 0.3$$

Figure 5.31: Variation of objective function J_4 over the design space described by grid-1.

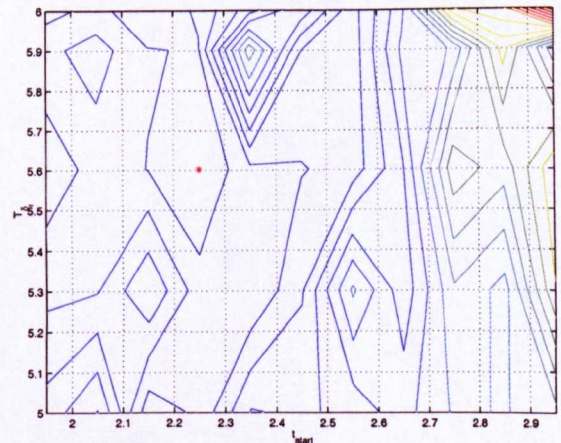
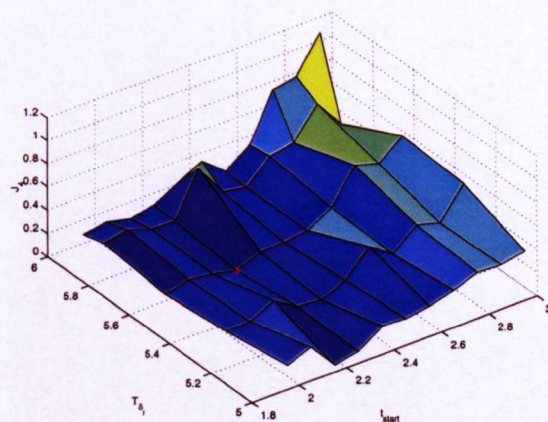
5.4. GRID RESOLUTION FOR THE PERIOD OF ACTUATION.



$$k = 0.128, c_1 = 1, c_2 = 0.01, c_3 = 0.3$$



$$k = 0.154, c_1 = 1, c_2 = 0.01, c_3 = 0.3$$



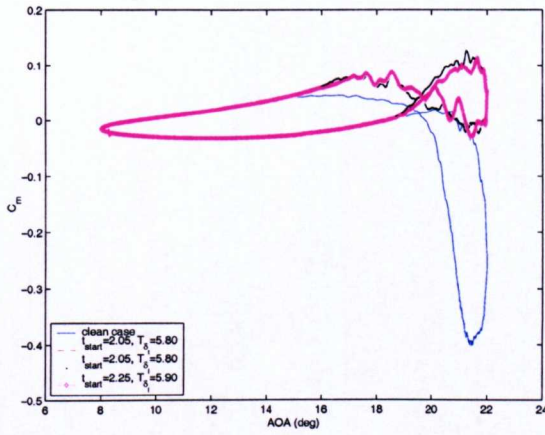
$$k = 0.180, c_1 = 1, c_2 = 0.01, c_3 = 0.3$$

Figure 5.32: Variation of objective function J_4 over the design space described by grid-2.

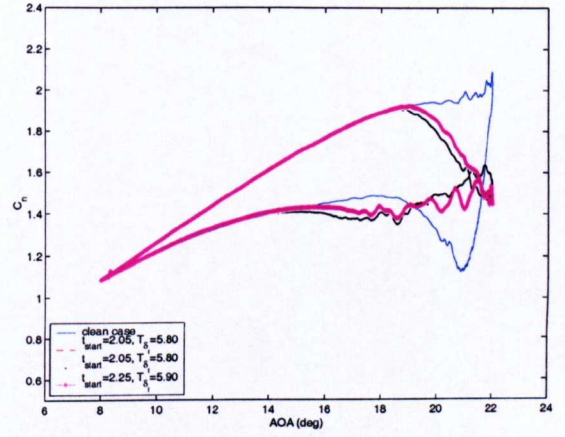
case IV:				
$k = 0.128$ (grid-1):				
c_1 for C_{m_-} :	c_2 for C_{m_+} :	t_{start}	T_{δ_f}	J_{4min}
1	1	2.950000	5.600000	0.485497
1	0.1	2.050000	5.800000	0.115446
$k = 0.128$ (grid-2):				
1	1	2.950000	5.600000	0.455757
1	0.1	2.250000	5.900000	0.115898
$k = 0.154$ (grid-1):				
c_1 for C_{m_-} :	c_2 for C_{m_+} :	t_{start}	T_{δ_f}	J_{4min}
1	1	2.850000	5.600000	0.211877
1	0.1	2.050000	6.000000	0.079986
$k = 0.154$ (grid-2):				
1	1	2.850000	5.600000	0.213834
1	0.1	2.450000	5.900000	0.073772
$k = 0.180$ (grid-1):				
c_1 for C_{m_-} :	c_2 for C_{m_+} :	t_{start}	T_{δ_f}	J_{4min}
1	1	2.250000	5.600000	0.107329
1	0.1	2.050000	5.800000	0.037464
$k = 0.180$ (grid-2):				
1	1	2.250000	5.600000	0.087099
1	0.1	2.250000	5.600000	0.043814

Table 5.16: Summary of weighting coefficients, optimisation parameters, design space variables and objective function values for T_{δ_f} grid resolution (optimisation case IV).

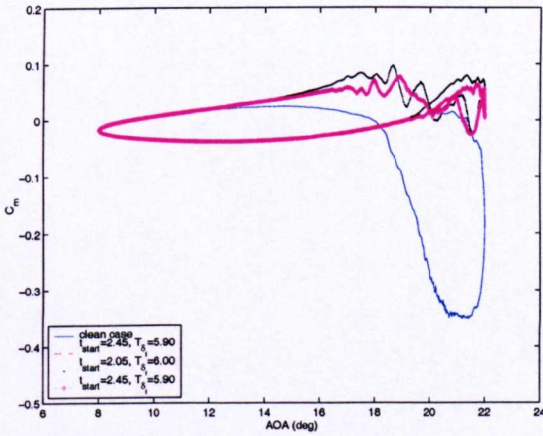
5.4. GRID RESOLUTION FOR THE PERIOD OF ACTUATION.



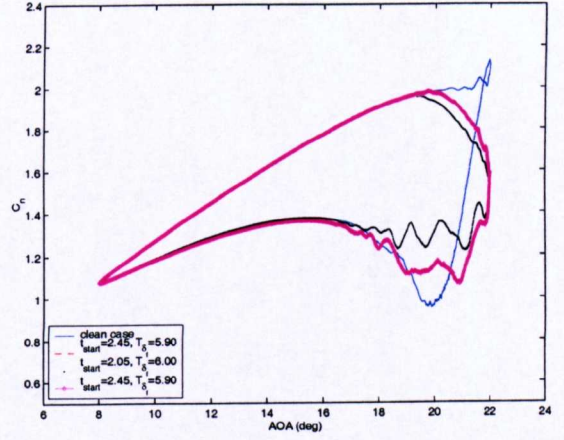
(a) C_m , $k = 0.128$



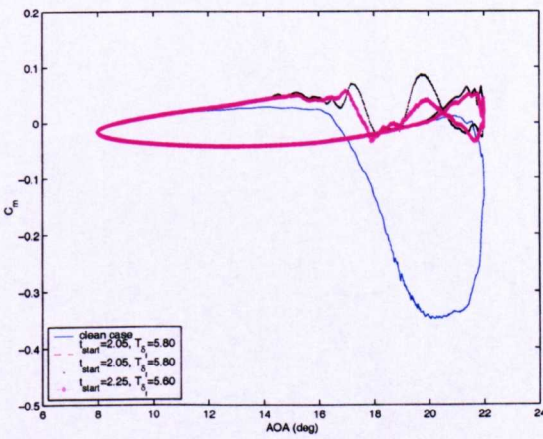
(b) C_n , $k = 0.128$



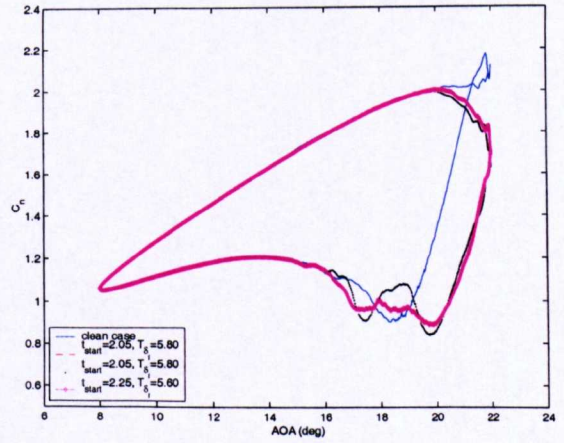
(c) C_m , $k = 0.154$



(d) C_n , $k = 0.154$



(e) C_m , $k = 0.180$



(f) C_n , $k = 0.180$

Figure 5.33: Airloads variation subject to the grid resolution displayed in table 5.16.

5.5 Concluding remarks

The current unconstrained optimisation strategy is conducted adopting the methodology described in the beginning of the chapter. The choice of the controls, i.e. t_{start} and T_{δ_f} appeared to be meaningful in delivering the desired modified airloads, particularly with respect to the sectional pitching moment. Finally the controls are correlated as function of the aerofoil reduced frequency varying between $0.128 \leq k \leq 0.180$. Within this range the aforementioned correlation is shown to be meaningful in terms of airloads modification.

In addition sensitivity analysis is performed with respect to the optimisation parameters and exhaustively with respect to the grid resolution. This revealed that the grid resolution, particularly with respect to the period of actuation, was found not to significantly affect the modification of the airloads. This fact is actually connected with a number of factors such as reduced frequency range, nature of optimisation procedure, flap harmonics and, numerical and experimental inaccuracies.

Regarding the reduced frequency range, this is chosen according to the range of the experimental database used throughout the current investigation which was used up to the maximum reduced frequency available,[118]. On the other hand this range is thought to be indicative for the flow mode of light dynamic stall.

The nature of the optimisation method, i.e. unconstrained optimisation implies the determination of the absolute minimum within the defined design space. Although the grid resolution analysis revealed that the controls showed little variation with increasing grid in general, all presented airloads showed the desired modification with more emphasis to the sectional pitching moment. It should be mentioned that even the controls that showed evident variation with grid resolution, they were not varying largely from those determined on the original grid. This variation was found at the expense of the pitching moment which sometimes was found with some extra overshoot and/or undershoot. If this is combined with numerical and experimental inaccuracy, the fact that only a single aerofoil pitch profile is considered, and, the reduced frequency range, then the aforementioned variation of the controls with grid resolution is greatly justified.

Overall it looks like C_{m-} is the only parameter to be considered. The rest is found to do little to the optimum point apparently due to the values of the cost coefficients used and the large variation of C_{m-} in comparison. However the chosen cost coefficients values were employed after a vary large set of values were tested. As already mentioned earlier in this chapter, the insensitivity of the cost coefficients is linked with the non-linear nature of the problem. However this suggests that inclusion of additional aerofoil motion profiles into the adopted control strategy might yield to a different behaviour (i.e. more sensitive subject to changes) of the cost coefficients. In addition

it is recommended the adopted optimisation algorithm should be compared with other minimisation algorithms for unconstrained optimisation, certainly when it comes to the inclusion of a larger data sets resulting from more aerofoil pitch profiles.

On the other hand, only the first flap harmonic⁶ is examined since this is thought and shown to be sufficient for manipulation of the trailing edge vorticity resulting in the desired airloads with more emphasis put on the sectional pitching moment. This justifies to a great extent the insensitivity of the controls to the grid resolution, in other words the sufficiency of the adopted grid, i.e. grid-A⁷. However when employing higher flap harmonic inputs, it might be worth examining finer grid resolution.

So far only open-loop control is presented and consequently one has to be careful about the range of applicability. In addition, although the modified airloads subject to the current optimisation scheme were shown to be satisfactory, more design parameters such as flap deflection power, drag force and flap deflection amplitude at more aerofoil mean and oscillating angles should be employed for a more complete optimisation scheme.

Since aerofoil aerodynamic damping is shown to be a parameter of great importance in the scientific literature including the current work, it is suggested that the flap related aerodynamic damping could be include in the optimi-

⁶The flap undergoes once per rev actuation.

⁷This is the simulations grid.

sation scheme.

Chapter 6

Conclusions and future work

6.1 Conclusions

Through the current investigation of two-dimensional flapped aerofoil dynamic stall a number of conclusive issues have been raised concerning the stall onset mechanism, the flap's geometric and actuation properties, and the adopted optimisation procedure. The actively controlled flap incorporated into the proposed flow control scheme demonstrates the alleviation of the severity introduced during pitching dynamic stall by generating new aerodynamic loads. In addition the suggested aerodynamic mechanism works throughout a range of reduced frequencies typical of rotorcraft dynamic stall. The current chapter outlines the main contributions to the field of aerofoil dynamic stall.

- A flap size having a nominal chordal length of $c_f=15\%c$ appeared to be sufficient in reducing the sectional pitching moment undershoot for the reduced frequency range, i.e.: $0.128 \leq k \leq 0.180$.
- As a consequence of the above pitching moment undershoot reduction, the negative aerodynamic damping shows significant reduction as well.
- For the light stall flow mode examined a $\frac{1}{rev}$ flap pitch input is found to be sufficient in modifying the sectional pitching moment undershoot for the reduced frequency range, i.e.: $0.128 \leq k \leq 0.180$.
- The flap deflection amplitude should be of the order of the maximum aerofoil incidence for the flow mode of light stall.
- As a consequence of the above, a flap amplitude of $\delta_f = 20^\circ$ appears to be sufficient in reducing the negative pitching moment magnitude.
- The maximum flap deflection should occur at around the maximum angle of oscillation for the flow mode (i.e. light stall, $0.128 \leq k \leq 0.180$) examined.
- The employed flap size (i.e. $c_f = 15\%c$) deflected at a maximum flap amplitude of $\delta_{f_{max}} = 20^\circ$ is found to add almost no extra positive aerodynamic damping into the sectional pitching moment hysteresis loop.

- The proposed flap aerodynamic mechanism appears successful in reducing the sectional pitching moment undershoot through modification of the DSV's trajectory for the reduced frequency range, i.e. $0.128 \leq k \leq 0.180$.
- Due to introduction of negative camber onto the aerofoil owing to the negative flap deflection (i.e. upward), the dynamic lift is not maintained.
- The flap's inertial hinge moment is found to be negligible compared to the aerodynamic hinge moment.
- The simulations suggested that the cause of the severe nose-down pitching moment is a result of the vortical pair described by the dynamic stall vortex (DSV) together with the trailing edge vortex (TEV) and not only due to the DSV.
- The initiation aerofoil AOA of the DSV increases with reduced frequency.
- The selection of flap control parameters (i.e. t_{start} and T_{δ_f}) indicate that the start and the period of the actuation appeared to be meaningful quantities for two-dimensional aerofoil dynamic stall control.
- The adopted grid resolution for the current optimisation scheme is shown to be sufficient for the first flap harmonic.

- A compromise should be sought between the start and the period of actuation in order to maintain most of the (dynamic) lift.

6.2 Future work

From the investigation conducted so far, a series of useful conclusions have been derived and outlined in the previous chapter. However since aerofoil dynamic stall forms a broad region in fluid mechanics, there is still a continuous need for further improvement. Several assumptions have been made in an attempt to reduce the aerofoil dynamic stall complexity. These assumptions along with several questions that have been raised while conducting the present research aimed to be addressed. Moreover the current application might serve for improvements in different aspects of rotorcraft aerodynamics. Therefore some thoughts are listed below which are thought to be of use and form an extension of the current work.

- The trailing edge flap could be further combined with other type of flow control solutions, e.g. suction.
- Actuation of the flap at the advancing side of the rotor disc might be beneficial for reduction of blade vortex interaction (BVI) levels.
- The current research could be further expanded with inclusion of plunging and for-aft motions of the aerofoil.

- The assumption for the flap deflection amplitude given by eqn. 3.3 should be further examined with more aerofoil pitch profiles.
- Although the current discrete vortex method (DVM) appears to capture satisfactorily the quantitative features of trailing edge type aerofoil dynamic stall, it lacks the ability to capture compressibility and leading edge stall. On the other hand capturing deep dynamic stall becomes a rather formidable task with a vortex-based flow solver.
- The results obtained from the current investigation are thought to be useful as starting criteria so that they could be included within a comprehensive code to evaluate the actual performance improvements on a typical helicopter rotor.
- The current work is based entirely on a constant free stream velocity value. In addition the obtained results are thought to be useful for extension of the present research in three dimensions. However in the case of 3-D dynamic stall, the afore mentioned assumptions listed in chapter 2 cannot be employed.
- All results for the flapped aerofoil presented within the current investigation are based on simulations using the discrete vortex method described in chapter 2. Although a flapped case is actuated after validation against the clean case, experimental evidence is thought to be complementary for further advancement of the present investigation.

In addition experimental evidence of the proposed flap aerodynamic mechanism is suggested.

- Expansion of the suggested optimisation scheme with more design variables such as flap power, drag force, flap deflection amplitude and flap aerodynamic damping. In addition data for more aerofoil mean and oscillating angles at wider range of reduced frequencies should be generated which is obviously a very lengthy process in temporal terms. However alternative methods such as neural networks could be employed for the generation of the aforementioned data.
- It is recommended that the obtained optimisation results should be validated against Theodorsen's analytic theory for flapped aerofoil.
- More optimisation algorithms should be employed in order to check the validity of the current minimisation approach.

Appendix A

A.1 Unsteady Bernoulli equation

The Bernoulli equation can be derived after performing integration along a streamline under the assumption of constant density of the Euler's equation which is given below:

$$\frac{\partial \vec{u}}{\partial t} + \nabla \left(\frac{u^2}{2} \right) - \vec{u} \times \vec{\omega} = -\nabla \left(\frac{P}{\rho} + gy \right) \quad (\text{A.1})$$

with \vec{u} being the velocity vector, t being the time, ω the vorticity, P the pressure of the fluid along a streamline, ρ the fluid density, g being the acceleration due to gravity and y being the elevation in the direction of gravity.

Introduction of the velocity potential ($\vec{u} = \nabla \phi$) into eqn. A.1 gives:

$$\nabla \left(\frac{\partial \phi}{\partial t} \right) + \nabla \left(\frac{1}{2} |\nabla \phi|^2 \right) = -\nabla \left(\frac{P}{\rho} + gy \right) \quad (\text{A.2})$$

or

$$\nabla \left(\frac{\partial \phi}{\partial t} + \frac{1}{2} |\nabla \phi|^2 + \frac{P}{\rho} + gy \right) = 0 \quad . \quad (\text{A.3})$$

After integration we obtain:

$$\frac{\partial\phi}{\partial t} + \frac{1}{2}|\nabla\phi|^2 + \frac{P}{\rho} + gy = f(t). \tag{A.4}$$

The above equation is valid everywhere in the fluid for unsteady potential flow. Rearranging and solving for p , eqn. A.4 becomes:

$$p = -\rho\left(\frac{\partial\phi}{\partial t} + \frac{1}{2}|\nabla\phi|^2 + gy\right) + F(t). \tag{A.5}$$

Equation A.5 is the Bernoulli equation for unsteady potential flow. The inertial effects of a fluid particle moving along a streamline are accommodated in the $\frac{\partial\phi}{\partial t}$ terms while taking the gradient of eqn. A.5, the acceleration effects are given.

A.2 Circulatory & non-circulatory terms

In a strict sense, a fictitious mass of fluid is added to the mass of the body to represent the force required to accelerate the body through the fluid. In addition the apparent mass has inertia and momentum equal to the apparent increase of the inertia and momentum of the body. In essence these terms lead to a change in the effective mass of the body and thus to an alteration of the flow dynamics.

The non-circulatory or apparent mass terms result from flow acceleration effects. Moreover they are a result of the unsteady Bernoulli equation (eqn. A.5), particularly from the term $\frac{\partial\phi}{\partial t}$ and account for the pressure forces required

for the acceleration of the fluid (see the previous section) in the vicinity of the aerofoil [1].

A.3 Vorticity stream function and vorticity transport equation

By definition, vorticity is the curl of velocity. In a Cartesian space we have thus:

$$\nabla \times V = \begin{vmatrix} i & j & k \\ \frac{\partial}{\partial x} & \frac{\partial}{\partial y} & \frac{\partial}{\partial z} \\ u & v & w \end{vmatrix} = i\left(\frac{\partial w}{\partial y} - \frac{\partial v}{\partial z}\right) + j\left(\frac{\partial u}{\partial z} - \frac{\partial w}{\partial x}\right) + k\left(\frac{\partial v}{\partial x} - \frac{\partial u}{\partial y}\right)$$

with V denoting the velocity vector, i, j, k the unit vectors, u, v, w the velocity components in x, y, z directions respectively. In the case of 2-D flows as in the present work, the vorticity vector has only a single non-zero component, i.e. $\omega = \omega_z = \frac{\partial v}{\partial x} - \frac{\partial u}{\partial y}$. Then we introduce the velocity potential given by

$$u = \frac{\partial \Psi}{\partial y} \tag{A.6}$$

and

$$v = -\frac{\partial \Psi}{\partial x} \tag{A.7}$$

Substitution of eqns. A.6, A.7 in ω_z yields:

$$\omega = \frac{\partial}{\partial x}\left(-\frac{\partial \Psi}{\partial x}\right) - \frac{\partial}{\partial y}\left(\frac{\partial \Psi}{\partial y}\right) = -\nabla^2 \Psi \tag{A.8}$$

Equation A.8 is identical to eqn. 2.4 .

The derivation of the vorticity transport equation is given next. Writing out fully the substantial derivative on the LHS of the Navier-Stokes equation given by eqn. 2.3, we have:

$$\frac{\partial u}{\partial t} + (u \cdot \nabla)u = -\frac{1}{\rho} \nabla P + \nu \nabla^2 u \tag{A.9}$$

Before we take the curl of eqn. A.9 using the definition of vorticity, we employ the following identities given by

$$\frac{1}{2} \nabla(u \cdot u) = (u \cdot \nabla)u + u \times (\nabla \times u) \tag{A.10}$$

$$\nabla \times \nabla \phi = 0 \tag{A.11}$$

$$\nabla \times (u \times \omega) = (\omega \cdot \nabla)u - (u \cdot \nabla)\omega + \underbrace{u \cdot \nabla \omega}_0 - \underbrace{\omega \cdot \nabla u}_0 \tag{A.12}$$

with the last two terms of eqn. A.12 vanishing since $\nabla \cdot \omega = \nabla \cdot (\nabla \times u) = \text{div}(\text{curl}(u)) = 0$ and the continuity equation given by eqn. 2.2 .

Combination of eqns. A.9 and A.10 gives:

$$\frac{\partial u}{\partial t} + \frac{1}{2} \nabla(u \cdot u) - \underbrace{u \times (\nabla \times u)}_{\omega} = -\frac{1}{\rho} \nabla P + \nu \nabla^2 u \tag{A.13}$$

which gives

$$\frac{\partial u}{\partial t} + \frac{1}{2} \nabla(u \cdot u) - u \times \omega = -\frac{1}{\rho} \nabla P + \nu \nabla^2 u \tag{A.14}$$

Taking the curl of eqn. A.14 we have for the LHS and RHS respectively:

$$\nabla \times LHS = \frac{\partial}{\partial t} \underbrace{(\nabla \times u)}_{\omega} + \frac{1}{2} \underbrace{\nabla \times \nabla(u \cdot u)}_{=0} - \nabla \times (u \times \omega) \tag{A.15}$$

$$\nabla \times RHS = -\frac{1}{\rho} \underbrace{(\nabla \times \nabla p)}_{=0} + \nu \nabla^2 \underbrace{(\nabla \times u)}_{=\omega} \quad (\text{A.16})$$

Finally collecting the non zero terms we obtain:

$$\frac{\partial \omega}{\partial t} + (\vec{u} \cdot \nabla) \omega = \frac{1}{Re} \nabla^2 \omega \quad (\text{A.17})$$

which is identical to the expression given by eqn. 2.5 in chapter 2 .

A.4 Theorems

A series of theorems are given in this section, essential to the current research. They are presented in the next paragraphs with direct application to the current investigation.

A.4.1 Gauss' and Green's theorems

The first Green's identity is given by eqn. B.13 in Appendix B and it is used to calculate the flap's polar moment of inertia. The second Green's identity (symmetric form) is proved next. Flow field properties such as velocity potential and stream function are used for convenience. Recalling eqn. 2.10,

$$\oint_{S_i} (\phi \nabla \psi_i - \psi_i \nabla \phi) \cdot \vec{n} dS_i = \iint_{B_i} (\phi \nabla^2 \psi_i - \psi_i \underbrace{\nabla^2 \phi}_{=0}) dB_i = - \iint_{B_i} 2\Omega_i \phi dB_i \quad .$$

The LHS of the above equation may be split in I_1 and I_2 , i.e.:

$$I_1 = \oint_{S_i} (\phi \nabla \psi_i) \cdot \vec{n} dS_i \quad (\text{A.18})$$

and

$$I_2 = \oint_{S_i} (-\psi_i \nabla \phi) \cdot \vec{n} dS_i \quad . \quad (\text{A.19})$$

For solving I_1 and I_2 , application of Gauss theorem is required which relates an integral over a closed geometrical object (curve or surface) to an integral over a contained region (surface or volume) [18] and it is given by,

$$\oint_{S_i} (F) \cdot \vec{n} dS_i = \iiint_{B_i} \nabla F dB_i \quad (\text{A.20})$$

with $F = \phi \nabla \psi_i$ for I_1 and $F = -\psi_i \nabla \phi$ for I_2 respectively. Then applying eqn. A.20 to I_1 we have,

$$\begin{aligned} I_1 &= \oint_{S_i} (\phi \nabla \psi_i) \cdot \vec{n} dS_i = \\ &= \iiint_{B_i} \nabla (\phi \nabla \psi_i) dB_i = \\ &= \iiint_{B_i} (\phi \nabla^2 \psi_i + \nabla \psi_i \nabla \phi) dB_i \quad . \end{aligned} \quad (\text{A.21})$$

Hence $\vec{n} \cdot (\phi \nabla \psi_i) = \phi (\vec{n} \cdot \nabla \psi_i) = \phi \frac{\partial \psi_i}{\partial \eta}$ [17]. After substitution into eqn. A.21, I_1 becomes,

$$\begin{aligned} I_1 &= \oint_{S_i} \phi \frac{\partial \psi_i}{\partial \eta} dS_i = \\ &= \iiint_{B_i} (\phi \nabla^2 \psi_i) dB_i + \iiint_{B_i} (\nabla \phi \nabla \psi_i) dB_i \Rightarrow \\ \iiint_{B_i} (\nabla \phi \nabla \psi_i) dB_i &= \oint_{S_i} \phi \frac{\partial \psi_i}{\partial \eta} dS_i + \iiint_{B_i} \phi \nabla^2 \psi_i dB_i \quad . \end{aligned} \quad (\text{A.22})$$

Similarly by symmetry and interchange of ϕ and ψ_i we obtain for I_2 ,

$$\begin{aligned}
 I_2 &= \oint_{S_i} \psi_i \frac{\partial \phi}{\partial \eta} dS_i = \\
 &\quad - \iint_{B_i} (\psi_i \nabla^2 \phi) dB_i - \iint_{B_i} (\nabla \psi_i \nabla \phi) dB_i \Rightarrow \\
 \iint_{B_i} (\nabla \psi_i \nabla \phi) dB_i &= \oint_{S_i} \psi_i \frac{\partial \phi}{\partial \eta} dS_i - \iint_{B_i} \psi_i \nabla^2 \phi dB_i \quad . \quad (A.23)
 \end{aligned}$$

Equating the LHS of eqns. A.22 and A.23 we finally obtain,

$$\oint_{S_i} (\phi \nabla \psi_i - \psi_i \nabla \phi) \cdot \vec{n} dS_i = \iint_{B_i} (\phi \nabla^2 \psi_i - \psi_i \nabla^2 \phi) dB_i = - \iint_{B_i} 2\Omega_i \phi dB_i \quad (A.24)$$

which is identical to the RHS of eqn. 2.10 with the term $\psi \nabla^2 \phi = 0$ due to the fact that $\nabla^2 \phi = 0$.

A.4.2 Stoke's Theorem

Stoke's theorem allows us to reduce any surface integral to a line integral along the rim of the surface, provided that both surfaces have the same rim C [30], [18]. In this regard it is very similar to Green's theorem.

$$\oint_C F \cdot dr = \iint_S (\nabla \times F) \cdot n ds \quad (A.25)$$

with C denoting the rim of the surface defined in anticlockwise direction, n the unit vector pointing out of the surface S as defined by the right hand rule. This term is borrowed from the electromagnetic theory. The magnitude of the force F felt by a charge q moving with velocity v through a magnetic

field B equals $F = qvB\sin(\theta)$, with $F \perp B, v$. The right hand rule determines the direction of F, v, B . The thumb points in the direction of v , the fingers point in the direction of B while F points out of the hand, i.e. that the fingers will corkscrew in the direction of F .

A.4.3 Biot-Savart law

Consider a vortex filament extending to $\pm\infty$. This filament induces a flow field in the surrounding space, carrying Γ amount of circulation. Taking a segment of the filament (i.e. dl) and a point p located at distance r , then the induced velocity dv at p equals to: $dU = \frac{\Gamma}{4\pi} \frac{dl \times r}{|r^3|}$. Integrating for the whole vortex filament we obtain [5]:

$$U = \int_{-\infty}^{+\infty} \frac{\Gamma}{4\pi} \frac{dl \times r}{|r^3|} \quad (\text{A.26})$$

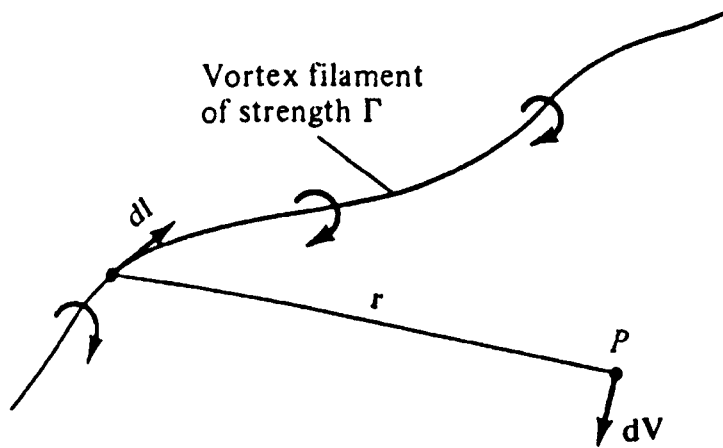


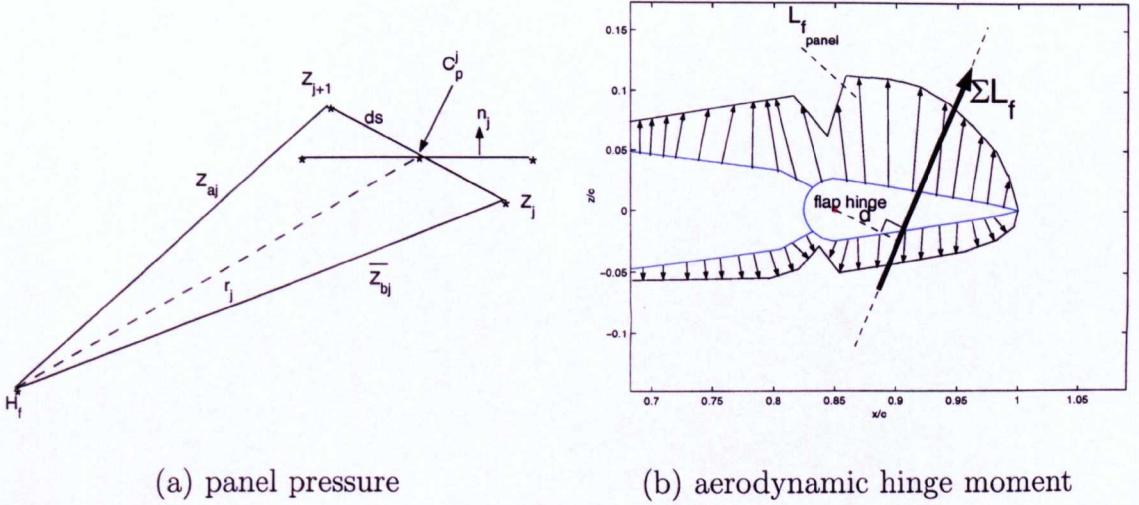
Figure A.1: Illustration of the Biot-Savart law applied to a vortex filament, adapted from Anderson [5].

A derivation of the Biot-Savart's law applicability to vortical flows is provided by Stepniewski and keys [34].

Appendix B

B.1 Flap aerodynamic hinge moment

A single flap panel with span extending from node Z_j to node Z_{j+1} is shown in fig. B.1(a). The j^{th} panel has length ds , the distance between the flap hinge location H_f and the middle of the panel is denoted by r_j , and C_p^j is the pressure acting on the panel as a result of the force C_f^j (not shown) with the normal of the panel also displayed, see fig. B.1(a):



(a) panel pressure

(b) aerodynamic hinge moment

Figure B.1: Illustration of panel pressure and aerodynamic flap hinge moment.

The moment of the force C_f^j applied in the middle of the panel about the flap hinge equals to:

$$\Delta C_{m_h} = r_j \times \Delta C_f^j \tag{B.1}$$

and with $C_f^j = n_j \cdot C_p^j \cdot ds$, this gives

$$\Delta C_{m_h} = r_j \times (n_j \cdot C_p^j \cdot ds) \tag{B.2}$$

The distances from the flap hinge to the nodes Z_j and Z_{j+1} are denoted by Z_{aj} and $\overline{Z_{bj}}$ respectively, where $\overline{Z_{bj}}$ is the complex conjugate of Z_{bj} , i.e. $Z_{bj} = \overline{\overline{Z_{bj}}}$. If $Z_{aj} = x_1 + iy_1$ and $\overline{Z_{bj}} = x_2 - iy_2$, we have:

$$Z_{aj} \overline{Z_{bj}} = (x_1 + iy_1)(x_2 - iy_2) = (x_1x_2 + y_1y_2) + i(y_1x_2 - x_1y_2) \tag{B.3}$$

Equation B.3 can be rewritten as:

$$Z_{aj}\overline{Z_{bj}} = \underbrace{Re(Z_{aj}\overline{Z_{bj}})}_{=Z_{aj}} \cdot \overline{Z_{bj}} - \underbrace{Im(Z_{aj}\overline{Z_{bj}})}_{=Z_{aj} \times \overline{Z_{bj}}} \quad (B.4)$$

Substitution of eqn.B.3 into eqn. B.2 we finally obtain:

$$\Delta C_{m_h} = -Im(Z_{aj}\overline{Z_{bj}})C_p^j \cdot ds \quad . \quad (B.5)$$

Summation of eqn. B.5 over the number of panel describing the suction and pressure flap surface gives the aerodynamic moment about the flap hinge as shown in fig B.1(b). For illustrative purposes, a schematic representation of the flap’s hinge moment representation is given in fig. B.1(b) where a summation of the elementary lift (i.e. lift at every flap panel $L_{f_{panel}} \equiv L_{f_j}$) occurs yielding to the total flap lift. The cross product of the resultant flap lift vector with the arm d (i.e. the perpendicular distance from the flap hinge to the $L_{f_{panel}}$ working line) delivers the aerodynamic flap hinge moment. The total moment about the flap hinge consists of two parts, the aerodynamic and the inertial one and it is given by eqn. B.6.

$$M_{H_f} = M_{pressure} + M_{inertial} \quad (B.6)$$

B.2 Flap moment of inertia

The flap is assumed to have a uniform constant material density distribution throughout its entire volume¹, in other words each spanwise and chordwise

¹Since the current research is 2D, the flap volume equals to unity.

section is essentially rigid, i.e:

$$\rho_{flap} = \rho_{flap}(x, y, z) = constant \quad (B.7)$$

Concerning the realisation of the current application this won't be the case since the flap's internal part should accommodate the actuation mechanism. It is worth mentioning that for the determination of the required flap hinge moment, the friction forces at the hinge should be taken into account as well. In particular these forces depend strongly on the materials that blade, flap and actuator unit are manufactured and types of bearings at the flap hinge axis. Since a similar investigation falls far beyond the main aim of the current work, it is further assumed that the flap is equipped with a frictionless hinge, therefore no friction forces that the flap hinge encounters during actuation are taken into account. The calculations displayed below are solely based on these assumptions therefore delivering results higher than real actual values. Another issue that should be included regarding the current research, is the effectiveness of the flap to reduce the pitching moment and/or maintain the dynamic lift the longest possible. This fact is actually associated with the finite thickness of the boundary layer over the aft portion of the aerofoil (i.e. the trailing edge flap) [72]. More specific, their values should be determined based on observed data [72]. Regarding the current work their value is actually set to unity.

B.2.1 Flap centroid determination

For the determination of the unbalanced flap's centre of gravity (cg), only the determination of the x-coordinate of its centre of gravity is derived and given below. The location of the y- and z- cg coordinates are easily obtained by making use of symmetry conditions. For the upper half of the flap cross-section representation (fig. B.2), a ninth order polynomial is fitted, eqn. B.8:

$$\begin{aligned}
 y = f(x) = & 0.0125 x^9 - 0.1041 x^8 + 0.3842 x^7 \\
 & - 0.8267 x^6 + 1.1432 x^5 - 1.0535 x^4 \\
 & + 0.6470 x^3 - 0.2554 x^2 + 0.0588 x - 0.0060 \quad (B.8)
 \end{aligned}$$

For reasons of accuracy and consistency, both geometrical and mass centroids of the flap are determined. These should coincide under the assumption of constant flap material density. The chordwise coordinate (i.e. x-coordinate) of the flap's **geometric** centroid can be determined by eqn. B.9, i.e:

$$\bar{x} = \frac{\int_{flap'sLE}^{flap'sTE} x(f(x) - g(x))dx}{\int_{flap'sLE}^{flap'sTE} (f(x) - g(x))dx} \quad (B.9)$$

with $f(x)$ given by eqn. B.8 and $g(x)$ given by the line which coincides with the x-axis as shown in fig. B.2. After performing the integration of eqn. B.9 and taking into account the flap's symmetry conditions, the geometrical flap centroid is found to be, $[\bar{x}_g, \bar{y}_g, \bar{z}_g] = [0.8865(\frac{x}{c}), 0, 0]$. For the determination of the x-coordinate of the flap's **mass** centroid and under the assumption of uniform flap material density distribution, the sum of each individual

moment is taken of every elementary mass over the entire flap volume. Then the location of the chordwise coordinate of the flap's cg is given by eqn. B.10, i.e:

$$\bar{x} = \frac{M_{yz}}{m} \quad (\text{B.10})$$

with M_{yz} being the moment of all concentrated masses over the entire flap volume about the yz plane and equals to, i.e.:

$$M_{yz} = \lim_{\Delta m \rightarrow 0} \sum \tilde{x} \Delta m = \int \tilde{x} dm \quad (\text{B.11})$$

Combining eqns. B.10, B.11 finally we obtain:

$$\bar{x} = \frac{\int \tilde{x} dm}{\int dm} \quad (\text{B.12})$$

After performing integration of eqn. B.12 and taking into account the flap's structural symmetry conditions, the chordwise location of the flap's mass centroid appears to be, $[\bar{x}_m, \bar{y}_m, \bar{z}_m] = [0.8901(\frac{x}{c}), 0, 0]$ As expected the geometric and mass centroid of the flap seem to actually coincide since the flap material density is constant throughout the entire flap volume. There is though a very small procentual variation of the chordwise coordinate between the geometric and the mass flap's centroid and is found to be approximately 0.4%. Summarising the unbalanced average flap's centroid coordinates, we have, $[\bar{x}_0, \bar{y}_0, \bar{z}_0] = [0.8883(\frac{x}{c}), 0, 0]$. Both geometric and mass flap's centroids, their average and their procentual difference are illustrated in table B.1.

geometric flap centroid:	mass flap centroid:
$[\bar{x}_g, \bar{y}_g, \bar{z}_g] = [0.8865(\frac{x}{c}), 0, 0]$	$[\bar{x}_m, \bar{y}_m, \bar{z}_m] = [0.8901(\frac{x}{c}), 0, 0]$
procentual difference between geometrical and mass centroid:	0.4%
average value between geometrical and mass centroid:	$[\bar{x}_0, \bar{y}_0, \bar{z}_0] = [0.8883(\frac{x}{c}), 0, 0]$

Table B.1: Location of flap's mass & geometrical centroid.

B.2.2 Calculation of flap moment of inertia

The cross-sectional flap area is calculated as follows, i.e.: the non-dimensional flap cross sectional area is found to be $A_{flap} = 0.0051796[]^2$ and $A_{flap} = 0.00530[]^2$ after utilisation of surface discretisation $dA_{flap} = dx dy$ and Green's Theorem respectively. Both results are listed in table B.2 .

surface discretisation:	Green's Theorem:
$A_{flap} = 0.0051796 []^2$	$A_{flap} = 0.00530 []^2$
procentual difference: 2.27%	
average value: $A_{flap} = 0.00520 []^2$	

Table B.2: Flap non-dimensional cross sectional area.

The flap cross sectional area is illustrated in fig. B.2.

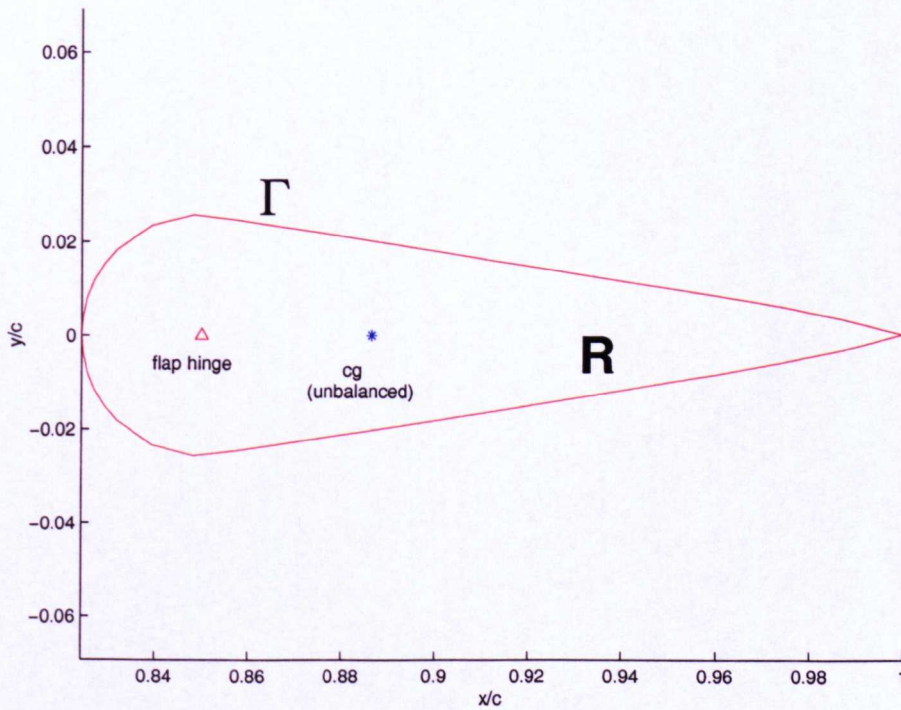


Figure B.2: Flap crosssectional area with location of cg and hinge

Another way of calculating the flap cross-sectional area, denoted by R as

shown in fig. B.2, is by applying Green's theorem along the flap contour Γ , i.e:

$$\iint_R \left(\frac{\partial g}{\partial x} - \frac{\partial f}{\partial y} \right) dx dy = \oint_{\Gamma} (f dx + g dy) \tag{B.13}$$

with $f(x, y)$ and $g(x, y)$ being continuous functions and have continuous partial derivatives [24] $\frac{\partial g}{\partial x}, \frac{\partial f}{\partial y}$ everywhere in R with boundaries defined between i.e.: $0.8243 \leq x \leq 1$ and $u(x) \leq y \leq v(x)$ with $u(x) = 0$ and $v(x) = f(x)$ given by eqn. B.8 and $0 \leq y \leq 0.0254$ and $q(y) \leq x \leq p(y)$ with $q(y) = 0$ and $p(y) = f(x)$ again, given by eqn. B.8, with $x \equiv \frac{x}{c}$ and $y \equiv \frac{y}{c}$.

$$I_1 = - \iint_R \left(\frac{\partial f}{\partial y} \right) dx dy \tag{B.14}$$

$$I_2 = \iint_R \left(\frac{\partial g}{\partial x} \right) dx dy \tag{B.15}$$

Then I_1 and I_2 become respectively, i.e:

$$I_1 = - \int_{0.8243}^1 \int_{u(x)}^{v(x)} \left[\frac{\partial f}{\partial y} dy \right] dx$$

$$I_2 = \int_0^{0.0254} \int_{p(y)}^{q(y)} \left[\frac{\partial g}{\partial x} dx \right] dy$$

Evaluating the inner integrals, we have, i.e:

$$I_1 = - \int_{0.8243}^1 \left(f[x, v(x)] - f[x, u(x)] \right) dx$$

$$I_2 = \int_0^{0.0254} \left(g[q(y), y] - g[p(y), y] \right) dy$$

Finally we obtain $I_1 + I_2 = 0.00530$. Both numerical and analytical results for the flap area are illustrated in table B.2.

The determination of the unbalanced trailing edge flap’s mass moment of inertia about the z-axis (i.e. axis perpendicular to the plane of paper, otherwise the polar moment of inertia) becomes [31]:

$$I_{z_0z_0} = \sum r_i^2 m_i = \rho \int r_{z_0}^2 dm \tag{B.16}$$

where r_i is the radial distance from the inertia axis to the elementary mass m_i integrated over the whole body and ρ being the density of the flap, assumed to be constant over its whole volume. The flap’s elementary mass dm equals to:

$$dm = \rho dV = \rho l_{flap} dR \tag{B.17}$$

$$dR = dx dy \tag{B.18}$$

with dV, dR being the elementary flap- volume, area respectively and l_{flap} the entire flap length. Substitution of equation (B.17) into equation (B.16) yields, i.e:

$$I_{z_0z_0} = \rho l_{flap} \iint_R (x_0^2 + y_0^2) dx dy \tag{B.19}$$

Transformation of the above integral into a line integral of its normal derivative using Green’s Theorem yields to:

$$\iint_R \nabla^2 w dx dy = \int_{\Gamma} \frac{\partial w}{\partial n} ds \tag{B.20}$$

with the function $w(x, y)$ being continuous in R (fig. B.2) with continuous

first and second derivatives. Recalling equation B.13 we have:

$$\iint_R \nabla^2 w \, dx \, dy = \iint_R \left(\frac{\partial^2 w}{\partial x^2} - \frac{\partial^2 w}{\partial y^2} \right) dx \, dy = \int_{\Gamma} \left(\frac{\partial w}{\partial y} dx - \frac{\partial w}{\partial x} dy \right) . \quad (\text{B.21})$$

Setting

$$\frac{\partial^2 w}{\partial x^2} = y^2 \Rightarrow \frac{\partial w}{\partial x} = x y^2 + g_1(y) \quad (\text{B.22})$$

$$\frac{\partial^2 w}{\partial y^2} = x^2 \Rightarrow \frac{\partial w}{\partial y} = x^2 y + h_1(x) . \quad (\text{B.23})$$

Finally we obtain:

$$w(x) = \frac{x^2 y^2}{2} + x g_1(y) + g_2(y) \quad (\text{B.24})$$

$$w(y) = \frac{x^2 y^2}{2} + y h_1(y) + h_2(y) . \quad (\text{B.25})$$

After differentiation of eqns. B.24, B.25, we have:

$$\frac{\partial w}{\partial x} = x y^2 + y \quad (\text{B.26})$$

$$\frac{\partial w}{\partial y} = x^2 y + x . \quad (\text{B.27})$$

So the mass moment of inertia (eqn. B.19) becomes the line integral along

the flap contour Γ i.e:

$$I_{z_0z_0} = \rho l_{flap} \iint_R (x_0^2 + y_0^2) dx dy \Rightarrow$$

$$I_{z_0z_0} = \rho l_{flap} \oint_{\Gamma} (x y^2 + y) dx + (x^2 y + x) dy \quad . \quad (B.28)$$

By denoting the second and first integral by w_1 and w_2 respectively, taking their first partial derivatives and applying Green's theorem along the flap contour Γ , we obtain:

$$w_1 = x^2 y + x \Rightarrow \frac{\partial w_1}{\partial y} = x^2 \quad (B.29)$$

$$w_2 = x y^2 + y \Rightarrow \frac{\partial w_2}{\partial x} = 2xy \quad (B.30)$$

Substitution of w_1 and w_2 into eqn. B.28 yields to,

$$\oint_{\Gamma} (x y^2 + y) dx + (x^2 y + x) dy =$$

$$\iint_R \left(\frac{\partial w_2}{\partial x} - \frac{\partial w_1}{\partial y} \right) dy dx =$$

$$\int_{0.8243}^1 \int_0^y (-2xy - x^2) dy dx =$$

$$(B.31)$$

$$= 8.7764 \times 10^{-6} \quad (B.32)$$

Making use of symmetry conditions about the x-axis, taking twice the above result in order to represent the whole flap cross-section, the non-dimensional

flap mass moment of inertia per unit span becomes, $I_{z_0z_0} = 1.7553e(-5)[\]$. Another way of calculating the flap sectional mass moment of inertia is by discretisation of the corresponding area in x and y direction. By employing eqn. B.16 we have: $I_{z_0z_0} = 1.5305e(-5)[\]$. The procentual difference between the two different methods presented above is about 13%. Since the discretisation method yields to numerical inaccuracies, it is decided that the analytic result obtained using Green’s theorem will be used throughout the present work. Both values for the flap moment of inertia are summarised in table B.3.

flap moment of inertia:	
surface discretisation:	Green’s Theorem:
$I_{z_0z_0} = 1.5305e(-5)[\]$	$I_{z_0z_0} = 1.7553e(-5)[\]$
procentual difference: 13%	

Table B.3: Flap non-dimensional polar moment of inertia.

B.2.3 Flap dynamic mass balancing

For reasons of completeness, another important property that should be discussed concerns the flap’s weight balance. As it is apparent in fig. B.2 and still under the assumption of constant flap material density, there is a gap between the chordwise hinge location and its centre of gravity. As the blade

sweeps over the azimuth particularly when the flap will undergo deflection, flutter will be amplified due to this offset between the flap's *cg* and hinge point at certain frequencies. The main issue arising here is not identification of the aforementioned frequencies neither suppression of them. For reasons of reference and clarity this can be simply and efficiently resolved by placement of a weight strip, solution adequate enough to reduce this offset to zero, over the aft portion of the flap. The balancing of control surfaces such as flaps and ailerons has always played a key role in flutter prevention. Attempting to significantly reduce or completely vanish the factors that enhance flutter, there should be a break up of any coupling between the various degrees of freedom [28].

For illustrative purposes, consider a two-dimensional blade cross section fitted with a trailing-edge flap whose centroid is located behind the hinge line, likewise for the present (yet unbalanced) situation. After the introduction of a sudden pitching motion of the blade, a flap deflection will be induced by the pitching of the blade by the inertial force, i.e. *inertia coupling*. Due to the presence of an aerodynamic moment the flap will show again the tendency to deflect, i.e. *aerodynamic coupling*. In addition there might exist an elastic linkage [28] so that the pitching motion of the blade might introduce a flap deflection, i.e. *elastic coupling*. Although no effective precautions can be taken over aerodynamic- and elastic coupling which is not the case for

the inertial coupling, a problem which can be satisfactorily tackled by means of dynamic mass balancing. The latest procedure contributes to a weight redistribution by adding extra weight, aiming finally to coincide the flap's centroid and its hinge point.

It becomes worth mentioning that within the mass balancing presented in this paragraph, the flap is still treated as having a uniform mass distribution, in other words without involving the actuation mechanism. In fact for a complete dynamic mass balancing of the flap, the dimensions & dynamics of the flap actuator have to be taken into account. Bernhard [74] and Lee [73] present an extensive research on the actuator- choice and modelling. Since the final choice of the flap actuator falls outside of the current work scope, the present investigation focus on the qualitative effects of employing a plain trailing edge flap as a useful means of alleviating rotorcraft retreating blade stall.

Bibliography

- [1] J.G. Leishman. *Principles of Helicopter Aerodynamics*. Cambridge University Press, ISBN 0-521-66060-2, 2000.
- [2] W.J. McCroskey. Unsteady airfoils. *Ann. Rev. Fluid Mech.*, 14(3):pp.285–311, 1982.
- [3] F.K. Straub and B.D. Charles. A new approach to active control. In *Presented at the Aeromechanics Specialists Conference, San Francisco, Jan. 19-21, 1994*.
- [4] H. Lin. *Prediction of seperated flows around pitching airfoils using a discrete vortex method*. PhD thesis, Univ. of Glasgow, Department of Aerospace Engineering, 1997.
- [5] J.D. Anderson. *Fundamentals of Aerodynamics*. McGraw-Hill international editions, ISBN 0-07-100767-9, 1991.
- [6] A.A. Hassan, L.N. Sankar, and H. Tadghighi. Effects of leading and

- trailing edge flaps on the aerodynamics of airfoil/vortex interactions. *J. American Helicopter Soc.*, 39(2):pp.35–46, 1994.
- [7] R.D. Joslin, R.A. Nicolaides, G. Erlebacher, M.Y. Hussaini, and M.D. Gunzburger. Active control of boundary layer instabilities. part ii: Use of sensors and spectral controller. *AIAA(Journal)*, 33(8):pp.1521–33, 1995.
- [8] P.F. Lorber, F.O. Carta, and R.G. Carlson. The aerodynamics of an oscillating jet flap. *J. American Helicopter Soc.*, 34(2):pp.24–32, 1989.
- [9] L.E. Ericsson and J.P. Reding. Dynamic stall of helicopter blades. *J. American Helicopter Soc.*, 17(1):pp.11–19, 1972.
- [10] A. Seifert, A. Darabi, and I. Wygnanski. On the delay of airfoil stall by periodic excitation. *J. of Aircraft*, 33(4):pp.691–699, 1996.
- [11] R.B. Green, R.A. McD. Galbraith, and A.J. Niven. Measurements on the dynamic stall vortex convection speed. *The Aeronautical Journal*, October(Paper No. 1864):pp.319–325, 1992.
- [12] A. Seifert, T. Bachar, D. Koss, and I. Wygnanski. Oscillatory blowing, a tool to delay boundary layer separation. *AIAA Journal.*, 31(11):pp.2052–2060, 1993.
- [13] A. Seifert and L.G. Pack. Oscillatory control of separation at high Reynolds numbers. *AIAA Journal*, 37(9):pp.1062–1071, 1999.

- [14] L.G. Pack and R.D. Joslin. Overview of active flow control at NASA Langley Research Center. In *SPIE's 5th Annual International Symposium on Smart Structures and Materials, San Diego, California, March 1-5, 1998*.
- [15] Y.Guy, J. Morrow, T. Mcuaghlin, and I. Wagnanski. Parametric investigation of the effects of active flow control on the normal force of a delta wing. In *AIAA 38th Aerospace Sciences Meeting, 10-13 January 2000, AIAA Paper 2000-549, 2000*.
- [16] K.R. McManus, H.H. Legner, and S.J. Davis. Pulsed vortex generator jets for active control of flow separation. In *Fluid Dynamics Conference, 25th, Colorado Springs, CO, June 20-23, 1994 AIAA Paper 94-2218, 1994*.
- [17] G.D. Smith. *Vector Analysis including the dynamics of a rigid body*. Oxford University Press, N/A, 1962.
- [18] J.E. Marsden and A.J. Tromba. *Vector Calculus*. W.H. Freeman and Company, ISBN 0-7167-1856-1, 1988.
- [19] R.L. Finney G.B. Thomas Jr. *Calculus and analytic geometry*. Addison Wesley Longman Publishing Co, ISBN 0-201-16309-8, 1994.
- [20] The MathWorks Inc. *Matlab manual*, 1996.
- [21] The MathWorks Inc. *Spline Toolbox for use with Matlab*, 1996.

- [22] F. K. Tsiachris. Presentation: Alleviation of retreating blade stall using trailing edge flaps. Helicopter study weekend at the Burn, Annual event organised by the Univ. of Glasgow, Dept. of Aerospace Engineering, 12-13 April. 2002.
- [23] C.W. Haines. *Analysis for Engineers*. West Publishing Corporation, ISBN 0-8299-0011-X, 1980.
- [24] E. Kreyszig. *Advanced engineering mathematics*. John Wiley & Sons, Inc., ISBN 0-471-15496-2, 1998.
- [25] E.R. Johnston F.P. Beer. *Vector mechanics for engineers*. McGraw-Hill-Europe, ISBN 0-07-548404-8, 1983.
- [26] W. Murray. *Numerical methods for unconstrained optimization*. Academic Press, ISBN 0-12-512250-0, 1972.
- [27] R.L. Bisplinghoff, H. Ashley, and R. Halfman. *Aeroelasticity*. Dover Publications, ISBN 0-486-69189-6, 1996.
- [28] Y.C. Fung. *An introduction to the theory of Aeroelasticity*. Dover Publications, ISBN 0-486-67871-7, 1994.
- [29] A.S.W. Thomas. Active wave control of boundary layer transition. In Dennis M. Bushnell and Jerry N. Hefner, editors, *Progress in Astronautics and Aeronautics Series, V-123, Viscous Drag Reduction in Boundary Layers*, pages pp.179–199. AIAA, 1990.

- [30] Kaldewaij en Van Tiel. *Voortgezette wiskunde, Differentiaalrekening en Integraalrekening, Deel I*. Bohn Stafleu Van Loghum, ISBN 90-313-0875-7, 3e druk edition, 1992.
- [31] J.L. Meriam and L.G. Kraige. *Engineering Mechanics: Dynamics*. John Wiley & Sons, Inc., ISBN 0-471-24167-9, 1998.
- [32] W.Johnson. *Helicopter theory*. Dover publications, ISBN 0-486-68230-7, 1980.
- [33] S.Newman. *The foundations of helicopter flight*. Butterworth-Heinemann, ISBN 0-340-587024, 1994.
- [34] W.Z.Stepniewsky and C.N.Keys. *Rotary-wing Aerodynamics*. Dover publications, ISBN 0-486-64647-5, 1984.
- [35] P. Lancaster and K. Salkauskas. *Curve and surface fitting: an introduction*. Academic Press, ISBN 0-12-436060-2, 1986.
- [36] Y. Lian, J. Steen, M. Trygg-Wilander, and W. Shy. Low Reynolds number turbulent flows around a dynamically shaped airfoil. In *AIAA Fluid dynamics Conference and Exhibit, 31st, Anaheim CA, 11-14 June 2001*, 2001.
- [37] P. Lorber, D. McCormick, T. Anderson, and D. MacMartin B. Wake. Rotorcraft retreating blade stall control. In *AIAA 00-2475, 2000, Fluids 2000 Conference and Exhibit, Denver Colorado, 19-22 June, 2000*.

- [38] E.F. Sheta, V.J. Harrand, and L.J. Huttsel. Active vortical flow control for alleviation of twin-tail buffet of generic fighter aircraft,. In *Aerospace Sciences Meeting and Exhibit, 38th, Reno, NV, Jan. 10-13, AIAA Paper 2000-906*, 2000.
- [39] A. Kumar and J.N. Hefner. Future challenges and opportunities in aerodynamics. In *Congress of the International Council of the Aeronautical Sciences, 22nd, Harrogate, United Kingdom, August 27-September 1, 2000*.
- [40] F. Tinapp and W. Nitsche. On active control of high lift flow. In W. Rodi and D. Laurence, editors, *Engineering turbulence modelling and experiments 4*, pages pp.179–199. Elsevier, 1999.
- [41] W.C. Reynolds and L.W. Carr. Review of unsteady driven separated flows. In *AIAA Paper 85-0527*, 1985.
- [42] V.Giurgiutiu, Z. Chaudhry, and C.A. Rogers. Active control of helicopter rotor blades with induced strain actuators. In *AIAA/ASME/ASCE/ASC 35th Structures, Structural Dynamics and Materials Conference and Active Structures Forum, April 18-22, South Carolina, Paper 94-1*, 1994.
- [43] V.Giurgiutiu and C.A. Rogers. Incrementally adjustable rotor-blade tracking tab using SMA composites. In *AIAA/ASME/ASCE/ASC*

- 38th Structures, Structural Dynamics and Materials Conference and Active Structures Forum, April 7-10, Kissimmee, FL, Paper 97-1387, 1997.*
- [44] G.A. Fleming and A.W. Burner. Deformation measurements of smart aerodynamic surfaces. In *Annual SPIE International Symposium on Optical Science, Engineering and Instrumentation, 44th, Denver, Colorado, July 18-23,, 1999.*
- [45] W.G. Bousman. A qualitative examination of dynamic stall from flight test data. *J. American Helicopter Soc.*, 43(4):pp.279–295, 1998.
- [46] B. Popescu and V.Giurgiutiu. Several considerations regarding the variable length rotor. *J. of Aircraft*, 31(4):pp.975–977, 1993.
- [47] R. Barret, Frye P., and Schliesman M. Design construction and characterisation of a flightworthy piezoelectric solid state adaptive rotor. *Smart Mater. Struct.*, 7:pp.422–431, 1998.
- [48] W. Geissler., H. Sobieczky, and H. Vollmers. Numerical study of the unsteady flow on a pitching airfoil with oscillating flap. In *European Rotorcraft forum, 24th, Marseilles, France, 15th-17th September, pp. AE 09, 1988.*
- [49] R.W. Prouty. *Helicopter performance, stability and control.* PWS Engineering Boston, ISBN 0-534-06360-8, 1985.

- [50] G.E.A. Meier. Active control of boundary layer separation. In G.E.A. Meier and G. H. Schnerr, editors, *Control of Flow Instabilities and Unsteady flows*. Springer-Verlag, Vienna, 1996.
- [51] P.R. Ashill and J.L. Fulker. A review of flow control research at DERA. In *IUTAM Symposium on Mechanics of Passive and Active Flow Control, Gottingen, Germany, 7-11 September, 1998*.
- [52] M.S. Chandrasekhara, M.C. Wilder, and L.W. Carr. The control of compressible dynamic stall using adaptive airfoils. In *IUTAM Symposium on Mechanics of Passive and Active Flow Control, Gottingen, Germany, 7-11 September, 1998*.
- [53] M.S. Chandrasekhara, M.C. Wilder, and L.W. Carr. Design and development of a dynamically deforming leading edge airfoil for unsteady flow control. In *ICIASF International Congress on Instrumentation in Aerospace Facilities, pp 132-140, 1997*.
- [54] M.Tenker, W.Geissler, and H.Sobieczky. Airfoils with dynamic transonic flow control. In *AIAA Applied Aerodynamics Conference, 18th, Denver, CO, August 14-17, 2000*.
- [55] M.S. Chandrasekhara, M.C. Wilder, and L.W. Carr. Competing mechanisms of compressible dynamic stall. In *AIAA Fluid Dynamics Conference, 27th, New Orleans, LA, June 17-20,, 1996*.

- [56] H. Lin, M. Vezza, and R.A. McD Galbraith. Discrete vortex method for simulating unsteady flow around pitching airfoils. *AAIA Journal*, 35(3):pp.494–499, 1995.
- [57] P.G. Wilby. The 1997 Cierva lecture: Shockwaves in the rotor world-A personal perspective of 30 years of rotor aerodynamic developments in the UK. *AAIA Journal*, 35(3):pp.494–499, 1995.
- [58] M. Kretz. Active elimination of stall conditions. *Vertica*, 6:pp.49–58, 1982.
- [59] P.G. Saffman and S. Tanveer. Prandtl-Batchelor model flow past a flat plate with a forward facing flap. *J. of Fluid Mech.*, 143:pp.351–365, 1984.
- [60] F. Tsiachris. Alleviation of dynamic stall on a helicopter rotor by means of a plain trailing edge flap. *Report 1*, Univ. of Glasgow(Department of Aerospace Engineering), 2001.
- [61] F. Tsiachris. Flap phasing and vorticity issues on a NACA 0015 fitted with a plain trailing edge flap. *Report 2*, Univ. of Glasgow(Department of Aerospace Engineering), 2002.
- [62] S.R. Hall and E.F. Prechtl. Development of a piezoelectric servoflap for helicopter rotor control. *Smart. Mater. Struct.*, 5:22–34, 1996.

- [63] E.F. Prechtl and S.R. Hall. Closed loop vibration control experiments on a rotor with blade mounted actuation. *Journal of Intelligent Material Systems and Structures*, 15(1):37–47, 2004.
- [64] J. Narkiewicz and M. Rogusz. Smart flap for helicopter rotor blade performance improvement.
- [65] R.P. Pescara. Screw propeller of helicopter flying machines. *U.S. Patent 1,449,129*. filed July 17th 1920, issued March 20, 1923.
- [66] C. D’Ascanio. Helicopter. *U.S. Patent 1,960,141*. filed February 5, 1930, issued May 22, 1934.
- [67] R.A. Young. Blade control mechanism for helicopters. *U.S. Patent 2,716,460*. filed February 28, 1952, issued August 30, 1955.
- [68] E.A. Stalker. Rotary wing aircraft. U.S. Patent 2,372,030. filed February 13, 1941, issued March 20, 1945.
- [69] C.I. Kaman. Aircraft of rotary wing type. U.S. Patent 2,455,866. filed August 19, 1946, issued December 7, 1948.
- [70] I.I. Sikorsky. Direct lift aircraft. U.S. Patent 1,994,448. filed June 27, 1931, issued March 19, 1935.
- [71] J.F. Donovan, L.D. Kral, and A.W. Cary. Active flow control applied to an airfoil. In *AIAA Aerospace Sciences Meeting, 36th, Reno, NV, Jan. 12-15, AIAA 1998-0210*, 1998.

- [72] J.H. Milgram. *A comprehensive aeroelastic analysis of helicopter main rotors with trailing edge flaps for vibration reduction*. PhD thesis, Univ. of Maryland, Department of Aerospace Engineering, 1997.
- [73] T. Lee. *High displacement piezoelectric trailing edge flap mechanism for helicopter rotors*. PhD thesis, Univ. of Maryland, Department of Aerospace Engineering, 1999.
- [74] A.P.F. Bernhard. *Smart helicopter rotor with active blade flaps*. PhD thesis, Univ. of Maryland, Department of Aerospace Engineering, 2000.
- [75] J.G. Reuster. *Dynamic stall alleviation using leading edge deformation*. PhD thesis, Univ. of Maryland, Department of Aerospace Engineering, 2001.
- [76] I.J. Taylor. *Study of bluff body flow fields and aeroelastic stability using a discrete vortex method*. PhD thesis, Univ. of Glasgow, Department of Aerospace Engineering, 1999.
- [77] G. R. Lowey. Recent developments in smart structures with aeronautical applications. *Smart Mater. Struct.*, 6:pp.R11–R42, 1997.
- [78] W. Johnson and N.D. Ham. On the mechanism on dynamic stall. *J. American Helicopter Soc.*, 17(4):pp.36–45, 1972.
- [79] W. Johnson. The effect of dynamic stall on the response and airloading

- of helicopter rotor blades. *J. American Helicopter Soc.*, 14(2):pp.68–79, 1969.
- [80] J. Liiva and F.J. Davenport. Dynamic stall of airfoil sections for high speed rotors. *J. American Helicopter Soc.*, 14(2):pp.26–33, 1969.
- [81] N.D. Ham and M.S. Garelick. Dynamic stall considerations in helicopter rotors. *J. American Helicopter Soc.*, 13(2):pp.49–55, 1968.
- [82] L.W. Carr. Progress in analysis and prediction of dynamic stall. *J. of Aircraft*, 25(1):pp.6–17, 1988.
- [83] M. Gad el Hak. Introduction to flow control. In *Flow control: fundamentals and practices*, page ISBN: 3540639365. Springer-Verlag, Berlin, 1998.
- [84] N.D. Ham. Aerodynamic loading on a two-dimensional airfoil during dynamic stall. *AIAA Journal*, 6(10):pp.1927–1934, 1969.
- [85] M. Achary and M.H. Metwally. Unsteady pressure field and vorticity production over a pitching airfoil. *AIAA Journal*, 30(2):pp.403–411, 1992.
- [86] W.J. McCroskey and R.K. Fisher. Detailed aerodynamic measurements on a model rotor in the blade stall regime. *J. American Helicopter Soc.*, 17(1):pp.20–30, 1972.

- [87] W.J. McCroskey, L.W. Carr, and K.W. McAlister. Dynamic stall experiments on oscillating airfoils. *AIAA Journal*, 14:pp.57–63, 1976.
- [88] W.J. McCroskey. The phenomenon of dynamic stall. Technical Report NASA TM-81264, 1981.
- [89] R.E. Mineck and P.M. Hartwich. Effect of full-chord porosity on aerodynamic characteristics of the NACA 0012 airfoil. Technical Report NASA TP-3591, 1996.
- [90] Jr W.H. Young. Fluid mechanics mechanisms in the stall process of airfoils for helicopters. Technical Report NASA TM-81956, 1981.
- [91] R.D. Joslin, G. Erlebacher, and M.Y. Hussaini. Active control of instabilities in laminar boundary layer flow: Part i: an overview. Technical Report NASA CR-195016, 1994.
- [92] S.S. Ravindran. Active control of flow separation over an aerofoil. Technical Report NASA TM-1999-209838, 1999.
- [93] H.A. Madsen F.Rasmussen, J.T.Petersen. Dynamic stall and aerodynamic damping. In *Aerospace Sciences Meeting and Exhibit, and 1998 ASME Wind Energy Symposium, Reno, NV, Jan. 12-15, AIAA-1998-0024*, 1998.
- [94] Y.H. Yu, S.Lee, K. McAlister, and C.Tung. Dynamic stall control for advanced rotorcraft application. *AIAA Journal*, 33(2):289–295, 1995.

- [95] P.V. Vorobieff and D.O. Rockwell. Vortex breakdown on pitching delta wing: Control by intermittent trailing edge blowing. *AIAA Journal*, 36(4):pp.585–589, 1998.
- [96] Kwing-So Choi, J. DeBisschop, and B.R. Clayton. Turbulent boundary layer control by means of spanwise oscillation. *AIAA Journal*, 36(4):pp.585–589, 1998.
- [97] I.J. Taylor, M. Vezza, and R.A. McD Galbraith. Computation of unsteady wind loading on bluff bodies using a discrete vortex method. *Wind and Structures*, 2(4):pp.285–303, 1999.
- [98] H.W. Liepmann and D.M. Nosenchuck. Active control of laminar turbulent transition. *J.of Fluid Mech.*, 118:pp.201–204, 1982.
- [99] H.W. Liepmann and D.M. Nosenchuck. Control of laminar instability waves using a new technique. *J.of Fluid Mech.*, 118:pp.187–200, 1982.
- [100] W.J. McCroskey. Some current research in unsteady fluid dynamics. *Journal of Fluids Engineering, Transactions of the ASME*(the 1976 Freeman Scholar Lecture):pp.8–39, 1977.
- [101] J.F. Currier and K.Y. Fung. Analysis of the onset of dynamic stall. *AIAA(Journal)*, 30(10):pp.2469–2477, 1992.
- [102] W.J. McCroskey, K.W. McAlister, L.W. Carr, and S.L. Pucci. Dy-

- dynamic stall on advanced airfoil sections. In *Annual Forum of the Am. Helicopter Soc., 36th, Washington DC, May 13-15, 1980.*
- [103] K. Nguyen. Active suppression of stall on helicopter rotors. In *European Rotorcraft Forum, 25th, Rome, Italy, September 14-16, 1999.*
- [104] R. Celi. Stabilization of helicopter blades with severed pitch links using trailing-edge flaps. *Journal of Guidance, Control and Dynamics*, 26(4):pp.585–592, 2003.
- [105] A.J. Potthast and A.W. Kerr. Rotor moment control with flap-moment feedback. *J. American Helicopter Soc.*, 20(2), 1975.
- [106] M.C. Robinson, H.E. Helin, and M.W. Luttges. Control of wake structure behind an oscillating aerofoil. In *AIAA CP-86-2282, Atmospheric flight mechanics conference*, 1986.
- [107] H.E. Helin, M.C. Robinson, and M.W. Luttges. Vortex control using a movable nose with pressure feedback. In *AIAA CP-86-2281, Atmospheric flight mechanics conference*, 1986.
- [108] C. Shih, L.M. Lourenco, and A. Krothapalli. Investigation of flow at leading and trailing edges of pitching-up airfoil. *AIAA journal*, 33(8):pp.1369–1376, 1995.
- [109] C. Shih, M. Lee, and C.M. Ho. Control of separated flow on a symmetric

- aerofoil. In *Proceedings of the IUTAM Symposium, Bangalore, India, Jan. 13-23, Berlin & New York Springer-Verlag, 1987.*
- [110] C. Shih, L. Lourenco, L. van Dommelen, and A. Krothopalli. Unsteady flow past an airfoil pitched at constant rate. In *ASME, International symposium on nonsteady fluid dynamics, 1990.*
- [111] L.A. Darden, K.G. Peterson, and N.M. Komerath. Vortex control using a moveable nose with pressure feedback. In *AIAA Atmospheric Flight Mechanics Conference, Baltimore, MD, Aug. 7-10, 1995, Technical Papers (A95-39269 10-08), AIAA-1995-3468, Washington, DC, 1995.*
- [112] W.J. McCroskey. Dynamic stall of airfoils and helicopter rotors. Technical Report AGARD R-595, 1972.
- [113] W. J. McCroskey. Recent developments in rotor blade stall. Technical Report AGARD CP-111, 1972.
- [114] W.P. Jones. Unsteady aerodynamics on helicopter rotors. Technical Report AGARD R-595, 1972.
- [115] M. Vezza. A new vortex method for modelling two-dimensional, unsteady, incompressible, viscous flows. Technical Report Glasgow Univ., G.U. Aero Report No.9245, 1992.

- [116] M. Vezza and R.A.McD. Galbraith. A method for predicting unsteady potential flow about an aerofoil. Technical Report Glasgow Univ., G.U. Aero Report No.8401, 1984.
- [117] M. Vezza and R.A.McD. Galbraith. Modelling of unsteady, incompressible separation on an aerofoil using an inviscid flow algorithm. Technical Report Glasgow Univ., G.U. Aero Report No.8412, 1984.
- [118] R.A.McD. Galbraith, M.W. Gracey, and E.Leitch. Summary of pressure data for thirteen aerofoils on the University of Glasgow's aerofoil database. Technical Report Glasgow Univ., G.U. Aero Report No.9221, 1992.
- [119] T.S. Beddoes. Representation of airfoil behaviour. *Vertica*, 7(2):pp.183-197, 1983.
- [120] T.S. Beddoes. A synthesis of unsteady aerodynamic effects including stall hysteresis. *Vertica*, 1:pp.113-123, 1976.
- [121] A.T. Conlisk. Modern helicopter aerodynamics. *Annu. Rev. Fluid Mech.*, 29:pp.515-567, 1997.
- [122] J.G. Leishman. Unsteady lift of a flapped airfoil by indicial concepts. *J. of Aircraft*, 31(2):pp.288-297, 1994.
- [123] N. Hariharan and J.G. Leishman. Unsteady aerodynamics of a flapped

- airfoil in subsonic flow by indicial concepts. *J. of Aircraft*, 33(5):pp.855–868, 1996.
- [124] R.B. Green, R.A. McD. Galbraith, and A.J. Niven. The convection speed of the dynamic stall vortex. Technical Report Glasgow Univ., G.U. Aero Report No.9202, 1992.
- [125] F. Nitzsche and E. Breitbach. Vibration control of rotary wings using smart structures. *Smart Mater. Struct.*, 3:pp.181–189, 1994.
- [126] K. Nguyen. Active control of helicopter blade stall. *J. of Aircraft*, 35(1):pp.91–98, 1998.
- [127] F.K. Straub. A feasibility study of using smart materials for rotor control. *Smart Mater. Struct.*, 5:pp.1–10, 1996.
- [128] O.S. Ryzhov. The formation of ordered vortex structures from unstable oscillations in the boundary layer. *USSR Comput. Maths. Math.Phys.*, 30(6):146–154, 1990.
- [129] F.T. Smith. Concerning dynamic stall. *Aero. Q.*, November(1982):331–352, 1990.
- [130] J.R. Olson. Reducing helicopter operating costs. *Vertiflite*, 39(1):10–16, 1993.
- [131] J.L. McCloud III. The promise of multicyclic control. *Vertica*, 4(1):29–41, 1980.

- [132] T.F. Myrtle and P.P. Friedmann. Vibration reduction in rotorcraft using the actively control trailing edge flap and issues for practical implementation. In *Annual Forum of the Am. Helicopter Soc., 54th, Washington DC, May 20-22, 1998.*
- [133] M.V. Fulton and R.A. Ormiston. Small-scale rotor experiments with on-blade elevons to reduce blade vibratory loads in forward flight. In *Annual Forum of the Am. Helicopter Soc., 54th, Washington DC, May 20-22, 1998.*
- [134] J.D. Baeder and B. Sim. Blade-vortex interaction noise reduction by active trailing edge flaps. In *Annual Forum of the Am. Helicopter Soc., 54th, Washington DC, May 20-22, 1998.*
- [135] F.O. Carta. An analysis of the stall flutter instability of helicopter rotor blades. In *Annual Forum of the Am. Helicopter Soc., 23rd, Washington DC, May 10-12, 1967.*
- [136] O. Ben-Zeev and I. Chopra. Advances in the development of an intelligent rotor employing smart trailing edge flaps. *Smart Mater. Struct.*, 5:pp.11–25, 1996.
- [137] D.K. Samak and I. Chopra. Design of high force, high displacement actuators for helicopter rotors. *Smart Mater. Struct.*, 5:pp.58–67, 1996.

- [138] R.L. Roglin and S.V. Hanagud. A helicopter with adaptive rotor blades for collective control. *Smart Mater. Struct.*, 5:pp.76–88, 1996.
- [139] R. Barret. All-moving active aerodynamic surface research. *Smart Mater. Struct.*, 4:pp.65–74, 1995.
- [140] R. Barret and J. Stutts. Design and testing of a 1/12th-scale solid state adaptive rotor. *Smart Mater. Struct.*, 6:pp.491–497, 1997.
- [141] A. Chattopadhyay, C.E. Seely, and L. Mitchell. Design of a smart flap using polymeric c-block actuators and a hybrid optimisation technique. *Smart Mater. Struct.*, 6:pp.134–144, 1997.

